Dissertation

submitted to the

Combined Faculty of Natural Sciences and Mathematics

of the Ruperto Carola University Heidelberg, Germany

for the degree of

Doctor of Natural sciences

Presented by

M.Sc. Markus Kurth

born in: Düren, Germany

Dissertation

submitted to the

Combined Faculty of Natural Sciences and Mathematics

of the Ruperto Carola University Heidelberg, Germany

for the degree of

Doctor of Natural sciences

Presented by

M.Sc. Markus Kurth

born in: Düren, Germany

Oral examination: 21.03.2019

Probing the lipid environment of the G-protein coupled receptor Metabotropic glutamate receptor 2

Referees: Prof. Dr. rer. nat. Britta Brügger

Prof. Dr. rer. nat. Irmgard Sinning

I. Table of contents

II. Table of figures

II Table of figures

III. Summary

The Metabotropic glutamate receptor 2 (mGluR2) belongs to the family of G-protein coupled receptors, a specific class of transmembrane proteins involved in cellular signaling. The functionality of such transmembrane proteins has been identified to largely depend on their microenvironment, namely the lipid bilayer surrounding them. However, the regulation of the receptors by their lipid microenvironment remains poorly understood. In particular, it remains unclear how specific protein-lipid interactions may modulate the function of mGluR2.

In the last years, general motifs for non-covalent cholesterol and sphingolipid interaction within helical domains of transmembrane proteins have been described. In these motifs, both tryptophan and tyrosine residues have been found to play a decisive role. For that reason, an alanine mutagenesis screening, targeting tryptophan and tyrosine residues at the transmembrane surface, was carried out in the search of specific sphingolipid or cholesterol interaction sites for mGluR2. For the different Y→A and W→A variants, surface biotinylation and co-immunoprecipitation showed that neither trafficking nor dimerization were disturbed by substitution of these aromatic residues. In contrast, cellular photo-crosslinking assays demonstrated that cholesterol binding was compromised if one tyrosine residue located at the helix five or another at the helix six was replaced.

Thus, these experiments suggested these two helices to contain specific cholesterol binding sites. To get a better molecular insight into these specific protein-lipid interactions, lipid binding to the transmembrane domain of mGluR2 was investigated in molecular dynamics (MD) simulation. The molecular dynamics simulations in GROMACS were performed in collaboration with the Max Planck tandem group of Dr. Camilo Aponte-Santamaría. All-atom and coarse-grained MD simulations of the mGluR2 transmembrane domain confirmed the experimental observation, by revealing a highly-localized density of cholesterol near these residues in helices five and six, which smeared out when they were changed to alanine *in silico*. The simulations also revealed flexibility of the protein structure at the exoplasmic end of helix six which changed upon introduction of point mutations. Overall, the work combining functional assays and MD simulations demonstrated the existence of specific cholesterol binding sites in mGluR2. It will be highly interesting to investigate the functional implications of this newly-found specific protein–cholesterol interaction on the activity and conformation of the receptor.

IV. Zusammenfassung

Der metabotrope Glutamatrezeptoren 2 (mGluR2) gehört zu der Familie der G-Protein-gekoppelten Rezeptoren (GPCRs). GPCRs sind Transmembranproteine, die an der zellulären Signaltransduktion beteiligt sind. Die Funktionalität dieser Transmembranproteine wird wesentlich von den zellulären Membranen und deren Lipidzusammensetzung beeinflusst. Die genaue Interaktion der Membranlipide mit den Transmembranproteinen ist jedoch oft nur unvollständig verstanden. Im Besonderen ist für den Rezeptor mGluR2 der Einfluss solcher Protein-Lipid-Interaktionen noch nicht vollständig begriffen.

In den letzten Jahren wurden Motive für die Interaktion von Cholesterin und Sphingolipiden mit α-helikalen Transmembranproteinen beschrieben. Die aromatischen Aminosäuren Tryptophan (W) und Tyrosin (Y) waren häufig Teil dieser Interaktionsmotive. Aus diesem Grund wurden diese beiden aromatischen Aminosäurereste in einem Alanin-Screening der Transmembrandomäne des mGluR2 Rezeptors einzeln ausgetauscht. Die acht Y→A oder W→A mGluR2 Varianten zeigten im zellulären Transport keine Auffälligkeiten; alle acht schienen korrekt durch den anterograden Transportweg zur Plasmamembran zu gelangen. Überdies hatte der Austausch der aromatischen Aminosäurereste gegen Alanin keinen entscheidenden Einfluss auf die Homodimerisierung des Rezeptors zu haben. Im Gegensatz dazu zeigte sich in zellulären Kreuzvernetzungsansätzen mit bifunktionalen Lipiden, dass die Cholesterininteraktion bei den Varianten Y745A und Y781A, lokalisiert in den Transmembranhelices fünf und sechs, im unter *steady state*-Bedingungen reduziert war.

Um den molekularen Mechanismus der reduzierten Cholesterininteraktion an den Helices fünf und sechs zu entschlüsseln, wurde die Transmembrandomäne des mGluR2 Rezeptors in einer computergestützten Molekulardynamik (MD)-Simulation näher untersucht. Die MD-Simulationen wurden mit dem Programm GROMACS in Zusammenarbeit mit Dr. Camilo Aponte-Santamaría (Max Planck-Tandem Gruppe Computational Biophysics, Universität Los Andes, Bogotá) durchgeführt. Die atomistischen und coarse-grained Simulationen in Phospholipid-Membranen zeigten unter anderem an den Helices fünf und sechs signifikant erhöhte Affinität zu Cholesterin. Diese Cholesterininteraktion wurde durch die Einführung der Y745A- und Y781A-Variante auch *in silico* gestört. Zusammengefasst legen die Daten eine spezifische Interaktion zwischen dem mGluR2 Rezeptor und Cholesterin nahe, die unter Umständen auch Einfluss auf die Konformation der Transmembrandomäne haben könnte, wie erste Untersuchungen zur Root mean square fluctuation (RMSF) der Aminosäurereste angedeutet haben.

1 Introduction

The eukaryotic cell is separated into different compartments which are enclosed by biological membranes. The membranes are self-assembling and conformationally flexible lipid bilayers of about 5 nm. Depending on the cellular compartment they have changing lipid compositions (1). The lipid bilayers of the secretory pathway exhibit an increasing complexity from the endoplasmic reticulum (ER), to the Golgi apparatus and the plasma membrane. The early secretory pathway of the ER and *cis*-Golgi apparatus is distinguished by a low charge density and loose packing (2). From the *trans*-Golgi to the plasma membrane, the bilayer sees an increasing cholesterol content and saturation of fatty acids which pack more tightly in the membrane (2). In addition, the membrane composition becomes more complex with a lateral asymmetry existing between the leaflets of the plasma membrane (reviewed by van Meer, Voelker (3)) (Figure 1.1).

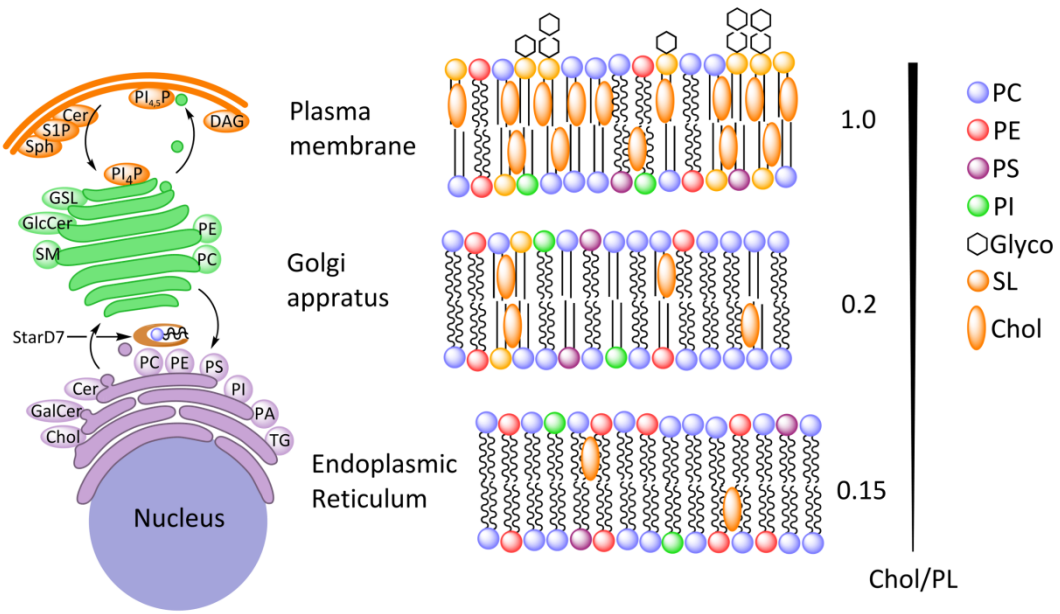

Figure 1.1 | Lipid metabolism and transport in mammalian cells. The graphics represents an overview of the lipid metabolism and transport from the endoplasmic reticulum (ER) to the plasma membrane. The glycero-lipids phosphatidylcholin (PC), phosphatidylethanolamine (PE), phosphatidylserine (PS), phosphatidylinositol (PI), and triayclglycerol (TAG) are synthesized in the ER along with the sphingolipids ceramide (Cer), galactoyslcermide (GalCer), as well as cholesterol (Chol). The lipids shuttle through the secretory pathway via vesicular transport or transfer proteins, such as the PC carrier StarD7. In the Golgi appartus sphingomyelin (SM), glucosylcermide and complex gangliosides (GSL) are synthesized. Some lipids, like phosphorylated PI species, are specifically localized to distinct membranes, like PI(4,5)P_2 to the plasma membrane. In the plasma membrane signal induced hydrolysis of sphingolipids to sphingosine-1-phosphate (S1P) and sphingosine (Sph) takes places. From the ER to the plasma membrane the cholesterol content increases (Chol/Phospholipids(PL)) and the membrane becomes increasingly packed and with a lateral asymmetry between the leaflets. Drafted in ChemDraw (Ver. 16.0.1.4, PerkinElmer Informatics, Waltham, USA) with modifications from van Meer, Voelker (3) and Holthuis and Levine (2).

The resulting properties of these mixtures of lipids are often broken down to the parameter of liquid (dis-)order: the disordered phase shows a higher content of low melting lipids ((poly-)unsaturated fatty acyl chains, low cholesterol content) whereas the ordered phase is rich in high melting lipids (saturated fatty acyl chains, high cholesterol content) (4). In complex lipid mixtures phases may coexist within one membrane structure. The resulting alternating biophysical properties between and within the membrane structures contribute to the function of the peripheral or integral membrane proteins. The function of the lipid bilayer as microenvironment of membrane proteins is not well understood and is the subject of this thesis.

1.1 Protein-lipid interactions

Both peripheral and integral membrane proteins shape the curvature, thickness and composition of membranes and are themselves attracted by certain biophysical or biochemical properties of membranes (2, 5). The binding of peripheral proteins can for example dependent on the packing of the membrane. One example is the ArfGAP1 protein involved in COPI trafficking within the early secretory pathway. ArfGAP1 binds via its ALPS motif to highly curved membranes, which are characterized by packing defects in the lipid bilayer (6). Others proteins depend on the presence of specific lipid headgroups at the surface of the lipid bilayer, such as phosphoinositide-binding proteins. Different phosphorylation states of the phosphatidylinositol (PI) headgroup were found as organelle marker and recruit proteins with different Pleckstrin homology domains (7). An example is PI(4,5)P_2, which is a plasma membrane marker and is involved in transient recruitment of soluble proteins to the membrane (8). Some lipid transport proteins not only recognize specific lipid classes but also have binding pockets that can accommodate specific lipid species. Examples are START-domain proteins that have a ~210 amino acid domain which forms a binding pocket for the cytosolic transport of lipids (9). One of these proteins, Star-D7, was found to have a specific function in phosphatidylcholine (PC) transport (10).

For the presented examples in lipid transport and signaling, distinct consensus motifs within the peripheral proteins have evolved. These consensus motifs allowed uncovering additional family members once the functional motif had been identified. This was for example done for the START-domain lipid transporters or the signaling proteins with a Pleckstrin homology domain (7, 11, 12). Compared to that, so far a few conserved amino acid sequences or structural domains within integral membrane proteins have been described to participate in

covalent lipid modifications or non-covalent interactions with lipids. This is due to their often transient nature and the low conservation of modification and interaction sites. Here we further go into detail as the lipid interaction of integral membrane proteins is the central subject of this thesis.

G-protein coupled receptor (GPCR) signaling complexes are often used as model to study both covalent lipid modification and non-covalent interactions (reviewed by Escriba, Wedegaertner (13)). This is because they are a highly relevant drug targets and at the same time are influenced by a nearly all known lipid modification and interactions events. The GPCRs make up a total of about 800 genes in the human genome which have been mostly characterized by the hepta-α-helical transmembrane domain (14). The seven α-helices are connected by three intra- and three extracellular loops with the N- and C-termini being extra- and intracellular, respectively (14, 15). While the fold of the transmembrane domain is conserved, the N- and C-terminal end showed greater variation in length and structure (16). The C-terminal end is usually unstructured but is often associated with regulatory post-translational modifications (see Section 1.2.4). The N-terminal end can greatly vary in length and structure. While for family A usually is very short N-termini, the other families possess large extracellular ligand binding sites (16). Other features, like G-protein coupling, the ligand and its binding site, have not been uncovered for all receptors (17). According to the International Union of Basic and Clinical Pharmacology, the human GPCRs are classified into four classes: Rhodopsin receptors (Family A), Secretin receptors (Family B), Metabotropic glutamate receptor (mGluR) family (Family C) and Frizzled receptors (Family F) (18).

1.1.1 Covalent lipid modifications of proteins

Both peripheral and integral membrane proteins can be covalently modified with lipids. Especially for GPCR complexes a diverse set of lipid modifications is found both on the (integral) membrane receptors, on which this work is focused, as well as on the downstream located (peripheral) trimeric G-proteins (see Figure **1.2**).

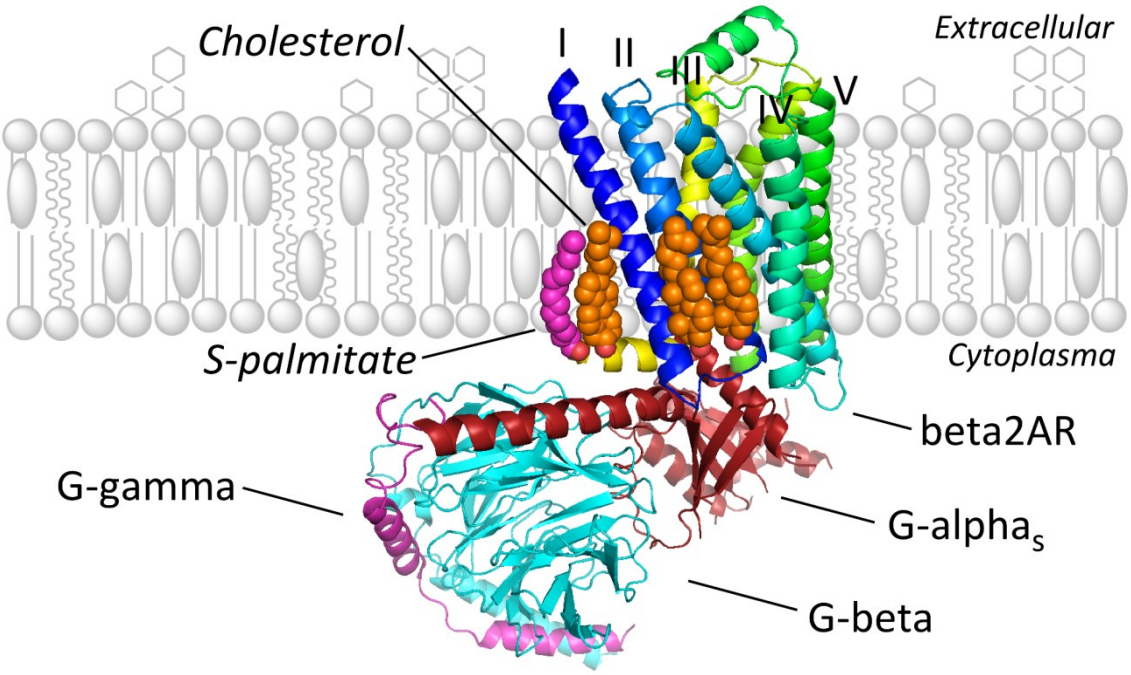

Figure 1.2 | β2-adrenergic receptor coupled to heterotrimeric $G\alpha_S/\beta\gamma$. The graphic shows an approximated binding site of the heterotrimeric G-protein complex (G-alpha$_S$, G-beta, G-gamma) to the β2-adrenergic receptor (beta2AR) coupled on the cytoplasmic side (19, 20). The beta2AR structure was crystallized with the S-palmitoylation (purple spheres) at C341 and one adjacent cholesterol molecule (orange spheres). Two more cholesterols are bound at a cleft between helix I and IV (indicated above the transmembrane helices). Drafted in ChemDraw with modifications from Liang, Khoshouei (19) and Cherezov, Rosenbaum (20). The relative position of the G-protein to the receptor and the membrane are approxiamated and do not depict a physiological assembly.

1.1.1.1 Modification of GPCRs by S-palmitoylation

All GPCRs are integral membrane proteins with a hepta-α-helical transmembrane domain. Therefore they require the hydrophobic core of the membrane as solvent but do not depend on covalent lipid modification to ensure membrane localization (13). However, the receptors are subject to regulatory post-translational lipid modifications of which S-fatty acylation is the most prominent one (13). S-palmitoylation via a thioester to cysteine residues usually occurs in the cytoplasmically localized C-terminal domain of the receptors and is catalyzed by DHHC-family palmitoyltransferases (21, 22). With a total of 23 enzymes, the members of the DHHC-family are located in the early and late secretory pathway (23). This goes along with the finding that S-fatty acylation of GPCRs was found in some cases to be required for correct trafficking, for example for the Chemokine receptor 5 (24). For other GPCRs, such as the beta2-Adrenergic receptor (β2AR), S-palmitoylation was suggested to be involved in modulating receptor activity or, like for the 5-Hydroxytryptamine 1A Receptor (5-HT-1A), in association with specific membrane domains (25, 26) (see also Figure 1.2). As opposed by other types of protein acylation, palmitoylation can be reversed by the action of acylprotein thioesterases. Thus, S-palmitoylation is considered a flexible post-translational modification

(27). However, both for S-palmitoylation and depalmitoylation only a few enzyme-receptor pairs have been assigned so far (28, 29). A fact that hampers the identification of new palmitoylation sites is that even though predictive algorithms are available no definite consensus sequence has been established so far (30). Web-based programs like CSS-Palm were trained with a data set of experimentally determined palmitoylation sites (31).

1.1.1.2 Covalent lipid modifications of G-proteins

G-proteins are the downstream effectors of GPCRs usually coupled to the receptors at the cytoplasmic side of the plasma membrane. In contrast to the receptor, both α- and βγ-subunit of the trimeric G-protein complex are peripheral and thus rely on lipidation for membrane association. To shuttle through the secretory pathway to the plasma membrane, the isoprenylated βγ-subunit of the heterotrimeric G-proteins needs to pair with the fatty acylated α-subunit in the ER or Golgi apparatus (32, 33).

For the G-protein α-subunit both S-palmitoylation and N-myristoylation sites were identified (reviewed by Escriba, Wedegaertner (13)). N-myristoylation is a co-translational and irreversible modification catalyzed by the N-myristoyltransferase at the N-terminal glycine of target proteins after the start methionine residue has been removed (34). While the N-myristoylation is static, the more flexible S-palmitoylation sites appeared for some α-subunits, as for example $G\alpha_S$ or $G\alpha_0$, to be connected to dynamic shuttling between plasma and Golgi membrane or endocytic vesicles (35-37). For the βγ-subunit of the heterotrimeric G-protein, isoprenylation sites on the consensus motif CaaX have been identified. The cysteine residue is irreversibly linked to a either a farnesyl or a geranylgeranyl moiety by either a farnesyl or a geranylgeranyl transferase. The cysteine residue is followed by two aliphatic amino acid residues and an amino acid X that determines the nature of the modification (13, 38).

1.1.2 Non-covalent lipid interactions of integral membrane proteins

In contrast to covalent lipid modifications of proteins, non-covalent protein-lipid interactions within the membrane are often more difficult to study because of their transient nature. Another layer of complexity is also the presence of annular and non-annular membrane lipids surrounding transmembrane proteins (39). The former one describes the first lipid shell at the surface of the transmembrane protein. At the roughened surface the fatty acyl chains of the annular lipids usually get distorted when they adapt to the more solid protein structure (40). This process is mainly driven by unspecific forces, such as hydrophobic interactions of the

acyl chains or electrostatic interactions of the head groups. Non-annular lipids display a different kind of interaction in binding with a low k_{off} rate distinct spots or pockets on the protein surface (5). This first lipid shell of lipids is also influenced by the overall thickness of the bilayer and the structure of the protein's transmembrane domain. To avoid hydrophobic mismatches either the lipid bilayer, the protein or both have to adapt (41).

1.1.2.1 Modulation of GPCR activity by interactions with cholesterol and glycerolipids

For the GPCR rhodopsin it has been shown that protein function depends on the presence of unsaturated PE, but also PC and PS, species in the rod membranes. Low-melting docosa-hexaenoic and oleic acid glycerolipids adapt to the α-helical surface structure and are thought to facilitate allosteric changes in the receptor structure towards an active state (42, 43). An increasing cholesterol content makes the membrane more rigid and shifted the equilibrium of rhodopsin towards the inactive state (44). For β2AR, cholesterol was co-crystallized with the receptor (45).Here, two cholesterol molecules were bound in a groove between the helices I, II, III and IV (see Figure 1.3 A). From the structure a cholesterol consensus motif (CCM) for GPCRs was determined: [4.39-4.43(R,K)]—[4.50(W,Y)]—[4.46(I,V,L)]—[2.41(F,Y)] according to the helix numbering by Ballesteros and Weinstein (46). The site distinguished itself by similarities with cholesterol binding motifs identified earlier and the spatial distribution of the conserved residues in family A receptors (45). The experimental findings were later confirmed by molecular dynamics simulations (47). These in silico studies showed that the CCM groove between helices I and IV on the intracellular site occupied by cholesterol in the crystal structure 3D4S was also occupied in atomistic molecular dynamics simulation (47). Notably the simulations, which were performed in a DOPC bilayer with up to 40mol% cholesterol, showed two more specific cholesterol binding sites within the dimer: one in an intracellular cleft between helices V and VI, and another one between helices VI and VII on the extracellular leaflet. Also coarse-grained molecular dynamic simulations – simulation conducted at a lower resolution – of β2AR dimers in a POPC bilayer system with 9-50mol% cholesterol showed a cholesterol density for the CCM motif (48). Further experiments found that the cholesterol binding had thermostabilizing activity (45). A similar effect was found for the Oxytocin receptor (49). Concerning the physiological meaning, further experimental data have suggested that while β2AR resided in disordered phase its interaction partners were found in raft-like regions (50, 51). Subsequently the depletion of cholesterol led to an increased basal activity.

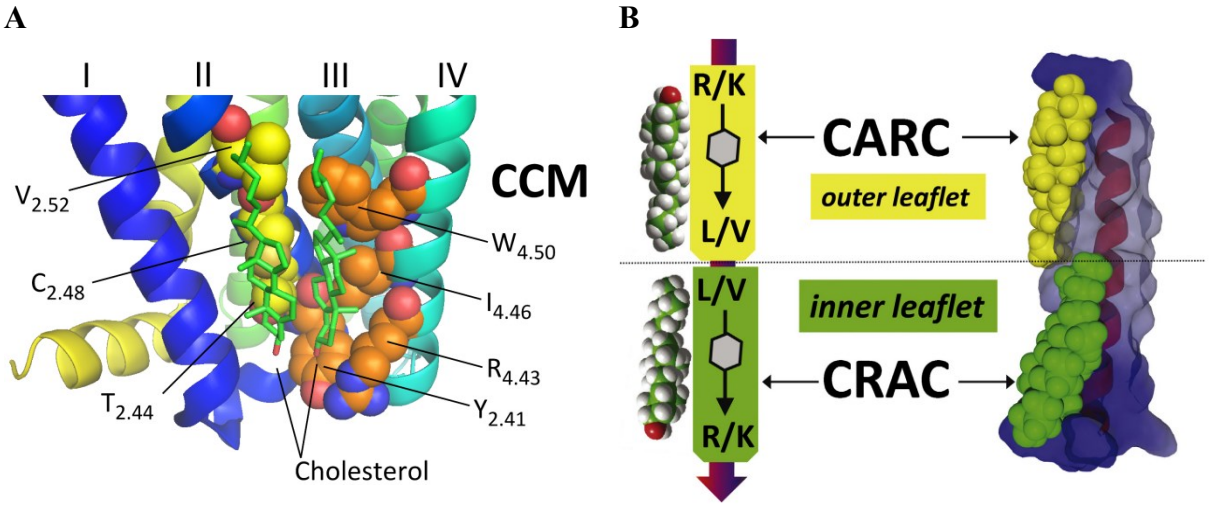

Figure 1.3 | Non-covalent cholesterol interaction sites. (**A**) A cholesterol consensus motif (CCM) in the beta2-Adrenergic receptor (45). The four amino acid residues assigned to the 3-dimernsional motif are localized in helices II and IV (indicated above): [4.39-4.43(R,K)]—[4.50(W,Y)]—[4.46(I,V,L)]—[2.41(F,Y)] (depicted in orange spheres). Notably there were also further residues involved in binding a second cholesterol with a reduced number and less conserved interaction sites (depicted in yellow spheres). The graphic was generated with Pymol (Ver. 1.7.0.3, Schrödinger, New York, USA) and ChemDraw. (**B**) The cholesterol recognition/interaction amino acid consensus (CRAC) with the consensus motif *N*-(L/V)X_{1-5}YX$_{1-5}$(R/K)-*C* and its inverted counter part CARC with the sequence *N*-(K/R)X_{1-5}(Y/F)X_{1-5}(L/V)-*C* bind cholesterol to α-helical structures (52, 53). By bioinformatics more sites were found in different GPCRs and other integral membrane proteins. Graphic retrieved with permission (License Number 4498110779910) from Fantini, Di Scala (54).

A direct role of cholesterol in modulating receptor activity was described for the 5-hydroxytryptamine receptor 1A (5-HT-1A) and the Metabotropic glutamate receptor 2 (mGluR2) (26, 55). 5-HT-1A was suggested to reside in raft-like membrane domains. Both partitioning to these domains and coupling to $G\alpha_i$ protein was reported to be dependent on palmitoylation of the GPCR (26). mGluR2 was reported to partion into liquid-ordered membrane regions upon activation and to alter its affinity toward an agonist upon cholesterol depletion (55). The mGluR2 homologue mGluR1 showed a similar behavior as ectopic expressed protein in human cells: Upon activation the protein shifted cholesterol-dependent into liquid-ordered phase (56). In the liquid-ordered phase, the cholesterol interaction with the receptor appeared to be at least partly dependent on another cholesterol binding motif, the cholesterol recognition/interaction amino acid consensus (CRAC) motif (see Figure 1.3 B). A *N*-(L/V)X_{1-5}YX$_{1-5}$(R/K)-*C* motif is present in the 5th helix of the heptahelical domain and is conserved throughout the whole mGluR family. Disruption of the motif by point mutations led to a decrease in coupling to downstream effectors (56). Notably also the 5-HT-1A and the Oxytocin receptor contain a CRAC motif within the transmembrane helix V (57).

The original CRAC motif was discovered in the cytosolic portion of a cholesterol transport protein, the Peripheral-type benzodiazepine receptor (52). A CRAC inverted motif *N*-(K/R)X_{1-5}(Y/F)X_{1-5}(L/V)-*C*, defined as CARC motif, was studied in the integral membrane

protein human Nicotinic acetylcholine receptor by molecular docking experiments after the cholesterol interaction to single helices in the receptor had been tested earlier (53, 58) (see Figure 1.3 B). Both the CRAC and the CARC motif are defined by a triad of basic (R/K), aromatic (F/Y) and aliphatic (L/V) amino acid residue (54). The basic residues are thought to interact with the 3'OH group of cholesterol that orients towards the surface of the membrane bilayer. The aromatic residue residing in the hydrophobic phase of the membrane bilayer was suggested to stack on the aliphatic ring system of cholesterol (59). Finally the aliphatic amino acid residue is thought to interact with the branched hydrocarbon chain attached to the C-17 atom of the cyclopentane ring (59). Both motifs are found in a variety of transmembrane domains even though only few of them have been confirmed experimentally or by *in silico* studies (reviewed by Fantini, Di Scala (54)).

Interaction of GPCRs with sphingolipids

In contrast to cholesterol, sphingolipids have gained less attention in protein-lipid interaction studies with GPCRs. This is remarkable because of the well-studied co-partitioning of cholesterol and sphingolipids into membrane domains. The findings published concerning GPCRs dealt mostly with effects of inhibition of the sphingolipid metabolism (60-62). Only few studies focused so far on specific interactions of GPCRs with sphingolipids. One example is a coarse-grained simulation study of the human 5-hydroxytryptamine (serotonin) receptor 1A (5-HT-1A) which showed binding of the sphingolipid monosialotetrahexosylganglioside (GM1) to the first extracellular loop of the protein (63). The motif was suggested to be homologues to a sphingolipid binding domain (SBD) identified as V3(-like) domain in HIV protein gp120, Prion protein and Alzheimer β-amyloid (64). As in these different proteins, the helix-loop-helix structure in 5-HT-1A showed a combination of aromatic, basic and turn-inducing amino acid residues (63) (Figure 1.4 A). The actual contact with the sugar tree of GM1 was established by an aromatic tryptophan residue in the loop. However, the SBD was more of a structural motif which had been established by homology (64).

Apart from the SDB, only one other sphingolipid interaction domain in proteins has been identified so far. In the COPI machinery protein p24 a specific sphingomyelin binding motif had been identified by means of cellular, *in vitro* and *in silico* experiments (65). The single-spanning integral p24 protein is the membrane resident anchor for the COPI vesicle budding machinery (66). The sphingomyelin interaction motif *N*-VX_2-TL-X_2IY-*C*, sensitive to perturbations by point mutations, was found opposite to the designated dimerization interface (65) (Figure 1.4 B). The simulation studies suggested an interaction of the tyrosine residue

with the choline moiety of sphingomyelin while the beta-branched residues and leucine interacted with sphingosine and fatty acid chain.

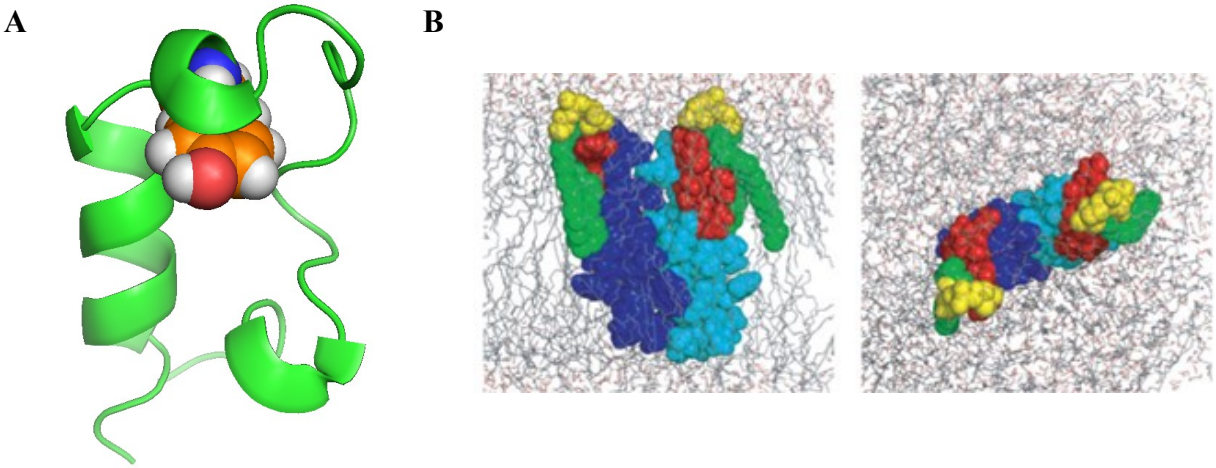

Figure 1.4 | Sphingolipid interaction motifs. (**A**) The V3(-like) domain in HIV protein gp120 was identified as structural sphingolipid binding domain (SBD). Presumably, the aromatic amino acid tyrosine in the loop (Carbon atoms highlighted as orange spheres) plays a role in the binding of the sugar tree of GM1 (64, 67). The graphic was generated in Pymol. (**B**) The sphingolipid interaction site in the transmembrane domain of the COPI machinery protein p24 (dimer, depicted in light and dark blue) is thought to have a sphingomyeline (cholin headgroup: yellow, acyl chains: green) interaction site (highlighted in red) opposite to the p24 dimerization interface. Graphic retrieved with permission (License Number 4498091273490) from Contreras, Ernst (65).

1.1.3 Methods to study protein-lipid interactions

The methods mentioned in the previous chapters can be divided into experimental and computational methods. The former ones were especially useful in identifying novel covalent lipid modification sites. The identified modification sites were then used to search for homologous motifs by means of bioinformatics. For some modifications, like isoprenylation, consensus motifs have been identified while for others, like S-palmitoylation, trained algorithms are available (31, 38). Such trained algorithms have also been used for non-covalent interaction sites, like the CCM or sphingolipid interaction motif (45, 68). As methods to define non-covalent lipid interaction sites in proteins are especially laborious, also molecular dynamics simulation have got more and more attention to confirm or also predict novel sites (69).

1.1.3.1 Experimental methods to identify and characterize protein-lipid interactions

The most powerful methods to date are X-ray crystallography, cryo-electron microscopy and native mass spectrometry. The CCM has been identified by co-crystallization and X-ray crystallography of the β2AR with cholesterol (45). Further interaction sites of GPCRs with cholesterol have been identified for example in the Serotonin receptor 5-HT-2B, of which two homologues are used in the thesis, and also mGluR1 was co-crystallized with cholesterol at

the dimer interface (70, 71). In the context of crystallization cholesterol could be both a non-annular lipid and/or a stabilizing agent. Close to that approaches was the electron 2D-crystallization performed by the group of Thomas Walz (72): the structure of the Aquaporin was resolved along with the annular glycerolipids bound to the surface. As for the X-ray crystallography, specific lipid types added to the stability of the crystal (73). Another way to resolve the lipid shell is mass spectrometry. One example is the identification of lipids driving the oligomerization integral membrane proteins by native mass spectrometry (74). Notably, the study identified the lipid set bound at the protein-protein interface but would not resolve the whole lipid shell (74). Another mass spectrometry-based approach was chosen to resolve the sphingolipid binding to the COPI protein p24 (75) (see also Section 0). A sphingomyelin lipid with diazirine group was incorporated into proteoliposomes with the p24 transmembrane domain which was then UV-crosslinked to the molecules. Prerequisite for this kind of experiments is knowledge of the binding preferences for the protein *in vivo*.

A technique to identify protein-lipid interaction *in vivo* is metabolic labeling of cells with functionalized lipid precursors that carry either a radioactive isotope or a terminal alkyne group amenable to click-chemistry (see Figure 1.5 A). Radioactive groups have proven powerful tools for the identification of covalent lipid modifications, such as palmitoylation (76). For non-covalent lipid interactions, reporter lipids are used that contain a diazirine group to allow for UV-crosslinking to proteins in closest proximity (77, 78) (see also Figure 1.5 B). Alternative introduction of alkyne groups in these photoactivatable lipids then also allowed identifying lipid interactomes (79, 80). Here the alkyne group is ‘clicked’ to biotin which is then used to pull-down all proteins interacting with the bifunctional lipid. Data from these experiments can again be used to enhance *in vitro* experiments or *in silico* approaches.

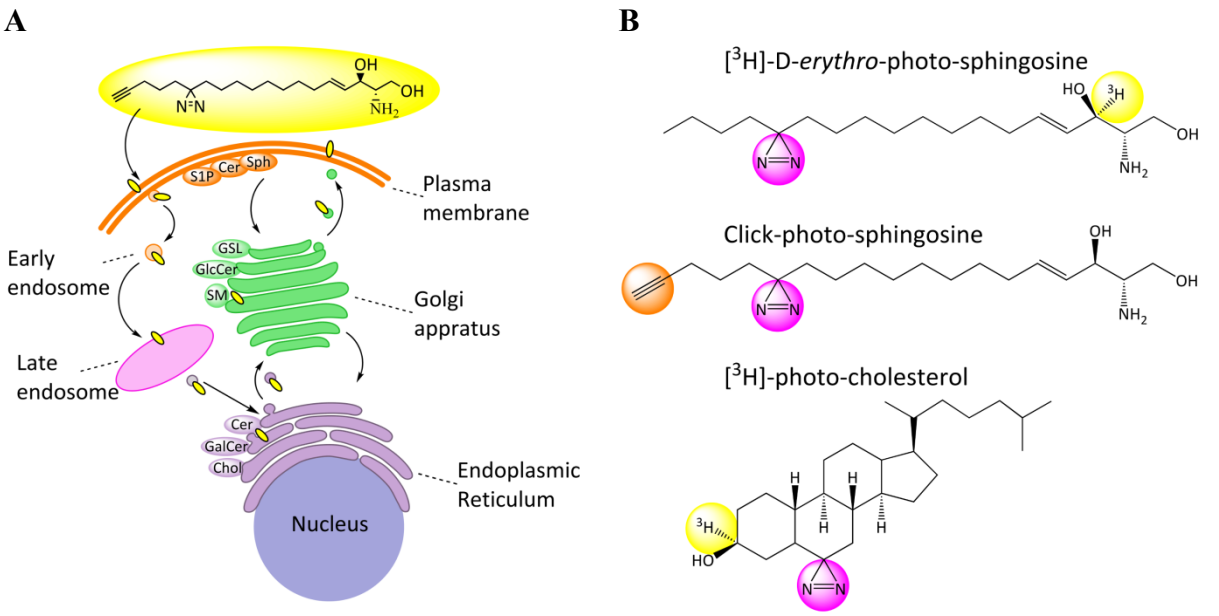

Figure 1.5 | Cellular distribution and metabolism of sphingolipid and cholesterol analogues. (**A**) The simplified depiction shows that the uptake of precursor lipid analogues, like photoactivatable and click-able(PAC)-sphingosine, via the endocytotic pathway (80). From there on the lipid probes are distributed and metabolized by different enzymes in the endoplasmic reticulum (Ceramide (Cer), Galactosylceramide (GalCer), Cholesterol (Chol)). Further metabolism happens in the Golgi (Sphingomyelin (SM), Glucosylceramide (GlcCer), Gangliosides (GSL)). At the plasma membrane functionalized lipids can be broken down again (Sphingosine-1-phosphate (S1P), Sphingosine (Sph)). (**B**) Different functionalized lipids carry groups for detection (Tritium or alkyne, labeled in yellow and orange), as well as for crosslinking (diazirine, violet). (**C**) A simplified scheme of the sphingolipid metabolism shows that the sphingosine analogues enter the metabolism via a degradation pathway (deep purple) while the *de novo* synthesis happens inside the ER (light purple). Graphic retrieved with permission (Account #3001385975) from Haberkant, Stein (80). Copyright (2018) American Chemical Society.

1.1.3.2 Molecular dynamics simulations to study protein-lipid interactions

It is often difficult for experimental methods, like crystallography, to capture the molecular picture of (non-)annular lipid binding to proteins. Molecular dynamics (MD) simulation is a well-established technique that in the recent years has proven successful to address this issue (69). MD simulations monitors the spatio-temporal evolution of biomolecular systems at atomistic or quasi-atomistic (coarse-grained) level, to thereby reveal functionally relevant structural, (thermo-)dynamic, and energetic information, that complements and guides experimental methodologies. MD has been exhaustively used to understand the interplay

between lipids and proteins in biological membranes (69, 81, 82). The simulations revealed key details on how proteins alter the conformational architecture of their surrounding lipids, how in turn lipids modulate the activity of membrane proteins, and how complex compositions of lipids and proteins coexist to give raise to diverse functionalities of biological membranes.

As mentioned above, there are two important kinds of MD simulations for protein-lipid interaction: atomistic and coarse-grained. While the former one assigns position, velocity, long- and short-range interactions for explicitly each atom, the latter one merges several atoms into one bead for which the physical properties are calculated (69). To conduct the simulation, one needs a force-field to parameterize the physical properties and a program in which to calculate. For membrane system the CHARMM36 (83) and for the coarse-grained simulations the Martini force field (84) were used in the thesis. Both have been designed for proteins and were extended to lipids later on. CHARMM36 is especially convenient because of the online program CHARMM-GUI which allows step-by-step assembly of the system with all data generated for the energy minimization and production run of the system generated automatically (85, 86). Likewise, for MARTINI the program Insane allows to assemble solvated bilayer system with a simple command line and obtain preset parameters for the production run (87).

For GPCRs, especially cholesterol binding has been extensively investigated by MD simulations (69). Combinations of both atomistic and coarse-grained simulations have been used to reveal distinct binding modes of cholesterol to this family of proteins. One example is the Chemokine receptor 4, whose function has been linked to cholesterol (88). Coarse-grained MD simulations in this case revealed how cholesterol binds to certain regions of the receptor and thereby alters its dimerization (89). Snap-shots from the coarse-grained simulation were then ‘backmapped’ to the atomistic level to identify cholesterol interaction sites on the amino acid residue level.

1.1.3.3 Combining experimental and molecular dynamic approaches to study protein-lipid interactions of COPI protein p24

To study sphingolipid binding to the COPI protein p24 a combined approach was chosen (65): The lipid binding was evaluated by *in vitro* and *in vivo* experiments on p24 with functionalized sphingolipids. The data were then used as input of subsequent MD simulations. In this case, the simulations, along with a point mutation screening of the p24 transmembrane

helix, revealed the putative sphingolipid interaction motif *N*-V-$(X)_2$-TL-$(X)_2$IY-*C*. In a subsequent screening for similar (linear) interaction motifs a number of GPCRs were found (68). Among the found GPCRs, there were also members of the mGluR family, which had been associated with specific cholesterol binding earlier by structural and biochemical means (55, 56, 71). For that reason, one family member, namely human mGluR2 contained the *N*-T-$(X)_2$-TT-$(X)_2$IW-*C* motif, was chosen as model for most of the later experiments in this thesis. The putative sphingolipid interaction motif *N*-T-$(X)_2$-TT-$(X)_2$IW-*C* was located in transmembrane helix VI of mGluR2. Helix VI has been associated with receptor activation in other GPCRs (90). Therefore, it was regarded as an interesting target to study the influence of cholesterol and sphingolipid binding to GPCRs.

1.2 Metabotropic glutamate receptors

The previous chapter has shown multiple examples how GPCRs and their downstream effectors, namely the heterotrimeric G-protein, are affected by covalent lipid modifications and non-covalent protein-lipid interactions. However, the life of a GPCR protein in the eukaryotic cell has also other aspects, such as the control of the expression and translation, the trafficking and activity control.

1.2.1 GPCRs: Structures and common features

Between the different families only few residues in the amino acid sequence were found to be conserved in the transmembrane domain (14). In contrast to that, advancements in the crystallization of the receptors have shown that the fold of the transmembrane domain is conserved between the families: The crystal structure of the mGluR1 and mGluR5 transmembrane domains were well aligned to family A, B and F receptors with their transmembrane helices I-IV and VI (71, 91). Greater variation was seen for the helices V and VII which were shifted inwards as compared to the other structures. The more compact packing of the helix bundle in family C receptors was associated with the fact that they bind their natural ligand in the extracellular domain (71); other than the family A receptors which bind their ligand usually in the transmembrane bundle. Two other important structural features which have been uncovered in the different structures were the E(D)RY-motif and the cysteine bond in the extracellular loops. The E(D)RY motif is an ionic lock between helix VI and helix III that is thought to control receptor activation by controlling the movement of helix VI. It was found with slightly different characteristic in family A and C, but not B and F

(71, 91-95). In the same structures, the second extracellular loop tied to the transmembrane core by a disulfide bridge to helix III.

The family C receptors distinguish themselves structurally by large N-terminal extracellular ligand binding sites (16). For mGluRs the ligand binding cleft is found between two lopes and therefore nicknamed Venus flytrap domain. Between the eight different receptors the binding affinity of the Venus flytrap domain for their ligand varies (see Table 1.1). The domain is connected to the helix bundle by a cysteine-rich linker. The linker is found throughout the family C expect for the Gamma-aminobutyric acid (GABA) receptors and found to be involved in allosteric signal transduction to the transmembrane domain (96, 97).

Within the family C of GPCRs, the phylogenetic subgroup of the Metabotropic glutamate receptors (mGluRs) is subdivided by sequence and pharmacology into Group I, II and III (15) (see also Table 1.1). All mGluRs share a high sequence similarity (~70% identity within and ~45% between groups (98)) and glutamic acid as common ligand. The three different groups couple to distinct sets of G-proteins (see Table 1.1). The physiology and function of mGluRs is well understood in the neuronal context (reviewed by Nicoletti, Bruno (99) and Benarroch (100)), but less is known about functions of mGluRs, which are expressed in non-neuronal tissues (101).

Table 1.1 | Phylogenetic subgroup of the Metabotropic glutamate receptors. The table lists the principle characteristics of the eight known Metabotropic glutamate receptors (mGluRs). The values were retrieved from Pin, De Colle (102), IUPHAR/BPS Guide to PHARMACOLOGY (103) and UniProt (104). EC50 = effect concentration 50, GO Term = gene ontology term.

Group	Members (UniProt ID)	Ligand affinity Glutamic acid (EC50)	Principal transduction	GO term 'Plasma membrane'
I	mGluR1 (Q13255)	9-13 µM	$G\alpha_{q/11}$	Postsynaptic membrane
	mGluR5 (P41594)	3-10 µM	$G\alpha_{q/11}$	Postsynaptic membrane
II	mGluR2 (Q14416)	4-20 µM	$G\alpha_{i/o}$	Presynaptic membrane
	mGluR3 (Q14832)	4-5 µM	$G\alpha_{i/o}$	Pre-/Postsynaptic membrane
III	mGluR4 (Q14833)	3-20 µM	$G\alpha_{i/o}$	Presynaptic membrane
	mGluR6 (O15303)	16 µM	$G\alpha_{i/o}$	Presynaptic membrane
	mGluR7 (Q14831)	1000 µM	$G\alpha_{i/o}$	Pre-/Postsynaptic membrane
	mGluR8 (O00222)	2.5-11 µM	$G\alpha_{i/o}$	Presynaptic membrane

1.2.2 Transcription and translation of Metabotropic glutamate receptors

The different homologues encoded one GPCR receptor type are just one layer of complexity. According to bioinformatical analysis, about 50% of the human GPCR genes are intronless, while the other 50% contain at least one intron and may have splice variants (105). Many of these splice variants have not received much attention and for most it is not known if they result in a functional isoform of the receptor. However, some studies have investigated the

impact of alternative splicing on GPCRs. Receptor isoforms resulting from alternative splicing can impact ligand binding, G-protein coupling or post-translational modifications (reviewed by Markovic and Challiss (105)).

For the phylogenetic group of Metabotropic glutamate receptors, there are there are several splice variants described, such as for mGluR1, mGluR3, mGluR5, mGluR6, mGluR7 and mGluR8 (106). Notably for mGluR2 no isoforms were reported for the UniProt entry Q14416 (104). In contrast to that, the closest 'relative' of mGluR2, mGluR3, a truncation isoform was described lacking the whole transmembrane domain. It was shown that this truncated isoform was expressed at the cell surface of human neurons (107). Recent studies have shown that the isoform acts via dominant-negative inhibition of ligand binding in heterodimers formed with a full length version of mGluR3 (108). Another example of splicing variants within the mGluR family is the alpha and beta isoform of mGluR1. As for most isoforms of mGluRs, alternative splicing targets the C-terminal tail of the receptor. The alpha-form has a longer C-terminal end as compared to the truncated mGluR1β isoform. Several studies investigated how the interaction with tail-binding proteins and the trafficking was affected by the different termini of mGluR1 (109-111). One important different between the isoforms was the RRKK signal peptide in the C-terminal tail which appeared to be sterically blocked in the alpha-isoform while it caused ER retention in the beta-isoform when expressed in Hek293 cells. This was the reasons mGluR1α was used as representative for group I mGluRs in the thesis.

The next step after transcription is the translation of GPCRs into the ER. The vast majority of family C GPCRs carries a signal peptide at the N-terminal end which is necessary for the correct translation of the nascent chain into the ER (112). Translation of membrane proteins into the ER is aided by the low cholesterol content and the presence of glycerophospholipids with unsaturated fatty acyl moieties (3). The resulting biophysical properties make the ER membrane more adaptable to protein structures that are 'designed' to reside in the plasma membrane (113, 114). However, it should be noted that overall few GPCRs carry a cleavable N-terminal signal peptide (112). Kochl, Alken (115) proposed that it is only necessary for big and/or stably folded N-terminal peptide chains. In the case that there is no signal peptide the first transmembrane domain serves as signal anchor sequence, which is the case for most family A and B GPCRs (112).

1.2.3 Trafficking and dimerization

During the insertion of the nascent polypeptide of mGluRs into the ER, the receptors are co-translationally modified by glycosylation. N-glycosylation is one of the most common co-/post-translational modification of family C receptors and has been described mostly by means of bioinformatic analysis of the consensus sequence *N*-N-X-(S/T)-*C* where amino acid X is any amino acid except proline (116). Experimental data on Metabotropic glutamate receptors glycosylation are available for mGluR1α, mGluR3 and mGluR5 (117-119). Interestingly, for mGluR3 and mGluR5 it was shown that many of putative N-glycosylation sites seem not to be modified (118, 119). However, only for mGluR1α the physiological implication was investigated and suggested that while surface expression was not affected agonist response was reduced (117).

The other important modification in maturation of mGluRs is the formation of disulfide bridges. For mGluRs, the disulfide bonds are found at three distinct sites within the protein (see also Figure 1.6). The first site is the disulfide tether between transmembrane helix III and the second extracellular loop; the connection is thought to be a structural hallmark of GPCRs (71, 91). The second one is in the cysteine-rich linker connecting transmembrane and Venus flytrap domain (96). Here, several beta-sheets and loops are linked to one another by cystine bonds (120). Finally, the mGluR protomers are covalently connected with a disulfide bridge between the Venus flytrap domains mediated by C121 in the mGluR2 homodimer (96, 121). Several studies suggested that mGluR (homo-)dimers are the physiological active forms (reviewed by Pin and Bettler (122)).

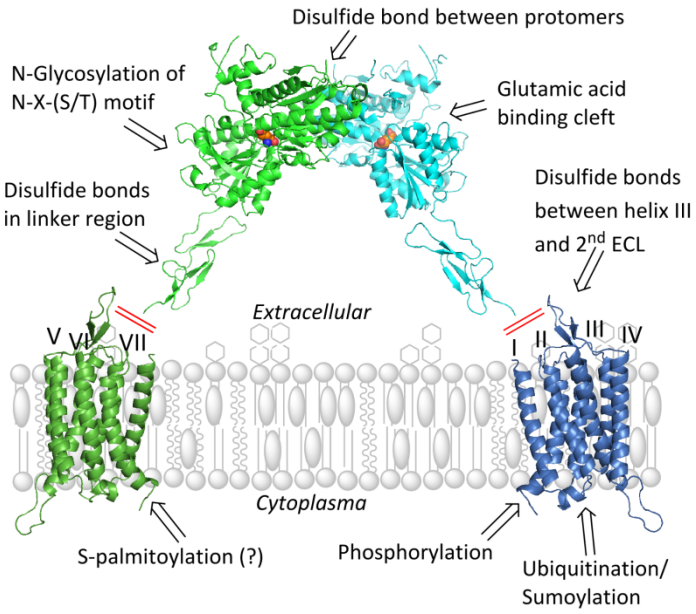

Figure 1.6 | Schematic overview of the post-translational modifications on Metabotropic glutamate receptors. The graphic shows the crystal structure of mGluR3 complexed with glutamic acid (orange spheres) (96). The transmembrane domains are models of the mGluR2 transmembrane domain in SwissModel (71, 123). The exact arrangement between the domains is not know as no structure for the full length receptor has been determined (border indicated by red bars). The disulfide bonds and N-glycans are found on the extracellular side, including a cystine bond between transmembrane helix III and the 2nd extracellular loop (ECL). S-palmitoylation, ubiquitination and sumoylation are suggested to occure at the C-terminal tail (unstructured, no model available), while phosphorylation might also occur in the intracellular loops (discussed in Section 1.2.3).

Lipidation can also occur as early as in the ER and has been shown for some GPCRs to be important for trafficking (24, 124) (see Section 1.1.1.1). However, little information on lipidation of mGluRs is available (116). Among the mGluRs, only mGluR4 was reported with a S-palmitoylation site but neither the position nor the physiological relevance have been further investigated (125). This is why mGluR4 was included as representative for group III mGluRs in the palmitate labeling of the thesis.

For the COPII mediated ER export of the family C receptors ER retention signals have been identified in some family C receptors (126): In mGluR1 the signal the RRKK signal is found in the C-terminal tail (111). The signal is thought to be sterically shielded in alpha-isoform while the beta-isoform required heterodimerization to be trafficked further through the secretory pathway (127). Dimerization is also a prerequisite for GABA receptor trafficking (128, 129). A RXR-based ER retention signal was found in the C-terminal tail of the isoform B1 that is shielded upon dimerization with isoform B2. The tails form a coil-coiled structure which buries the signal. For other family C receptors, such as mGluR2 or mGluR4, no such ER retention signals have been identified to date.

1.2.4 Physiological activity and post-translational modifications of mGluRs

Metabotropic glutamate receptors usually reside at the plasma membrane and are only functional as dimers (130, 131). Notably the disulfide bond between the protomers was neither a prerequisite for dimerization nor for signaling (120, 121, 132, 133). In the dimer

both or just one of the Venus flytrap domains can be in the open or closed state, that is the inactive or active state, respectively (134, 135). In the open state the agonist is bound and the hinge relocated the lopes by 70°. One agonist is sufficient to activate the receptor but both binding sites needed to be occupied for full activity (136). Upon activation by the agonist, the signal is transferred from the extracellular Venus flytrap domain in an allosteric fashion via the cysteine-rich linker and the transmembrane domain to the cytoplasmic effectors (97, 137). The receptor forms a ternary complex with the cytoplasmic effector that then triggers the (intra-)cellular response (see Figure 1.7).

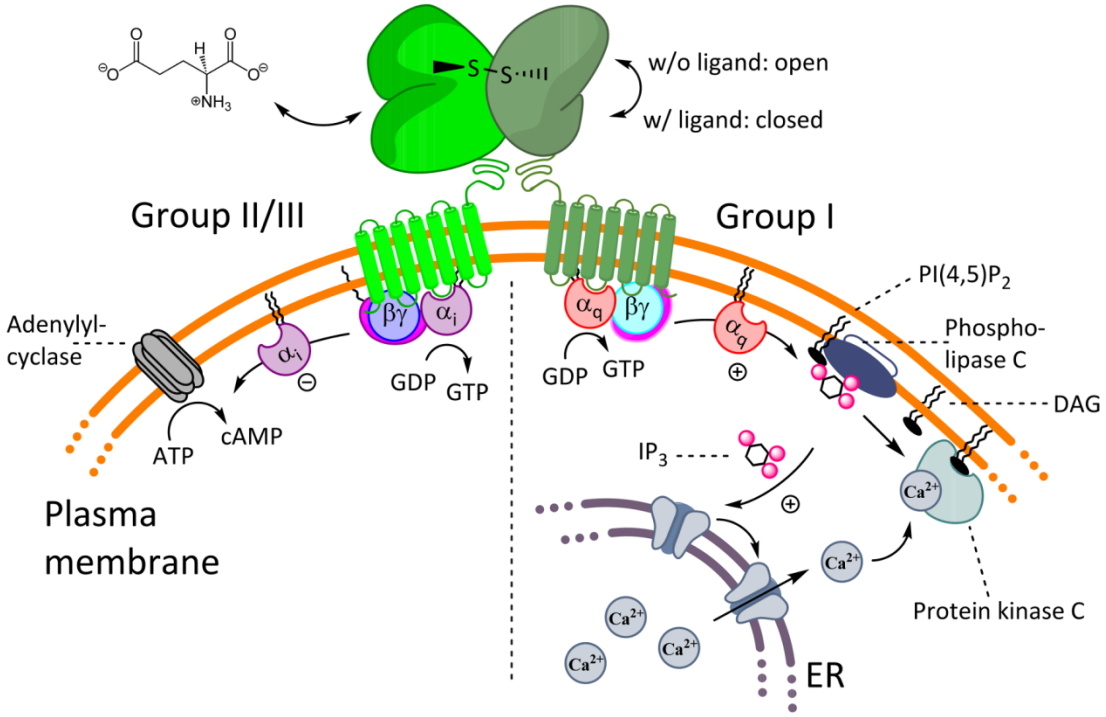

Figure 1.7 | Signaling pathways of Metabotropic glutamate receptors. Metabotropic glutamate receptors signal either via $G\alpha_i$ (Group II and III receptors) or $G\alpha_q$ (Group I receptors). The activation of the receptor by gluatmic acid leads to a closing of the lopes. Full activation requires the binding of orthosteric agonists to both protomers. The trimeric G-protein is activated by exchange of guanosine diphosphate (GDP) to guanosine triphosphate (GTP). The $G\alpha_i$ pathway downregulates the activity of the membrane resident enzyme adenylylcyclase. The $G\alpha_q$ pathway signal via hydrolysis of phosphatidylinositol 4,5-bisphosphate ($PI(4,5)P_2$) into diacylglycerol (DAG) and inositol 1,4,5-trisphosphate (IP_3). The later opens calcium channels in the endoplasmic reticulum (ER) that in concert with DAG activate the protein kinase C. Drafted in ChemDraw with modifications from Conn and Pin (98) and Alberts, Johnson (138).

Like for other GPCRs, the intracellular effector for mGluRs is a trimeric G-protein. The trimeric G-protein consist of a α- and a βγ-subunit, which are both anchored to the membrane via covalent lipid modifications (Section 1.1.1.2), couples to the receptor via helices II and IV and the second intracellular loop (137, 139). The second intracellular loop seems to determine the specificity of G-protein coupling. There are mainly two main pathways described: One via $G\alpha_i$ which inhibits adenylyl cyclase and another one via $G\alpha_q$ that activates phospholipase C and releases calcium ions from the ER. The former one is the principal transduction way of

group II and III mGluRs while the later seems to be important for group I mGluRs (reviewed by Conn and Pin (98)) (Figure 1.7).

Apart from the previously mentioned modifications related to folding and trafficking, namely glycosylation, disulfide bonding and lipidation (Section 1.2.3), other post-translational modifications were found to be more related to the regulation the receptor activity (116). The most commonly described modification is phosphorylation. For the group I receptors mGluR1α and mGluR5 it was shown that phosphorylation in the C-terminal tail and intracellular loops by protein kinase C led to desensitization after agonist stimulation (140, 141). Group II and III receptors were found to be phosphorylated at distinct sites in the C-terminal tail by Protein kinase A, which had an inhibitory effect on signaling as well (142, 143). For mGluR2, phosphorylation was reported to occur at position S843 in the C-terminal tail (143). In addition, for mGluR1 ubiquitination was reported and was suggested to be linked to endocytosis and degradation (144, 145). Sumoylation-dependent trafficking and surface expression was reported for mGluR7 (146). Notably none of the later modifications has been identified in mGluR2.

1.3 Aim of the thesis

In a collaborative work with the group of Prof. Irmgard Sinning, mGluR2 has been found to be regulated by the cholesterol content in the membrane and might also harbor a sphingolipid binding site (55, 68). The goal of my PhD thesis was to identify specific lipid binding sites in mGluR2 which may modulate its function. By applying biochemical and molecular biological methods, I aimed identified a potential binding site for cholesterol and sphingolipids at the hydrophobic surface of the mGluR2 transmembrane domain. The goal was to map single amino acid residues which stabilize lipid interaction at a particular position. To verify the experimental data, I started collaboration with the Max Planck tandem group of Dr. Camilo Aponte-Santamaría at the University of Los Andes in Bogotá (Colombia). In this project of the projected we aimed to study the binding of lipids at the molecular level and describe the functional consequences of this process using computer simulations.

2 Results

2.1 Design of constructs for expression of tagged proteins in mammalian cells

The constructs used for the expression of mGluR2 and other proteins were based on the pCMV6-Entry vector which is commercially available at OriGene (Rockville, USA) as pCMV6-Entry Tagged Cloning Vector (Section 4.2.5).

The two tags encoded in the vector are a c-Myc or Myc-tag, and a Flag-tag, also called in resemblance of the single-letter amino acid code DDK-tag. The cloning of the expression constructs was conducted with a pCMV6 construct that already contained the open reading frame (ORF) for GRM2 (NM_000839.4, NP_000830.2): pCMV6_GRM2_MycFlag (Origene, RC218103). The tags were encoded downstream (3' end) of the GRM2 ORF (Figure 2.1), and thus were positioned at the C-terminal end of the protein. C-terminal tagging was preferred at this stage, because it would not interfere with the N-terminally localized signal peptide and in addition would only be detectable in fully translated proteins.

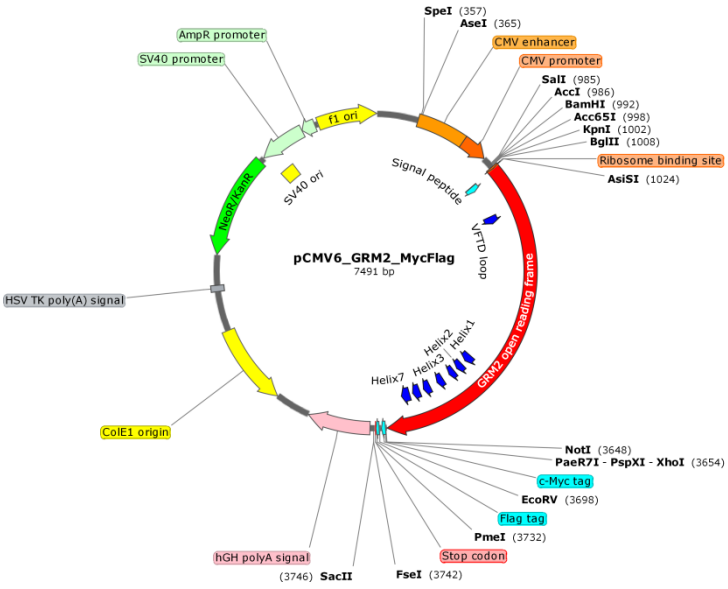

Figure 2.1 | Vector map of the pCMV6_GRM2_MycFlag vector. For protein expression in mammalian cells, the GRM2 ORF (red) was under the control of a constitutive active CMV enhancer/promotor (orange). Both a c-Myc and a Flag-tag were available for C-terminal tagging (light blue). The helices I-VII of the transmembrane domain are indicated in dark blue. For propagation in a bacterial context, the plasmid contained a ColE1 origin (of replication), as well as an kanamycin resistance gene for selection. Graphic built in SnapGene Viewer.

In these constructs, the ORF was under the control of an upstream (5' end) CMV enhancer/promotor that shows constitutive activity without tissue or mammalian species selectivity (147, 148) (Figure 2.1). A neomycin resistance gene under the control of the constitutive SV40 promotor allows for selection of plasmid-harboring cells.

The pCMV6_GRM2_MycFlag vector was used to generate the pCMV6 vector control, as well as the single-tag constructs of GRM2 and other GPCRs (Sections 4.2.6 and 4.2.10). To generate the pCMV6 vector control, the pCMV6_GRM2_MycFlag vector was digested to excise the ORF of GRM2 and the filled up sticky ends were blunt ligated (Section 4.2.5). The product was a vector similar to the pCMV6-Entry vector sold by OriGene (PS100001). The overlap with OriGenes' pCMV6-Entry vector was 98.6%. The difference resulted from a loss of 63 bp at the ligation site in the self-made pCMV6 vector control (Figure 2.2 B). This would have been disadvantageous if the pCMV6 vector had served as acceptor for insert fragments, as the deletion site had contained multiple cloning site features. However, pCMV6 vector control was used solely to mock transfect mammalian cells.

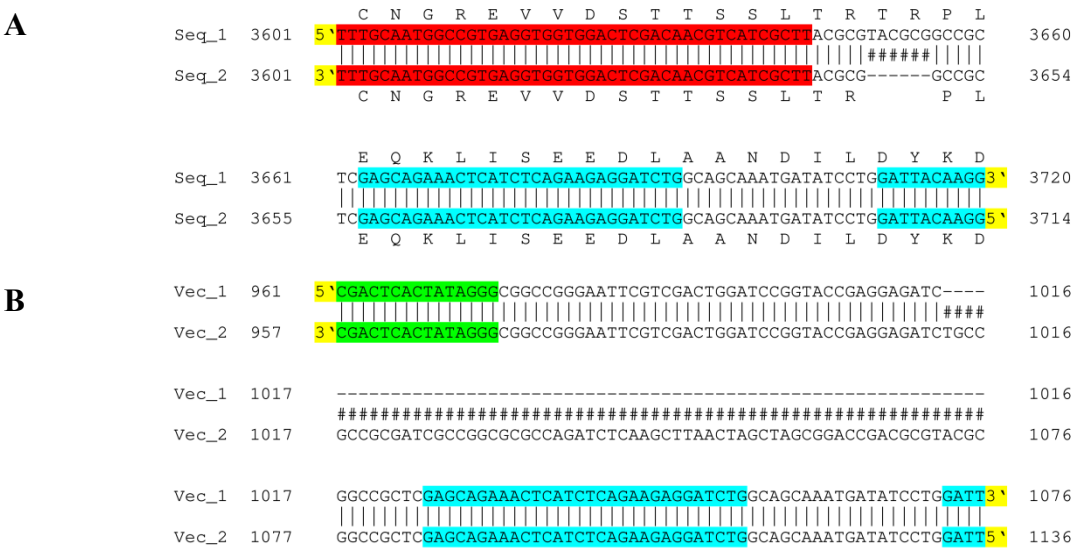

Figure 2.2 | Cloning work with pCMV6 vector. (**A**) The commerically available vector pCMV6_GRM2_MycFlag (OriGene, RC218103) inherently contained a deletion of 6 bp downstream of the GRM2 ORF (red), within the linker regions to the Myc-tag (blue). The deletion was silent and did not cause any frameshift in the downstream encoded regions. (**B**) The pCMV6 vector control was generated by excision of the GRM2 ORF from the pCMV6_GRM2_MycFlag vector and subsequent blunt ligation of the Klenow DNA Polymerase I fragment-treated loose ends (details see Section 4.2.5). Shown is the sequence alignment between pCMV6 vector control (Vec_1) and OriGene pCMV6-Entry (Vec_2). The self-made vector control showed a loss of 63 bp at the multiple cloning site downstream of the T7 primer binding site (green) and upstream of the Tag-coding regions (blue). The alignment was mapped with SerialCloner.

2.1.1 eGFP^{A207K}-tagged GRM2 constructs

In order to monitor the expression of GRM2 constructs in Hek293 cells, the GRM2 ORF was tagged C-terminally with eGFP. eGFP is an enhanced version of the wild type GFP (149). In addition to the enhancement in the fluorophore, a mutation (A207K) was introduced to prevent clustering of eGFP or eGFP-tagged proteins (150). The eGFP^{A207K} was attached at the C-terminal end of mGluR2. Two constructs were cloned: one without and one with a Gly_4Ser-linker between GRM2 and eGFP^{A207K} ORF (Figure 2.3). The Gly_4Ser-linker is a commonly

used linker that was introduced in the construct in case that without linker the eGFP^{A207K} protein would not fold – or would not exhibit a fluorescent signal (151). However, the C-terminal tail is usually considered to be unstructured and can as such be described as linker on the structural level (71, 91).

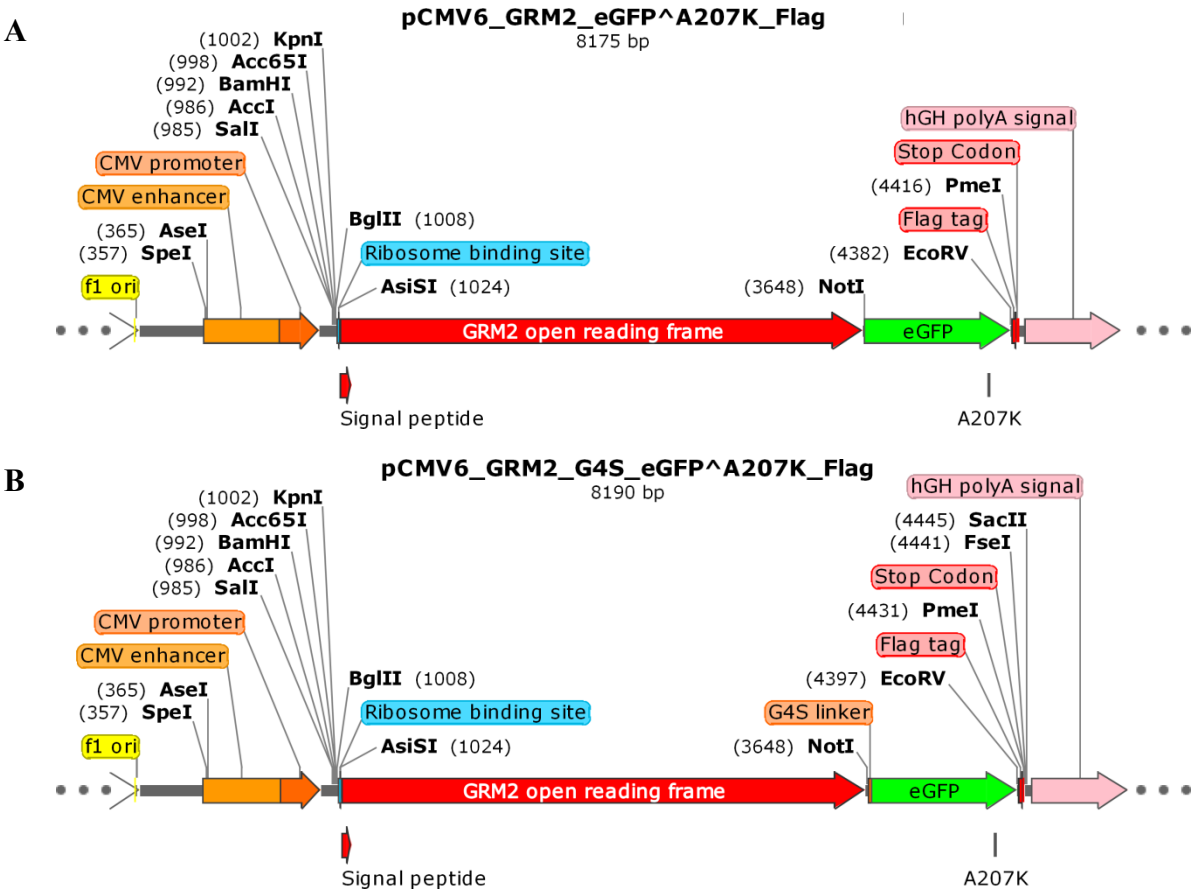

Figure 2.3 | eGFP^{A207K}_Flag-tagged GRM2 constructs. Two different constructs were cloned into the pCMV6 expression vector: (**A**) GRM2- eGFP^{A207K}-Flag and (**B**) GRM2- G_4S-eGFP^{A207K}-Flag. The ORF was under the control of a CMV promotor and expressed as fusion protein. The start codon from the eGFP^{A207K} had been removed (details see Section 4.2.8). The possible restriction sites are printed bold with the nucleotide number on the plasmid in brackets. Genetical features are mapped coloured. The map was drawn with SnapGene Viewer.

2.1.2 Generation of Myc- and Flag-tagged GPCR constructs and corresponding point mutants

Different metabotropic glutamate, adrenergic and serotonin receptors were cloned for expression into the pCMV6 vector. Only C-terminally tagged GPCR variants were used because it would only detect fully translated proteins and not interfere with the N-terminal translocation signal. The only exception here was the Beta-2 adrenergic receptor (ADRB2).

While the original pCMV6_GRM2_MycFlag vector had been delivered as C-terminally tagged construct by OriGene, the ADRB2 construct had been obtained as N-terminally tagged

construct from Addgene (Watertown, USA). The ADRB2 construct had been deposited by the lab of Robert Lefkowitz (152). The deposited construct had an additional signal peptide sequence (*N*-MKTIIALSYIFCLVFA-*C*) just before the Flag-coding region, upstream of the ADRB2 ORF, to enhance expression (152, 153) (Figure 2.4 A). Notably, no such signal peptide sequence was found in the original ADRB2 mRNA sequence (NM_000024.5, NP_000015.1). In addition to the original construct, a C-terminally tagged ADRB2 version was cloned with the Flag-tag connected by a short linker to the ORF, just as for the other constructs (Figure 2.4 B). The constructs would be later compared in the [^{3}H]-photo-cholesterol labeling assay.

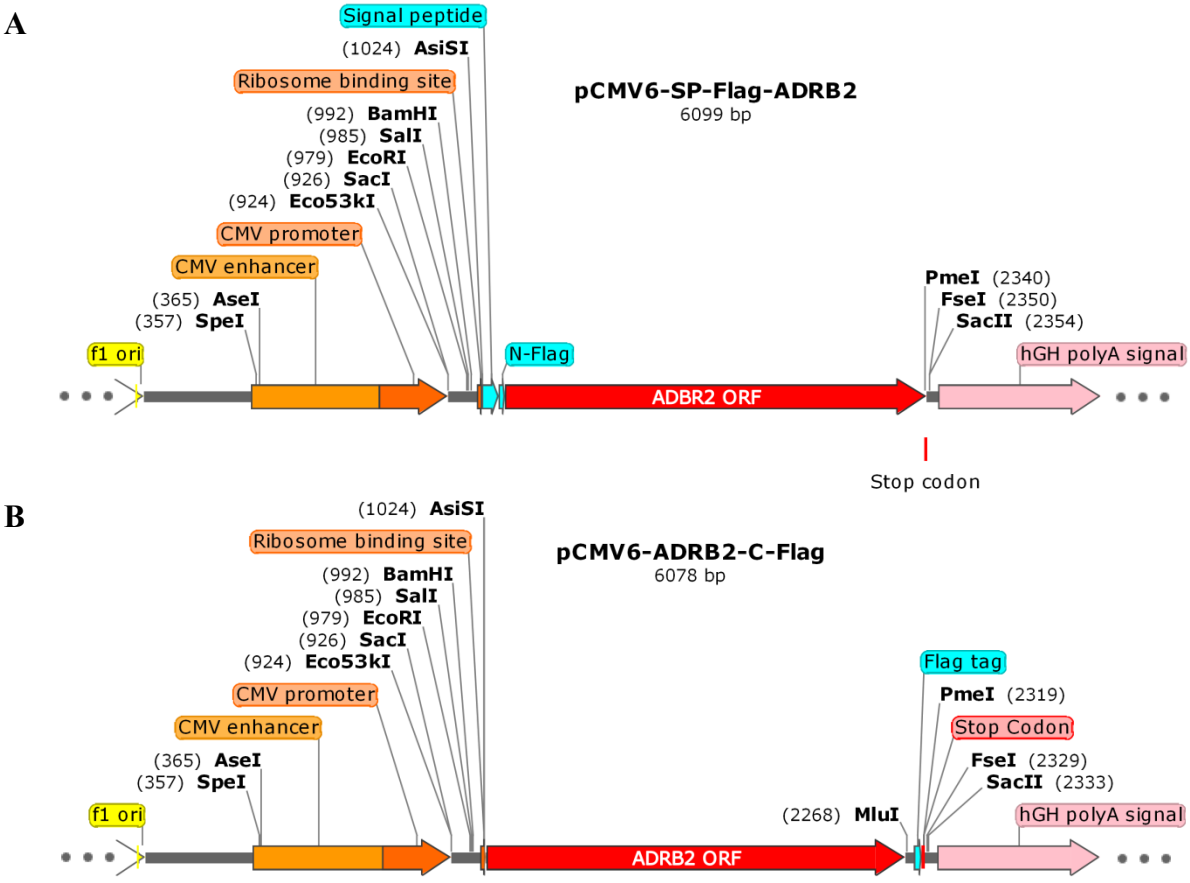

Figure 2.4 | N- and C-terminally Flag-tagged pCMV6_ADRB2 constructs. The ADRB2 ORF (NM_000024.5, NP_000015.1, clone obtained from Lefkowitz lab (152)) was cloned into the pCMV6 vector as (**A**) N-terminally or (**B**) C-terminally Flag-tagged construct (details see Section 4.2.10.1). The former one contained an additional signal peptide sequence (*N*-MKTIIALSYIFCLVFA-*C*) upstream of the ADRB2 ORF absent in the N-terminally tagged version. The map was drawn with SnapGene Viewer.

The other GPCR ORFs, namely GRM1 (NM_001278064.1, NP_001264993.1), GRM4 (NM_000841.3, NP_000832.1), ADRA2 (NM_000681.3, NP_000672.3), Htr1a (NM_008308.4, NP_032334.2) and HTR2A (NM_000621.4, NP_000612.1) were all tagged with a C-terminal Flag and /or Myc-tag. The Flag-tag (*N*-DYKDDDDK-*C*) was linked to the protein with a *N*-TRAANDIL-*C* peptide linker, while the Myc-tag (*N*-EQKLISEEDL-*C*) was

joined by a short *N*-(TR)TRPL-*C* peptide linker. Both the tags and the linker sequences were adapted from the original pCMV6_GRM2_MycFlag plasmid.

2.1.2.1 Loss-of-function at S-fatty acylation sites

S-fatty acylation, or also called S-palmitoylation referring to the common fatty acid found attached to the cysteine residue, for mGluRs has been poorly investigated so far (116). Only one receptor has been identified to date: Alaluf, Mulvihill (125) reported a S-palmitoylation site in mGluR4, but did not assign it to any amino acid residue or domain for the modification. To investigate if mGluR2 or other mGluRs were S-palmitoylated, also with regard to a possible implication to cholesterol binding as shown for the mouse 5-hydroxytryptamine receptor 1A (5-HT-1A), different Flag-tagged mGluR constructs were tested for S-acylation in a [^{3}H]-palmitic acid labeling (26). In order to have positive and negative controls at hand, known S-palmitoylated cysteine residues in other GPCRs were subjected to C→A point mutations (Figure 2.5). The alanine variants served as controls to exclude the possibility of false positive signals due to incorporation of radioactive metabolites into amino acids or post-translational modifications (76).

Two serotonin receptors were included in the S- fatty acylation assay (Figure 2.5): the above mentioned 5-HT-1A from mouse is also a $G\alpha_i$-coupled receptor, just as mGluR2. It has been shown that $G\alpha_i$-coupling to the receptor is dependent on S-palmitoylation in its C-terminal tail (26). Thus a similar effect could govern G-protein coupling –and eventually also cholesterol binding – in mGluR2. Moreover, an interaction partner of mGluR2, human 5-hydroxytryptamine receptor 2A (5-HT-2A), was considered as well because the receptors might share a similar membrane environment and also a 5-HT-2A homologue in mouse had been found in a S-fatty acylation screening (154, 155). In addition to that, two human adrenergic receptors were included in the palmitate labeling (Figure 2.5). As mGluR2, the Alpha-2A adrenergic receptor (α-2AAR) is coupled to $G\alpha_i$, and had been reported with a S-palmitoylation site in the C-terminal tail (156). Furthermore, the Beta-2 adrenergic receptor (β2AR) was used in the assay, as it had both a defined cholesterol interaction site and C-terminal palmitate modification (45, 76).

For the C→A mutants, ADRB2 and 5-HT-1A were chosen as the S-fatty acylation mutants because they were relatively well described with no reported trafficking defects upon loss of S-palmitoylation site in the respective cell lines used (26, 157). The mutants were generated by mutating the reported cysteine residues in the C-terminal tail to alanine by mutagenesis

PCR (mPCR) (Section 4.2.11). The target sites were C341 in ADRB2, and C417 and C420 in 5-HT-1A (Figure 2.5). Notably, another designated S-palmitoylation site in the ADRA2A ORF could not be mutated by mPCR despite efforts to adjust the reaction conditions.

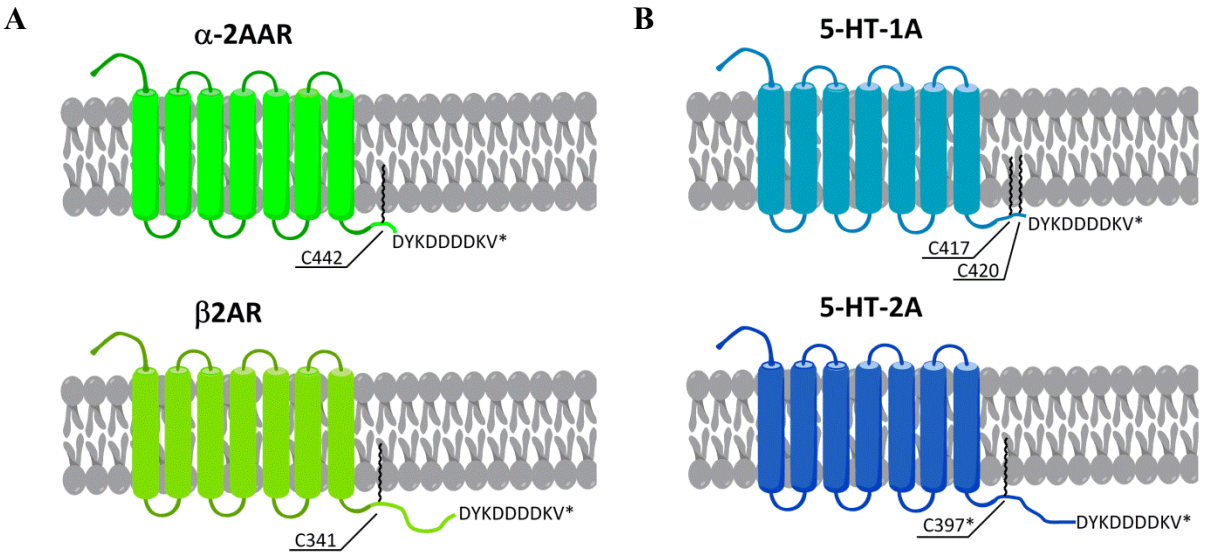

Figure 2.5 | Palmitoylation sites in GPCRs. Two different serotonin receptors with known palmitoylation sites, namely (**A**) 5-hydroxytryptamine receptor 1A (5-HT-1A) from mouse and human 5-hydroxytryptamine receptor 2A (5-HT-2A), and two human adrenergic receptors, (**B**) the Alpha-2A adrenergic receptor (α-2AAR) and Beta-2 adrenergic receptor (β2AR), were chosen as controls for the [^{3}H]-palmitic acid labeling (26, 76, 155, 156). The graphic indicates the approximated position of the fatty acid modification at the C-terminal tail of the GPCRs. The position C397* for 5-HT-2A was approximated from the mouse analog. All constructs were Flag-tagged, here written as peptide (*N*-DYDDDDK-*C*). The graphics were designed with ChemDraw.

On the site of the metabotropic glutamate receptors, the above mentioned mGluR4 was chosen as representative for the Group III mGluRs, while mGluR1α was picked as representative for the group I mGluRs. The later one was reported negative for palmitoylation in the study published by Alaluf, Mulvihill (125). The protein of interest, mGluR2 belonged to the group II of the mGluR family.

2.1.2.2 Cholesterol and sphingolipid interaction: W→A and Y→A variants of GRM2

In the case of the non-covalent cholesterol and sphingolipid interaction sites, assumptions on putative interaction motifs in the transmembrane domain of mGluR2 were made based on the published linear and three-dimensional motifs (45, 52, 53, 65). However, the selection of the target sites was complex as general several residues would presumably be involved in the interaction with the non-annular lipids at one particular spot.

For cholesterol interaction, there are two published linear motifs: The “Cholesterol Recognition/interaction Amino acid Consensus sequence” (CRAC) motifs was originally identified as *N*-L/V-(X)$_{1–5}$-Y-(X)$_{1–5}$-R/K-*C* in the mitochondrial cholesterol transport protein

Peripheral-type benzodiazepine receptor (52). An inverted motif, termed "CARC", was described in the α-helical transmembrane domain of the human nicotinic acetylcholine receptor (53). The motif was later also identified in helix V of the transmembrane domain of the mGluR family (56). The first experimentally determined three dimensional motif in a GPCR was the four component cholesterol interaction site in a crystal structure of β2AR (45). Considering the specific interaction of cholesterol with a set of amino acid residues conserved in family A receptors, the cholesterol consensus motif (CCM) motif was reported as *N*-[4.39-4.43(R,K)]-[4.50(W,Y)]-[4.46(I,V,L)]-[2.41(F,Y)]-*C* sequence based on the Ballesteros-Weinstein numbering system for family A GPCRs (45, 46). For sphingolipids, there was one published linear motif in a α-helical transmembrane domain (65). The sequence in the single-spanning Transmembrane emp24 domain-containing protein 2 (p24) was identified as e *N*-V-$(X)_2$-TL-$(X)_2$IY-*C*. Subsequently, a similar motif was identified in the transmembrane helix VI of mGluR2, 7 and 8 (68). Notably, there is also another published structural motif for sphingolipid binding to V3-like domains (helix-turn-helix motif) (64). However, apart from the involvement of aromatic amino acids in the turn, no sequence specificity was reported.

For the linear CRAC and CARC, the tyrosine residue was considered a crucial part of the interaction motif, however, not necessarily for intramembrane interactions sites where it might be replaced by phenylalanine (53, 54). For the three dimensional CCM, aromatic amino acid residues were identified at the interaction sites with the CHπ-hydrogen bonding system of cholesterols' sterol rings as well as with its 3β hydroxyl group (45). Aromatic tyrosine and tryptophan residues were also found in the p24 sphingolipid interaction motif and the V3-like sphingolipid binding domain (65). For this reasons the tyrosine and the tryptophan residues in the transmembrane domain of mGluR2 were targeted in an alanine screening. The phenylalanine residues were left aside to reduce the complexity of the screening.

The tryptophan and tyrosine residues were selected on the basis of a homology model of the mGluR2 transmembrane domain. The amino acid sequence of the domain was used to build the homology model with SWISS-MODEL (158-161). To build the homology model with SWISS-MODEL, effectively two crystal structures were available: the transmembrane domain of mGluR5 co-crystallized as T4-lysozyme fusion construct, and mGluR1 with an N-terminal fusion to thermostabilized apocytochrome b_{562}RIL (71, 91). Other suggested GPCRs, namely Rhodopsin and the Chemokine receptor type 4 showed only a poor sequence identity (Table 2.1).

Table 2.1 | SWISS-MODEL template library for mGluR2 transmembrane domain. The table returned the description of the different templates (RCSB access number) and their sequence identity (Seq Identity) with the mGluR2 transmembrane domain (incl. loops) as calculated in SWISS-MODEL. BLAST and HHblits are two different sequence alignment algorithms used to search for matching amino acid sequences (162, 163). The table also shows the oligostate as well as the resolution of the template and its coverage of the target sequence. The Quaternary structure quality estimate (QSQE) reflects the expected accuracy of the interchain contacts for a model based on a given alignment and template (0-1).

Template (RCSB)	Seq Identity	Oligostate	QSQE	Found by	Resolution	Coverage	Description
4or2.1.A	53.53	homo-dimer	0.10	BLAST	2.80Å	0.96	Soluble cytochrome b562, Metabotropic glutamate receptor 1
4or2.1.A	51.02	homo-dimer	0.11	HHblits	2.80Å	0.97	Soluble cytochrome b562, Metabotropic glutamate receptor 1
5cgd.1.A	51.22	monomer		HHblits	2.60Å	0.98	Metabotropic glutamate receptor 5,Endolysin,Metabo-tropic glutamate receptor 5
5cgd.1.A	53.16	monomer		BLAST	2.60Å	0.63	Metabotropic glutamate receptor 5,Endolysin,Metabo-tropic glutamate receptor 5
5cgd.1.A	51.52	monomer		BLAST	2.60Å	0.39	Metabotropic glutamate receptor 5,Endolysin, Metabo-tropic glutamate receptor 5
5dys.1.A	9.10	monomer		HHblits	2.30Å	0.33	Rhodopsin
3oe6.1.A	9.57	monomer		HHblits	3.20Å	0.37	C-X-C chemokine receptor type 4, Lysozyme Chimera

A sequence identity of >50% in the primary structure was obtained for the X-ray structures of mGluR1 and mGluR5 (Table 2.1). The mGluR1 template 4or2.1.A was used to build the homology model of the mGluR2 transmembrane domain, because it had the highest sequence identity as calculated with BLAST (71).

The model was reported with the QMEAN4 score, a quality estimate for the overall model of the protein, which compared the model with experimental available structures and thus estimates its 'nativeness' (160). The QMEAN4 consisted of four statistical scores (Figure 2.6): The All atom and CBeta factors described the long-range interactions on the atom and the residue level, respectively. The Solvation factor described how well the residues were buried in the structure. The backbone geometry of the model was calculated with the Torsion. The Torsion described the torsion angels over three consecutive amino acid residues of the amino acid backbone. The modelled structure of the mGluR2 transmembrane domain showed overall a low QMEAN4 (Table 2.1 A). A QMEAN4 score of <-4.0 is considered of low

quality, while better scores would have shown a tendency to positive values (123). While the overall QMEAN4 was not satisfactory, the local scores for the transmembrane domains with values above 0.6 were considered reasonable (Table 2.1 B). While the α-helical regions of the transmembrane domain were resembled with an acceptable quality, the intra- and extracellular loops were only poorly described (Table 2.1 C). Here, the amino acid sequence showed a lower conservation between mGluR1 and mGluR2 and for that reason was more difficult to fit into the X-ray structure of the former one, which served as template. The α-helical regions on the other side were well enough resembled to make assumption on the surface exposure of single residues.

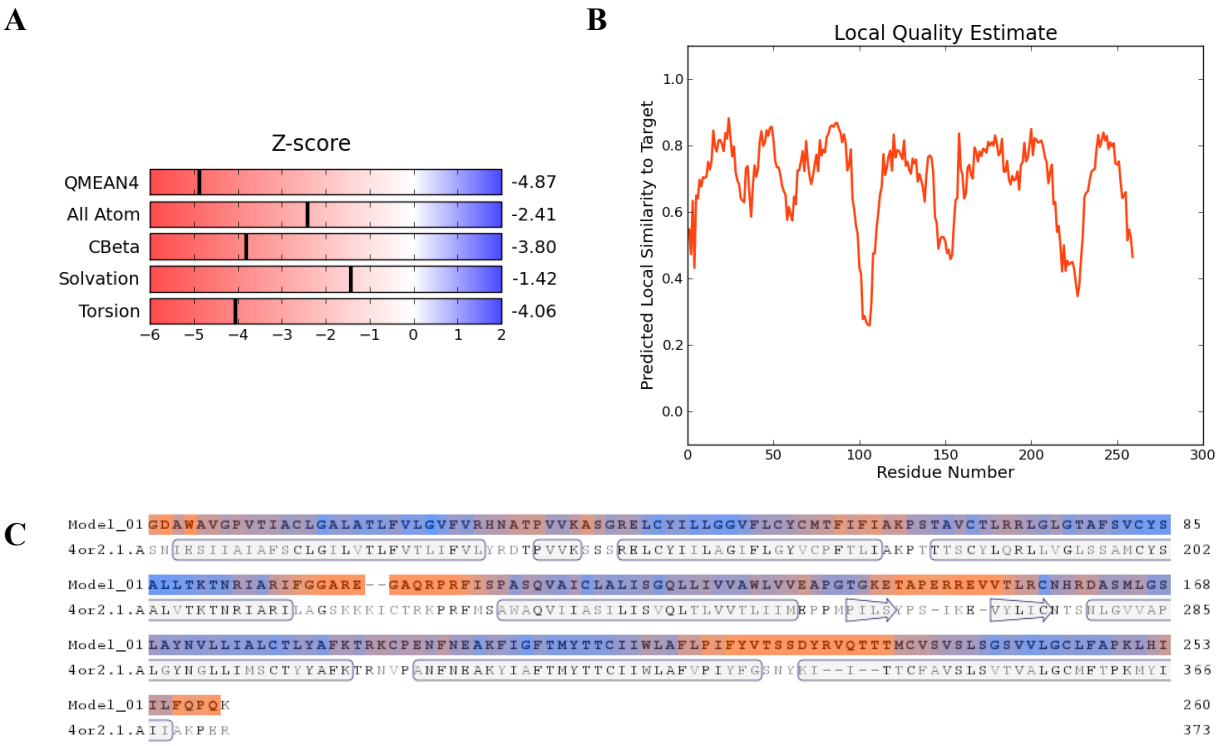

Figure 2.6 | Model of mGluR2 transmembrane domain using SWISS-MODEL. The model of the mGluR2 transmembrane domain was built based in the mGluR1 (RCSB 4or1) crystal structure (71) (details see Section 4.13.1). (**A**) The QMEAN4 score consisted of a linear combination of four structural descriptors: All atom and CBeta described distance dependent interactions, Solvation described the solvent accessibility of the residues, and Torsion was a measure for the torsion angel over three consecutive residues. (**B**) The Local quality estimate showed the expected similarity to the X-ray structure for each amino acid residue. (**C**) The alignment showed the QMEAN score per residue between the input sequence (Model_01, mGluR2 transmembrane domain) and the template (4or2.1.A, mGluR1 template). The boxes around the template sequence indicate the α-helical regions while the arrows show beta-sheets. In between are the unstructures regions of the intra- and extracellular loops.

The quality of the model was also validated by visual comparison to the experimentally determined X-ray structures: the mGluR2 transmembrane model was aligned to the mGluR1 (RCSB 4OR1), as well as to the mGluR5 (RCSB 4OO9) crystal structure (71, 91) (Figure 2.7). In both cases the mGluR2 transmembrane model was fitted to the X-ray structures with the ‘align’ tool in Pymol (Schrödinger, New York) which also returned root mean square

deviation (RMSD) between the mGluR2 model and the experimental structures. Whereas in both cases the α-helical regions were well aligned, the loops were often not well reproduced in the mGluR2 model (Figure 2.7). In the mGluR1 X-ray structure for example, data for the second intracellular loop were missing which were modelled as unstructured region for mGluR2 (Figure 2.7 A, bottom left). On the other side, the beta-sheet of the second extracellular loop was well resembled in the mGluR2 model (Figure 2.7 A, top).

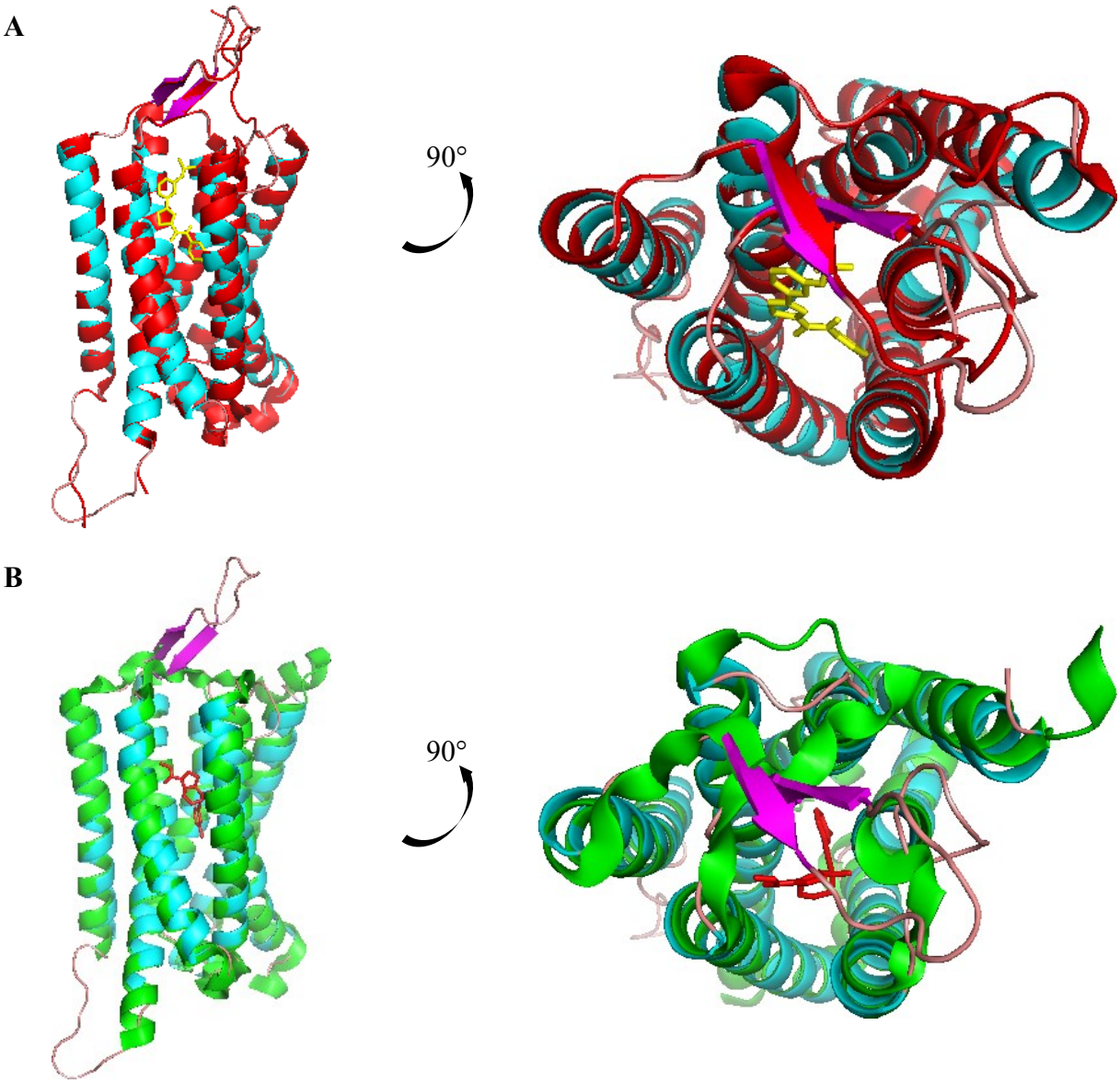

Figure 2.7 | Alignment of mGluR2 transmembrane model with mGluR1 and mGluR5 X-ray structures in Pymol. The transmembrane model of mGluR2 (Helix:Sheet:Loop colour mode, Cyan:Purple:Rosé) was aligned in Pymol with the experimental crystal structures of (**A**) mGluR1 (4OR2; protein: red; allosteric ligand FITM: yellow) and (**B**) mGluR5 (4OO9; protein: green; allosteric ligand M-MPEP: red) (71, 91). The RMSD between the mGluR2 model and the experimentally determined structures was 0.152 Å (1223 to 1223 atoms) for mGluR1 and 0.696 Å (1266 to 1266 atoms) for mGluR5.

The mGluR2 model showed a low RMSD of 0.152 Å from the mGluR1 X-ray structure it was modelled from (Figure 2.7). In contrast to that, the deviation from the mGluR5 structure was about fourfold higher: 0.696 Å. For mGluR5, the extracellular loops had adopted an α-helical structure in the crystal whereas it was a beta-sheet for the second extracellular loop in case of the model or unstructured for the other loops (Figure 2.7 B).

The transmembrane model allowed to investigate the sites of the CRAC and the sphingolipid interaction motifs which had been previously identified by sequence homology (56, 68). The former one appeared to be completely accessible on the protein surface, including the central tyrosine residue Y745 (Figure 2.8). For the sphingolipid interaction domain, not all residues appeared to face the surface of the transmembrane domain (Figure 2.8). However, the aromatic residue W773 was at least partly tilted towards the protein-lipid interface.

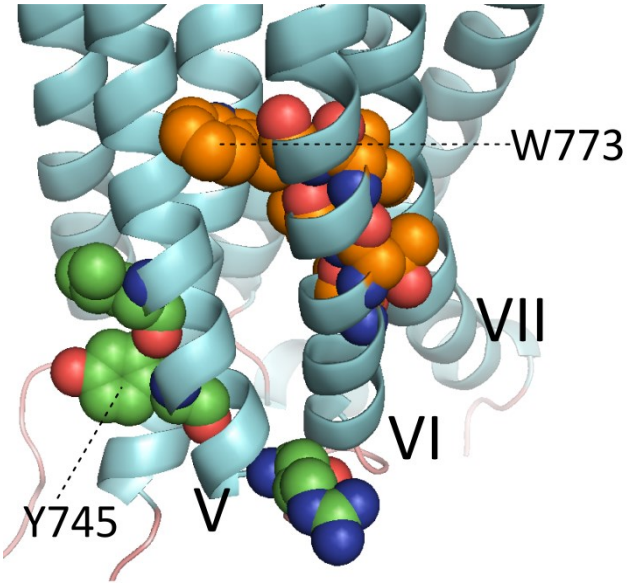

Figure 2.8 | CRAC and sphingolipid interaction motifs in the transmembrane model of mGluR2. The cholesterol interaction motif CRAC was identified as *N*-**L**CTL**Y**$_{745}$AFKT**R**-*C* sequence at the cytosolic end of transmembrane helix V (56). The residues of CRAC motif are highlighted as spheres with green carbon atoms. The sphingolipid interaction site was identified as putative p24-like motif in a bioinformatic screening as *N*-**T**MY**TT**CI**IW**$_{773}$-*C* sequence in transmembrane helix VI (68). The residues of sphingolipid interaction motif are highlighted as spheres with orange carbon atoms. The figure was assembled with Pymol and ChemDraw. The numbering of the transmembrane helices are indicated in roman letters.

From the model of the mGluR2 transmembrane domain, eight point mutation sites were chosen by visual inspection of the amino acid residues (Figure 2.9 A). The position for the alanine exchange was estimated from the exposure of the side chains to the protein surface: W567, Y607, W697, Y734, Y745, Y767, W773 and Y781 (Figure 2.9 B-I). The position included also the residues Y745 and W773 which were part of putative cholesterol and sphingolipid interactions sites, respectively (Figure 2.8). The tyrosine and tryptophan residues were mutated as single point mutants to alanine by mutagenesis PCR (Section 4.2.9). Like that, four sets of W/Y→A variants were established. The first set consisted of eight C-terminally Flag-tagged point mutants of mGluR2, while the second set were double mutants that contained also a C121A mutation in the extracellular domain. The third and fourth set were cloned accordingly but with a C-terminal Myc-tag. The double mutants were used to

find out if the lack of the covalent linkage between the protomers would allow observing stronger phenotypes in the bioassays, especially the cellular photocrosslinking with bifunctional lipids. The majority of bioassays was conducted with the Flag-tagged variants. The Myc-tagged versions were solely used for the co-immunoprecipitation experiments.

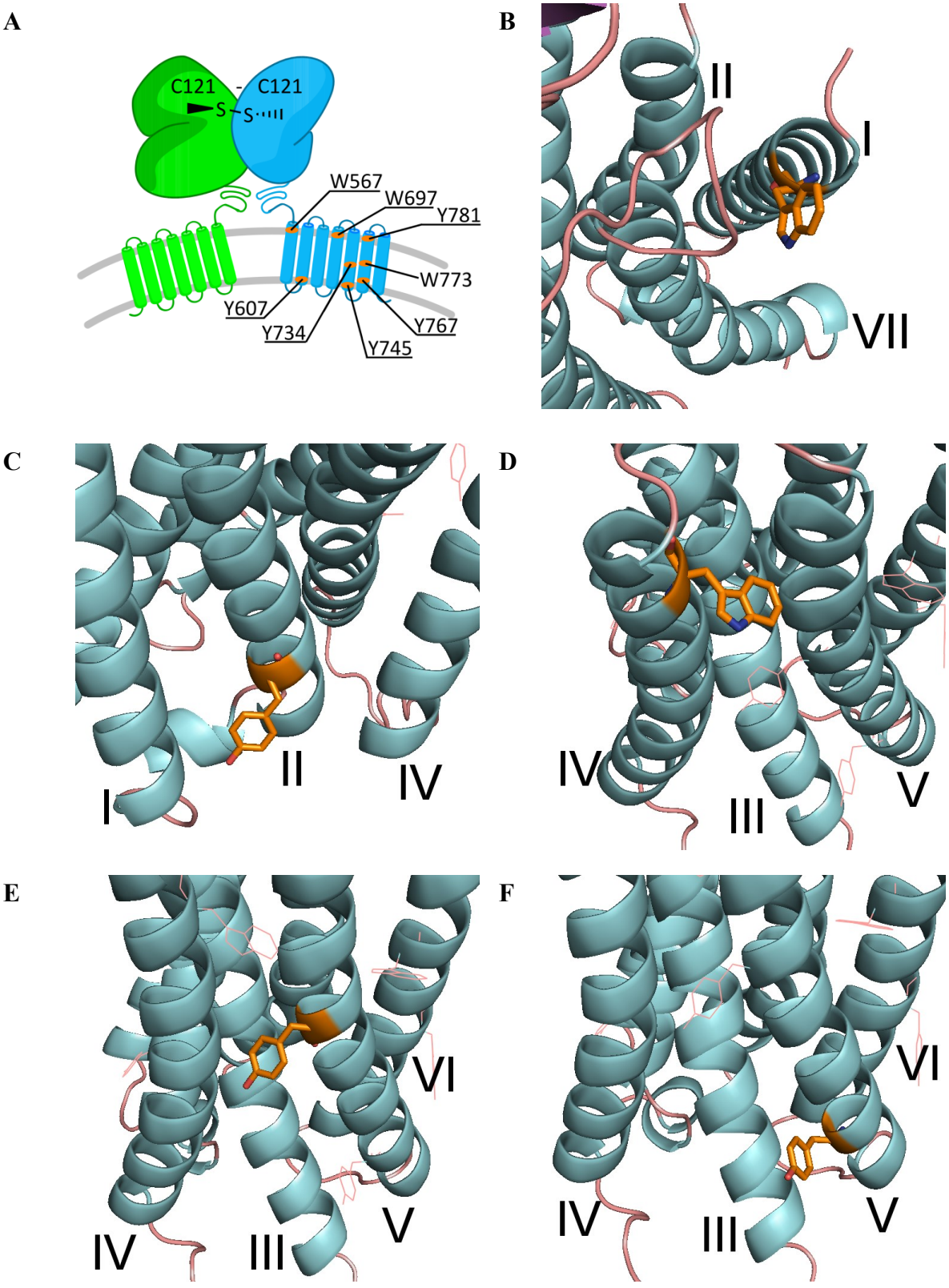

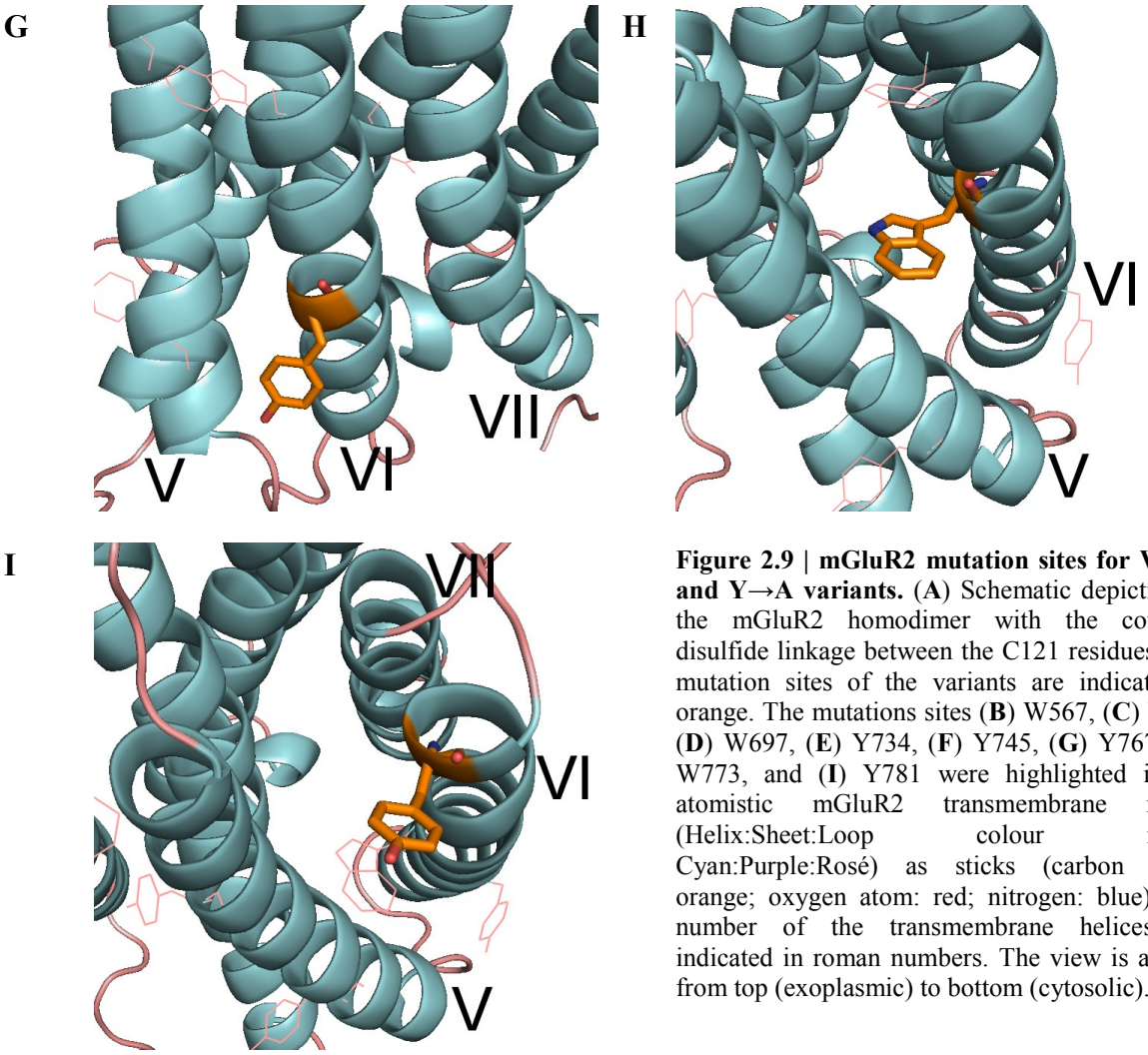

Figure 2.9 | mGluR2 mutation sites for W→A and Y→A variants. (**A**) Schematic depiction of the mGluR2 homodimer with the covalent disulfide linkage between the C121 residues. The mutation sites of the variants are indicated in orange. The mutations sites (**B**) W567, (**C**) Y607, (**D**) W697, (**E**) Y734, (**F**) Y745, (**G**) Y767, (**H**) W773, and (**I**) Y781 were highlighted in the atomistic mGluR2 transmembrane model (Helix:Sheet:Loop colour mode, Cyan:Purple:Rosé) as sticks (carbon atom: orange; oxygen atom: red; nitrogen: blue). The number of the transmembrane helices are indicated in roman numbers. The view is always from top (exoplasmic) to bottom (cytosolic).

2.1.3 The plasmid DNA concentration determines the transfection efficiency

To study the transfection efficiency of the pCMV6 vectors, Hek293 cells were transfected with eGFP constructs described in Section 2.1.1. The constructs were transiently transfected into the cells with FuGENE HD – a commercially available transfection agent – and the expression quantified by flow cytometry (details see Section 4.4).

To test how the amount of plasmid DNA would influence the transfection efficiency, different amounts of eGFP constructs were transfected into Hek293 cells along with pCMV6 vector as negative control. After 48 h transfection, the cells were harvested and the eGFP fluorescence quantified by flow cytometry at 530 nm. It appeared that the transfection efficiency measured as eGFP fluorescence in the flow cytometer declined with the amount of plasmid DNA used for the transfection (Figure 2.10). The trend appeared to be independent of the construct used for the ectopic expression. A drop of >50% transfection efficiency was observed from the

highest to the lowest DNA concentration in the experiments: the transfection was >80% at 1000 ng per well while it dropped to about 30% at 250 ng (Figure 2.10).

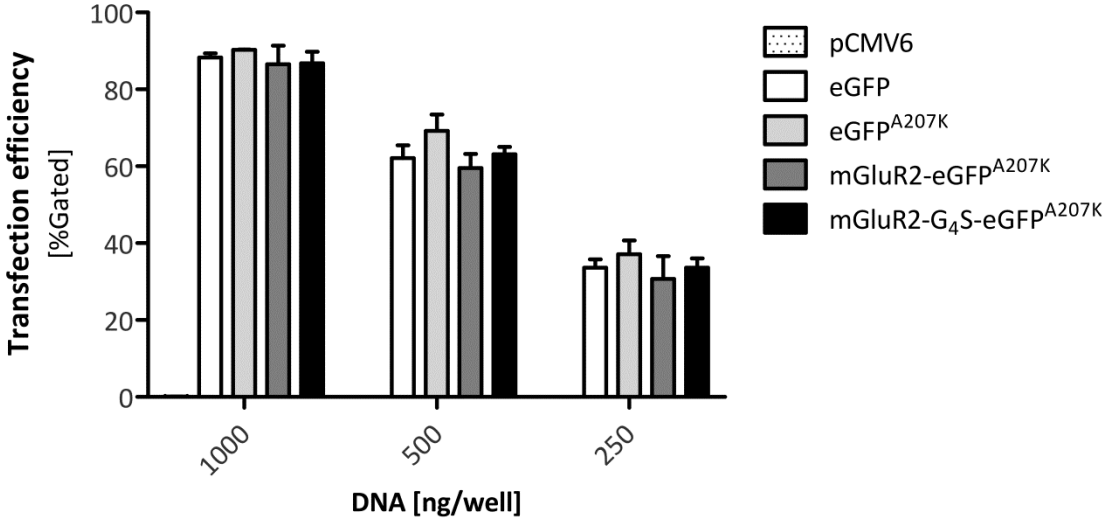

Figure 2.10 | Transfection efficiency with the FuGENE HD protocol in Hek293 cells. To quantify the transfection efficiency, Hek293 cells were transiently transfected in a 6-well cell culture plate format using either pCMV6 vector control or different eGFP constructs as indicated. The expression of the constructs was quantified 48 h post-transfection by measuring the fluorescence of eGFP at 530 nm in the flow cytometer (details see Section 4.4). The grouped bar plot represents n=2 independent experiments plotted as mean+SEM in GraphPad Prism.

The different eGFP constructs showed a dependency of the transfection efficiency on the amount of plasmid but no difference was observed between the different eGFP constructs (Figure 2.10). In the next experiment, a similar setup was used to test a wider range of plasmid DNA concentrations. Here, just eGFP^{A207K}-tagged mGluR2 fusion proteins were considered.

The measurement in the flow cytometer showed that there was a consistent dependency between the amounts of transiently transfected plasmid DNA and the transfection efficiency (Figure 2.11). Also in the second experiment the overall trend remained: the transfection efficiency declined with the DNA level. Notably the absolute values were lower as compared to the initial experiment (compare Figure 2.10 and Figure 2.11): while at 1000 ng per well an efficiency or more than 85% had been measured in the first experiment for mGluR2-eGFP^{A207K} fusion proteins, the value dropped to 71% and 76% for the fusion proteins without and with glycine-serine linker, respectively. Also at 500 ng and 250 ng DNA per well, slightly lower values were measured for the two mGluR2 fusion proteins as compared to the first experiment. At the lower concentrations of 125 ng and 50 ng per well, which had not been included in the previous assay, the average transfection efficiency dropped to 10% and 3%,

respectively (Figure 2.11). The smaller eGFP^{A207K} protein was with 83% at 1000 ng per well still expressed at the same level as observed beforehand.

The differences in the transfection efficiency between the first and the second assay were eventually connected to the different passage number of the Hek293 cells. While in the first experiments a low passage number was used, the second one was conducted at a higher passage number. To avoid larger differences in future experiments, cells were used for the experiments just between passage three and 20.

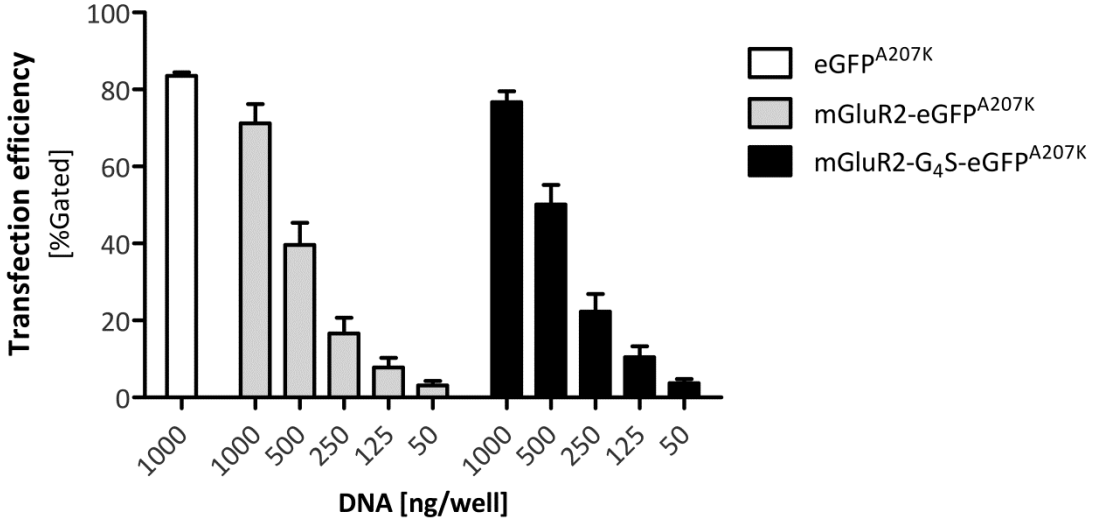

Figure 2.11 | Transfection efficiency of GRM2 constructs at different plasmid DNA levels. To quantify the transfection efficiency, Hek293 cells were transiently transfected in a 6-well cell culture plate format using either eGFP^{A207K} control or tagged GRM2 constructs as indicated. The expression of the constructs was quantified 48 h post-transfection by measuring the fluorescence of eGFP at 530 nm in the flow cytometer (details see Section 4.4). The grouped bar plot represents n=5 independent experiments plotted as mean+SEM in GraphPad Prism.

From the experiments was concluded that the transfection efficiency played a decisive role in the context of transient transfection experiments in Hek293 cells. For the further experiments this effect would need to be considered to avoid artifacts.

2.2 Biochemical characterization of mGluR2 and its variants

Before starting the actual labeling experiments with the tritiated lipids, the Flag-tagged W→A and Y→A variants of mGluR2 were tested in transient expression experiments for their basic biochemical properties in comparison to the wild type. The two main properties the experiments were focused on were the (intra-)cellular trafficking on the one hand, and the dimerization on the other. With the testing this biochemical properties it was to be assured

that the effect later quantified in the cellular lipid photocrosslinking experiments would not result from secondary effects, such as an impaired trafficking.

2.2.1 Trafficking and cell surface arrival of mGluR2

2.2.1.1 Cell surface arrival of Flag-tagged W/Y→A mGluR2 variants measured in a biotinylation assay

The cell surface arrival of mGluR2-Flag was considered a central quality measure for the receptor and its variants. It allowed making conclusion on the cellular distribution of the receptors and indirectly the lipid environment that they faced. The question in the next experiment was if that distribution would change at different plasmid concentration used for the transient transfection. While intuitively a high amount of DNA for the experiments appeared to be desirable, this would have eventually been connected to an overexpression of the protein to the manifold and severe stress for single cells. In order to get reliable results for the follow-up experiments and at the same time limiting the overexpression, the aim of the experiment was to limit the transfection level while at the same time allow a stable trafficking. The issue was met with a quantification of the cell surface arrival of the receptors at different transfection levels. The starting point for the experiment was the range of transient transfection levels which had been established in the initial experiments with the mGluR2-eGFP^{A207K} fusion proteins (Figure 2.11). Now, the mGluR2-Flag and mGluR2^{C121A}-Flag proteins were transiently expressed in He293 cells transfected with increasing levels of plasmid DNA (Figure 2.12). To capture proteins residing at the plasma membrane, the cells were treated with non-membrane permeable Sulfo-NHS-SS-Biotin which would form covalent bonds with primary amines (164) (details see Section 4.8).

For mGluR2-Flag, the efficiency of cell surface arrival was found to be independent of the DNA concentration used for transfection in a range between 125 ng and 1000 ng plasmid DNA per well (Figure 2.12 C). At the different DNA concentrations, the averaged results for Flag-tagged wild type varied between 46-55%. Similar quantification results were seen for mGluR2^{C121A}-Flag, but here the variation between the DNA levels was higher at lower DNA concentrations (Figure 2.12 D). In the range between 125 ng and 1000 ng the averaged cell surface arrival varied between 45-69%. In both cases a DNA concentration of less than 125 ng per well used for transfection lead to increasing variations in the cell surface delivery. For example, a cell surface arrival of 110% was measured for mGluR2^{C121A}-Flag at 50 ng, the lowest DNA concentration in the experiment. This result suggested a quantification artifact.

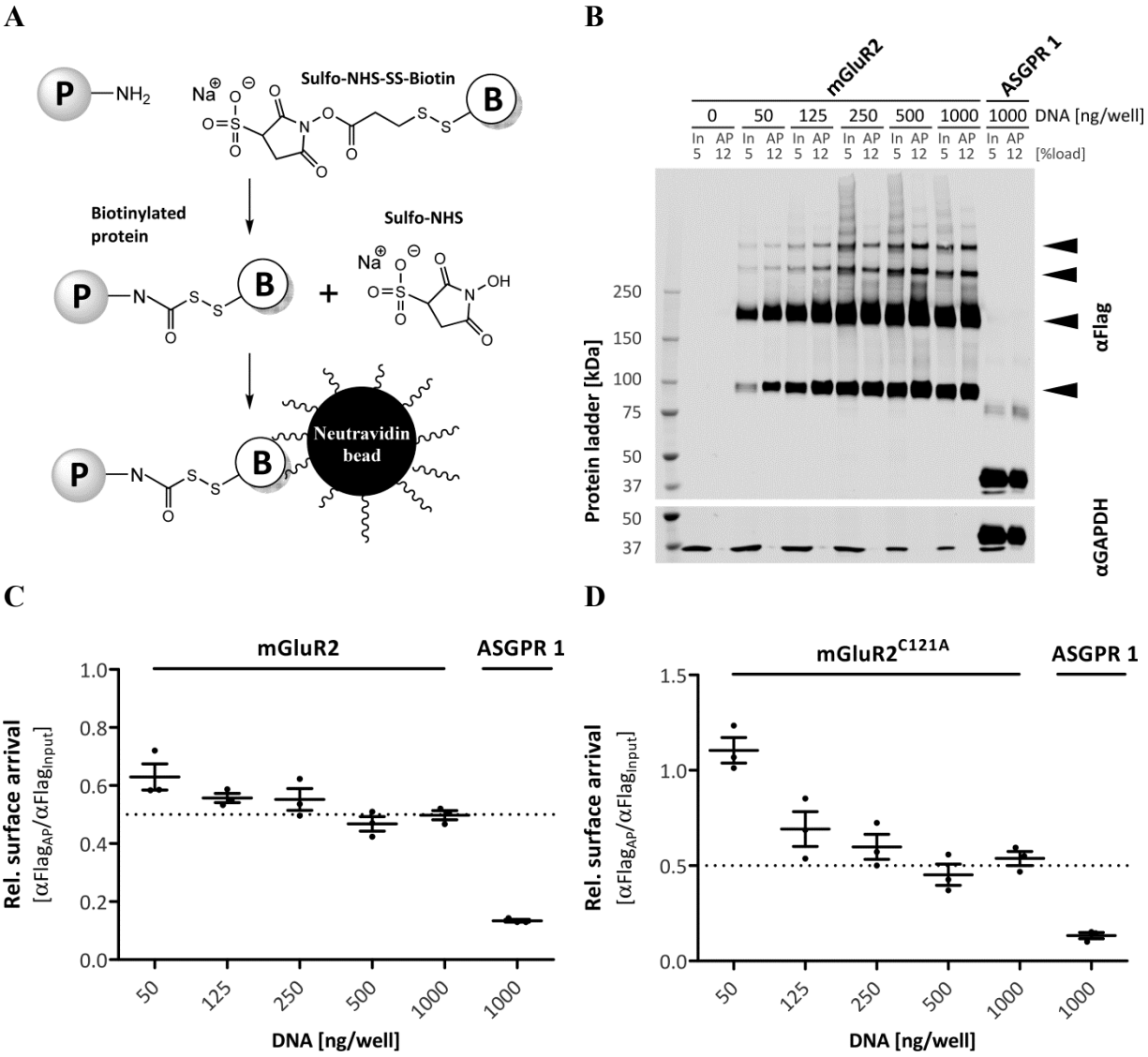

Figure 2.12 | Cell surface biotinylation of mGluR2 at different transfection and expression levels. The relative surface arrival of transiently expressed mGluR2-Flag protein was measured following transfection with different DNA concentration in a 6-well plate format (details see Section 4.8). (**A**) Schematic depiction of the assay principle. Deprotonated primary amines of cell surface proteins ('P') react with the NHS ester of Sulfo-NHS-SS-Biotin in a one-step reaction. The protein P is biotinylated ('B') and *N*-hydroxysulfosuccinimide (Sulfo-NHS) released as byproduct. The proteins are captured by the interaction with neutravidin (avidin preparation) on agarose beads. The disulfide bond in the spacer arm is cleaved during sample preparation by a reductive agent and the protein is released again (164). The picture was realized with ChemDraw. (**B**) Input (In) and affinity purification (AP) samples were separated by SDS-PAGE. On the immunoblot the αFlag signal of monomer and oligomers was quantified as indicated (black arrow heads). The αGAPDH signal was used as negative and ASGPR1-MycFlag signal as postive control. The blot is representative for n=3 independent experiments with mGluR2-Flag. The blots for mGluR2^{C121A}-Flag are not shown. (**C**) The relative surface arrival for mGluR2-Flag was quantified as ratio of the affinity purified αFlag signal versus the total input signal. The dot plot in GraphPad Prism shows the values for the three replicates as mean±SEM. (**D**) The relative surface arrival for mGluR2^{C121A}-Flag was analyzed as described for mGluR2-Flag.

From the experiments was concluded that transient transfections with a different DNA concentration would result in a stable cell surface expression of the receptors, but below a certain DNA concentration artifacts would be more likely to occur. A reproducible cell surface arrival for mGluR2-Flag was observed at a transfection level between 125 ng and

1000 ng plasmid DNA per well (Figure 2.12). For mGluR2^{C121A}-Flag proteins, a stable surface expression was measured in a range from 250 ng to 1000 ng plasmid DNA per well. Here, the loss of the disulfide bridge did not seem to block surface trafficking. Thus, the cell surface arrival was only assayed for the different mGluR2-Flag W→A and Y→A variants. The variants' cell surface arrival was compared to the mGluR2-Flag wild type (Figure 2.13). The transfection levels were adjusted to either 125 ng or 250 ng. Variants with a strong expression were adjusted to 125 ng and those that were weakly expressed to 250 ng. This was done to avoid quantification artifacts on the immunoblot.

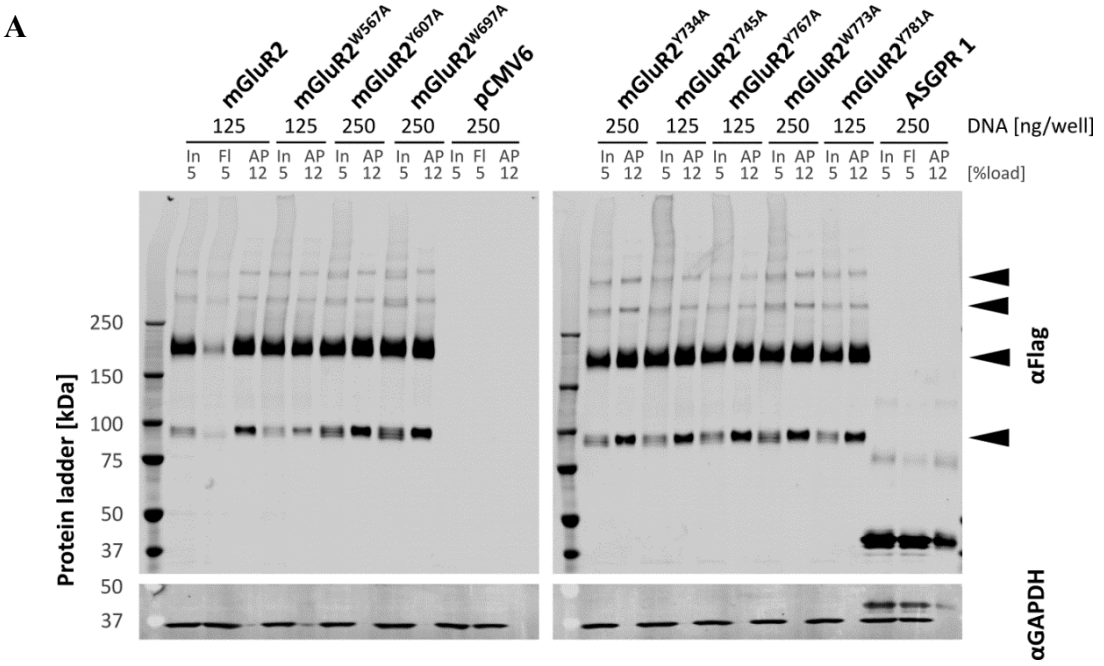

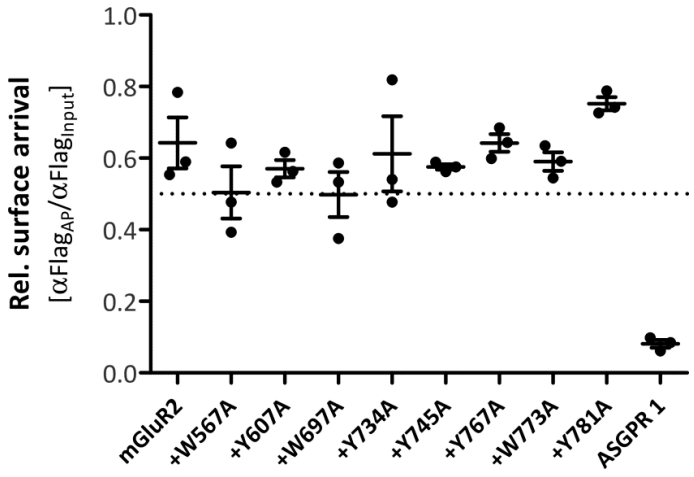

Figure 2.13 | Cell surface arrival of transiently expressed W→A and Y→A mGluR2-Flag variants in Hek293 cells. The relative cell surface arrival of transiently expressed mGluR2-Flag variants was measured at a DNA concentration of 125 ng or 250 ng in a 6-well plate format (details see Section 4.8). (**A**) The input (In) and affinity purification (AP) samples were separated by SDS-PAGE. On the immunoblot the αFlag signal of monomer and oligomers was quantified as indicated (black arrow heads). The αGAPDH signal was used as negative and ASGPR1-MycFlag signal as postive control. The blot is representative for n=3 independent experiments. (**B**) The relative surface arrival was quantified as ratio of the affinity purified αFlag signal versus the total input signal. The dot plot in GraphPad Prism shows the values for the three replicates as mean±SEM.

The surface arrival of the different W→A and Y→A mGluR2 variants did not show significant differences as compared to the wildtype in a statistical test with a 1way ANOVA (Dunnetts' post test in GraphPad Prism versus wild type, α=0.05) (Figure 2.13 B).For most of the variants 50-70% of total protein had reached the cell surface; an averaged value of 64% was measured for the wild type mGluR2-Flag. In summary, none of the Flag-tagged mGluR2 variants tested showed critical folding defects leading to retention in the endoplasmic reticulum (ER). A similar experiment with mGluR2^{C121A}-Flag double mutants showed larger variations within the measurements but no major difference between the variants (data not shown).

2.2.1.2 Estimation of intracellular trafficking of mGluR2 variants by enzymatic deglycosylation with EndoH and PNGaseF

The quantification of the surface arrival showed that proteins had successfully passed the secretory pathway. As a complementing approach to study intracellular transport of mGluR2-Flag variants, the glycosylation state was investigated using endoglycosidase treatment. mGluR2 contains five potential glycosylation sites (UniProt entry Q14416 (GRM2_HUMAN). Proteins that are retained in the ER show a different N-glycosylation pattern than the ones shuttling through the Golgi (109, 165). Due to a different glycolyation pattern, ER resident proteins are sensitive to deglycosylation with endoglycosidase H (EndoH) which cleaves only N-linked high mannose and some hybrid oligosaccharides within the chitobiose core (166). In contrast, the enzyme Glycopeptide N-glycosidase (PNGaseF) hydrolyses both high mannose and complex N-linked oligosaccharids by attacking the N_4-(acetyl-beta-D-glucosaminyl)asparagine residue of glycoproteins (167, 168).

The different W→A and Y→A mGluR2-Flag variants were deglycosylated with either EndoH or PNGaseF after transient expression in Hek293 cells to find out whether there would be any difference in the sensitivity towards one of the enzymes (Figure 2.14 B) (details see Section 4.9). The experiments showed that all receptors treated with PNGaseF migrated further on separation by SDS-PAGE (Figure 2.14 B, +P). Both for the mGluR2 monomer and dimer, PNGaseF treatment led to a shift towards lower apparent molecular weights. This indicated that the proteins had carried one or more N-glycan.

In contrast to PNGaseF, Endo H cleavage led to a partial shift of the proteins to a lower molecular weight band, suggesting that a fraction of the proteins was still Endo H-sensitive (Figure 2.14 B, +E, monomer). The shifted fraction was migrating approximately at the same

height as the PNGaseF treated samples. Taken together, these data suggest that a significant amount of the W→A and Y→A mGluR2-Flag variants had passed the secretory pathway and localized to the plasma membrane (109, 165).

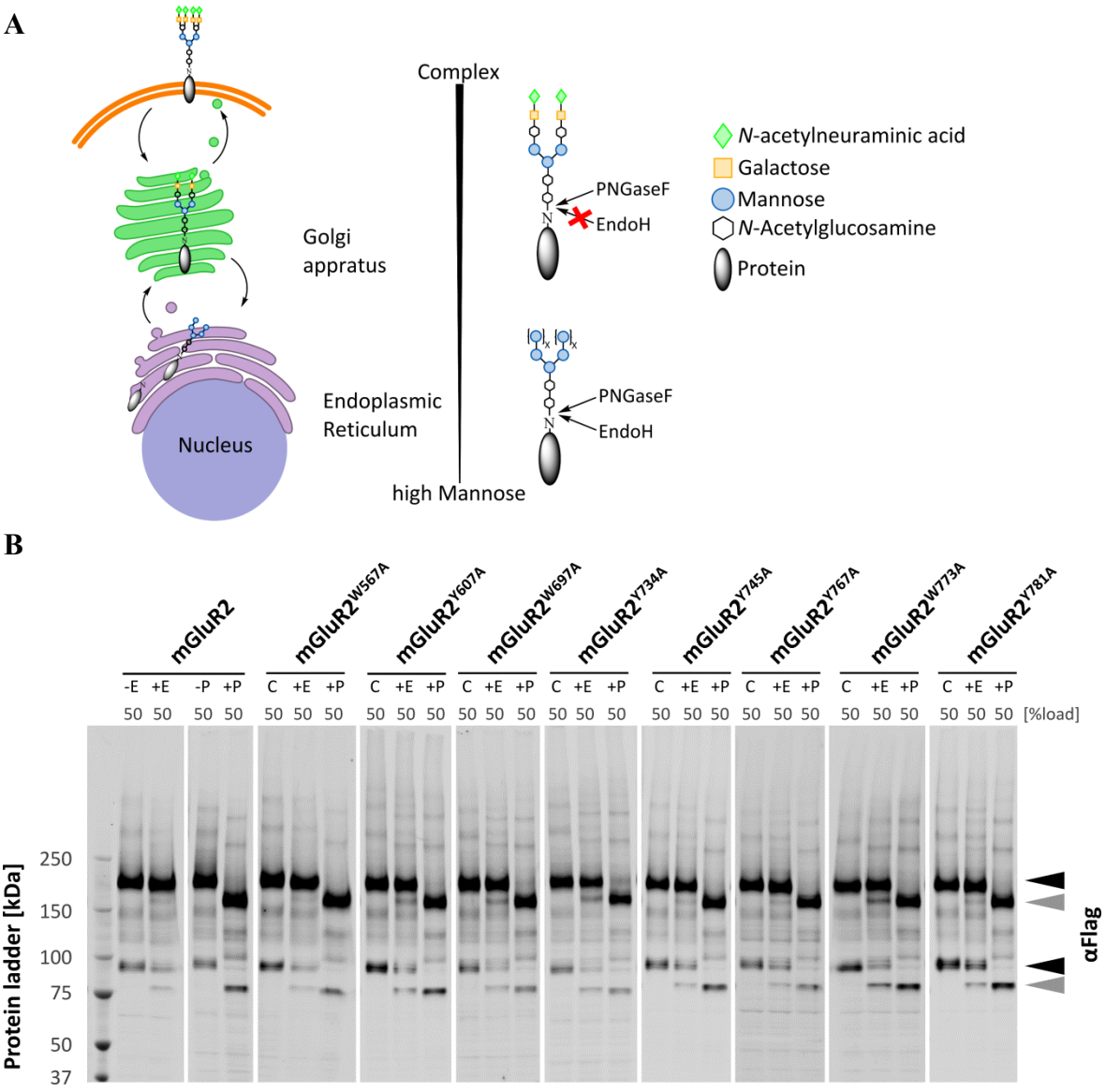

Figure 2.14 | Deglycosylation of mGluR2 W→A and Y→A variants with EndoH and PNGaseF. mGluR2-Flag W→A and Y→A variants were transiently expressed in Hek293 cells. After 48 h, the cells were harvested and the total protein fraction was subjected to enzymatic deglycolysation using EndoH (+E) or PNGaseF (+P). The controls (C) were mock treated in reaction buffer which had been provided with the enzymes (details see Section 4.9). (**A**) Schematic depiction of the assay principle. Proteins of the secretory pathway are modified at the consesus site N-x-S/T (x any amino acid but proline) in the lumen of the ER. In several steps, the N-glycan modification becomes increasing complex as the protein shuttles through the secretory pathway (138). While PNGaseF can cleave any N-linked glycan, EndoH can only cleave high mannose and some hybrid N-glycans (169). The picture was realized with ChemDraw. (**B**) The deglycosylated samples were separated by SDS-PAGE. On the immunoblot the αFlag signal of fully glycosylated monomer and dimer was indicated with black arrow heads. The shifted bands after deglyocylation was indicated with gray arrow heads. The blot is representative for n=3 independent experiments. The αFlag signal on the immunoblot was adjusted to optimal contrast for each variant.

2.2.2 Dimerization of mGluR2 W/Y→A variants

Dimerization is considered a hallmark of mGluR2 function, as shown both by structural and biochemical data (131, 170). For that reason, the oligomeric state of mGluR2 variants was tested using cysteine crosslinking, non-reducing SDS-PAGE and co-immunoprecipitation (Co-IP) experiments.

2.2.2.1 Transmembrane cysteine crosslinking assay with *N*-Ethylmaleimide

Biochemical data published by the group of Jean-Philipp Pin suggested an activity dependent dimerization interface between transmembrane helices IV, V and VI of mGluR2 (121) (see also Section 4.7). In this study, the dimerization interfaces of mGluR2 were probed by introducing cysteine residues at distinct sites within the transmembrane domain of the protein. Adjacent cysteine residues in the transmembrane domain were oxidized to cystine in the presence of Dichloro(1,10-phenanthroline)copper(II) (CuP) to determine interactions of the individual transmembrane helices. Free sulfhydryl groups were blocked by *N*-ethylmaleimide (NEM) (Figure 2.15 A).

To test the dimer interface of mGluR2 using this crosslinking approach, cysteine residues were introduced by mutagenesis PCR on the background of a C121A mutation in the extracellular domain of mGluR2 (Section 4.2.7). This C121 residue was shown to mediate covalent crosslinking of the mGluR2 homodimer and thus, had to be removed to allow for probing of TMD-TMD interactions (96, 121). By site-directed mutagenesis, the residues L698 in transmembrane helix IV, Y734 in helix V or V782 in helix VI were changed to cysteine residues on the mGluR2^{C121A}-MycFlag background.

Cysteine-mediated crosslinking was measured by the increase in the dimerization ratio. For all mGluR2 cysteine variants tested, the dimerization ratio increased in the CuP crosslink as compared to the control without CuP and the C121A single mutant (Figure 2.15 C). For the mGluR2$^{C121A/L698C}$-MycFlag and mGluR2$^{C121A/Y734C}$-MycFlag variants, the ratio increased from 54% and 54% to 99% and 96%, respectively. With 70% the ‘basal’ crosslinking was highest for mGluR2$^{C121A/V782C}$-MycFlag in helix VI. The dimerization increased to 96% in the presence of CuP. This might be attributed to a better accessibility of the residues towards one another which would allow formation of disulfide bridges also in the absence of CuP, or a preference for the interface in the current setup. Notably, the dimerization rate was 99% for the wild type and ~60% for C121A both in the presence and absence of CuP.

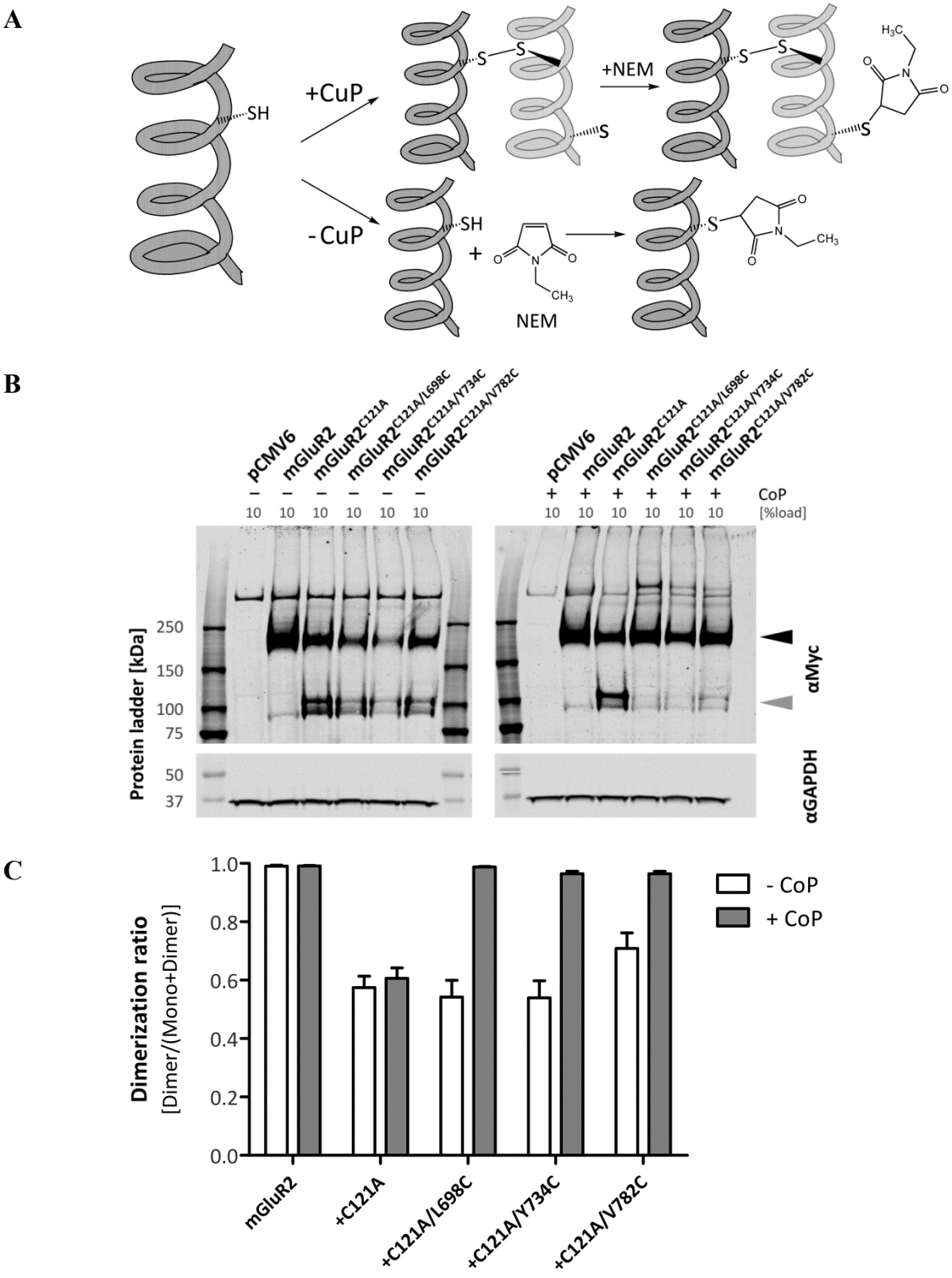

Figure 2.15 | Cysteine crosslinking of transmembrane helices using Dichloro(1,10-phenanthroline)-copper(II). The MycFlag-tagged mGluR2 wild type and the derived C121A single and double mutants were transiently expressed in Hek293 cells. The crosslinking procedure was applied to intact cells as described in Section 4.7. The negative control (-CuP) was conducted without Dichloro(1,10-phenan¬throline)¬copper(II) (CuP) in the corresponding buffer. (**A**) Schematic depiction of the assay principle. The cysteines are crosslinked in the presence of CuP with adjacent cysteine residues to disulfide bridges. *N*-ethylmaleimide then blocks all free thiol groups (121). The picture was realized with ChemDraw. (**B**) The blot (scanned at an intensity of 3-4) is representative blot for n=3 independent experiments. Quantified dimer bands are indicated with a black arrow head, the monomer bands with a grey arrow head. (**C**) The bar plot in GraphPad Prism shows the values for the three replicates as mean+SEM.

However, the assay confirmed the published data and that a dimerization interface was present also within the transmembrane domain (121). Furthermore, it indicated that the mGluR2 protein had been expressed correctly in the current setup.

2.2.2.2 Non-reducing PAGE showed the importance of C121 disulfide bridges in mGluR2

Disulfide bridge-mediated dimerization of mGluRs can also be analyzed by non-reducing SDS-PAGE (132): under non-reducing conditions disulfide bonds stay intact and monomer and dimer receptor protein can be separated from each other. To avoid unspecific formation of disulfide bridges by unpaired cysteine residues during sample preparation, the sulfhydryl groups were alkylated with NEM as described for the previous experiment (details see Section 4.10). Metabotropic glutamate receptors are especially prone to the formation of such unspecific disulfide bonds as they contain a cysteine-rich linker region between the extracellular domain and the transmembrane domain (170). For that reason higher oligomers (trimers, tetramers or more) are often visible on the western blot, but are not considered physiologically relevant (131).

The non-reducing SDS-PAGE was performed with all Flag-tagged W→A and Y→A variants which had been cloned as single mutants in the background of a wild type mGluR2 or as double mutants with an additional C121A modification in the extracellular domain (Figure 2.16 A). The immunoblot for the single mutants showed a broad signal at an apparent size of 200-250 kDa which corresponds to the predicted size for the dimer of ~190 kDa. The band corresponding to the monomer at an apparent molecular weight of 100 kDa (predicted ~95 kDa) was by far weaker. Here, the dimerization ratio for the Flag-tagged wild type and the corresponding variants averaged between 96-99%. In contrast to that, mGluR2^{C121A}-Flag and the corresponding W→A and Y→A double mutants showed a stronger signal for the monomer band. Subsequently, the dimerization ratio was reduced by 40-50% as compared to the single mutants (Figure 2.16 B). The dimerization ratio for the double mutants averaged between 38-50%. No significant difference within the single or double mutant set was observed (1Way ANOVA with Dunnetts' post test in GraphPad, W→A and Y→A variants versus mGluR2-Flag or mGluR2^{C121A}-Flag, α=0.05). The only significant difference ($P < 0.05$) was found between mGluR2-Flag and mGluR2^{C121A}-Flag.

Thus in the current experiment, the non-reducing conditions allowed the C121-C121 disulfide bridge in the mGluR2-Flag homodimer to stay intact. The disulfide bridge appeared to be still intact also for the different variants of mGluR2-Flag, which suggested that the receptor had

been expressed correctly – as already seen in the trafficking assays (Section 2.2.1). Notably, the interaction in the homodimer of the mGluR2^{C121A}-Flag variants could not be broken completely even the disulfide bridge was absent. This argued for strong non-covalent interactions between the protomers (Figure 2.16).

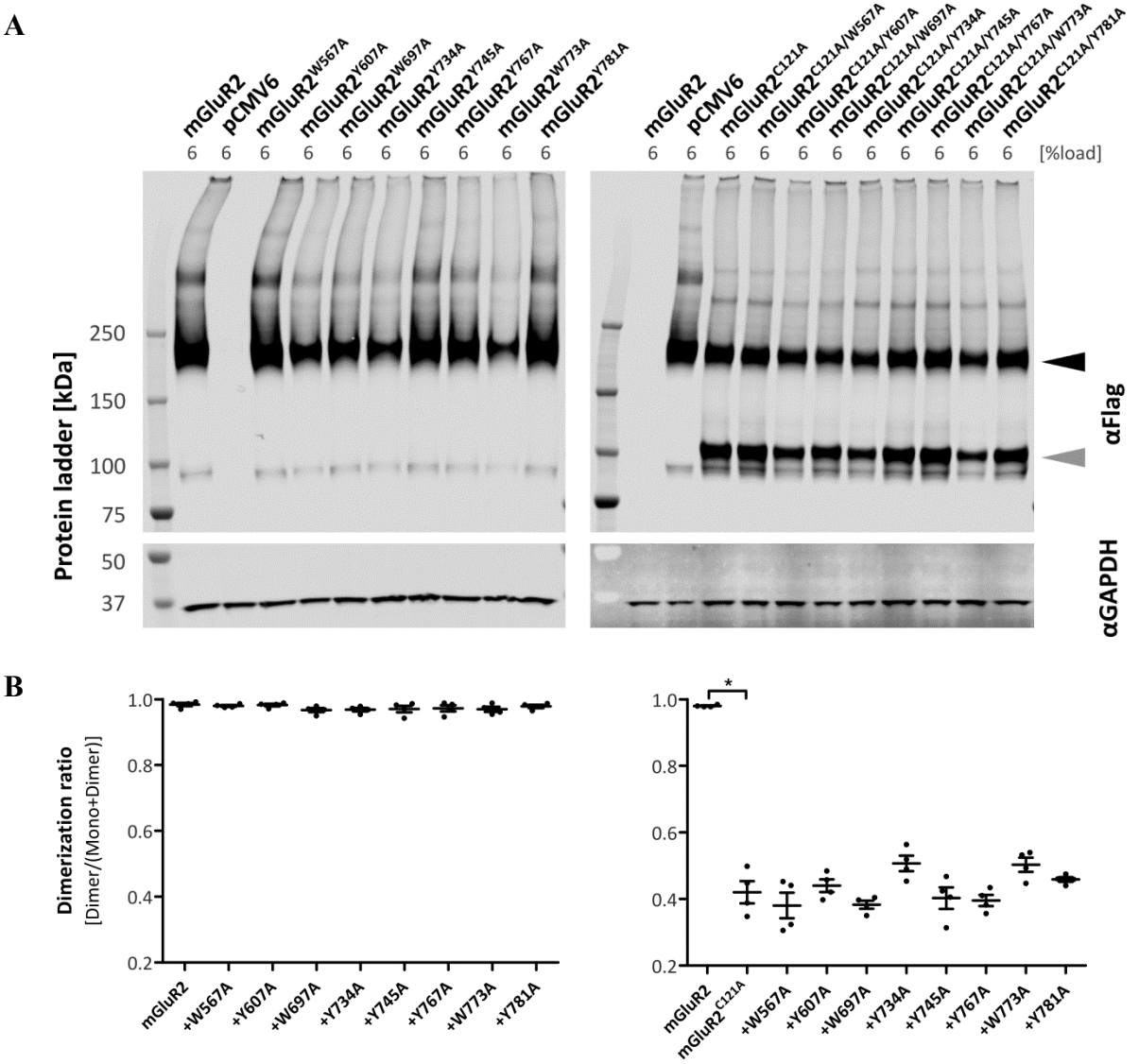

Figure 2.16 | W→A and Y→A single and double mutants were alkylated with NEM and subjected to non-reducing SDS-PAGE. For the experiment, mGluR2-(Myc)Flag or mGluR2^{C121A}-Flag constructs were transiently expressed in Hek293 cells (details see Section 4.10). (**A**) The protein samples were separated by non-reducing SDS-PAGE. On the immunoblot the αFlag (Mouse, F1804) signals of monomer (grey arrow heads) and dimer (black arrow heads) were quantified as indicated. The αGAPDH signal was used as loading control. For each set of variants, the blots are representative for n=4 independent experiments scanned at intensity of 2.5. (**B**) The dot plot in GraphPad Prism shows the values for the four experiments as mean±SEM. Statistics with 1way ANOVA versus mGluR2-Flag or mGluR2^{C121A}-Flag (*=P<0.05).

2.2.2.3 Co-immunoprecipitation as measure for dimerization of mGluR2 wild type and variants

As a complementing approach to the cysteine crosslinking experiments and the SDS-PAGE under non-reducing conditions, Co-IP experiments were performed to find whether the W→A and Y→A variants of mGluR2 would still heterodimerize with the wild type receptor. In two steps the Co-IP conditions were optimized for specificity and sensitivity.

In the first step, the detergent composition was adjusted. Six different detergent compositions were tested: Triton X-100 (TX100) combined with only sodium deoxycholate (Dx), or with Dx and sodium dodecylsulfate (SDS). Likewise, NonIdet-P40 (NP-40) was combined with the two ionic detergents (Figure 2.17 A). For the experiments, the cells were lysed with the respective buffers and subsequently subjected to Co-IP using the Flag-tagged mGluR2 or mGluR2^{C121A} variant as bait and the respective Myc-tagged variant as prey. For the relative abundance of the Myc-bait after Co-IP, a value of at most 50% was expected. The value can be explained by looking at the binomial $(a+b)^2$. The term is solved as $a^2+ab+ba+b^2$ where a and b represent the Flag- and Myc-tagged proteins, respectively. That is to say when co-expressed the Flag+Flag- and Myc+Myc-tagged 'homodimers' compete with the Flag+Myc-tagged 'heterodimers'. In case that there would be no influence of the tag on dimerization, around 50% recovery of the Myc prey was to be expected.

αFlag signal was enriched under all detergent compositions tested, which showed that the bait protein had bound to the αFlag beads (Figure 2.17 B). Thus none of the detergent compositions hampered the binding of the Flag-tagged epitope to the antibody. Moreover, the αGAPDH loading control showed that no soluble protein had been retained in the IP-fraction. Finally, a αMyc signal was observed on the blot in all setups (Figure 2.17 A). The quantification of the αMyc signal in the mGluR2-Flag Co-IP showed that the relative abundance of the prey protein after Co-IP was rather insensitive to the detergent composition (Figure 2.17 C). For the NP-40 based buffers a recovery of 48% was measured which did hardly change in the presence of the Dx and SDS. For the TX100 buffers, there was a slight increase observable when applying more stringent conditions: for TX100 the averaged recovery was 35% while in the presence of all three detergents the value increased to 43%.

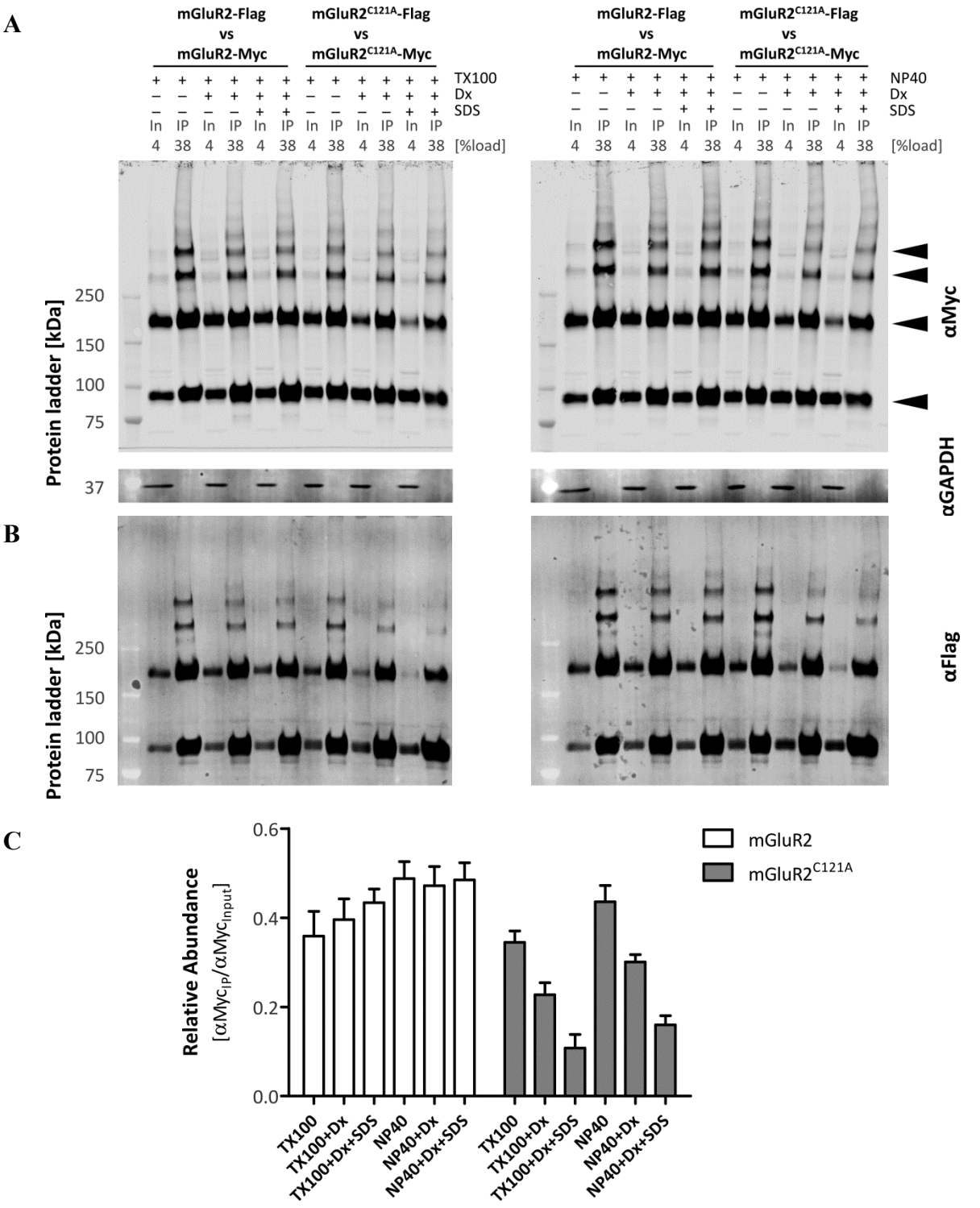

Figure 2.17 | Co-immunoprecipitation with different combinations of non-ionic and ionic detergents. mGluR2-Flag or mGluR2^{C121A}-Flag were co-expressed in Hek293 cells with their corresponding Myc-tagged variant. The lysis and co-immunoprecipitation was carried out with the indicated buffer (details see Section 4.11.1). (**A+B**) The input (In) and immunoprecipitated (IP) protein samples were separated by SDS-PAGE. On the immunoblot, αMyc (Rabbit, NB600-336) signals were quantified as indicated (mGluR2: black arrow heads, β2AR: grey arrow head). αFlag (Mouse, F1804) signals were used as pull-down and αGAPDH signals as loading control. The blots are representative for n=3 experiments scanned at an intensity of 2.5. (**C**) The bar plot in GraphPad Prism shows the relative abundance of the prey protein for the three experiments as mean±SEM.

In contrast to that, the mGluR2^{C121A}-Flag variants appeared to be sensitive to the presence of ionic detergents (Figure 2.17 C). While for TX100 and NP-40 34% and 43% of the Myc-tagged prey protein were recovered after the Co-IP, the averaged values dropped to 10% and 15% in the presence of both Dx and SDS. Moreover, NP-40 appeared to be less disruptive than TX100. The Co-IP performance of the buffer with 1% NP-40 came closest to the theoretical value of 50% recovery and was subsequently chosen as basis for the further experiments.

From the comparison of the different detergent combinations it could be concluded that the missing disulfide bond in the extracellular domain of the mGluR2^{C121A}-Flag made the system more sensitive towards changes in the detergent composition. Overall the *gedanken-experiment* concerning the bionomical was in accordance with the obtained result: on average no more than 50% prey protein was recovered (Figure 2.17 C). This also suggested that the N-terminal tags did not alter the dimerization preference.

In a second step, the experimental conditions were further adjusted and more controls were included to get a better insight into the specificity of the system. The mGluR2^{C121A}-Flag protein was used as bait protein for the corresponding Myc-tagged construct. As controls, the C-terminally Myc-tagged mGluR2 wild type or Beta-2 adrenergic receptor (β2AR) were co-expressed as prey proteins. The experimental conditions were adjusted following the protocols described by Milligan and Bouvier (171). As suggested, an alkylating substance was included following the already established protocol with NEM described for the cysteine-crosslinking (Section 2.2.2.1). Second, an ultracentrifugation step was included after lysis to remove non-solubilized proteins. Third, to avoid unspecific binding of the Myc-tagged prey proteins and thus an increase in the relative abundance after Co-IP, the salt conditions of the wash buffer were tested using low versus high salt conditions (Figure 2.18 A) (details see Section 4.11.2).

As in the first Co-IP experiment, the αFlag signal showed that the bait protein was binding to the αFlag beads under all given conditions (Figure 2.18 B), also including the more stringent conditions with the NEM alkylation step. The quantification of the immunoblot showed that the Co-IP of the mGluR2^{C121A}- mGluR2^{C121A} homodimer was by magnitudes more efficient than for the mGluR2^{C121A}- mGluR2 wild type heterodimer (Figure 2.18 C). For the homodimer, the relative abundance of the bait after Co-IP in all experimental conditions tested was quantified with 29-31% while for the heterodimer the averaged values varied

between 3-6%. This observation showed that the dimerization interface was sensitive also to subtle changes. For the homodimer, it appeared not to make a major difference whether the alkylation step with NEM or more stringent washing conditions were applied; the recovery remained largely unchanged. However, with the adjusted Co-IP conditions the relative signal for the C121A-C121A homodimer dropped from 43% to about 30% (compare Figure 2.17 and Figure 2.18).

To date, no interactions between mGluR2 and β2AR have been reported. For that reason β2AR was chosen as negative control. It became evident that – at least by means of quantification – the most stringent conditions including alkylation with NEM and high salt washing conditions were necessary to suppress unspecific binding of the family A GPCR. To wash the loaded αFlag beads with high salt wash buffer was sufficient to reduce 27% binding of β2AR-Myc measured at low salt conditions by about 60% (Figure 2.18 C). By applying also NEM alkylation, this value was again reduced by ~50% to an averaged recovery of only 4%. This suggested that both unspecific non-covalent interaction as well as spontaneous formation of unspecific disulfide bonds were involved in mGluR2-β2AR heteroreceptor formation. However, the immunoblot signals obtained for the β2AR were weak, raising the possibility of quantification artifacts (Figure 2.18 A). Nevertheless, based on these quantification results the most stringent conditions, including the NEM alkylation step and high salt washing, were chosen for further experiments.

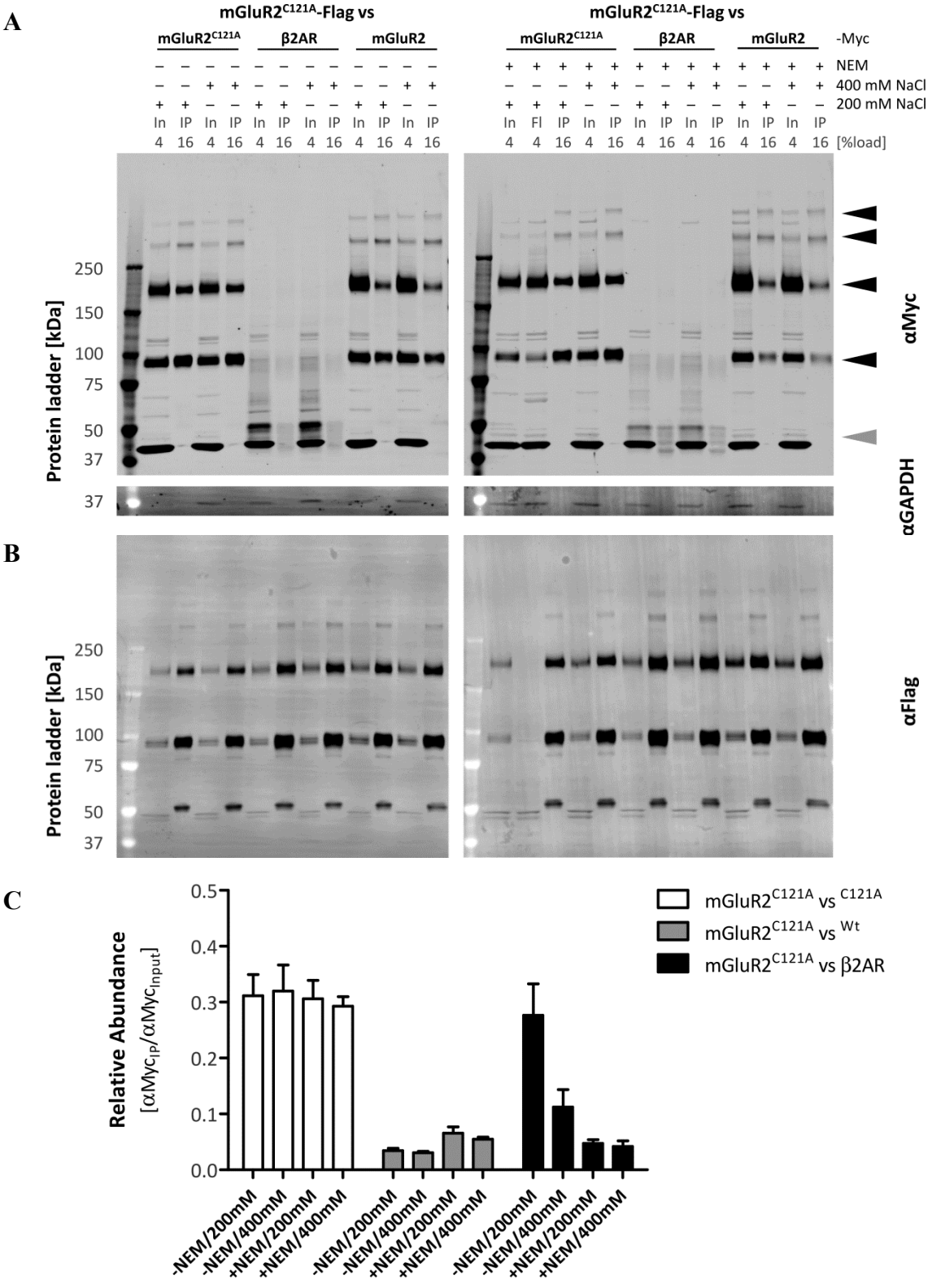

Figure 2.18 | Optimization of co-immunoprecipitation using different salt and alkylation conditions. mGluR2^{C121A}-Flag proteins were co-expressed in Hek293 cells with the indicated Myc-tagged preys. The lysis and co-immunoprecipitation was carried out with or without NEM-alkylation and with high or low salt washing buffer (details see Section 4.11.2). (A+B) The input (In), flow through (Fl) and immunoprecipitated (IP) protein samples were separated by SDS-PAGE. On the immunoblot, αMyc (Rabbit, NB600-336) signals were quantified as indicated (mGluR2$^{(C121A)}$-Myc: black arrow heads, β2AR-Myc: grey arrow head). αFlag (Mouse, F1804) signals were used as pull-down and αGAPDH signals as loading control. The blots are representative for n=3 experiments scanned at an intensity of 1.5. (C) The bar plot in GraphPad Prism shows the relative abundance of the prey protein after Co-IP for the three experiments as mean±SEM.

With the adjusted conditions, Co-IP experiments with various W→A and Y→A mGluR2 variants were performed. Either mGluR2-Flag or mGluR2^{C121A}-Flag were used as bait protein and they were co-expressed with the corresponding Myc-tagged variants (for mGluR2-Flag see Figure 2.19 A, mGluR2^{C121A}-Flag blots not shown). In addition to the co-expressed mGluR2-variant pairs, β2AR-Myc was included as negative control. The 'Myc vs Myc' and 'Flag vs Flag' controls were Co-IPs with only the Myc-tagged or only the Flag-tagged bait or prey, respectively. Finally, for the lysate control mGluR2 bait and prey proteins that had not been co-expressed were co-incubated during the IP (154). The aim of the lysate control was to check if the dimerization would also happen post-lysis.

For the Co-IP of the mGluR2-Flag protein and the corresponding W→A or Y→A variants no significant difference was observed (1way ANOVA Dunnetts' post test in GraphPad Prism versus mGluR2-Flag, α=0.05) (Figure 2.19). The average values were in a range of around 30-40% recovery of Myc-tagged prey after Co-IP (Figure 2.19 C). The controls showed that the experimental setup for the Co-IP worked as expected: i) the recovery for β2AR-Myc was around 2%, which suggested that binding by random protein-protein interactions was neglectable, ii) the mGluR2 'Myc vs Myc' and 'Flag vs Flag' signals indicated that there was no unspecific binding of Myc epitope to the αFlag beads during the Co-IP and, vice versa, no cross-signaling of the αMyc antibody with the Flag epitope on the immunoblot, and iii) the 'lysate control' showed that there was no dimerization occurring during cell lysis or IP. Together these data suggested that the W→A and Y→A substitutions in the Flag-tagged mGluR2 variants had no effect on 'heterodimerization' with the wild type receptor.

The controls in the mGluR2^{C121A}-Flag Co-IP experiment did not show any deviations from the controls in the previous experiment (Figure 2.19 C). However, the Co-IP of mGluR2^{C121A}-Flag with the corresponding Myc-tagged W→A or Y→A variants showed a higher variation. While for some, like mGluR2$^{C121A/Y734A}$-Myc, rather reproducible results were obtained, others showed strong deviations between experiments. Nevertheless, the mean values did not show any effects of the point mutations on mGluR2^{C121A}-variant dimer formation (1way ANOVA Dunnetts' post test in GraphPad Prism versus mGluR2^{C121A}-Flag, α=0.05).

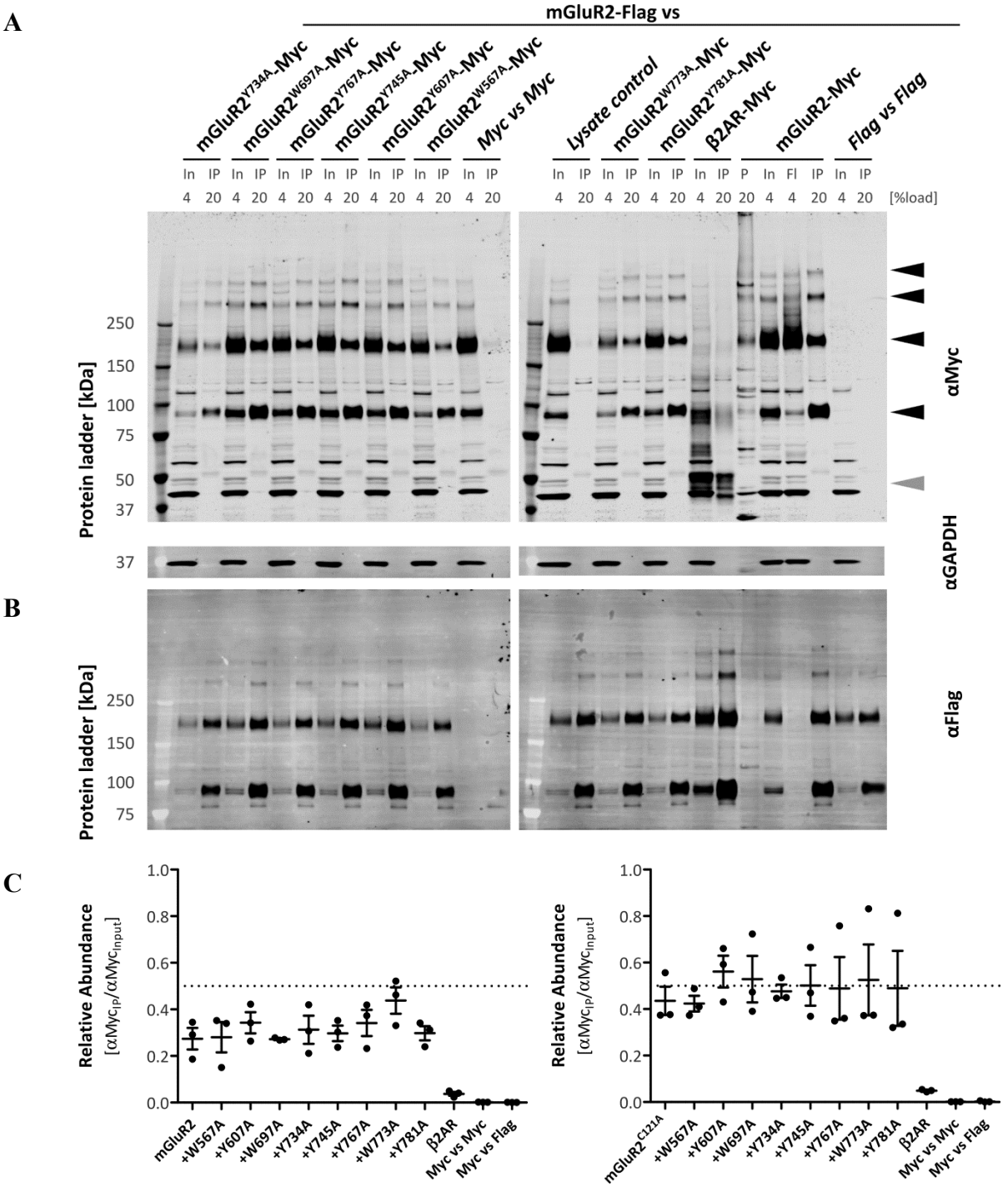

Figure 2.19 | Co-immunoprecipitation of Myc-tagged proteins with a Flag-tagged bait. mGluR2-Flag proteins were co-expressed in Hek293 cells with the indicated Myc-tagged preys. Cell lysis and co-immunoprecipitation was carried out including an NEM-alkylation step and high salt conditions (details see Section 4.11.3). (**A**+**B**) Input (In), pellet (P), flow through (Fl) and immunoprecipitated (IP) protein samples were separated by SDS-PAGE. On the immunoblot, αMyc (Rabbit, NB600-336) signals were quantified as indicated (mGluR2-Myc: black arrow heads, β2AR-Myc: grey arrow head). αFlag (Mouse, F1804) signals were used as pull-down and αGAPDH signals as loading control. Controls are indicated in cursive letters: '*Myc vs Mys'* represents co-expression of Myc-tagged mGluR2, '*Lysate control*' shows a lysate mix of Flag- and Myc-tagged mGluR2, and '*Flag vs Flag*' is a co-expression of Flag-tagged wild type mGluR2. The blot is representative blot for n=3 independent experiments scanned at an intensity of 1.5. (**C**) The bar plot in GraphPad Prism shows the relative abundance of the prey protein after Co-IP for the three experiments as mean±SEM. The experiments with mGluR2^{C121A}-Flag double mutants were conducted and analysed likewise.

The more stable results in the first experiment can be explained by the presence of the covalent linker between the two protomers (Figure 2.19). Without the disulfide bond in the homodimer, the assay appeared to be more prone to experimental variation. In summary, both Co-IP experiments showed that the tested Flag-tagged mGluR2 W→A and Y→A variants had retained the ability to dimerize with the corresponding wild type or the C121A mutant.

2.3 Biochemical characterization of other GPCRs

Three different metabotropic glutamate receptors were used to assess the S-palmitoylation of the family C receptors. Apart from mGluR2, the receptors mGluR1α and mGluR4 were tested in the assay. Along with this three receptors, two adrenergic and two serotonin receptors and two of their respective S-palmitoylation mutants were tested. This was done to validate the assay and minimized the risk of false negative finding because of the lack of specific palmitoyltransferases in Hek293 (reviewed by Fukata and Fukata (172)), as well as the risk of false positive due to incorporation of tritium into other biomolecules such as amino acids (76).

2.3.1 Cell surface arrival of transiently expressed GPCRs in Hek293 cells

The GPCRS, which were used for the S-palmitoylation assay, were subjected to cell surface biotinylation to test if their surface arrival was comparable to the one of mGluR2. As described in Section 4.8, the receptors were transiently expressed in Hek293 cells and then biotinylated with Sulfo-NHS-SS-Biotin. In comparison to the experiments with mGluR2 (compare Section 2.2.1.1), a higher plasmid DNA concentration was used to account for the weaker expression of the Serotonin receptors (Figure 2.20).

Flag-tagged mGluR1α and mGluR4 were detected with an averaged surface arrival of approximately 27% and 30%, respectively (Figure 2.20 B). For mGluR2 the quantified value of 46% was higher and thus in the same range as previously observed for the mGluR2 variants (compare Figure 2.13 and Figure 2.20). In contrast to that, the family A GPCRs and also the positive control ASPRGI were only weakly detected at the cell surface (Figure 2.20 B). For the serotonin receptors, the average cell surface arrival for the Flag-tagged constructs was 4% for 5-HT-1A and 5% for 5-HT-2B. Here, the quantification of the signals on the immunoblot was hampered by the poor signal-to-noise ratio of the receptors, for example of 5-HT-1A from mouse (Figure 2.20 A). For adrenergic receptors, like β2AR-Flag, the input sample was clearly visible while only a minor fraction of the receptor appeared to be biotinylated: only 5% were detected in the affinity purification. A similar picture appeared for

the Alpha-2A adrenergic receptor (α-2AAR). For α-2AAR-Flag, a relative cell surface arrival of 6% was detected. For the respective C→A variants, the quantified values were in the same range. For the adrenergic receptors, it might also have been a problem, that both receptors carried only 2 lysine residue in their extracellular domain which might have lowered the possibility to carry biotinylated primary amines. In comparison, the mGluRs have between 37 and 50 lysine residues in the extracellular domain.

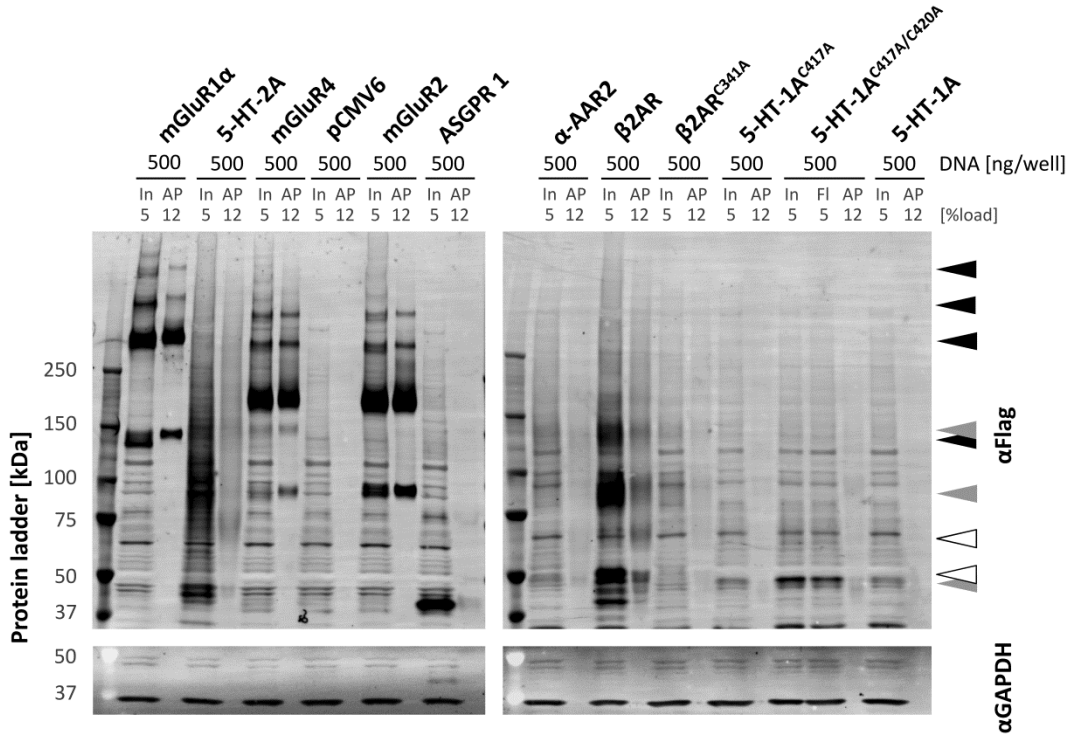

Figure 2.20 | Cell surface arrival of mGluRs, ARs and 5-HT-Rs and loss-of-function mutants. The relative surface arrival of transiently expressed Flag-tagged GPCRs in Hek293 cells was probed in a 6-well plate format (details see Section 4.8). (**A**) The input, flow through (Fl) and affinity purification (AP) samples were separated by SDS-PAGE. On the immunoblot the αFlag signal of monomer and oligomers was quantified as indicated (black arrow heads: mGluRs, grey arrow heads: ARs, white arrow heads: 5-HT-Rs). The αGAPDH signal was used as loading control and ASGPR1-MycFlag signal as postive control. The blot is representative for n=3 independent experiments. (**B**) The dot plot in GraphPad Prism shows relative surface arrival as ratio of the affinity purified αFlag signal versus the total input signal for the three experiments as mean±SEM.

The surface biotinylation assay showed that not all receptors were equally well expressed and detected on the immunoblot. For some like 5-HT-1A the detection was generally low, while for β2AR for example the number of available primary amines might had hampered a more efficient cell surface biotinylation.

2.3.2 Intracellular trafficking of GPCRs monitored by enzymatic deglycosylation

In addition to the cell surface arrival of the different wild type and version of the GPCRs, an enzymatic deglycosylation assay was performed for the mGluRs and the ARs (details see Section 4.9). 5-HTs were not included into the analysis because of their poor detection on the immunoblot (Figure 2.20). The assay was performed with EndoH and PNGaseF as previously described for the mGluR2 variants (Section 2.2.1.2).

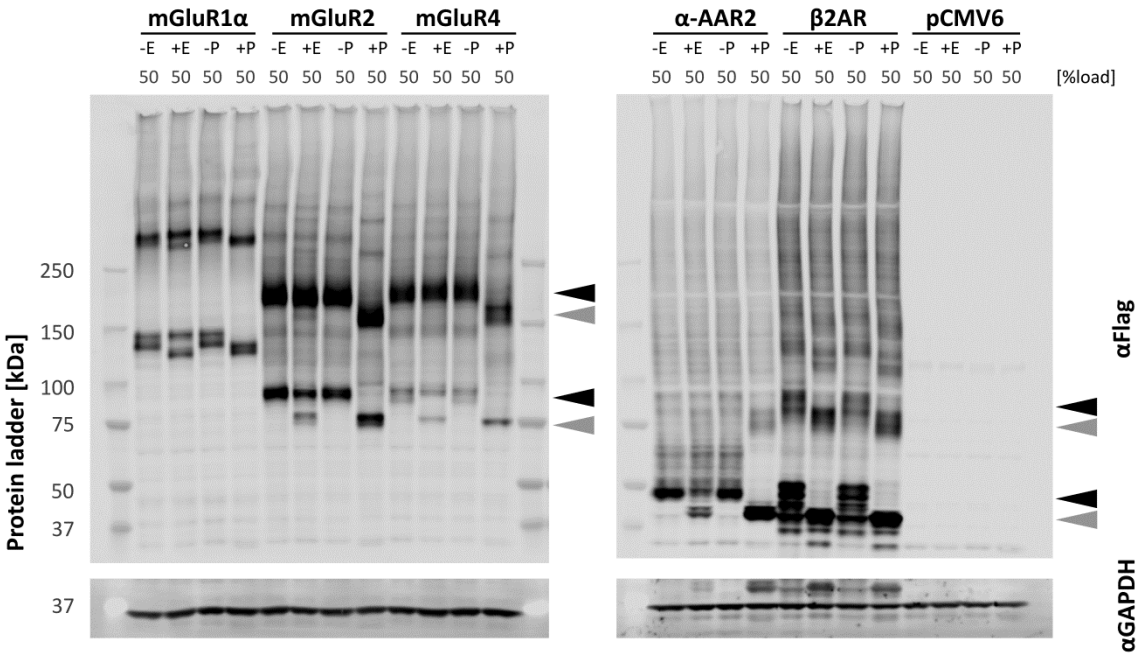

Figure 2.21 | Enzymatic deglycosylation of GPCRS with EndoH and PNGaseF. Flag-tagged GPCRs were transiently expressed in Hek293 cells. After 48 h, the cells were harvested and the total protein fraction subjected to enzymatic deglycolysation using EndoH (+E) or PNGaseF (+P). The controls (-E/-P) were mock treated in in Glycoprotein denaturating buffer and Glycobuffer which had been provided with the enzymes (details see Section 4.9). The deglycosylated samples were separated by SDS-PAGE. On the immunoblot the αFlag signal of fully glycosylated monomer and dimer was indicated with black arrow heads both for the mGluRs and the ARs. The shifted bands after deglyocylation was indicated with gray arrow heads. The αGAPDH signal was used as loading control. The blot is representative for n=3 independent experiments.

For the different mGluRs, a similar pattern was visible as seen in the deglycosylation of the mGluR2 variants (Section 2.2.1.2): The enzymatic deglycosylation with EndoH showed an additional faster migrating band both for the monomer and the dimer as compared to the mock treated samples (Figure 2.21 +/-E). However, this faster migrating band represented a fraction

of the total signal and thus not all proteins were deglycosylated. Upon treatment with PNGaseF the whole fraction migrated faster on the immunoblot (Figure 2.21 +/-P). For the α-2AAR the pattern was similar to the mGluRs: Upon treatment with EndoH a fraction of the proteins was deglycosylated and PNGaseF shifted the whole banding pattern into a faster migrating band. In contrast to that, all detectable bands of the β2AR shifted already upon treatment with EndoH. About four different bands were observed running at the height of the monomer which shifted into one upon enzymatic deglycosylation.

From the experiments was concluded that the mGluRs had successfully trafficked through the secretory pathway to the surface of the Hek293 cells. For the α-2AAR at least a fraction appeared to have passed the Golgi. For the β2AR, the results indicate that the receptor 'smeared' through the secretory pathway. The previous experiment had shown that a fraction had arrived at the surface of the cell (Figure 2.20). Notably, it was suggested in the literature that even incorrectly glycosylated β2AR can be trafficked to the surface of the cell (173).

2.4 S-palmitoylation of GPCRs

It has been shown that S-palmitoylation in the C-terminal domain can alter the membrane localization of GPCRs, such as for the 5-HT-1A in mouse (26). For that reason the mGluRs were probed for a potential S-fatty acylation site.

Palmitoyl residues are often added to the C-terminal tail of GPCRs and can be either more static or, despite their covalent linkage to cysteine residues, subject to continues enzymatic acylation and deacylation (25, 124, 174, 175). The transient nature of the S-palmitoylation allowed to add the [9,10-^{3}H(N)]- palmitic acid only after the transient expression of the constructs. The cells expressing the Flag-tagged GPCRs were incubated for 3 h with the tritiated palmitic acid before harvesting the cells. The proteins were isolated by immunoprecipitation with αFlag beads and subsequently separated by SDS-PAGE and blotted on PVDF membrane (details see Section 4.12.5). The PVDF membrane was subjected to digital autoradiography to detect the incorporation of radioactivity into the protein samples (Figure 2.22 A). The tritium signals were then compared to the αFlag immunoblot (Figure 2.22 B).

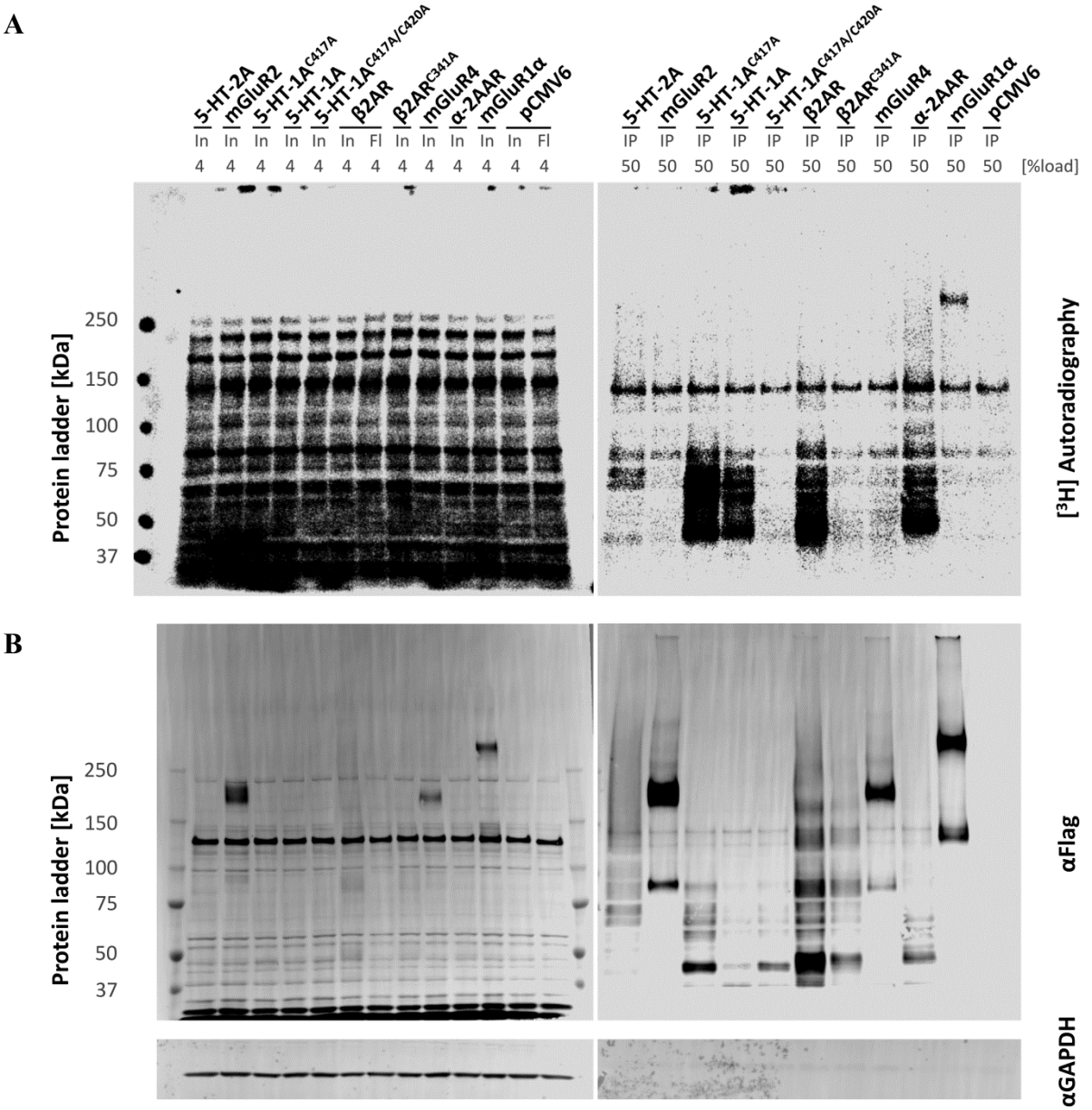

Figure 2.22 | Labeling of Flag-tagged GPCRs with [^{3}H]-palmitic acid. Flag-tagged GPCRs were transiently expressed in Hek293 cells for 48 h. The cells were labeled with tritiated palmitic acid 3 h before harvest. Cells were lysed and Flag-tagged proteins immunoprecipitated (details see Section 4.12.5). (**A**) The input (In), flow through (Fl), and immunoprecipitated (IP) protein samples were separated under non-reducing conditions by SDS-PAGE and blotted on a PVDF membrane. The radioactive signals on the membranes were measured for 24 h by digital autoradiography. (**B**) Subsequently Flag-tagged proteins were visualized by immunostaining with αFlag. The αGAPDH signal was used as loading control. The blots are representative for n=3 independent experiments.

The autoradiography of the protein samples showed a homogenous staining pattern for in the input lanes (Figure 2.22 A). Thus the tritiated palmitic acid had been taken up by the Hek293 cells and was incorporated into the proteins. In the immunoprecipitated samples, a positive signal was obtained for 5-HT-1A and -2A and the adrenergic receptors β2AR and α-2AAR suggesting S-palmitoylation of these proteins. The corresponding (double) C→A mutants of 5-HT-1A and β2AR did not show any signal in the autoradiography; 5-HT-1A$^{C417A/C420A}$ and

$\beta 2AR^{C341A}$ appeared not to carry a S-fatty acyl modification. Compared to the immunoblot, the autoradiography showed a more pronounced signal for both the serotonin and adrenergic receptors (Figure 2.22 B). This indicated that these proteins were equally well expressed but not well recognized by the αFlag antibody. Among the metabotropic glutamate receptors, only one candidate showed a signal in the autoradiography after immunoprecipitation: mGluR1α. The signal corresponded to the dimer band of the receptor on the immunoblot. If there had been a signal for the monomer band, it would have superimposed with the background band visible in all labelings including the vector control. In contrast to that, no signal was seen for mGluR2 or mGluR4.

The non-reducing separation of the proteins allowed the detection of the radioactive palmitate labeling of the different GPCRs (Figure 2.22). To challenge the results of [^{3}H]-palmitic acid labeling, the protein samples were treated with the reductive agent β-mercaptoethanol. The reductive agent should cleave the thioester bond between the acyl chain and the cysteine residue of the GPCR (176). Both the input samples as wells as the immunoprecipitated samples were separated under reducing conditions. False positive were expected to retain their signal under these conditions. The results were visualized again by digital autoradiography and αFlag immunostaining (Figure 2.23).

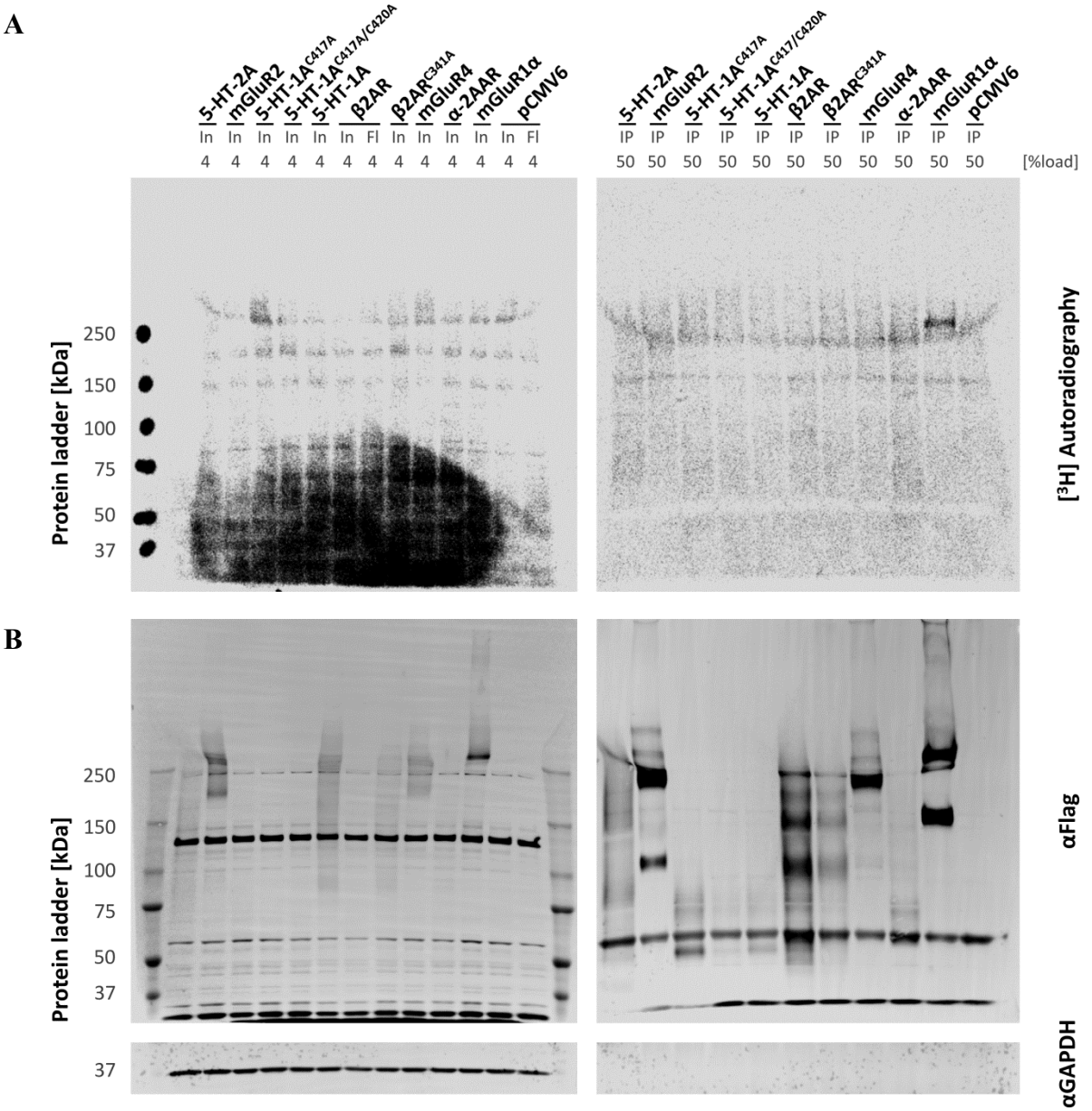

Figure 2.23 | Separation of [^{3}H]-palmitic acid-labeled samples under reducing conditions. Flag-tagged GPCRs were transiently expressed in Hek293 cells for 48 h. The cells were labeled with tritiated palmitic acid 3 h before harvest. Cells were lysed and Flag-tagged proteins immunoprecipitated (details see Section 4.12.5). (**A**) The input (In), flow through (Fl), and immunoprecipitated (IP) protein samples were separated under reducing conditions (15%$_{(V/V)}$ β-mercaptoethanol) by SDS-PAGE and blotted on a PVDF membrane. The radioactive signals on the membranes were measured for 24 h by digital autoradiography. (**B**) Subsequently Flag-tagged proteins were visualized by immunostaining with αFlag. The αGAPDH signal was used as loading control. The blots are representative for n=3 independent experiments.

The reducing SDS-PAGE delivered inconclusive results as the blot showed a hemicycle that divided the running pattern in upper and lower half (Figure 2.23). This pattern was observed in all SDS-PAGEs conducted with β-mercaptoethanol as reductive agent (Figure 2.24). For the input and flow through samples, a loss of the signal in the autoradiography was observed even though not to completion and a shadow remained in the lower half of the blot. The immunoprecipitated samples appeared to be largely deacylated. Probably the total amount of

protein in the IP samples was lower and thus the ratio between reductive agent and protein higher. Concerning the running pattern in both gels, the artifacts can be probably attributed to the presence of β-mercaptoethanol as in no other SDS-PAGE a similar pattern had been observed (for example see Figure 2.22). Here, the optimal pH for the reduction of the protein samples with β-mercaptoethanol would have been 6.8 and not 8.3, as in the gel system and sample buffer which had been optimized for DTT (177) (Section 4.5). Thus, it also cannot be excluded that unspecific formation of thioester bonds to unbound [^{3}H]-palmitic acid and change of pH during the SDS-PAGE had cause the hemicycle visible on the western blot.

With the exception of mGluR1α, all IP samples were successfully reduced (Figure 2.23, Figure 2.24). This confirmed the nature of the S-palmitoylation for the GPCRs and indicated that the signal had not been measured due to an incorporation of tritium into amino acids or other post-translational modifications. On the other side, the results concerning a potential S-acylation site in mGluR1α were inconclusive. In the 2nd replicate, the signal on the autoradiography was gone and in the 3rd replicate the signal was partly removed. This left either the possibilities that the fatty acid was linked with an O- or N-linkage even though this has been poorly investigated for GPCRs (13). The other possibility would have been another modification of unknown nature that was at least partly sensitive to β-mercaptoethanol.

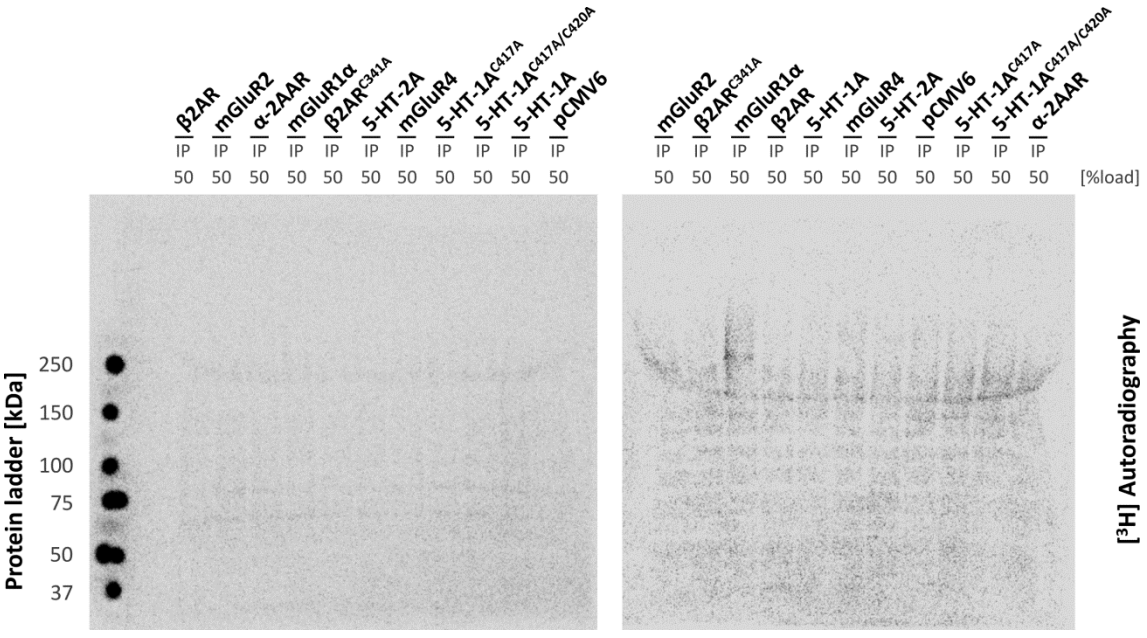

Figure 2.24 | Separation of [^{3}H]-palmitic acid-labeled samples under reducing conditions. Flag-tagged GPCRs were transiently expressed in Hek293 cells for 48 h. The cells were labeled with tritiated palmitic acid 3 h before harvest. Following, the cells were lysed and Flag-tagged proteins immunoprecipitated (details see Section 4.12.5). The immunoprecipitated (IP) protein samples were separated under reducing conditions (15%$_{(V/V)}$ β-mercaptoethanol) by SDS-PAGE and blotted on a PVDF membrane. The radioactive signals on the membranes were measured for 24 h by autoradiography The blots represent the 2nd and 3rd experiment (first experiment see Figure 2.23).

2.5 Non-covalent lipid interaction of GPCRs probed by metabolic labeling with tritiated lipids

To investigate non-covalent interactions of GPCRs with sphingolipids and cholesterol, the different W→A and Y→A variants of mGluR2 were subjected to metabolic labeling with either [^{3}H]-photo-sphingosine or [^{3}H]-photo-cholesterol. This photo-lipids carried a diazirine group which would allow to covalently UV-crosslink the photo-lipid to proteins in closest proximity (78). To screen for loss of lipid interaction sites, the different mGluR2 variants were transiently expressed in Hek293 cells which were incubated with the corresponding photo-lipid and subsequently crosslinked with UV-light.

2.5.1 [^{3}H]-(photo-)sphingolipid binding to mGluR2 variants

The [^{3}H]-sphingosine is subject to metabolisation within labeled cells and thus can end up in different metabolic products of the sphingolipid pathway (78) (Figure 1.5). The products of the labeling with [^{3}H]-sphingosine in pCMV6 vector control or pCMV6_GRM2_MycFlag transfected cells were compared to the reported lipid pattern (78). To estimate if there were any measureable differences in the (sphingo-)lipid metabolism caused by the transfection, [^{3}H]-sphingosine metabolism was compared for different transfection agents. The transfection agents can be grouped into cationic (polymers) and lipid-based agents. The former agents rely mostly on the endocytosis of the DNA complex. Some, like Calcium-phosphate (CaP) or poly Polyethylenimine (PEI), were prepared based on open-source protocols, while others, like Turbofect (ThermoScientific, USA), were commercially available (details see Section 4.3.7). Lipid-based agents were only purchased from commercial sources, but here the composition stayed unknown. The lipid blend in FuGENE (Promega, Germany), Lipofectamine2000 (ThermoScientific, USA), and X-tremeGene (Roche, Switzerland) raised the concern that some compounds in the lipid mix could affect the (sphingo-)lipid metabolism in the cells.

After transfection, labeling of cells and extraction of labeled lipids, the metabolism of [^{3}H]-sphingosine was compared by thin layer chromatography (TLC) (Figure 2.25 A). The dominant species in the labeling with approximately 60% was ceramide, followed by sphingomyelin and sphingosine with around 13%. Smaller fractions were the hexosylceramides with 6-9% and gangliosides with 3-6% (Figure 2.25 B). Here, the results did not show any major differences between the different transfection agents or between mock

transfected and mGluR2 expressing cells (Figure 2.25 B). Also, the comparison between the non-transfected control and the different transfection reagents did not reveal any changes in the metabolism of the labeled (sphingo-)lipids. However, the distribution between the different sphingolipid species was shifted towards the ceramide after 6 h of metabolic labeling with the Hek293 cells. This was in contrast to the findings with the [^{3}H]-D-*erythro*-photo-sphingosine ([^{3}H]-photoSph) (78). For [^{3}H]-photoSph, the sphingomyeline fraction peaked after 6 h according to the original published data. A similar distribution as in the published data was earlier measured for the Hek293 cells (data not shown). Eventually the metabolism of the tritiated sphingosine species was different from the analogue with a diazirine group, but no direct comparison has been made between the species.

From the results was concluded that the cellular metabolism of tritiated sphingosine appeared to be independent of the transfection agent and the ectopic expression of mGluR2-MycFlag. The experimental setup with FuGENE HD as transfection agent and pCMV6 vector constructs appeared to be valid as transient expression system for [^{3}H]-sphingosine labeling experiments.

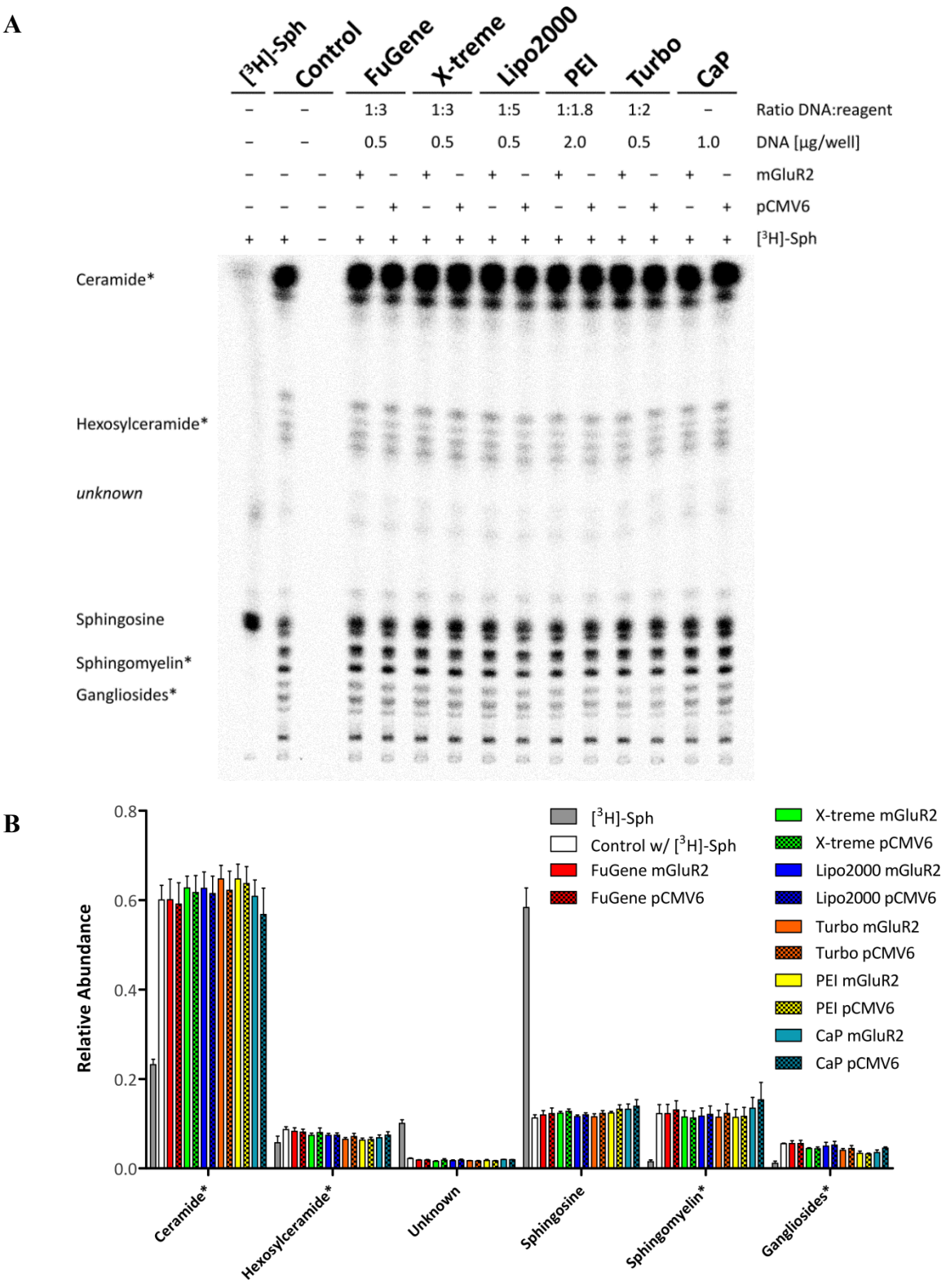

Figure 2.25 | Effect of transfection agents on [^{3}H]-sphingosine metabolism in Hek293 cells. The cells were transiently transfected with pCMV6 vector control (pCMV6) or GRM2-MycFlag construct and labeled for 6 h with 2 µCi (Spec.Activity 20 Ci/mmol) [^{3}H]-sphingosine. After 48 h, the cells were harvested and extracted with methanol (details see Section 4.12.4). (**A**) A total activity of 0.075 µCi methanol extract were loaded per lane on a TLC plate. The TLC was developed with a choloroform/MeOH/water mixture (65:25:4). The developed plate was subjected to autoradiography (representative picture). With the exception of the [^{3}H]-sphingosine standard, the pattern of the autoradiography was assigned by comparison to literature (Haberkant, Schmitt (78), marked with an asterisk). (**B**) The pattern was pixeled in ImageJ 1.51n. The data are shown as bar plot in GraphPad Prism (n=2, mean+SEM).

The activatable and clickable analog of sphingosine (pacSph), similar in its chemical structure to [^{3}H]-sphingosine, had shown to be prone to phosphorylation and subsequent degradation by sphingosine-1-lysase (S1PL) (80). This phenomenon was related to the fact that sphingosine is a degradation and recycling product within the sphingolipid metabolism and can enter both anabolic and catabolic pathways. The degradation products, specifically the hexadecanal, can be incorporated into other lipids, such as phosphatidylcholines. To avoid loss of signal to phosphatidylcholines and the resulting artifacts, the gene encoding sphingosine-1-lysase (*SGPL1*) was knocked out by CRISPR-Cas9 (178) (Figure 1.5). The wild type Hek293 cells were compared to the *SGPL1* knock out cells to see if [^{3}H]-sphingosine metabolisation differed between parental and knockout cells (Figure 2.26).

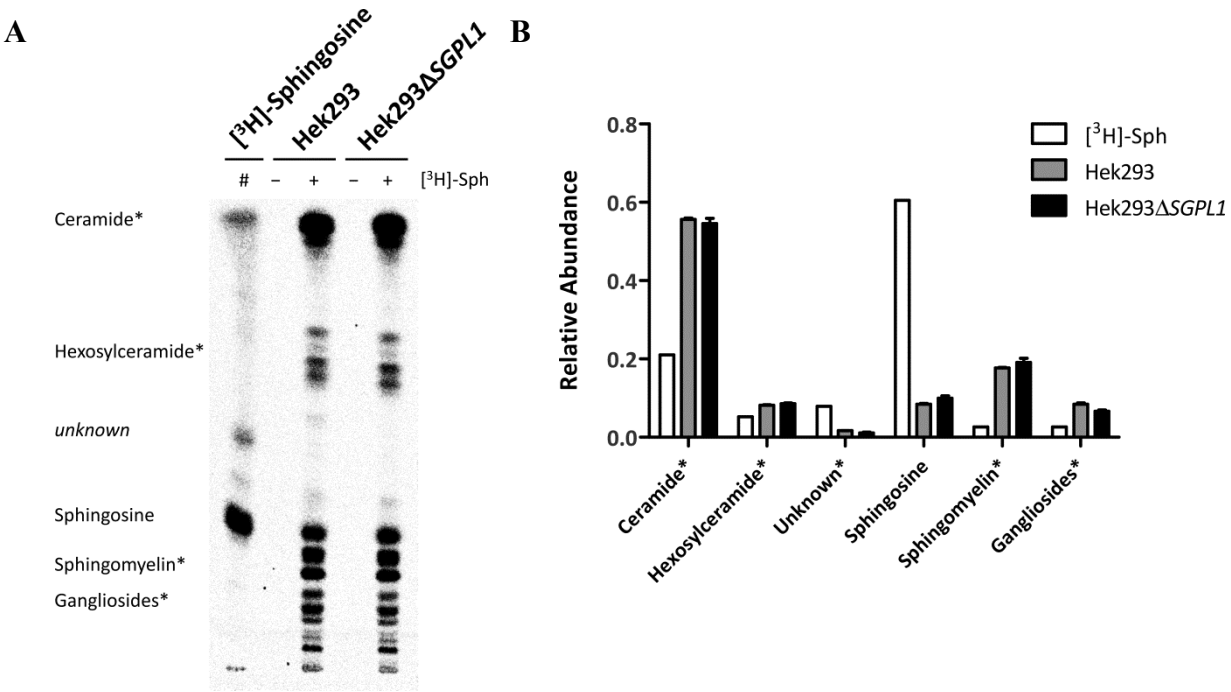

Figure 2.26 | Metabolism of [^{3}H]-sphingosine in Hek293 wild type and Δ*SPGL1* knock-out cells. Wild type and Δ*SPGL1* knock-out cells were incubated with 2 µCi (Spec.Activity 20 Ci/mmol) tritiated sphingosine for 6 h. After incubation, the cells were extracted with methanol (details see Section 4.12.4). (**A**) A total activity of 0.075 µCi methanol extract were loaded per lane on a TLC plate. The extract was separated in a choloroform/methanol/water mixture (65:25:4). The developed plate was subjected to digital autoradiography (representative picture). With the exception of [^{3}H]-sphingosine standard, the pattern of the autoradiography was assigned by comparison to literature (Haberkant, Schmitt (78), marked with an asterisk). (**B**) The pattern was pixeled in ImageJ 1.51n. The data are shown as bar plot in GraphPad Prism (n=3 in parallel, mean+SEM).

Apart from a faint band, which could not be assigned, there were no differences in the metabolism of [^{3}H]-sphingosine in Hek293Δ*SGPL1* knock out and the wild type cells (Figure 2.26 A, *unknown*). As in the previous labeling, ceramide was the most prominent metabolite after 6 h incubation with a fraction of ~55% both in wild type and knock out cells (Figure 2.26 B). The other metabolites were sphingomyelin with around 17-19% of the total activity, followed by hexosylceramide with ~8% in both cell lines and gangliosides with a share of 6-

8%. Notably, the [^{3}H]-sphingosine purchased from American Radiolabeled Chemicals (St.Louis, USA) appeared to contain different impurities which could not be assigned to the published pattern and eventually represent degradation or site products of the synthesis (Figure 2.26 A).

As wild type and Hek293Δ*SGPL1* knock out cells had not shown any differences in the metabolism of the [^{3}H]-sphingosine precursor lipid, the wild type cells were chosen for all further experiments with tritiated sphingosine. In the next experiments, mGluR2-Flag and its variants were subjected to cellular labelings with the photoaffinity probe [^{3}H]-photoSph (78). For the cellular photoaffinity labelings, also the influence of the different transfection levels in the transient expression system was accounted for: a plasmid DNA titration for pCMV6_GRM2_Flag was carried out as done earlier for the surface arrival (Figure 2.12). In the current titration, a DNA range from 125 ng to 500 ng was taken into consideration as this range had shown the most stable results in the previous experiments. The constructs were expressed for 48 h and the labeling with [^{3}H]-photoSph started 6 h before UV-crosslinking the functionalized sphingolipids. The Flag-tagged proteins were immunoprecipitated and the labeling measured by digital autoradiography signal which was then compared to the αFlag immunolabeling (details see Section 4.12.3).

The smear obtained for the input samples in the autoradiography indicated that both labeling and incorporation of [^{3}H]-photoSph as well as crosslinking of functionalized (sphingo-)lipids to cellular proteins had occurred (Figure 2.27 A). For the mock labeled cells, in the absence of [^{3}H]-photoSph, no signal was visible on the autoradiography. After the immunoprecipitation of the Flag-tagged proteins, a visually well distinguishable signal above background was only visible between 250 ng and 500 ng plasmid DNA (Figure 2.27 A). In this range, the transfection level allowed to measure a stable and reproducible labeling efficiency (Figure 2.27 B). At the lowest DNA concentration of 125 ng, the labeling was close to the background – both on the autoradiography and the immunoblot (Figure 2.27 A). For this reason it cannot be excluded that the extraordinary high averaged labeling efficiency, 6.1-fold increased as compared to the efficiency at 500 ng, originated from quantification artifacts (Figure 2.27 B). Also, the labeling efficiency at 125 ng showed a way higher variation as compared to the higher DNA concentrations. Apart from that, the signal for the ASGPR1-MycFlag background control, which had been chosen based on the earlier publications, was also quantifiable but labeled weaker compared to mGluR2-Flag (65, 68) (Figure 2.27 B). Here, the

labeling efficiency was around 23% compared to the labeling efficiency of mGluR2-Flag at the same DNA concentration.

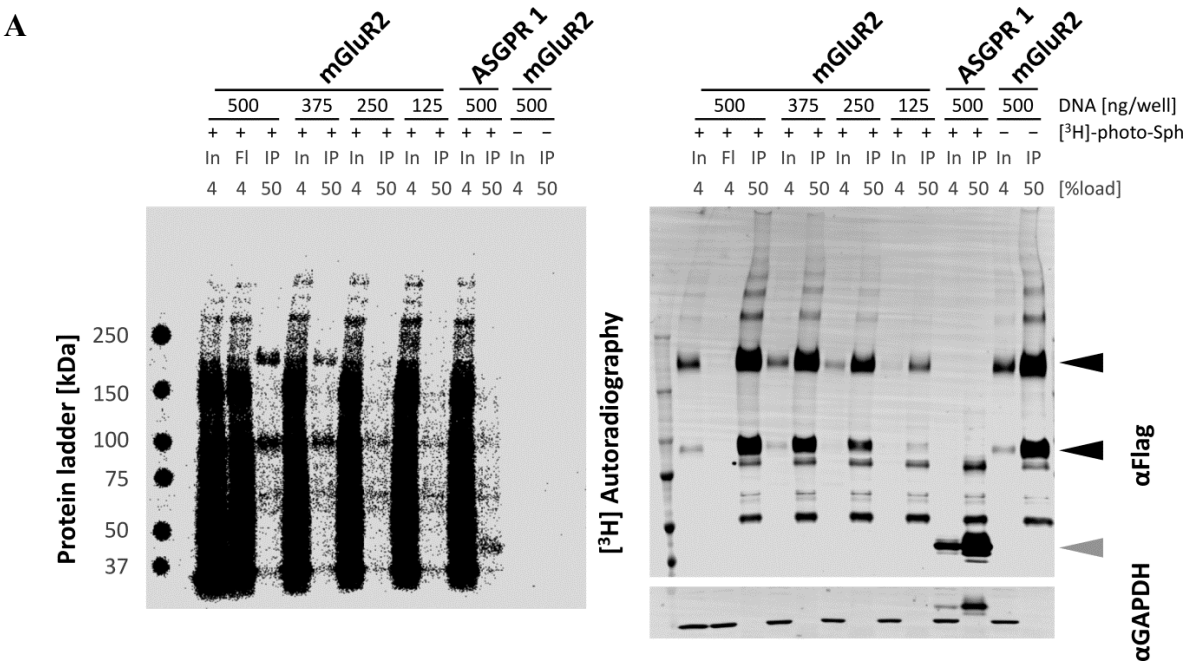

Figure 2.27 | Plasmid DNA titration of mGluR2 constructs in Hek293 cells. For the titration, Flag-tagged mGluR2 was transiently expressed in Hek293 cells, which were then labeled with 7.5 µCi (Spec.Activity 20 Ci/mmol) [^{3}H]-photoSph or solvent control for 6 h. After incubation, cells were UV-irradiated and subjected to immuno-precipitation (details see Section 4.12.3). (**A**) Input (In), flow through (Fl) and immunoprecipitated (IP) protein samples were separated by SDS-PAGE. The IP signals in the autoradiography and the αFlag (Mouse, F1804) immunoblot were quantified as indicated (black arrow heads: mGluR2, grey arrow heads: ASGPRI). αGAPDH signal was used as loading control. (**B**) Quotient of the autoradiography and immunoblot signal at DNA concentration x was normalized to the quotient at 500 ng. The data are shown as mean±SEM (n=4) in GraphPad Prism.

A stable labeling signal for [^{3}H]-photoSph was obtained for a concentration range between 250 ng and 500 ng plasmid DNA per well (Figure 2.27 B). However, to avoid quantification artifacts in cellular photocrosslinking assays with weakly expressed mGluR2-Flag variants, the highest DNA concentration (500 ng plasmid DNA/well) was chosen for the further labeling experiments with the mGluR2-Flag proteins. Here, the labeling of the proteins in the assay appeared in absolute terms more stable and quantifiable.

As in the previous experiments, the input lanes in the autoradiography showed that the cellular photocrosslinking with [^{3}H]-photoSph was successful. The radioactive photo-sphingosine had been taken up into the cells, incorporated into sphingolipids and UV-crosslinked to proteins (Figure 2.28 A). Free [^{3}H]-photoSph would not have been visible on the western blot as it was separated from the crosslinked activity during the SDS-PAGE. The autoradiography of the immunoprecipitated samples showed a labeling signal for all samples but the pCMV6 vector control. Among the different mGluR2-Flag variants, especially for mGluR2^{Y734A}-Flag a strong radioactive labeling was visible. For others, such as Y607A and W773A, the measured signal was close to background. These two variants appeared also to be rather weakly expressed, as can be seen on the immunoblot (Figure 2.28 B). This correlated with earlier observations in the transient expression system (Figure 2.13). Eventually the exchange for alanine slightly lowered the expression level here. Interestingly, β2AR-Flag – which had been intended mainly as positive control for the later [^{3}H]-cholesterol labelings – showed a very pronounced tritium signal (Figure 2.28 A). Contrary, ASGPRI-MycFlag labeling suggested a low affinity to sphingolipids in the steady state.

The quantification of the autoradiography and immunoblot signals showed that for most of the mGluR2-Flag W→A and Y→A variants a labeling efficiency comparable to that of the wild type receptor had been obtained (Figure 2.28 C). A significantly higher labeling efficiency was observed for mGluR2^{W697A}-Flag and mGluR2^{Y734A}-Flag (1way ANOVA, Dunnetts' post test in GraphPad Prism versus mGluR2-Flag, α=0.05). Here, the labeling efficiency was on average increased 2.7- and 2.6-fold, even though the variation between the replicates was rather high. However, the increased affinity was surprising as the different variants had been designed as loss-of-function. Notably, these two residues were in close proximity to each other, located in the exoplasmic leaflet of the transmembrane helices IV and V. Thus it cannot be excluded that the observations were interconnected and for example a gap in the surface had been created that now was occupied by sphingolipids. For the mGluR2-Flag variants Y767A, W773A and Y781A in helix VI – where the original p24-like sphingolipid interaction motif had been found – no significant increase or decrease in sphingolipid crosslinking was observed (68). The highest affinity in the assay was apparently to β2AR-Flag, which was on average 6.5-fold increased as compared to mGluR2-Flag.

Due to the low crosslinking efficiency of [^{3}H]-photoSph and the absence of sphingolipid binding defects in the selected mGluR2 variants, no further experiments with the mGluR2^{C121A}-Flag double mutants were conducted.

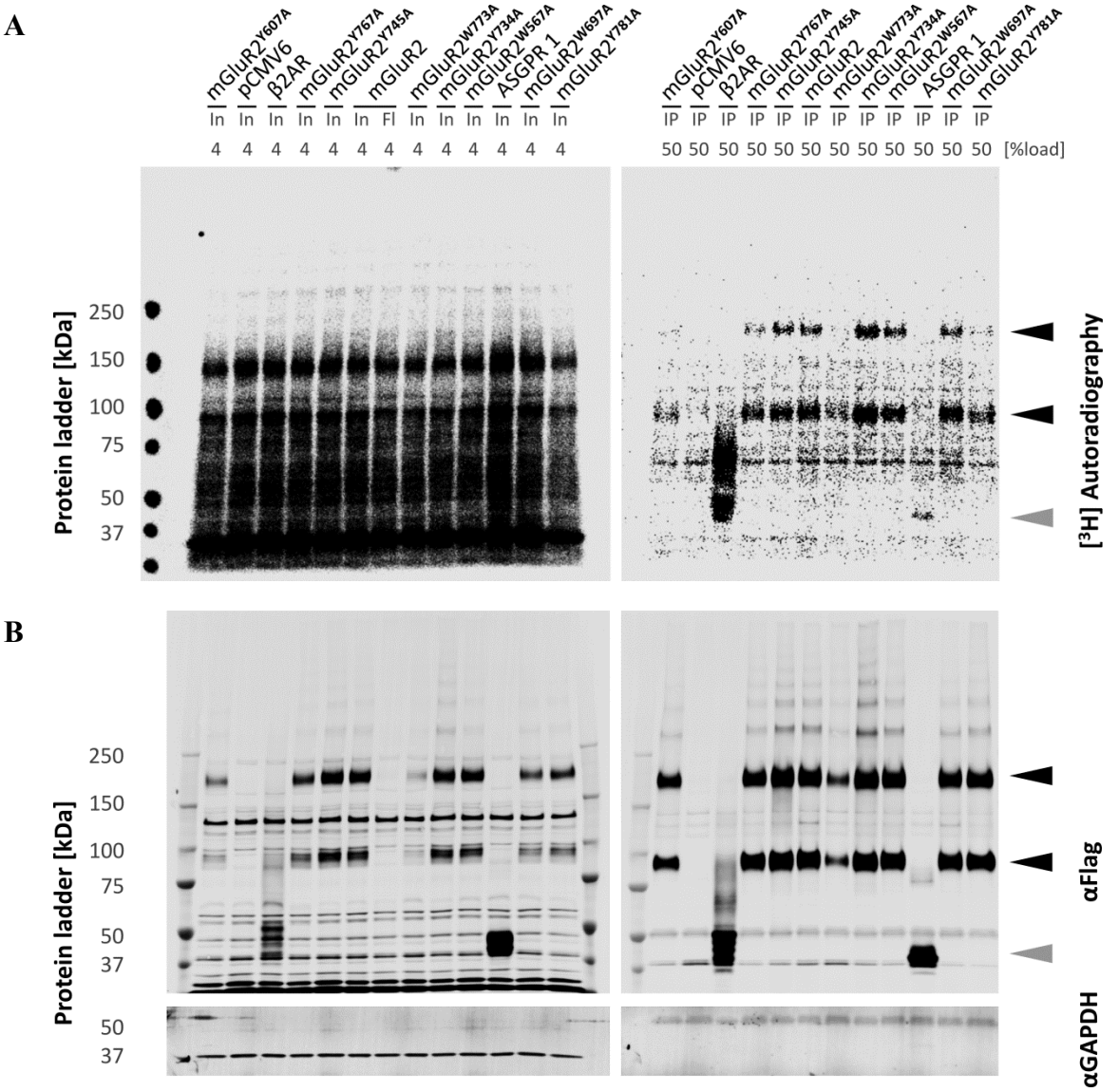

Figure 2.28 | [^{3}H]-photoSph labeling of mGluR2 variants in Hek293 cells. Flag-tagged W→A and Y→A mGluR2 variants were transiently expressed in Hek293 cells along with the negative control ASGPRI-MycFlag and the postive control β2AR-Flag. The cells were labeled with 7.5 µCi (Spec. Activity 20 Ci/mmol) [^{3}H]-photoSph 6 h prior to UV-crosslinking (details see Section 4.12.3). (**A**+**B**) Input (In), flow through (Fl) and immunoprecipitated (IP) protein samples were separated by SDS-PAGE. The IP signal in the (**A**) autoradiography and the (**B**) αFlag (Mouse, F1804) immunoblot were quantified as indicated (black arrow heads: mGluR2, grey arrow heads: ASGPRI, β2AR). αGAPDH signal was used as loading control. (**C**) Quotient of the autoradiography and immunoblot signal of protein or variant P was normalized to signal of mGluR2-Flag. The data are shown as dot plot with mean±SEM (n=3) in GraphPad Prism. Statistics with 1way ANOVA (*=P<0.05).

2.5.2 Altered [^{3}H]-photo-cholesterol binding of mGluR2 variants

Next, interactions of the different GPCRS with cholesterol were investigated. For cholesterol a bifunctional analogue originally synthesized by Christoph Thiele was used (77). The [^{3}H]-photo-cholesterol was tritiated and carried a diazirine group – thus had the same functionalities as [^{3}H]-photoSph. As for the sphingolipid photocrosslinking experiments, the aim was to investigate if any of the W→A or Y→A variants would show a loss-of-function.

For the [^{3}H]-photo-cholesterol, no such broad diversity of metabolic products was expected as for the [^{3}H]-photoSph (77). To test that assumption, the different [^{3}H]-photo-cholesterol stocks and commercially available [1,2-^{3}H(N)]-cholesterol were used for labeling in transiently transfected cells. After the transfection, labeling and extraction of labeled lipids, the metabolites of [^{3}H]-(photo-)cholesterol were separated by TLC. On the TLC, the tritiated lipids were compared to their respective stocks and commercially [1,2-^{3}H(N)]-cholesterol to monitor if there were any major side products formed within cells (Figure 2.29).

The autoradiography of the TLC showed that only one of the two [^{3}H]-photo-cholesterol stocks was usable (Figure 2.29, marked with #). The [^{3}H]-photo-cholesterol of the respective stock ran at the same height as the [1,2-^{3}H(N)]-cholesterol. Only one other faint band was visible. This pattern remained largely unchanged after 17 h labeling of Hek293T cells and even after UV-crosslinking *in vivo*. The pattern indicated that tritiated cholesterol was not subjected to such as complex metabolism as the one observed for [^{3}H]-sphingosine (Figure 2.26). Also, the diazirine group did not appear to have caused any larger changes in the running pattern as compared to the commercial [1,2-^{3}H(N)]-cholesterol. In contrast to that, the other stock (Figure 2.29, marked with *) showed presence of byproducts that were already visible in the stocks and were still present after cellular incubation. The fact that they had not even been metabolized by the cells indicated that they were either side products of the original synthesis that had not been removed successfully or were degradation products. For all further experiments only the first (#) stock was used.

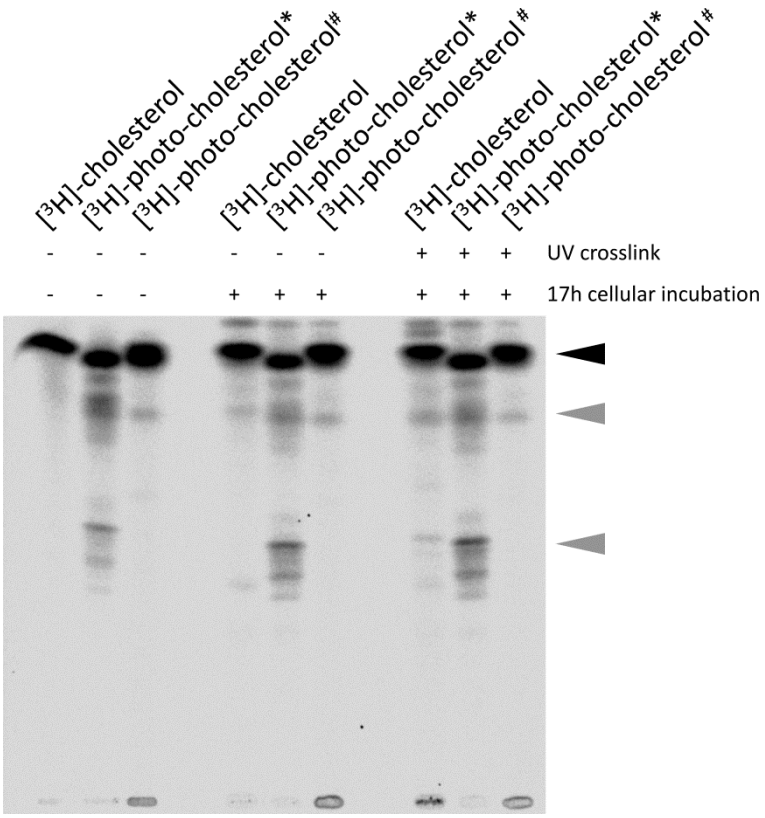

Figure 2.29 | Metabolism of different tritiated cholesterol stocks in Hek293T cells. Hek293T cells were transiently transfected with pCMV6_ADRB2_Flag. 17 h prior to harvest the cells were labeled with 15 µCi of the inidicated [^{3}H]-cholesterol batches (details see Section 4.12.2). Control cells were left untreated (-), compared to cells subjected to UV-crosslinking (+). After labeling, cells were extracted with methanol. 0.075 µCi extract per lane was separated in a choloroform/methanol/water mixture (65:25:4) on a TLC plate. The developed plate was subjected to digital autoradiography. The batches were loaded on the TLC plate as standard (-/-). [^{3}H]-cholesterol is marked with a black arrow head, major side products with a grey arrow head.

In contrast to sphingolipids, there have been numerous studies which investigated the interaction between GPCRs and cholesterol (57, 69). For an initial cellular photocrosslinking assay with [^{3}H]-photo-cholesterol, one adrenergic and one serotonin receptor were included in addition to mGluR2. The adrenergic receptor β2AR has been investigated in several experimental and computational studies resulting in a set of established cholesterol interaction sites (20, 45, 47). The established concept of cholesterol interaction with this receptor made it a suitable control to validate the technical performance of the labeling and UV-crosslinking with [^{3}H]-photo-cholesterol. Moreover, the serotonin receptor 5-HT-2A was included because it has been shown to interact with mGluR2 and thus should, at least in part, face a similar membrane environment (154). The labeling efficiency of 5-HT-2A-Flag and β2AR (including both a N-terminally and a C-terminally Flag-tagged version) was compared to mGluR2-Flag. As in the biochemical characterization described in Section 2.3, the cells were transfected with a high amount of DNA to ensure sufficient expression of the serotonin receptor.

The input lane showed that for all receptors [^{3}H]-photo-cholesterol had been taken up by cells and were successfully UV-crosslinked to adjacent proteins (Figure 2.30 A). Unbound [^{3}H]-photo-cholesterol was separated from the proteins during the SDS-PAGE. For all immunoprecipitated GPCRs a labeling with crosslinked activity was visible in the autoradiography which corresponded to the respective αFlag signal on the immunoblot. Here,

the quantification of the signals showed that both the N- and C-terminally Flag-tagged β2AR variant showed a highly efficient labeling which was on average about 6.9- and 5.2-fold stronger and significantly increased as compared to the labeling of mGluR2-Flag (1way ANOVA, Dunnetts' post test in GraphPad Prism versus mGluR2-Flag, α=0.05) (Figure 2.30 B). In contrast to that, 5-HT-2A-Flag labeling with [^{3}H]-photo-cholesterol was on average reduced by 45 percentage points compared to mGluR2-Flag. The designated negative control ASGPRI-MycFlag was expressed, as seen on the αFlag immunoblot, but gave only a barely visible signal in the labeling (Figure 2.30 A). Hence, only a weak labeling, which corresponded to about 0.5% of mGluR2-Flag, was measured here (Figure 2.30 B).

Similar to the cellular sphingolipid crosslinking assay with [^{3}H]-photo-sphingosine, the current experiment showed that Flag-tagged β2AR labeled very efficient with [^{3}H]-photo-cholesterol (Figure 2.28 C, Figure 2.30 B). No major differences were observed between the N- and C-terminally tagged β2AR variants, even though the banding pattern in the αFlag immunoblot appeared to be different (Figure 2.30 A). While for the C-terminally tagged protein multiple bands were seen between 37 kDa and 100 kDa, only one broad band was visible between 37 kDa and 50 kDa for NFlag-β2AR. In contrast to that, the radiolabeling showed a similar pattern for both variants: One defined band between 37 kDa and 50 kDa which indicted the monomer, and a broader smear between 50 kDa and 75 kDa (and even higher apparent molecular weights) which probably corresponded to oligomers. The comparison between the autoradiography and the αFlag immunoblot suggested that for the N-terminally tagged version not all proteins on the blot had been equally well-detected by the Flag antibody. For that reason the C-terminally tagged version was chosen as positive control for further experiments. Interestingly the other family A receptor, 5-HT-2A, labeled much weaker which indicated that (strong) cholesterol photocrosslinking was not an intrinsic property of GPCRs in the given setup.

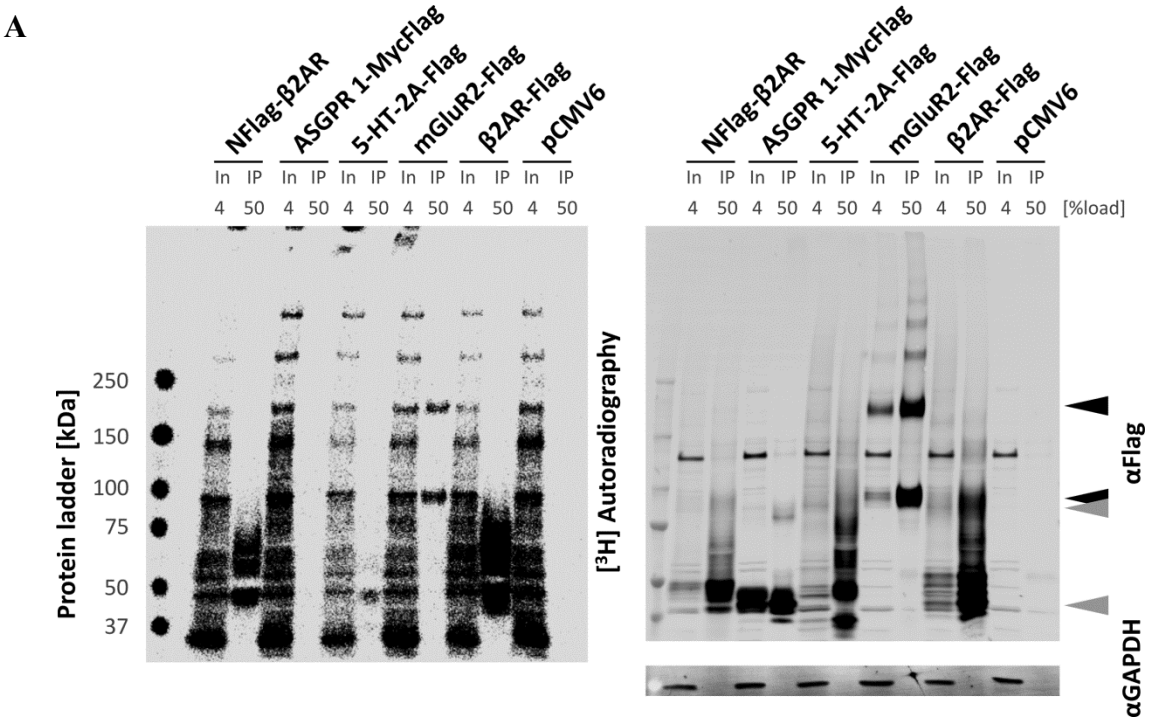

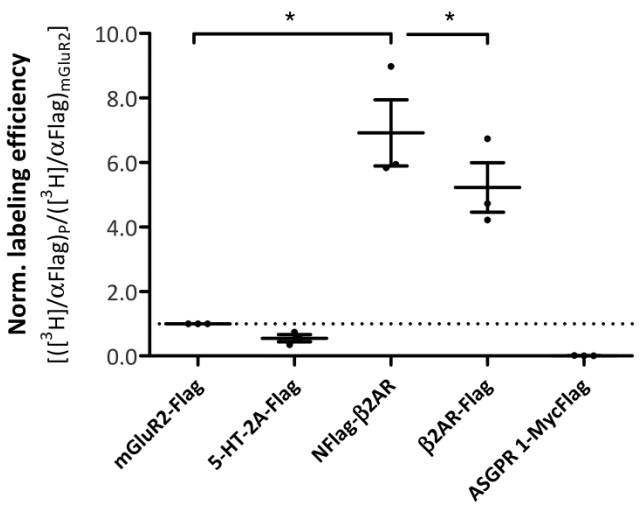

Figure 2.30 | Quantification of [^{3}H]-photo-cholesterol labeling controls. Different Flag-tagged GPCRs were transiently expressed in Hek293 cells and labeled for 17 h with 15 µCi [^{3}H]-photo-cholesterol per well which was then UV-crosslinked to neighbouring proteins. (details see Section 4.12.1). (**A**) Input (In) and immunoprecipitated (IP) protein samples were separated by SDS-PAGE. The autoradiography and the αFlag (Mouse, F1804) signals on the immunoblot, scanned at 1.5, were quantified as indicated (black arrow heads: mGluR2, grey arrow heads: ASGPRI, β2AR, 5-HT-2A). αGAPDH signal was used as loading control. (**B**) Quotient of the autoradiography and immunoblot signal of protein P was normalized to signal of mGluR2-Flag. The data are shown as dot plot with mean±SEM (n=3) in GraphPad Prism. Statistics with 1way ANOVA (*=P<0.05).

Next, the amount of plasmid DNA coding for mGluR2-Flag and mGluR2^{C121A}-Flag was titrated to estimate the influence of the transfection level on the labeling efficiency with [^{3}H]-photo-cholesterol. The goal was to establish a transfection level which would allow a reproducible labeling of the Flag-tagged mGluR2 variants. Now in the titration experiment, the labeling efficiency of the receptors was measured at four different DNA concentrations, 125 ng, 250 ng, 375 ng, and 500 ng, labeled with a constant amount of tritiated photo-cholesterol (Figure 2.31). An even lower concentration of 50 ng was skipped after the first experiment.

Consistent with the previous labeling experiments, UV-crosslinking of [^{3}H]-photo-cholesterol to cellular protein was identified as strong signals in the input lanes as analyzed by digital autoradiography (Figure 2.31 A). Here, probable protein precipitates were visible above the lanes, at the positions of the pockets of the SDS-gel. However, these signals did not correlate with αFlag signal on the immunoblot which indicated that the protein precipitates did not result from the mGluR2 proteins. For the immunoprecipitated samples, a clearly visible signal for the photocrosslink was obtained between 125 ng and 500 ng plasmid DNA. No background was visible in the immunoprecipitated fraction at 0 ng. For the Flag-tagged mGluR2 protein, the signal ratios were stable over the whole range of the tested transfection levels when normalized to the labeling efficiency at 500 ng (Figure 2.31 C). In contrast to that, mGluR2^{C121A}-Flag labeled on average twofold stronger at 125 ng plasmid DNA per well and showed a stable labeling efficiency only at between 250 ng and 500 ng. This observation was consistent with the cell surface arrival assay for mGluR2^{C121A}-Flag in which the lower DNA concentration had also shown a stronger phenotype (compare Figure 2.12). This observation left two possibilities: either the surface arrival was indeed higher at 125 ng DNA per well which allowed more interaction with cholesterol resident in the plasma membrane. Or, as previously suggested, the measured effects resulted from quantification artifacts in both cases because the signal on the autoradiography and on the immunoblot were too close to the background level to allow a reliable quantification. Since the latter case could not be ruled out, the lowest concentration at 125 ng was not considered for the further experiments.

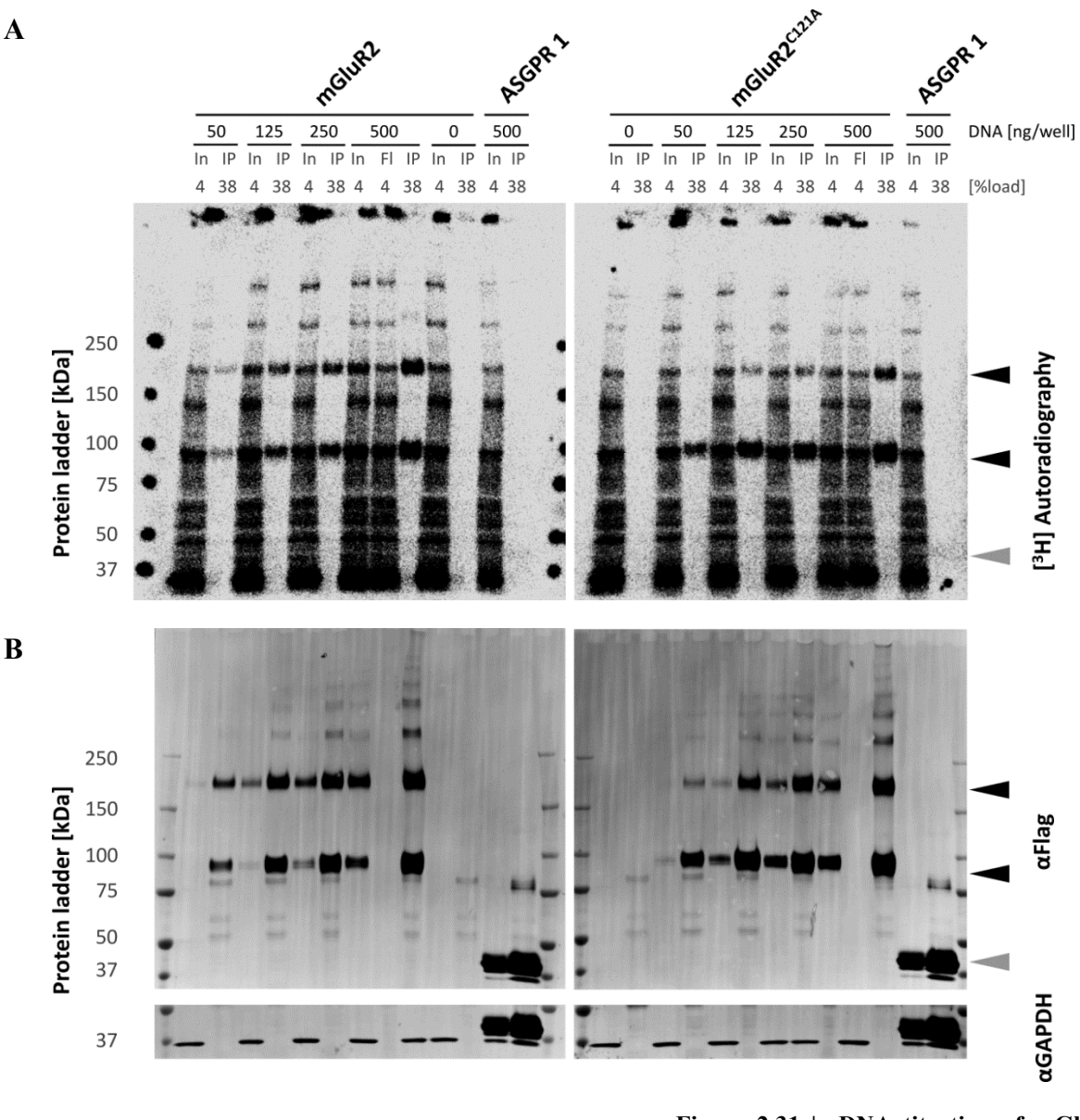

Figure 2.31 | cDNA titration of mGluR2 constructs in Hek293 cells. mGluR2-Flag and mGluR2^{C121A}-Flag were transiently expressed in Hek293 cells and labeled for 17 h with 15 µCi [^{3}H]-photo-cholesterol per well which was then UV-crosslinked to neighbouring proteins. (details see Section 4.12.1). (**A+B**) Input (In), flow through (Fl) and immunoprecipitated (IP) samples were separated by SDS-PAGE. The IP signal in the (**A**) autoradiography and the (**B**) αFlag (Mouse, F1804) signal on the immunoblot were quantified as indicated (black arrow heads: mGluR2, grey arrow heads: ASGPRI). αGAPDH signal was used as loading control. (**C**) Quotient of the autoradiography and immunoblot signal at DNA concentration x was normalized to the quotient at 500 ng. The data are shown as dot plot with mean±SEM (n=3) in GraphPad Prism.

From the titration experiment with was concluded that reproducible measurements for cellular photocrosslinking with [^{3}H]-photo-cholesterol would be obtained between 125 ng and 500 ng for mGluR2-Flag, and 250 ng and 500 ng for mGluR2^{C121A}-Flag. Accordingly, the DNA concentration was set to 250 ng for the W→A and Y→A mGluR2-Flag variants and 375 ng for the mGluR2^{C121A}-Flag variants. Thus, for both set of variants the transfection level was kept in the middle of the established range. The labeling efficiency was always compared to the positive control β2AR-Flag and the negative control ASPGR1-MycFlag.

For the W→A and Y→A mGluR2-Flag variants the input and the immunoprecipitated samples were blotted on separate membranes to get a better signal-to-noise ratio for each of them. For the input samples, all protein lanes showed a comparable banding pattern in the autoradiography (Figure 2.32 A). After immunoprecipitation, all Flag-tagged proteins showed a clearly visible crosslinking signal. For the mGluR2-Flag variants both dimer and monomer were labeled with [^{3}H]-photo-cholesterol. The strongest signal cholesterol labeling was obtained for the positive control β2AR-Flag. The adrenergic receptor labeled 4.1 times stronger as compared to mGluR2-Flag wild type (Figure 2.32 C). Among the mGluR2-Flag variants, two were significantly decreased in their labeling efficiency: mGluR2^{Y745A}-Flag and mGluR2^{Y781A}-Flag (1Way ANOVA, Dunnetts' post test, α=0.05). The former one was reduced by 30% and the later one by 55% as compared to the wild type. The two mutation sites were positioned at the end of helices five and six: Y745A was positioned at the cytoplasmic end of helix five and Y781A at the exoplasmic side of helix six (Figure 2.9).

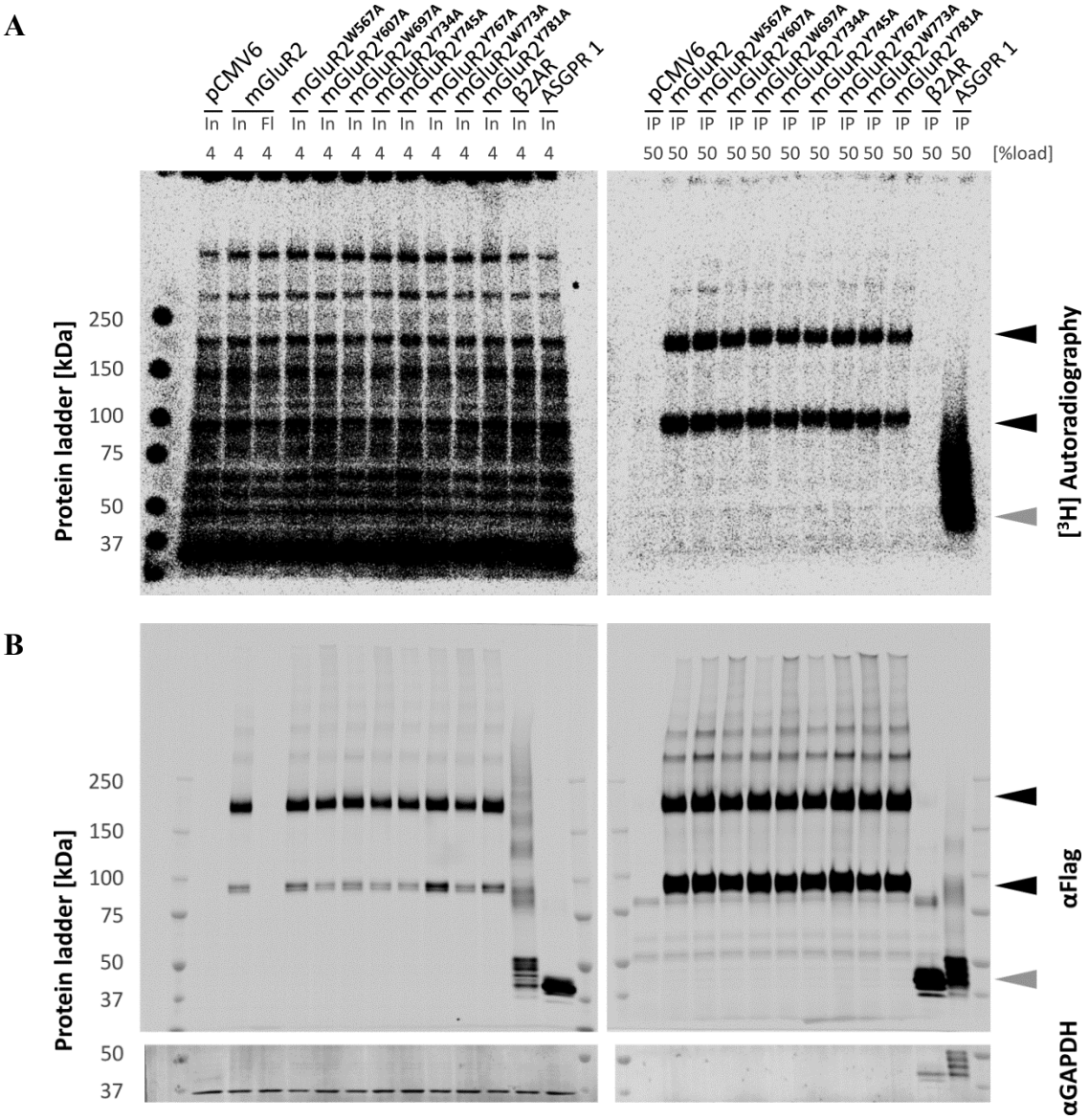

Figure 2.32 | Metabolic labeling of mGluR2 variants with [^{3}H]-photo-cholesterol. Different mGluR2-Flag variants and controls were transiently expressed for 48 h in Hek293 cells. The cells were labeled for 17 h with 15 µCi [^{3}H]-photo-cholesterol, UV-irradiated and Flag-tagged proteins subjected to immunoprecipitation. (details see Section 4.12.1). (**A**+**B**) Input (In), flow through (Fl) and immunoprecipitated (IP) protein samples were separated by SDS-PAGE. The IP signal in the (**A**) autoradiography and (**B**) the αFlag (Mouse, F1804) signal on the immunoblot were quantified as indicated (black arrow heads: mGluR2, grey arrow heads: ASGPRI, β2AR). αGAPDH signal was used as loading control. (**C**) Quotient of the autoradiography and immunoblot signal of protein or variant P was normalized to the signal of mGluR2-Flag. The data are shown as dot plot with mean±SEM (n=5) in GraphPad Prism. Statistics with 1way ANOVA (*=P<0.05).

The [^{3}H]-photo-cholesterol labeling experiment was also performed with the mGluR2^{C121A} double mutants (Figure 2.33). The mGluR2^{C121A}-Flag double mutants were tested with the same experimental setup up as the W/Y→A single mutants: The variants were transiently expressed for 48 h in Hek293 cells and labeled for 17 h with tritiated photo-cholesterol before UV-irradiation and immunoprecipitation of the tagged proteins.

The input samples showed the same signal pattern in the autoradiography as observed in the previous UV-crosslinking experiment with the W→A and Y→A mGluR2-Flag variants (compare Figure 2.32 A and Figure 2.33 A). Again, the distinct pattern indicated UV-crosslinking of functionalized cholesterol with a wide spectrum of cellular proteins. In the immunoprecipitation, the labeling controls ASGPRI-MycFlag and β2AR-Flag showed the same labeling efficiencies as measured in the first assays (compare Figure 2.32 C and Figure 2.33 C). The negative control ASGPRI-MycFlag exhibited a normalized labeling efficiency of about 3% as compared to 2.6% in the previous experiments. The positive control β2AR-Flag was on average 4.1-fold increased in comparison to mGluR^{C121A}-Flag, while it had been 4.3-relatively to mGluR2-Flag. Concerning the immunoprecipitated mGluR2^{C121A}-Flag W→A and Y→A variants, the labeling of the monomer appeared to be more efficient than for dimers (Figure 2.33 A+B). This can be explained by more efficient separation of dimers in the absence of the covalent intermolecular disulfide bridge (compare to Figure 2.16); the immunoblot showed that monomers were the prevalent signal on the blot. However, the average labeling efficiency was only reduced significantly for variant mGluR2$^{C121A/Y781A}$-Flag (1Way ANOVA, Dunnetts' post test, α=0.05) (Figure 2.33 C). As in the previous experiment, the efficiency was reduced by more than 55 percentage points. In contrast to that, no significant reduction was measured for mGluR2$^{C121A/Y745A}$-Flag.

In the [^{3}H]-photo-cholesterol photocrosslinking assays, both single mGluR2-Flag and double mGluR2^{C121A}-Flag W→A and Y→A variants showed a similar labeling efficiency in nine independent experiments (compare Figure 2.32 and Figure 2.33). The strongest reduction in the cholesterol photolabeling was observed for the mutation sites Y745A and Y781A in helices five and six, respectively, which had been earlier suggested to be involved in activation and dimerization of mGluR2 (121). Interestingly, position Y745A coincided with the CRAC motif which had been found for the mGluR family (56).

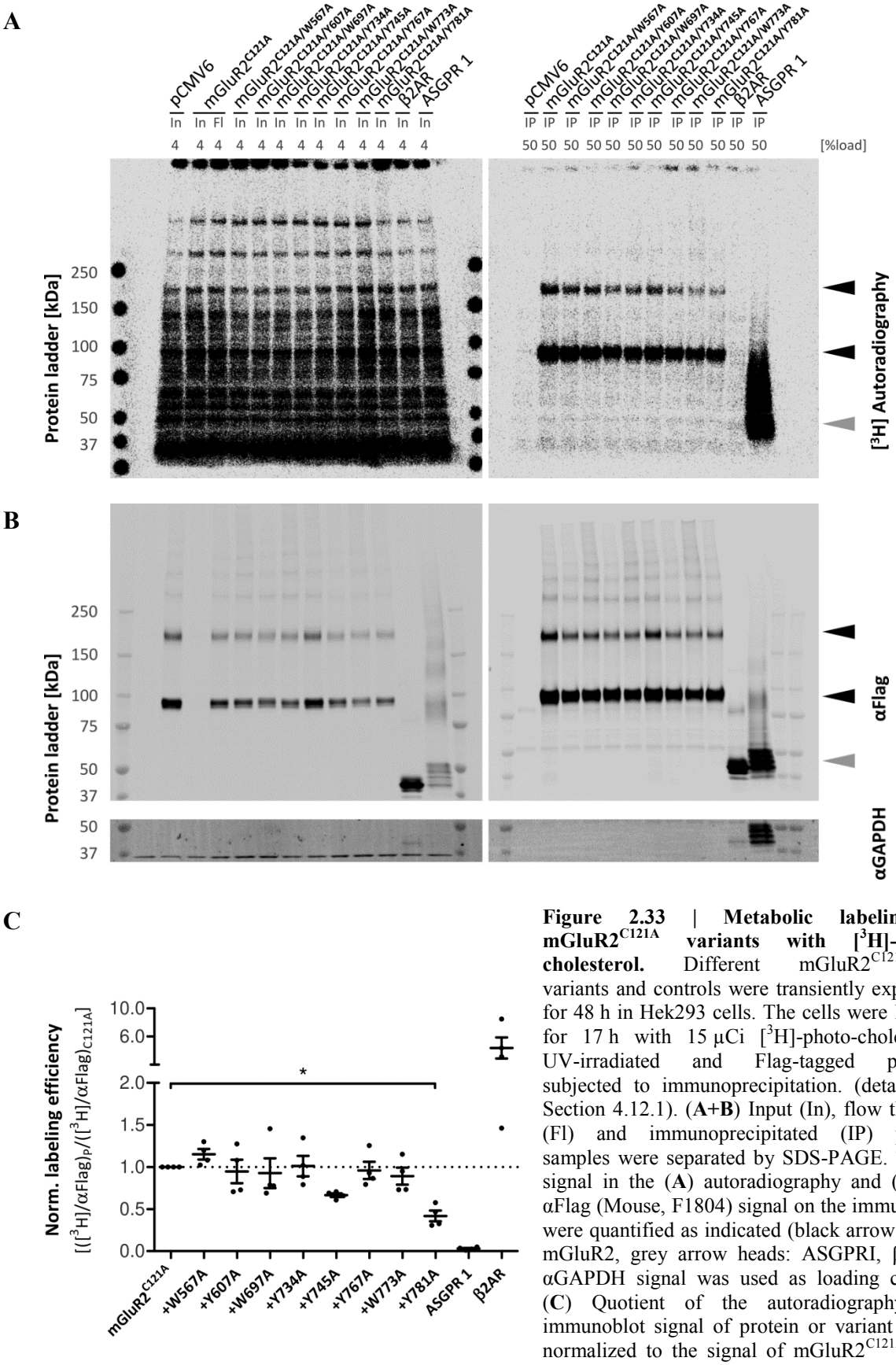

Figure 2.33 | Metabolic labeling of mGluR2^{C121A} variants with [^{3}H]-photo-cholesterol. Different mGluR2^{C121A}-Flag variants and controls were transiently expressed for 48 h in Hek293 cells. The cells were labeled for 17 h with 15 µCi [^{3}H]-photo-cholesterol, UV-irradiated and Flag-tagged proteins subjected to immunoprecipitation. (details see Section 4.12.1). (**A**+**B**) Input (In), flow through (Fl) and immunoprecipitated (IP) protein samples were separated by SDS-PAGE. The IP signal in the (**A**) autoradiography and (**B**) the αFlag (Mouse, F1804) signal on the immunoblot were quantified as indicated (black arrow heads: mGluR2, grey arrow heads: ASGPRI, β2AR). αGAPDH signal was used as loading control. (**C**) Quotient of the autoradiography and immunoblot signal of protein or variant P was normalized to the signal of mGluR2^{C121A}-Flag. The data are shown as dot plot with mean±SEM (n=4) in GraphPad Prism. Statistics with 1way ANOVA (*=P<0.05).

2.5.3 Cholesterol binding to TM-mGluR2 in molecular dynamics simulation

The experimental data suggested that point mutations to alanine are not sufficient to disturb the trafficking or dimerization of the mGluR2 variants. On the contrary, cholesterol binding appeared to be compromised by the mutation sites in the transmembrane helices V and VI (Figure 2.32). However, the molecular determinants governing the binding of cholesterol at those particular positions, as well as, whether cholesterol binding might be correlated with other processes of the receptor (such as conformational changes in the transmembrane domain) remained unknown. To tackle this issue, lipid binding to the transmembrane domain of mGluR2 was investigated by molecular dynamics (MD) simulation. The MD simulations were carried out with the software package GROMACS 2016.x (179-181). They were performed in collaboration with the Max Planck tandem group in Computational Biophysics at the University of Los Andes in Bogotá (Colombia), directed by Dr. Camilo Aponte-Santamaría. Within this collaboration, we performed atomistic and coarse-grained simulations of the transmembrane domain of mGluR2 (TM-mGluR2) embedded in a fully solvated lipid bilayer of 1-palmitoyl-2-oleoyl-sn-glycero-3-phosphocholine (POPC). The structural dynamics of the bilayer and the protein were quantified in the presence and in the absence of cholesterol.

In total, four atomistic and two coarse-grained simulations systems were considered (Section 2.1.2.2). In the atomistic systems, simulations were performed for TM-mGluR2 embedded in a pure POPC bilayer. In addition, the mutants TM-mGluR2^{Y745A} and TM-mGluR2^{Y781A}, which displayed experimentally a reduced cholesterol binding, were simulated in a POPC bilayer containing 15mol% cholesterol. For the coarse-grained simulations, two wild type transmembrane domains were initially separated by 7.5 nm while embedded into either a POPC or POPC/CHOL$_{15mol\%}$ bilayer system for further simulations.

2.5.3.1 Atomistic molecular dynamics simulations of TM-mGluR2

Initial positions of the protein were taken from the homology model of TM-mGluR2, after adding the neutral caps at the N- and C-terminal ends (Section 2.1.2.2). The TM-mGluR2 domain was placed in a POPC bilayer with ~145 POPC molecules in each layer (or ~130 POPC molecules and ~20 cholesterol molecules in each leaflet which corresponded to 15mol% cholesterol) by using the web-based CHARMM-GUI (85, 86, 182). The bilayer was fully solvated by around 25.500 explicit water molecules and sodium chloride to neutralize the charge of the protein and to achieve a physiological salt concentration of 0.15 M. The

resulting rectangular simulation box had a size of approximately (10x10x11.5) nm (Section 4.13.2). The CHARMM36 atomistic force field was used for the protein, the TIP3 water model for the water molecules, and the default CHARMM parameters for the ions (83). Bonded interactions between atoms were considered by harmonic bonds, constraining those involving hydrogen atoms with the LINCS algorithms (183). Short-range non-bonded interactions were included via a Lennard-Jones potential, which was set to a switching distances of 1.0 nm and truncated at 1.2 nm. Electrostatic interactions were treated by using the particle mesh Ewald summation technique (184). Neighboring atoms were considered though the Verlet Buffer particle-particle scheme (185, 186). The pressure was maintained constant by coupling the system to a Berendsen barostat during solvent-equilibration steps and Parrinello-Rahman during the production run (187, 188). Used coupling constant for the barostat in the equilibration and production run was 5 ps (Table 4.16). For the equilibration, temperature coupling was controlled by Berendsen, while for the production temperature was kept constant by coupling the system to a Nose-Hoover thermostat (189-191). Used coupling constant for the Berendsen and Nose-Hoover thermostat was 1 ps. Accordingly, the temperature of the system was fixed to 310 K and the pressure to 1 bar. For the run, GROMACS 2016.x was used. Simulations were performed in the BwForCluster MLS&WISO of the state of Baden-Württemberg.

For each of the four atomistic setups (wild type TM-mGluR2 in POPC and wild type TM-mGluR2, TM-mGluR2^{Y745A} and mGluR2^{Y781A} in POPC/CHOL$_{15mol\%}$), four independent simulations of 500 ns were run in parallel, yielding 2 µs of cumulative simulation time per case (8 µs in total). From the first set of simulations in a pure POPC bilayer conformational states were extracted that were then used for the next set of simulations in POPC/CHOL$_{15mol\%}$. Each production run was preceded by a set of equilibration steps in which the protein and the phosphorous atoms of the lipids were position-restrained. The strength of the position-restrains was gradually decreased during these steps (Table 4.16).

2.5.3.2 Coarse-grained molecular dynamics simulations

The coarse-grained simulation were performed by the MARTINI (Ver.2.2) model of TM-mGluR2 (details see Section 4.13.1). While the atomistic simulations considered every atom of the system, each MARTINI bead represented four heavy atoms (=non-hydrogen) classified as polar, nonpolar, apolar or charged bead (84). The protein, the lipids, the water molecules, and ions were treated by considering such mapping. The coarse-grained model of the TM-

mGluR2 was obtained by martinize.py script (192, 193). In addition, an elastic network was imposed on all the protein beads to maintain its secondary and tertiary structure. The elastic network was imposed to all beads separated by at least 2 beads and within a distance of 0.9 nm (Rubber force constant of 500 kJ/mol*nm). The adjacent beads were connected by bonds and angels of the force field Martini22 (non-polarized water) (193). Two TM-mGluR2 monomers were placed in a rectangular box of (15x15x12) nm with their center of masses placed 7.5 nm apart. The two monomers were embedded in a fully solvated POPC or $POPC/CHOL_{15mol\%}$ bilayer using the INSANE command (87) (Section 4.13.3). Sodium chloride at a concentration of 0.15 M was added to the system and an excess of 24 chloride ions compensated the net charge of the protein. 10% of anti-freezing beads was added to the solvent to prevent its crystallization. Short-range interactions were treated by a Lennard-Jones potential with a cutoff of 1.1 nm and shifted to zero within 0.9 and 1.1 nm. Electrostatic interactions were considered via a reaction-field scheme with the Coulomb potential truncated at a distance of 1.1 nm, shifted to zero between 0 and 1.1 nm, and with a dielectric constant of 15 beyond 1.1 nm. Neighbor beads were updated through the Verlet Buffer particle-particle scheme (186). An energy minimization and a 10 ns solvent relaxation step preceded the production runs (Table 4.17). During the relaxation the protein was kept fixed with position-restraints (Position restrain force constant 1000 kJ/mol*nm) and the equations of motion were integrated at discrete time steps of 10 fs. The position-restraints were removed and 99 production runs, of 5 µs each, were generated for the POPC system and 100 for the $POPC/CHOL_{15mol\%}$ system. In the production runs, equations of motion were integrated at a time step of 20 fs. All production runs accounted for 0.95 ms of cumulative simulation time.

2.5.3.3 Basic physical parameters of the Molecular dynamics simulation

Four global observables have been computed from the simulations to get insight into the stability of the simulation system. These observables are pressure, temperature, simulation box volume and density (details of the calculation of these parameters see Section 4.13.4).

Despite of the use a semiisotropic Parrinello-Rahman barostat, the pressure displayed high fluctuations over the course of the simulations (Figure 2.34 A). This is a common behavior of MD simulations. In any case, and despite of these high fluctuations, the mean value approached the reference pressure of 1 bar. In the coarse-grained systems the average pressure was 1.018 bar and 1.012 bar for the POPC and POPC/CHOL systems, respectively (Figure 2.34 A). In the all atom simulation, the POPC bilayer systems exhibited an average of

1.018 bar. In the systems with 15 mol% cholesterol, the pressure had an average of 1.056 bar for the wild type, 0.900 bar for TM-mGluR2^{Y45A} and 1.170 bar for TM-mGluR2^{Y781A}. The high fluctuations in the pressure are related to the rapid changes in the position of the atoms due to thermal collisions. Accordingly, the pressure oscillations were larger in the atomistic systems than in the coarse-grained systems.

The temperature was also controlled by coupling the system to a thermostat. This in practice implied a rescaling of the velocities of the atoms (beads in the coarse-grained simulations) to attain a reference temperature (here 310 K or 37°C). In all systems the 25th to 75th percentiles of the temperature were rather narrow and covered the reference temperature: Around (308-311) K for the coarse-grained and (309-310) K for the atomistic simulations (Figure 2.34 B). In contrast to the pressure, the fluctuation in the temperature was higher for the coarse-grained systems than for the atomistic systems.

The other parameters, density and volume, showed only small changes within a narrow inter-quartile distance (Figure 2.34 C+D). The densities for the atomistic systems were in all simulation approaches quantified with a mean of 1017 kg/m^3 with half of the values distributed between 1016 kg/m^3 and 1019 kg/m^3 (Figure 2.34 C). In the coarse-grained systems, the intervals between the first and third quartile around the mean densities of 1059 kg/m^3 were comparably narrow. Thus, the density showed differences between the force fields but within the atomistic and coarse-grained sets the values were stable. For the volume, the box sizes of the coarse-grained systems were larger as compared to the all atom systems because they harbored two instead of one TM-GluR2 domain. The former had a box size of approximately (15x15x12) nm in x,y,z-direction, and the averaged volume was 2537.4 nm^3 for the POPC system and 2483.8 nm^3 for the boxes with cholesterol. Compared to the starting volume of 2700 nm^3 both systems were shrunken in the equilibration. The same was observed for the atomistic systems, which had an initial box size of (10x10x11.5) nm or 1150 nm^3. For the POPC systems, 1144.3 nm^3 were measured as averaged volume, while for TM-mGluR2 and the mutants the values were fluctuating in a narrow range around 1125 nm^3 (Figure 2.34 D).

Hence, from these four observables we can be certain that the simulated systems were overall stable, with the size and density maintained relatively constant, while controlling the pressure and temperature.

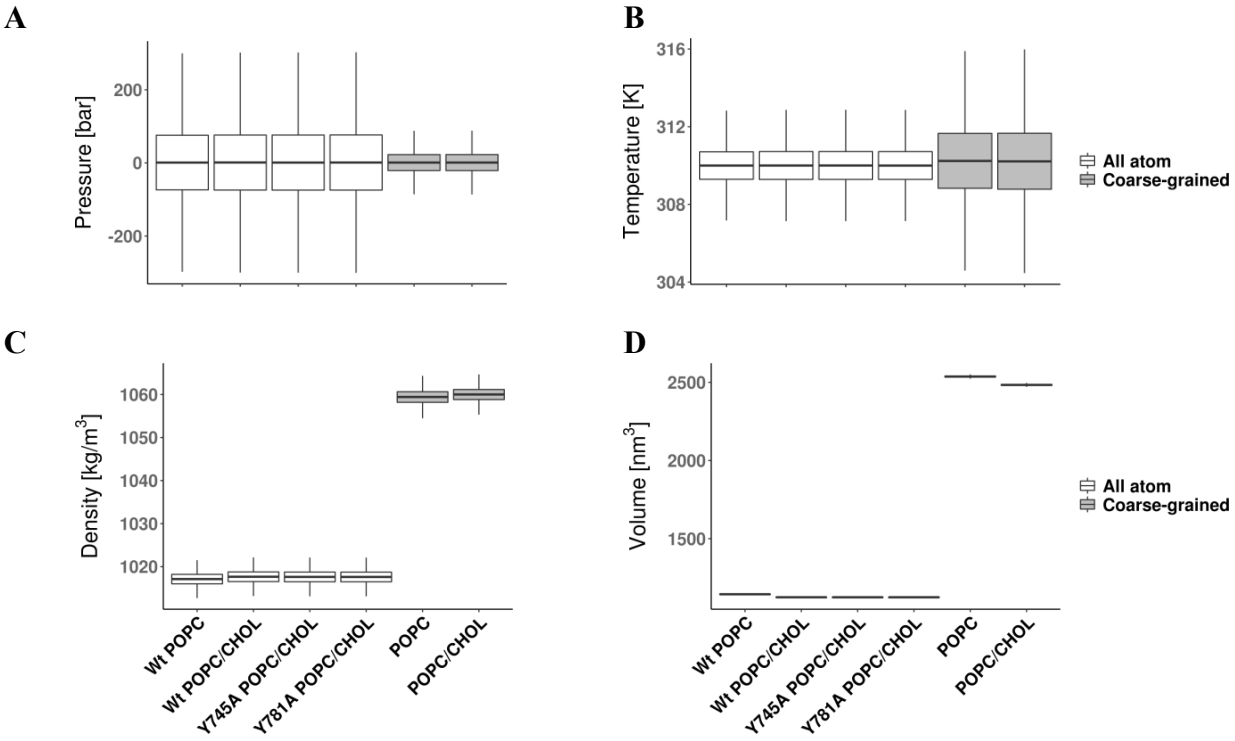

Figure 2.34 | Global observables of the indicated systems recovered from MD simulations. The box-whisker plots represent the physical properties of the simulation box during the production run of the simulation. Both coarse-grained and all atom systems were controlled by semiisotropic pressure coupling (Parrinello-Rahman barostat). The values were retrieved from the systems by GROMACS 'gmx energy' for (**A**) pressure, (**B**) temperature, (**C**) density and (**D**) volume (details see Section 4.13.4). The values are presented as box-whisker plots for n=4 (all atom) or n=99/100 (coarse-grained) independent simulations considering the whole trajectory. The values were plotted as Tukey box plot in RStudio with ggplot2. The boxes indicate the 25th and 75th percentiles, the whiskers 1.5 times the inter-quartile distance. The bar in the middle shows the median value.

2.5.3.4 Lipid density and deuterium order parameters

The characteristics of the membrane were quantified with GROMACS 2016.x to find out about the stability of the bilayer system and the behavior of the lipids in the simulation box.

The lipid membranes in the atomistic simulation systems showed a stable distribution for the membrane and soluble components (Figure 2.35 A+C). The water penetrated into the membrane approximately to the spatial extent of the POPC headgroups. The density of the POPC acyl chains peaked not at the center of the membrane in z-axis, but at a distance of 1 nm from the membrane core. In the simulation including cholesterol, these molecules were found to be embedded within the acyl chains and showed a similar distribution (Figure 2.35 C). Notably, the Deuterium order parameter in the simulations with cholesterol peaked around a value of 0.263±0.001 for SN1 at carbon index 5, while at the same position an averaged value of 0.221±0.001 was measured in the POPC simulations (Figure 2.35 B, Figure 2.35 D). However, the inclusion of cholesterol did not substantially modify the trend observed for the order parameters of SN1 and SN2. In the core of the membrane the Deuterium order

parameter for the SN2 acyl-chain was in both systems somewhat lower as compared to that of the SN1 acyl chain; at carbon index 7 an averaged value of 0.121±0.001 was measured for SN2 as compared to 0.257±0.001 for SN1 in the POPC/CHOL bilayer (Figure 2.35 B+D). This reduction in the order for SN2 may be attributed to the difference in saturation between these two chains. While the palmitoyl moiety is saturated, the oleoyl at SN2 contains a cis-9 double bond which is most likely the reason for the low Deuterium order parameter here.

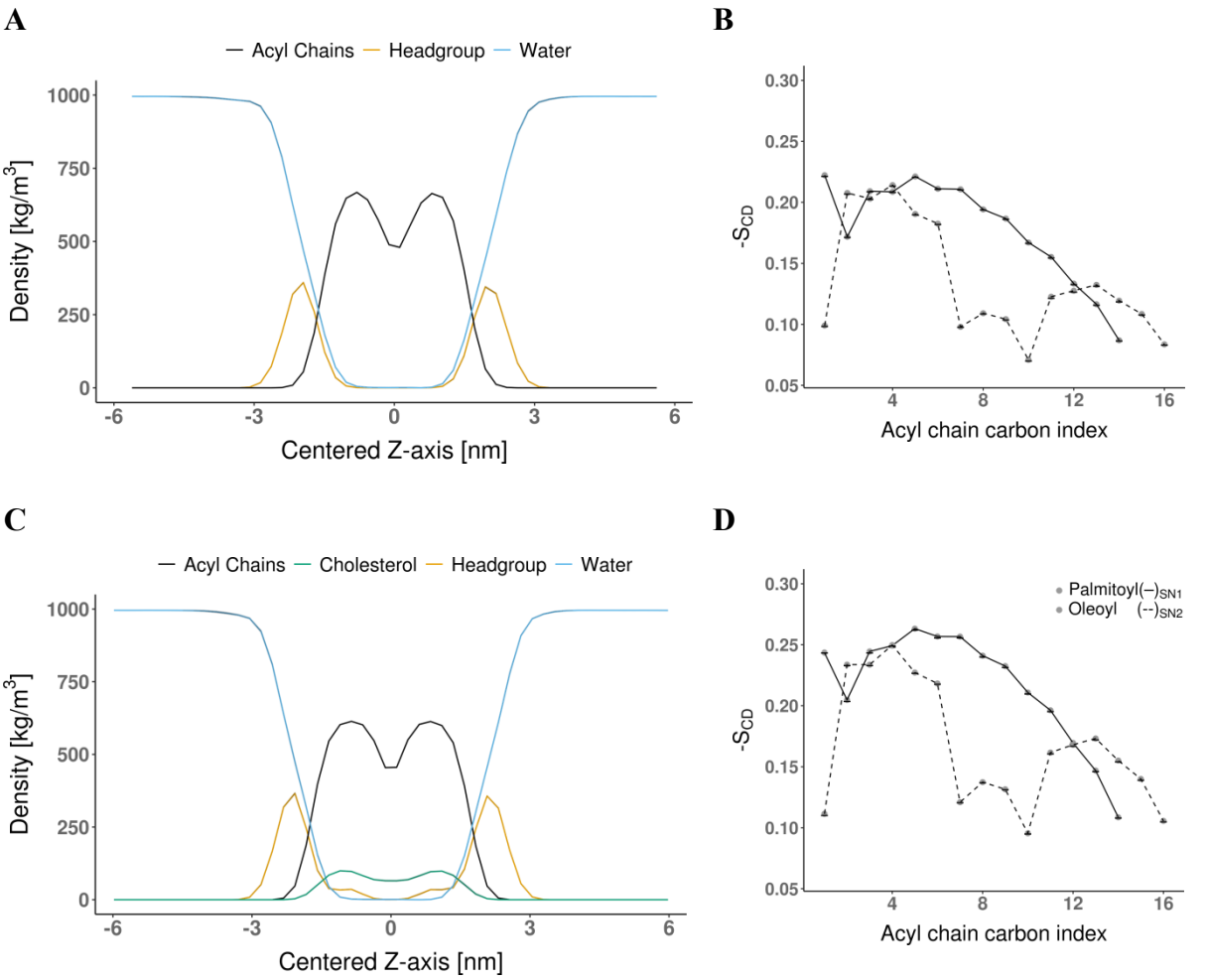

Figure 2.35 | Lipid distribution in the simulation box and Deuterium order parameter of acyl chains. The parameters were calcualted for the atomistic simulations of TM-mGluR2 in a POPC bilayer in the (**A+B**) absence and (**C+D**) presence of 15mol% cholesterol. (**A+C**)The density distribution as as a function of the coordinate normal to the membrane (Z-axis) is presented for the indicated lipid moieties and water. The values were calculated with GROMACS 'gmx denisty' (details see Section 4.13.6.1). The mean density was plotted as line and the SEM as ribbon (n=4). (**B+D**) The deuterium order parameter ($-S_{CD}$) as function of the acyl chain carbon index is presented. It was calculated separately for the SN1 and SN2 acyl chains of POPC with GROMACS 'gmx order' (details see Section 4.13.6.2). Here, the $-S_{CD}$ is presented as mean±SEM connected by lines (n=4). The double bond of the unsaturated oleoyl chain is located between the 9th and the 10th carbons, which is here carbon index 7 and 9.

Similar observations were made for the coarse-grained simulations of TM-mGluR2 (Figure 2.36). The density profile for the membrane components showed an even distribution of the water phase at either site of the membrane with the same bimodal distribution for the acyl

chains as observed for the atomistic simulations. In contrast to the atomistic simulations, the acyl chains peaked at ~1000 kg/m^3 and thus at the same density as the water phase. Also, the water appeared to penetrate slightly less into the headgroups of POPC as compared to the all atom systems: the density curve declined earlier than the one of the POPC headgroups. As observed before for the Deuterium order, the palmitoyl chain at position SN1 showed a higher order than the oleoyl at position SN2 (Figure 2.36 B+D). Compared to the atomistic simulation, the difference between the two acyl chains was less well resolved due to the coarse-graining (Figure 2.35 B+D, Figure 2.36 B+D).

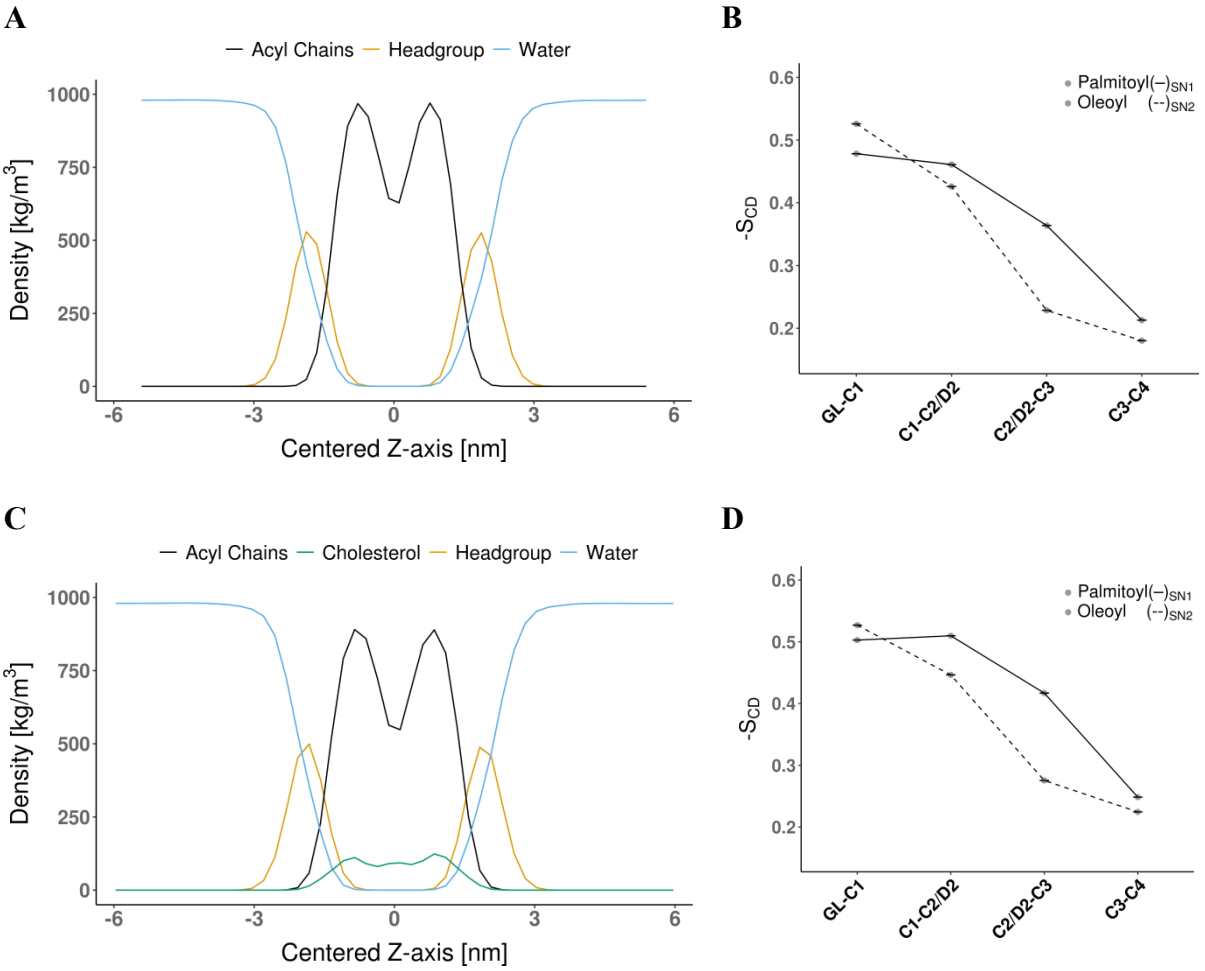

Figure 2.36 | Lipid distribution in the simulation box and Deuterium order parameter of acyl chains. The parameters were calcualted for the coarse-grained simulations of TM-mGluR2 in a POPC bilayer in the (**A+B**) absence and (**C+D**) presence of 15mol% cholesterol. (**A+C**)The density distribution as as a function of the coordinate normal to the membrane (Z-axis) is presented for the indicated lipid moieties and water. The values were calculated with GROMACS 'gmx denisty' (details see Section 4.13.6.1). The mean density was plotted as line and the SEM as ribbon (n=99/100) (**B+D**) The deuterium order parameter (-S_{CD}) as function of the acyl chain beads is presented. It was calculated separately for the SN1 and SN2 acyl chains of POPC with do-order-gmx5.py (details see Section 4.13.6.2). Here, the -S_{CD} is presented as mean±SEM connected by lines (n=99/100). The double bond of the unsaturated oleoyl chain is located between the 9th and the 10th carbons, which is here represented by bead D2.

In the coarse-grained system, the presence of cholesterol appeared to influence the palmitoyl moiety stronger than the oleoyl (Figure 2.36 B+D). For oleoyl at SN2, the first two beads did not show major differences in the order parameters with averages of ~0.52 and ~0.42-0.44 in both systems. Only the beads in the core of the membrane showed a higher order parameter in the presence of cholesterol, which sifted the averaged values from 0.228 to 0.275 and 0.180 to 0.224 for the third and fourth bead in the chain, respectively. In contrast to that, the Deuterium order parameter for palmitoyl increased for all beads when cholesterol was present.

Finally, the lateral diffusion constant of the POPC lipids was calculated by a linear fit through the mean square displacement (MSD) over time for the phosphate groups (Figure 2.37). For the system containing only POPC, the diffusion constant estimated for the coarse-grained system was about tenfold higher than the one measured in the atomistic system: the mean values calculated here were 0.0550×10^5 cm^2/s and 0.0068×10^5 cm^2/s, respectively. Because the diffusion estimate depends on the size the simulation system, comparisons between estimates of different systems or from experiments is difficult (194). However, relative differences due to the presence of cholesterol can still be assessed. For both systems the diffusion constant was reduced in the presence of cholesterol, by about 25% to on average 0.0416×10^5 cm^2/s and 0.0049×10^5 cm^2/s for coarse-grained and atomistic systems, respectively (Figure 2.37). This result was expected, as it is known that cholesterol rigidifies lipid membranes, thereby reducing the overall lateral diffusion in the system (195, 196).

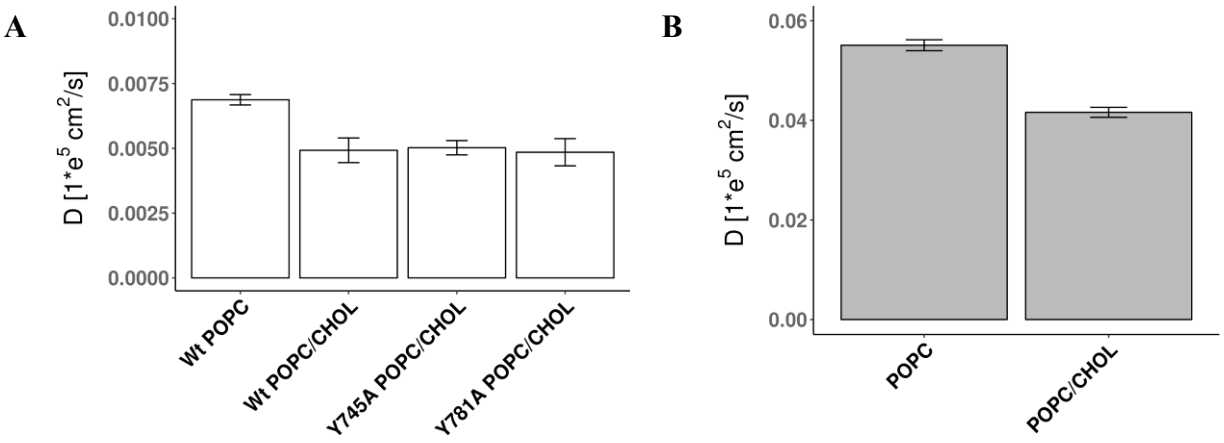

Figure 2.37 | Lateral diffusion constant of POPC lipids recovered from MD simulations. The lateral diffusion constant was calculated by least squares fitting the linear relationship (D*t+c) through the mean square displacement of POPCs' phosphate groups with GROMACS 'gmx msd' (details see Section 4.13.6.3). (**A**) The diffusion constant is presented for the four indicated systems, simulated atomistically: TM-mGluR2 in POPC bilayer (Wt POPC), TM-mGluR2 in POPC/$CHOL_{15mol\%}$ bilayer (Wt POPC/CHOL), TM-mGluR2^{Y745A} in POPC/$CHOL_{15mol\%}$ bilayer (Y745A POPC/CHOL), and TM-mGluR2^{Y781A} in POPC/$CHOL_{15mol\%}$ bilayer (Y781A POPC/CHOL). The bar plots in R represent mean±SEM from n=4 independent simulations. (**B**) For the coarse-grained simulation, the diffusion constant is presented for a pure POPC and a mixed POPC/$CHOL_{15mol\%}$ bilayer. The bar plots in R represent mean±SEM from n=99 (POPC) and n=100 (POPC/CHOL) independent simulations.

2.5.3.5 Protein dynamics during the MD simulations

We next investigated the stability and movement of the protein during the simulation. The stability could be assessed by computing the root mean square deviation (RMSD) from the initial conformation, the root mean square fluctuation (RMSF) for each amino acid residue of TM-mGluR2 and the radius of gyration of the protein.

The radius of gyration (gyration) for the TM-mGluR2 was found to be approximately 2 nm (Figure 2.38 A). Interestingly, only small differences were observed between the atomistic and the coarse-grained simulations. Thus in both systems the protein kept a steady value for the gyration over time which argued for their compactness and integrity throughout the simulation.

The RMSD was calculated for all given conformation compared to the reference structure at t_S=0 ps. In the atomistic simulations, the RMSD was on average 0.38 nm in the first simulation in POPC and reduced by about 20% in the later simulation in POPC/$CHOL_{15mol\%}$ (Figure 2.38 B). That observation can be explained by the fact that the structures for the run in POPC/$CHOL_{15mol\%}$ were extracted from the most occupied structures in the POPC system. Thus the structures in the second set were already equilibrated 500 ns. The RMSD was of the order of 0.25 nm in the coarse-grained simulations and showed a very small error (Figure 2.38 B). This can be explained by the fixation of the secondary and tertiary structure by the

elastic network (197) (Section 2.5.3.2). Both estimates are reasonable given that they come from a homology model.

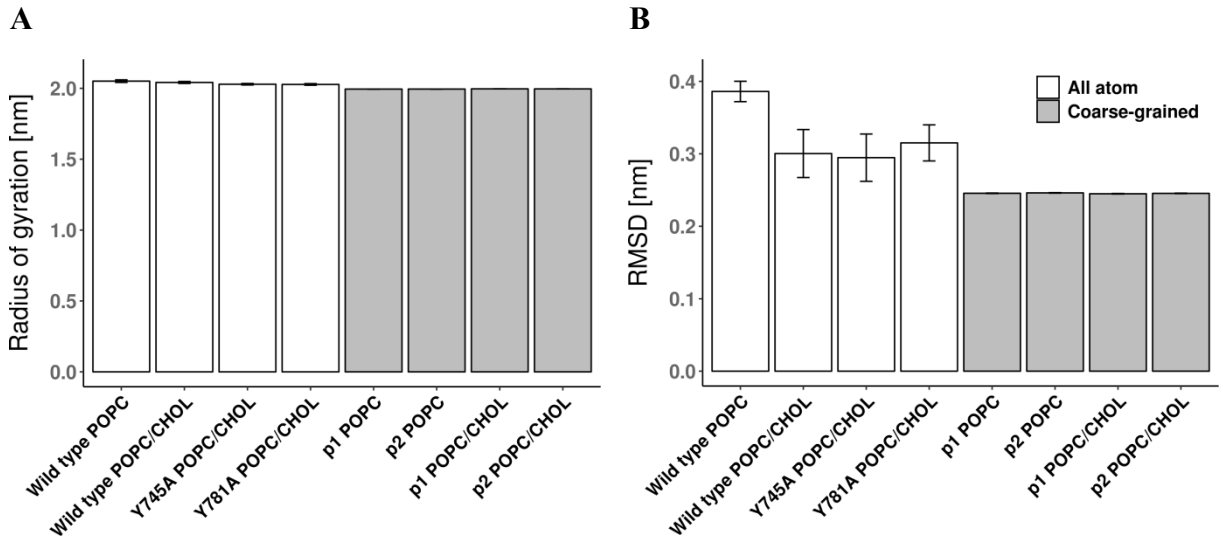

Figure 2.38 | Quality estimates for the TM-nGluR2 homology model in the MD simulations. The radius of gyration and the root mean square deviation (RMSD) were calculated with GROMACS 'gmx gyration' and 'gmx rms' (details see Section 4.13.5). (**A**) Radius of gyration and (**B**) RMSD of TM-mGluR2. The values for the radius of gyration and the RMSD were averaged over n=4 trajectories for the atomistic simulations and n=99/100 simulation for the coarse-grained simulations. The values for the two protomers in the coarse-grained simulations were calculated and plotted seperately. The results are shown as mean±SEM.

While the RMSD is a measure for the overall movement of the protein, the Root mean square fluctuation (RMSF) is a measure for the movement of single amino acid residues. The comparison between the atomistic simulation of TM-mGluR2 in a POPC bilayer in the presence and absence of cholesterol showed that the movement was slightly more restricted in the presence of cholesterol, as seen already for the RMSD (Figure 2.39 A). Here, the RMSF analysis revealed that the motion of the protein was not equally pronounced for all the residues but was especially strong for the intra- and extracellular loops between the helices; for the second intracellular loop between helices III and IV, as well as the for the second extracellular loop between the helices IV and V a strong fluctuation was observed (Figure 2.39 A). Interestingly, also transmembrane helix VI showed a higher flexibility at the extracellular site which propagated into the third extracellular loop.

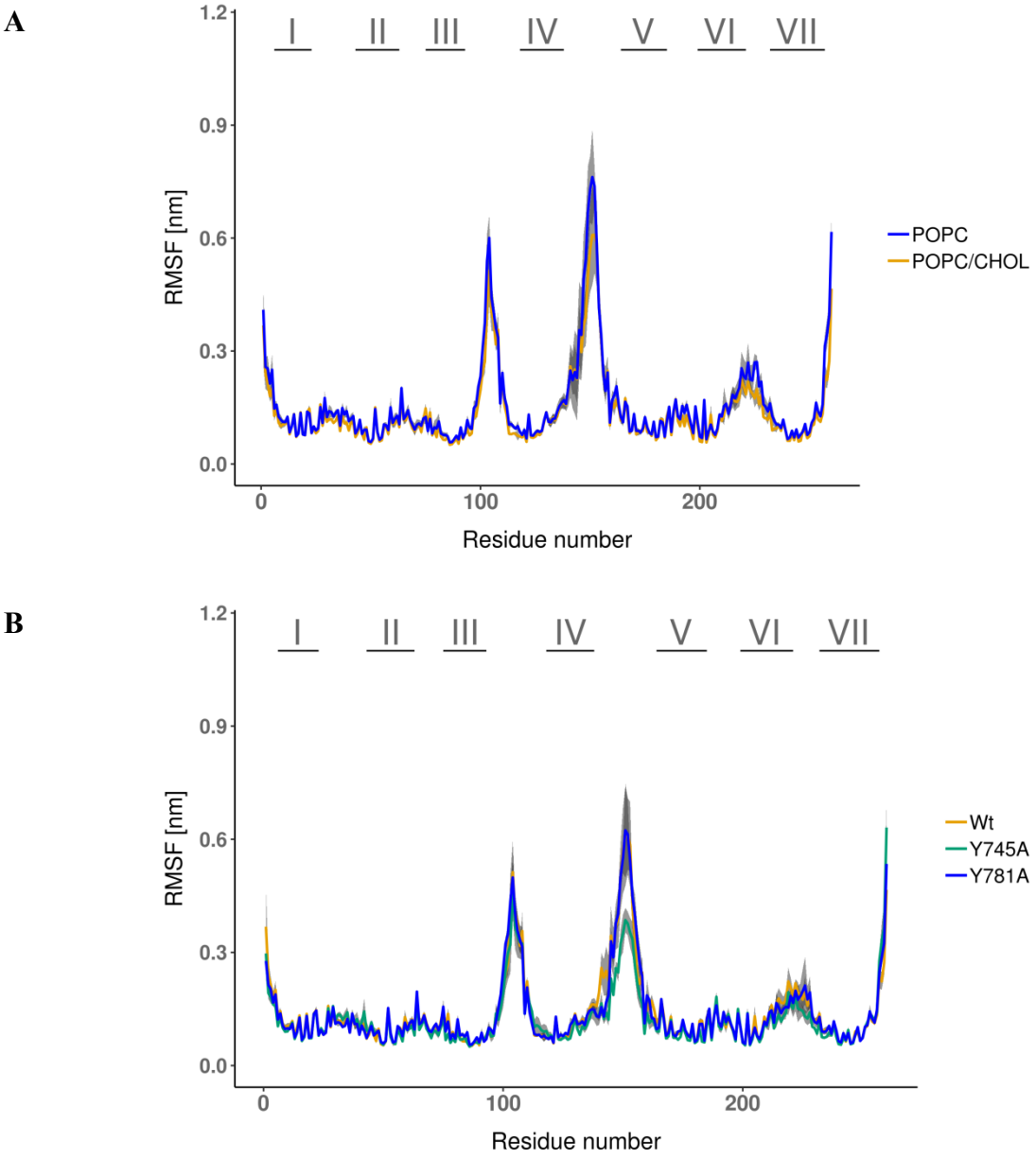

Figure 2.39 | Root mean square fluctuation analysis of TM-mGluR2 in atomistic systems. The graphics show the Root mean square fluctuation (RMSF) analysis for TM-GluR2 as calculated with GROMACS 'gmx rmsf' (details see Section 4.13.5). (**A**) For the first analysis, the RMSF values per amino acid residue were compared between TM-GluR2 in a POPC bilayer in the presence and absence of cholesterol. (**B**) For the second analysis, the RMSF was calculated for TM-mGluR2 variants in a POPC bilayer with 15mol% cholesterol. The plots represent the RMSF per amino acid residue for TM-GluR2 and its two mutants Y745A and Y781A. (**A+B**) The RMSF were calculated for each trajectory separatly and averaged over the whole set of simulations. The helices are indicated on top of the chart. The mean was plotted as line and the SEM as ribbon.

Next, a comparison was made between the RMSF measured for the protein in a POPC bilayer with 15mol% cholesterol. Here, the atomistic simulations of the wild type and the two designated cholesterol binding mutants TM-mGluR^{Y745A} and TM-mGluR^{Y781A} were compared (Figure 2.39 B). The comparison of the RMSF values showed that flexibility of the single residues had a similar pattern similar for the wild type TM-mGluR2 and its Y781A mutants. Differences between the simulations were seen for the upper end of transmembrane helix VI

where Y781A appeared to be slightly more flexible. Larger differences were seen for TM-mGluR2^{Y745A} which was less flexible as compared to the wild type and TM-mGluR2^{Y781A}. The RMSF for the second and third extracellular loop was lower which indicated a slightly lower flexibility of the transmembrane domain in these parts after introducing the mutation.

The RMSD analysis had suggested that the protein structure in the coarse-grained simulations was more stable because of the artificially fixed secondary and tertiary structure. A similar picture showed for the comparison of the RMSF between the atomistic and coarse-grained simulations in POPC (Figure 2.40). The RMSF for the coarse-grained simulations was with values below 0.3 nm for most structural components on average lower than for the atomistic simulation. However, one striking similarity between the two structures was the flexibility in the 2nd intracellular loop (between helices III and IV). Both the atomistic and the coarse-grained structure showed flexibility in this region. In contrast to that, the flexibility in the 2nd extracellular loop was not well resembled in the coarse-grained model. Also the upper half of helix 6 and the 3rd extracellular loop did not exhibit the flexibility of the all atom simulation. The RMSF calculated here might be underestimated it was calculated not calculated from a concatenated trajectory, but separately for each and averaged of the set of simulations.

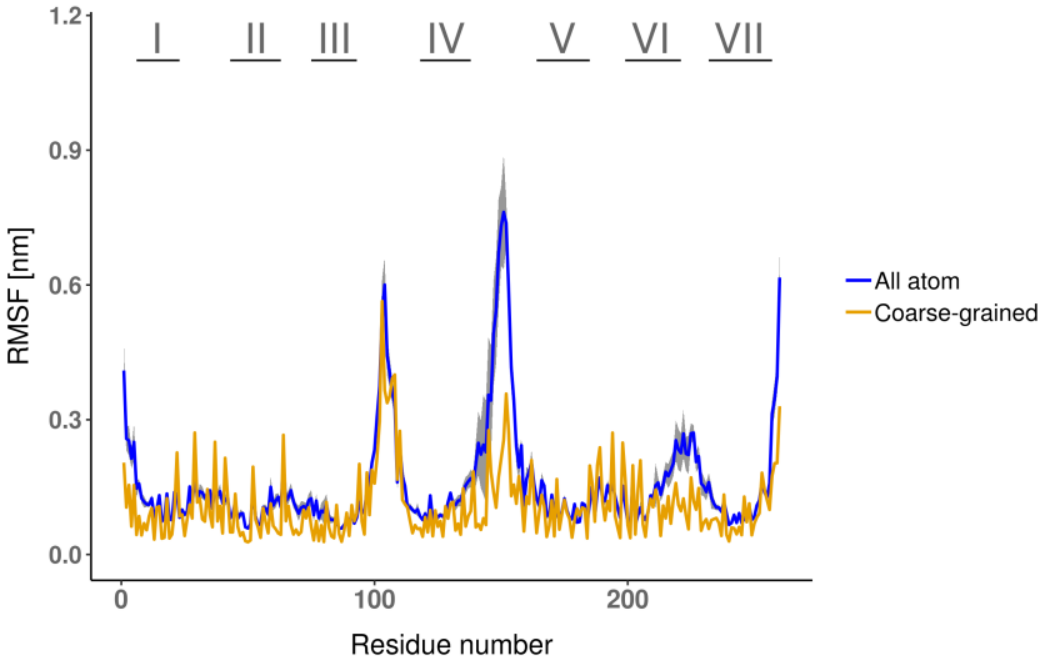

Figure 2.40 | Comparison of TM-mGluR2 in atomistic and coarse-grained simulations. The graphics show the analysis for TM-GluR2 in a POPC bilayer. The data for the RMSF analysis were sampled with GROMACS 'gmx rmsf' for each trajectory separatly and averaged over the whole set of simulation (details see Section 4.13.5). The averaged RMSF are shown as line for the TM-mGluR2 in the all atom (blue, n=4) and coarse-grained (orange, n=99) simulation setup with the SEM as grey ribbon. The helices are indicated on top of the chart.

The different parameters here suggested that the transmembrane model of mGluR2 had remained stable throughout the simulations. In the next step the interaction between the membrane resident cholesterol and the surface of the protein would be calculated.

2.5.3.6 Cholesterol binding to the protein surface

Finally, the localization of cholesterol around TM-mGluR2 was monitored. The time-average density map of cholesterol was computed to determine regions frequently occupied by these molecules. This map was calculated with the GROmaps toolset (198). The density was contoured at different confidence levels (Figure 2.41). This calculation revealed a large cholesterol density around transmembrane helices I and VII. Because of its size, this density region was indicative of unspecific positioning of cholesterol at these sites. The size of this density region remained visible throughout several density levels, further ensuring the unspecific nature of this region. The interaction site correlated well with the observations which had been made in the crystal structure of the transmembrane domain of mGluR1 (71): in the crystal structure six cholesterol molecules had been between the dimer interface around mirrored interface between helices I. In addition to that, this very large density region, four smaller density patches were observed: on at the cytosolic end in the cleft between helices I and IV, one at the extracellular half of helix IV, one at the intracellular patch of helix V and finally one in the extracellular leaflet around helix VI. The first two cholesterol density sites at the cytosolic cleft between helices I and IV, as well as the one on helix VI were still visible at 4σ. The density at the intracellular end of helix V was still visible at 3σ but then shrank at 4σ. Furthermore, the shape of densities approximately resembled the size of a single-cholesterol molecule as the confidence level increased. Thus we conclude from this calculation that single cholesterol molecules accommodated specifically at least three places on the surface of TM-mGluR2.

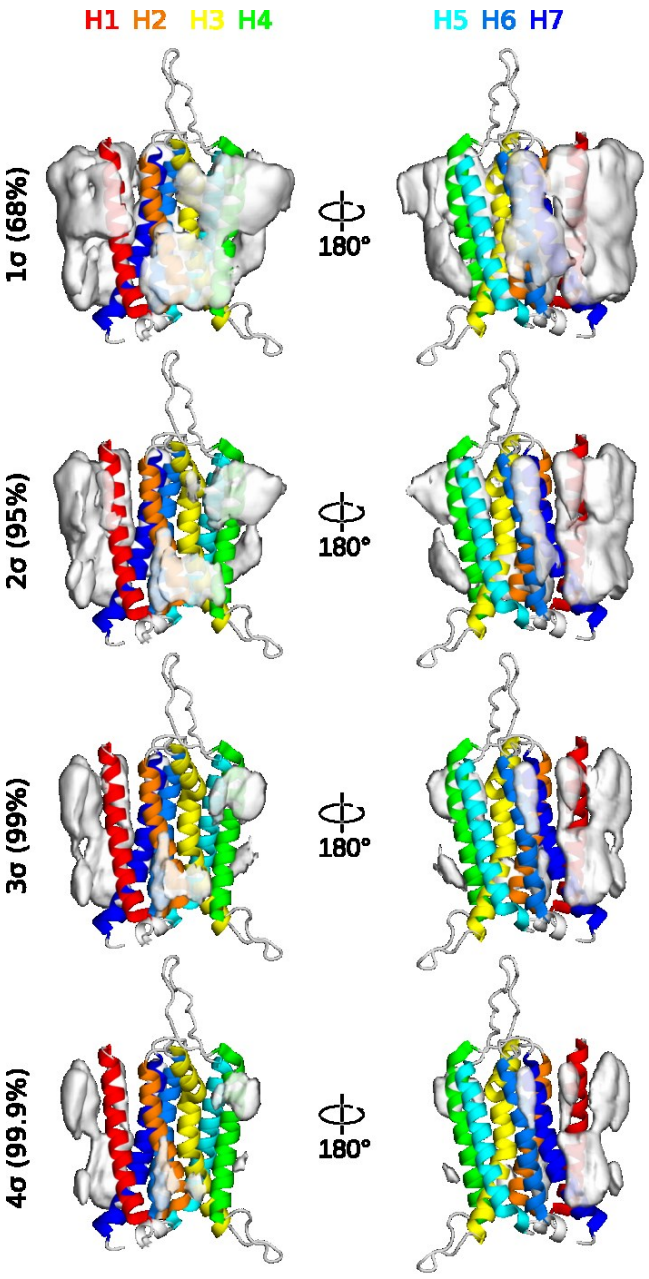

Figure 2.41 | Time-averaged density map of cholesterol TM-mGluR2. The cholesterol density was calculated with the GROmaps toolset (198). With GROmaps a cholesterol density map was built for a proximity of 0.8 nm around the surface of the protein (details see Section 4.13.7.2). The density is contoured as the white surface at different density levels (in standard deviation, sigma units). The background average density has been set to zero. The protein is depicted in cartoon representation, coloring the helices according to the labels at the top. Two orientations are shown for each density level.

We next investigated the change on the accommodation of cholesterol due to mutation of the tyrosines 745 and 781 by alanine (Figure 2.42). The large unspecific density around the helices I and VII and the density on the cytosolic site between helices I and IV were still visible for all variants even though the shape seemed to vary between the wild type and the mutants. In contrast to that, the density near helix IV, V, and VI altered for TM-mGluR2^{Y745A} and TM-mGluR2^{Y781A}, as described as follows. For TM-mGluR2^{Y745A}, the density on front of helix IV got smaller and the one at the lower end of helix V disappeared. The density at the exoplasmic side of helix VI got more smeared out. For Y781A, both regions of localized density around helices IV and V were lost. The density around helix VI split in two distinct density regions, presumably corresponding to two positions occupied by cholesterol in the

course of the simulations. The alterations in the localization of cholesterol due to the mutants observed in the simulations is consistent with the experimental of the *in vivo* labeling with [^{3}H]-photo-cholesterol in which the labeling efficiency for the two variants in the full length protein had decreased (compare Figure 2.42 and Figure 2.32). Interestingly, the exchange of one of the residues in helices five and six also appeared to change the density at other sites of the protein suggesting an allosteric mode of alteration for this particular mutant.

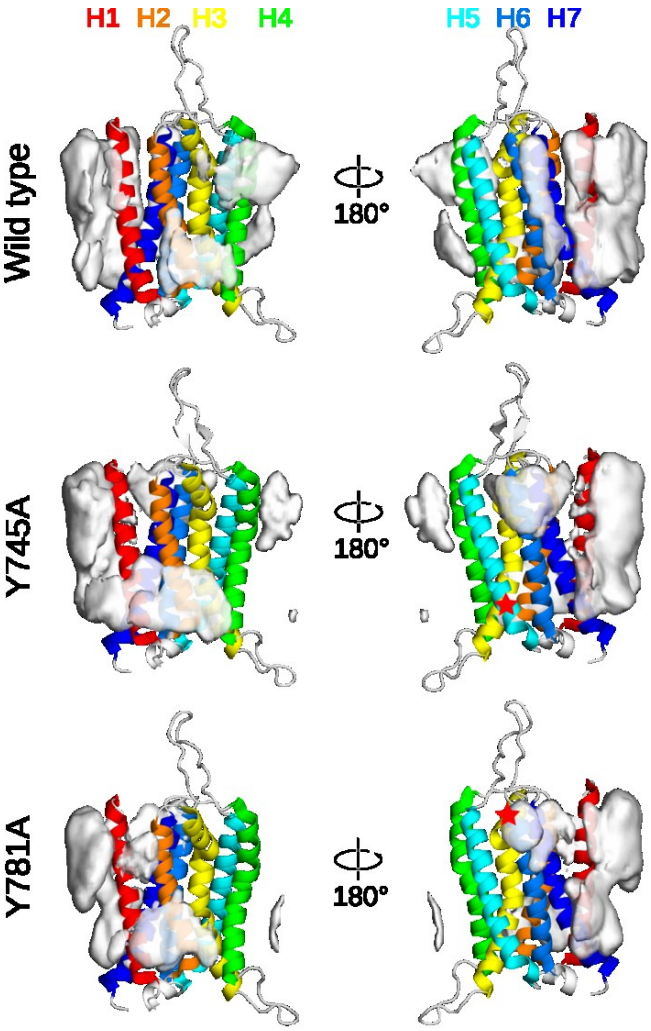

Figure 2.42 | Time-averaged density map of cholesterol density at the surface of wild type TM-mGluR2 and its two mutants Y745A and Y781A. The cholesterol density was calculated with the GROmaps toolset (198). With GROmaps a cholesterol density map was built for a proximity of 0.8 nm around the surface of the protein (details see Section 4.13.7.2). The density is contoured as the white surface at a density level of 2σ (in standard deviations). The background average density has been set to zero. The protein is depicted in cartoon representation, coloring the helices according to the labels at the top. The approximated mutations sites for Y745A and Y781A are indicated with a red star in helices V and VI respectively. Two orientations are shown for variant level.

We next monitored the localization of cholesterol in coarse-grained simulations (Figure 2.43). As the sampling increased, new features on the localization of cholesterol emerged. The large density region, previously observed in the atomistic simulations, in front of helices I and VII was less pronounced in the coarse-grained simulations (compare Figure 2.43 and Figure 2.41). In contrast to that, the density around helices II, III and IV had fused into one big batch and unspecific density region.

Most importantly, the region identified to specifically interact with cholesterol near helices V and VI also displayed a well-defined portion of density in the coarse-grained simulations,

which could be related to one or at the most two cholesterol molecules sitting at that region. Notably, the density at helix V was shifted into the middle of the membrane and the helix as compared to the atomistic simulations (Figure 2.43, Figure 2.41). Moreover, in the coarse-grained simulations two TM-mGluR2 protomers were considered and they often dimerized. Of note, dimerization did not affect the density around V and VI. Smaller changes were seen around helix I, which had shown to be at the dimerization interface in the mGluR1 X-ray structure (71). Overall, our coarse-grained simulations were consistent with the existence of this specific binding site for cholesterol near V and VI.

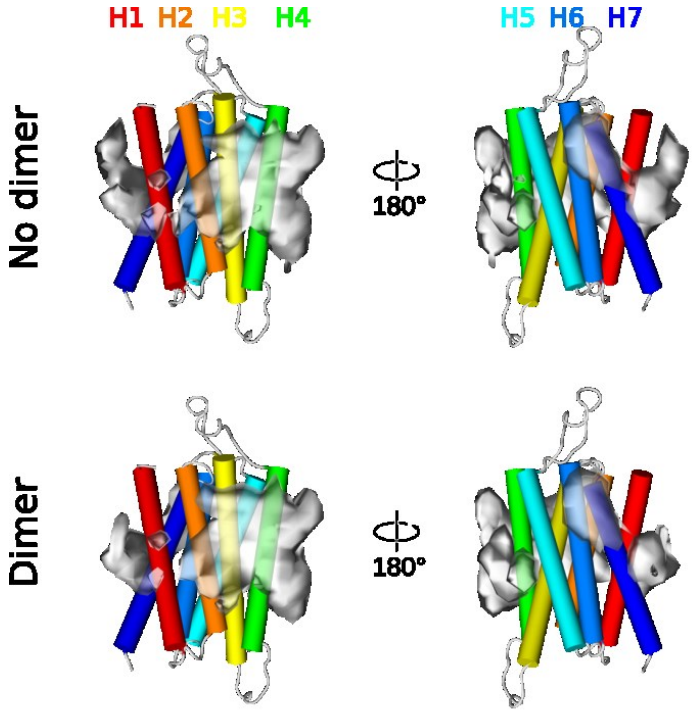

Figure 2.43 | Cholesterol density (99.9%) for the mGluR2 wild type transmembrane domain in coarse-grained simulation. The cholesterol density was calculated with the GROmaps toolset (198) With GROmaps a cholesterol density map was built for a proximity of 0.8 nm around the surface of the protein (details see Section 4.13.7.2). The density is contoured as the white surface at a density level of 4σ (in standard deviations). The background average density has been set to zero. The protein is depicted in cartoon representation, coloring the helices according to the labels at the top. Two orientations are shown for each variant.

3 Discussion

In this work the lipid environment of the G-protein coupled receptor (GPCR) mGluR2 was probed for covalent lipid modifications and the non-covalent lipid interactions. In the current experimental setup, there was no indication for S-palmitoylation of mGluR2. To study the non-covalent lipid interactions of mGluR2 a site-directed mutagenesis approach was chosen. It was shown that mutations at position Y745A in transmembrane helix V and Y781A in transmembrane helix VI of mGluR2 caused a significant reduction in the steady-state interaction with [^{3}H]-photo-cholesterol in a photocrosslinking assay in Hek293 cells. At the same time, these protein variants did not show alternations in intracellular trafficking or dimerization as compared to the wild type. Thus the loss of cholesterol binding most likely originated from a direct binding defect. Interaction of the mGluR2 transmembrane domains with cholesterol was further probed in a molecular dynamics (MD) simulation both in an atomistic and coarse-grained force field. The analysis of the cholesterol interaction showed that for the mGluR2 transmembrane domain (TM-mGluR2) cholesterol density was sampled next to the tyrosine residues at position 745 and 781. A simulation of the mutated transmembrane domains TM-mGluR^{Y745A} and TM-mGluR2^{Y781A} showed that the cholesterol density blurred out at the adjacent but also around distal sites. In contrast to the cholesterol binding experiments, a similar setup with [^{3}H]-photo-sphingosine ([^{3}H]-photoSph) did not deliver any conclusive results. The data showed that in contrast to the working hypothesis sphingolipid binding to the receptor was overall rather weak, and in some cases even increased when introducing the point mutations W697A or Y734A in helices IV or V of the transmembrane domain of mGluR2.

3.1 Experimental system

The basis of the experimental studies was the wild type Hek293 cell line – human embryonic cell line immortalized with adenovirus fragments (199). For the mGluRs the Hek293 system has been utilized many times, for other GPCRs –such as adrenergic and serotonin receptors – Hek293 cells are just one among other expression systems. While the mGluRs showed a robust detection in the immunoblot and correct shuttling to the cell surface in Hek293 cells, this was not the case for family A GPCRs. The results of this work suggested that improvements might be possible both on the side of the expression system, for example by including a second cell line as comparison, and on the side of the plasmid constructs of family

A GPCRs, for example by introducing artificial signal peptides for a more efficient ectopic expression.

3.1.1 Metabotropic glutamate receptors in Hek293 cells

First characterizations of the mGluR family as well as the isolation of the first mRNA sequences was conducted in a neuronal context (200). The sequence of the first receptors was cloned from neuronal rat tissue (201, 202). Likewise, many studies concerning the physiology of mGluRs have mainly addressed the function of the mGluRs in neurons. However, many studies concerned with the biochemistry of the receptors were conducted in ectopic expression systems. For example early studies on the homodimerization of mGluR1 and mGluR5 were performed in the context of Hek293 cells (132, 203). Also later studies concerned with heterodimerization within the mGluR family and intramembranous dimerization of mGluR2 were conducted in the cell line (121, 131). Furthermore, the Hek293 cells were used for protein-lipid interaction, such as for mGluR1α, or even pharmacological studies (56, 204). For that reason the cell line had been chosen as expression system.

Hek293 cells originate from human embryonic kidney tissue (199, 205). Hek293 cells express Homer proteins which have been investigated in a neuronal context, however, their function in kidney derived cell is not completely understood (206). Different Homer proteins were shown to bind to the extreme C-terminal end of group I mGluRs, namely isoforms mGluR1α and mGluR5a, which contain a proline-rich PPxxFR motif (207). Binding of one specific isoform, Homer1b, let to retention of receptors in the endoplasmic reticulum (208). It was shown in the thesis that all mGluRs were expressed at the surface of the Hek293 cells, but the cell surface arrival of mGluR1α was quantified with an average of 30%, about 15 percentage points lower compared to mGluR2 (Figure 2.20). Here, the presence of Homer proteins, such as Homer1b, could explain a depressed surface arrival. On the contrary, the surface expression for mGluR4 was on average 27%, but the receptor does not contain any known Homer binding sequence and no definite explanation can be given for that difference. However, there many more proteins that can interact with mGluRs (116). This includes kinases and ubiquitin ligases among others. The quantification of the surface arrival in the steady state might be especially dependent on the former one. For group III mGluRs it was shown that phosphorylation by Protein kinase A inhibits the function of the receptors by suppressing the coupling with GTP binding proteins (142). In contrast to that, in studies with $GABA_BR2$ it was found that phosphorylation of the receptor by Protein kinase A results in a

reduced desensitization and a stabilization of cell surface expression (209). How cell surface expression of other family C GPCRs is affected by phosphorylation is only poorly understood but might contribute to the observed differences in cell surface localization of mGluRs. Also other post-translational modifications in Hek293 cells could influence the surface expression of mGluRs: The expression level of mGluR1α was shown to depend on the presence of a ubiquitin ligase, the RING-finger-containing E3 ubiquitin ligase Siah3 (144). Notably, the effect of the overexpression was also dependent on the cell type: At the same transfection level, the receptor appeared to more prone to degradation in COS-7 and BHK-21 cells than in Hek293 cells. In Hek293 cells again only group I mGluRs were targeted by Siah3 for degradation (144). Thus, it might worth to consider conducting the biochemical experiment in two unrelated cell lines to account for cell type specific effects, which might depend on the expression pattern of interacting proteins.

For mGluR2 not only the surface arrival for one given plasmid DNA concentration was investigated, but a titration of DNA amounts used for transient transfection was performed to exclude artifacts originating from the transfection level. The transfection level was dependent on the DNA concentration as shown by flow cytometry (Figure 2.11). The flow cytometry experiment showed a decrease in transfection efficiency with decreasing DNA concentration. Thus at low DNA concentration only few cells expressed the construct. However, it was shown that cell surface expression of Flag-tagged mGluR2 and mGluR2^{C121A} was surprisingly stable at different transfection levels (Figure 2.12). This also held true for the different W→A or Y→A variants (Figure 2.13). From that data it was concluded that the transfection level was comparable for different mGluR2 variants. The DNA amounts used for transient transfection had only a minor influence on the cell surface expression and came only into effect at very low plasmid amounts.

The problem of the transfection efficiency has not seen much discussion in the literature. A comparison of different non-viral transfection reagents showed that FuGENE HD was suitable for a wide range of cell lines, even though Hek293 cells were not among them (210). Here, the transfection efficiency was studied only in terms of enzyme activity of luciferase which did not return any information about the percentage of transfected cells. The supplier of FuGENE HD, Promega, suggested in a recent electronic article on its website by Hook and Landreman (211) that FuGENE HD might very suitable for HeLa cells but not recommended for Hek293 cells. With this information future experiments might designed more rational.

3.1.2 Other GPCRs in Hek293 cells

The adrenergic and serotonin receptors investigated in this work were also expressed in Hek293 cells. As reviewed for the mGluR receptors in the previous section, these two receptor families were biochemically characterized in many cases using ectopic expression systems. For the adrenergic receptors, Saunders and Limbird (212) have reviewed several studies in COS-7, MDCKII and Hek293 cells among others. Comparison of different studies revealed that some effects were dependent on the cell type, including agonist triggered receptor internalization in CHO and Hek293 cells. However, even though Hek293 cells might not be the most common cell type used to study adrenergic receptors, several investigations, such as receptor S-palmitoylation or activation mechanism, have been partly conducted in this cell line (213-215). Many investigations on the function of adrenergic receptors were also performed in the insect cell line Sf9, including studies on ER targeting and pharmacological assays (25, 153, 215). Furthermore, the insect cells were also used for the investigation of S-palmitoylation of the serotonin receptors 5-HT-1A and -4A (176, 216). Later also mammalian cell lines were included, such as mouse N1E-115 neuroblastoma cells, to study receptor oligomerization, agonist response and raft localization (26, 217). Overall, as for the adrenergic receptors, Hek293 cells are one of several ectopic expression systems used for serotonin receptors (218).

The adrenergic and serotonin receptors were expressed from pCMV6 vector, which had been already used for the cloning of the mGluRs. In the thesis two different version of the Flag-tagged β2AR were used: one with a C-terminal Flag-tag which corresponded to the C-terminally Flag-tagged mGluR versions and one N-terminally Flag-tagged variant (Figure 2.4). The N-terminally tagged variant contained an artificial signal peptide in front of the Flag-tag which was not present in the wild type (compare UniProt P07550, (104)). For most experiments the C-terminally tagged version was used to detect only fully translated proteins. Just in one experiment the two variants were directly compared to evaluate if there were differences in the cellular photocrosslinking assay with [^{3}H]-photo-cholesterol (Figure 2.30). The C-terminally tagged variant was detected on the immunoblot as smear between 37-50 kDa and 75-100 kDa, suggesting the presence of different oligomeric states of the receptor (Figure 2.20). For the N-terminally tagged version the signal of the αFlag immunoblot was more distinct and only one broad signal between 37-50 kDa was clearly visible (Figure 2.30 A). In the input samples, only two bands were visible for the N-terminally tagged version while for the C-terminally tagged protein additional bands with lower apparent molecular

weight were detected. Thus, N-terminal tagging might have allowed for the detection of C-terminal degradation products. Indeed such an observation was made for an N- and C-terminally tagged human beta1-Adrenergic receptor (219). Here, C-terminal tagging allowed for the detection of various degradation products which originated from N-terminal degradation by metalloproteinase (219). [^{3}H]-photo-cholesterol labeling showed a similar patterns for the N- and C-Flag tagged variants: A presumably monomeric band around 45 kDa and a broad smear between 50 kDa and 75 kDa (Figure 2.30 A). Thus the different banding pattern visible on the immunoblot might simply result from different reactivity of the αFlag antibody due to the presence or absence of the terminal tags.

For the C-terminal Flag-tagged variant, various bands had been detected for the monomeric β2AR (Figure 2.30). An enzymatic deglycosylation experiment showed that the diffuse band pattern observed in the immunoblot was mainly due to different glycosylation stages (Figure 2.21). Both the digestion with EndoH and PNGaseF resulted in a shift of the smear into two bands: one at an apparent molecular weight of 40 kDa and one at 80 kDa. This EndoH sensitivity argued for poor modification with complex N-glycans. The cell surface biotinylation assay pointed into a similar direction, as relatively few receptors were found localized to the cell surface (Figure 2.20). Of the cell surface localized pool of the receptor only the slower migrating bands were visible. What was the reason for the observed pattern? The absence of a cleavable signal peptide might result in an inefficient translocation into the endoplasmic reticulum (ER). It was shown that ectopic expressed β2AR can be stabilized by introduction of an artificial signal peptide (153). Without artificial signal peptide the pattern for the β2AR looked similar for the monomer as in the current thesis (153). This is in contrast to the findings that only a long and/or rapid folded N-terminal ends as well as charged amino acid residues require the presence of a signal peptide (220, 221). This suggests that there are also other factors involved in efficient translational and trafficking eventually not present or insufficiently in ectopic expression systems, such as Hek293 cells (112).

The serotonin receptors used in the thesis, especially the 5-HT-1A variants, were detected only as weak αFlag signal on the immunoblot with only a small difference as compared to the vector control (Figure 2.20). When comparing 5-HT-1A-Flag and its two cysteine-to-alanine mutants, the mutants were detected with a slightly better signal on the immunoblot (176) (Figure 2.20, Figure 2.22). In contrast to the faint signals on the immunoblot for the 5-HT-1A-Flag variants, the autoradiography of the [^{3}H]-palmitic acid labeling clearly indicated a signal between 37 kDa and 75 kDa for the wild type and single mutant (Figure 2.22 A). The [^{3}H]

signal indicated a successful expression of the receptors which appeared to be difficult to detect by the C-terminal Flag epitope. Thus, most likely, it was not the low expression of this mouse protein in a human cell line but the immunodetection that resulted in a poor signal. The main reason for poor binding of the αFlag antibody was eventually partial refolding of the protein on the blot and subsequently difficult accessibility of the epitope. Also, the slightly better detection of the 5-HT-1A$^{C417A/C420A}$-Flag and 5-HT-1A^{C417A}-Flag indicated that the S-palmitoylation sites, situated in close proximity to the tag, might have shielded the Flag epitope. The initial observations for the other serotonin receptor, human 5-HT-2A, were similar (Figure 2.20, Figure 2.22 A). However, the later experiments with [^{3}H]-photo-cholesterol showed a better detection on the immunoblot (Figure 2.30). Here, the Flag tag in the C-terminal tail was separated by more than 70 amino acid residues from the designated S-palmitoylation site and not only by 9 residues as for 5-HT-1A. Nevertheless, the observations would argue for problems with the antibody binding at the C-terminal tail and for a longer linker region between tag and tail or a double Flag tag.

3.2 Post-translational modifications of GPCRs

As mentioned earlier, N-glycosylation, S-palmitoylation and disulfide bridges as post-translational modification of GPCRs contribute to the quality control of the receptors (116). In the current work, the presence of N-glycosylation and S-palmitoylation sites were probed experimentally, while the intramolecular disulfide bridges were not investigated. In addition to the intramolecular disulfide bridges, cystine bonds connect the two protomers of the mGluR homodimers covalently (132, 134, 203). For some experiments; the intermolecular disulfide bond in the mGluR2 homodimer was ruptured by exchange for alanine.

For the MD simulation only the transmembrane domain of mGluR2 was included in the setup. Thus, N-glycosylation sites and most of the disulfide bridges did not have to be considered as they are located in the extracellular domain (116). However, for the disulfide bridges, there was one exception: a cystine bond connected the second extracellular loop to the transmembrane helix III in the atomistic simulations based on the homology model which had been built earlier. The unstructured C-terminal end was truncated because according to the experimental data no S-palmitoyl modification had to be attached (Figure 2.22).

3.2.1 Disulfide bridges as source of stability and experimental artifacts

A conserved cystine bond in the structure of mGluRs is the bond that tethers the second extracellular loop to the transmembrane domain and thus restricts the access to the helix bundle (71). The tether was found both in family A and family C receptors (20, 71, 222). The presence – or the correct formation – of this intramolecular cystine bond was not explicitly checked in the experimental setups but was included in the simulation of the mGluR2 transmembrane domain (Section 4.13.2). For the atomistic simulations, the residue C721 (model: C159) in the second extracellular loop was connected with C632 (model: C70) in the transmembrane helix III. The connection in the mGluR2 model was estimated from the X-ray structures of the mGluR1 transmembrane domain (71, 91).

While the loss of the tether has not been investigated experimentally for mGluRs, the intramolecular disulfide bond that connects the mGluR homodimers has been studied intensively. It was found early on that the covalent connection is a hallmark of the mGluR family (96, 120, 203). Notably, the cysteine bridge between the protomers is of stabilizing nature but not mandatory for the formation of dimers (121). For that reason the cysteine residues C121 connecting the mGluR2 protomers were targeted by exchange to alanine, and the mutant named mGluR2^{C121A}. The idea was to enhance the effect of an eventual loss-of-lipid interaction in the alanine screening in the background of non-covalently linked dimers. Non-reducing SDS-PAGE confirmed the loss of the disulfide linking bridge in the mGluR2 homodimer. The relative abundance of the monomers after separation by SDS-PAGE increased from about around 5% for the wild type variants to 40-50% in the absence of the C121-C121 cystine bond (Figure 2.16). Similar experiments had been conducted for mGluR1 and mGluR5 respectively (132, 203). Notably, the absence of the disulfide bond was not sufficient to shift the mGluR2 dimer signal completely towards the monomer, which argues for strong non-covalent interactions in the dimer – both *in vivo* and in the sample preparation.

It was also found that mGluR2^{C121A}-Flag proteins were still expressed at the surface of Hek293 cells, as demonstrated in the cell surface biotinylation assay, and were still dimerizing *in vivo*, as seen in the cysteine crosslinking assay (Figure 2.12, Figure 2.15). However, in comparison to the Flag-tagged wild type the results were often not as stable – an observation which especially made for the Co-immunoprecipitation (Co-IP) assay. Here, the initial Co-IP experiments had shown that in the absence of the covalent bond the efficiency of the (Co-)IP was much more dependent on the experimental conditions (Figure 2.17). In the following Co-

IP of the C121A/W,Y→A double mutants it had not been possible to obtain reproducible results (data not shown). Here, the loss of the covalent linkage was a source of experimental variation. Also in the final [^{3}H]-photo-cholesterol labeling the experimental variation for the W→A or Y→A mutants on the background of mGluR2^{C121A} was higher compared to the single mutants (Figure 2.32, Figure 2.33). Despite that, the overall pattern of the labeling remained unchanged between the two sets of variants. Only mGluR2$^{C121A/Y745A}$-Flag dropped under the level of significance (Figure 2.33 C). From those findings was concluded that even in a presumably less stable dimer the absence of the disulfide bridge did not alter the binding of cholesterol to the transmembrane domain. Thus, the mGluR2^{C121A} variants were not a suitable tool in the current setup to generate a stronger phenotype in the cellular photo-crosslinking assay with bifunctional lipids.

Data from the literature indicate that despite the fact that the intermolecular cystine bond is found in all mGluR dimers, the receptor appears to be still functional in the absence of the covalent linkage: dimerization, surface expression and signaling take still place (96, 120, 121, 132, 135). So what then is the physiological relevance of this intermolecular disulfide bridge? For mGluR1α, for example, it was shown that the dimerized receptor in the absence of this intermolecular disulfide bridge had a lower affinity for the orthosteric agonist (223, 224). The intermolecular disulfide bond stabilizes the dimerization interface of the extracellular domain which also allows to control cooperativity and activation of the homodimers (120, 224). However, Ray and Hauschild (132) showed that the position of the disulfide bridge in the mGluR1 homodimer might be subject to small changes. This eventually has then also implication on the preferences for the formation of heterodimers with other mGluR family members. For the mGluR heterodimers it was shown that only certain pairings are functional (131).

The disulfide bridges contributes to the structure and function of mGluR proteins, but they can also be the source of experimental artifacts, such as higher oligomers (trimer, tetramer etc.), when separating the proteins by SDS-PAGE under reducing conditions (225) (for example see Figure 2.12). Here, the disulfide bridges initially opened by the reductive agent DTT, were most likely randomly formed from new during the sample treatment or separation which then resulted in distinct higher oligomers (225). Under non-reducing conditions, mostly monomer and dimer were visible and few higher oligomers in a smear indicated also random aggregation by presumably hydrophobic interaction in SDS micelles (Figure 2.16). However, all oligomers greater than the dimer are most likely artifacts which formed post-lysis during

sample preparation or SDS-PAGE. *In vivo* experiments have shown that the physiological active forms of mGluRs are dimers (reviewed by Pin and Bettler (122)). In this work, the random disulfide-induced oligomerization was partly suppressed by blocking free cysteine residues with *N*-ethylmaleimide *in vivo*, such as demonstrated by intramembranous crosslinking and the Co-IP experiments (Figure 2.15, Figure 2.19). But even here some formation of higher oligomers, caused probably by unblocked cysteines exposed during denaturation or by random hydrophobic interactions, was observed. Thus, artifacts in the SDS-PAGE can just be suppressed but not completely abolished.

3.2.2 N-glycosylation and surface arrival of GPCRs

N-glycosylation and the cell surface arrival of the Flag-tagged GPCRs were used as measure for the trafficking of the receptors through the secretory pathway. The assays showed that all mGluRs were modified with complex N-glycans and shuttled efficiently to the cell surface (Figure 2.20, Figure 2.21). In contrast to that, it appeared that the adrenergic receptors, especially β2AR, were transported less efficient to the cell surface. For the serotonin receptors 5-HT-1A from mouse and human 5-HT-2A quantification of trafficking and cell surface localization was hampered because of the poor immunodetection of the receptors (Section 3.1.2).

For the family C receptors mGluR1α, mGluR2 and mGluR4 there are four, five and five annotated N-glycosylation sites according to UniProt entries Q13255, Q14416 and Q14833, respectively (104). In the assay, these sites were largely resistant to EndoH after 48 h transient expression in He293 cells (Figure 2.21). Only the faster migrating band of the double bands proofed to be EndoH sensitive. This pattern was especially well-resolved for the monomer signals of mGluR1α and mGluR4, while for mGluR2 the signals were rather one smear than double bands. After enzymatic treatment with PNGaseF, the SDS-PAGE separated both the monomer and dimer signal of the mGluRs into a corresponding faster migrating band. The shift in the electrophoresis suggested that for all mGluRs several N-glycan modifications had been present but no definite conclusion can be drawn here. A mutation study performed in insect cells on Venus flytrap-only variants of the human mGluR3 suggested that not all predicted N-glycosylation sites are modified (118). This raises the question of the connection between surface expression and N-glycosylation status. The mGluRs had been shuttled to the cell surface at a rate of 30-50% (Figure 2.20). Only for mGluR1α the separation by SDS-PAGE had worked well enough to show that only the upper (complex N-glycan) band had

been pulled down with the surface biotinylation. This suggests that there is a correlation between modification with complex N-glycans – or resilience against EndoH – and cell surface arrival for mGluRs. In the literature, there has been not much work on N-glycoslyation in family C receptors, especially for the mGluRs. Inhibition of N-glycosylation by tunicamycin in CHO cells showed that the cell surface expression of human mGluR1α was not affected by its N-glycosylation status (117). This is contrasted by studies on the family C human extracellular Calcium sensing receptor (CaR) in Hek293 cells which showed that surface expression and agonist response was sensitive to disruption of N-glycosylation sites (165). Bai, Quinn (226) used the N-glycosylation status of CaR as read-out for the maturing of variants that carried physiologically relevant mutations at non-N-glycosylation sites. The enzymatic deglycosylation of the wild type resulted in a very similar pattern as observed for the mGluRs in the current experiments (226): the monomer signals were separated as double bands of which the faster migrating one was sensitive to EndoH, while both were shifted after PNGaseF treatment. Interestingly, CaRs with severe mutations, like calcium sensing mutant CaR^{R66C}, were only modified with mannose-rich N-glycans. From these experimental studies and the findings presented in the thesis it was reasoned that i) for family C receptors the N-glycosylation status is a relevant quality criteria for the maturing and shuttling of the receptors, and ii) the N-glycosylation pattern along with the cell surface biotinylation assay demonstrate a successful shuttling of the mGluRs through the secretory pathway.

For the mGluR2-Flag W→A and Y→A variants, both the enzymatic deglycosylation and the cell surface arrival assay showed that none of the point mutations introduced had a severe effect on trafficking of the receptors (Figure 2.13, Figure 2.14). Thus, the strategy to target only surface exposed aromatic amino acid side chain had proofed to be successful for the transmembrane domain (Section 2.1.2.2). A comparable trafficking of the mGluR2 variants was a prerequisite for the cellular studies on protein-lipid interactions.

Of the adrenergic receptor family, two receptors had been included in the study: Flag-tagged Alpha-2A adrenergic receptor (α-2AAR) and β2AR. Both showed a similar running pattern as the mGluR receptors: the proteins separated into monomeric and higher oligomeric forms upon separation by SDS-PAGE (Figure 2.21). This was probably due to unspecific hydrophobic interaction in SDS micelles during the sample preparation even though with urea an additional chaotropic substance had been included. Formation of oligomers due to formation of unspecific disulfide bonds, as suggested for the mGluRs, was probably less of a problem because the adrenergic receptors lack cysteine-rich regions (Section 3.2.1). However,

in the cell surface arrival assay, the signal for both receptors after affinity purification was surprisingly low (Figure 2.20). The low signal in the affinity purification might have been caused by technical issues: both receptors have only two lysine residues in their N-terminal domains, while mGluRs have approximately 30. Thus there are few residues available for the formation of amide bonds with the Sulfo-NHS-SS-biotin reagent (164) (Section 4.8). The sensitivity to EndoH is on the contrary a strong indicator for an altered trafficking through the secretory pathway (Figure 2.21). The digestion of α-2AAR with EndoH showed that, similar to the mGluRs, only a portion of the receptors was sensitive to the enzyme. This indicates that α-2AAR had shuttled successfully through the secretory pathway even though poorly detectable in the surface biotinylation assay (Figure 2.20). On the other side, the four signals for the presumably monomeric β2AR-Flag receptor were sensitive to EndoH treatment (Figure 2.21). Interesting here was also the appearance of four bands in the running pattern despite the fact that only two N-glycosylation sites have been reported for β2AR (173). Eventually we see a mix of unglycosylated β2AR, receptor modified with one or two mannose-rich N-glycans and finally proteins with two more complex N-glycans still sensitive to EndoH (169). Apart from the N-glycans, the S-palmitoyl modification at the C-terminal end might also explain the fifth band running at the lowest apparent molecular weight (Figure 2.21); the signal might neither carry the S-fatty acylation, nor the N-glycan modification. Taken together, the expression system worked well for α-2AAR, but for the Flag-tagged β2AR receptor Hek293 cells might not have been optimal cell line (Section 3.1.2). Introduction of an artificial signal peptide in combination with a C-terminal Flag-tag might be the optimal combination for ectopic expression of β2AR.

For the Serotonin receptors, the poor immunodetection hampered a reliable quantification of the cell surface arrival (Figure 2.20 and Section 3.1.2). Subsequently the deglycosylation assay for the receptors was not carried out.

3.2.3 S-palmitoylation

S-palmitoylation of mGluRs was investigated for the set of mGluRs and the adrenergic and serotonin receptors containing predicted or described palmitoylation sites and their respective non-palmitoylated C→A mutants. In the [^{3}H]-palmitate labeling, all annotated S-fatty acylation sites were confirmed for the family A GPCRs. Among the mGluR candidates tested, palmitoylation was found only for mGluR1α (Figure 2.22).

S-palmitoylation can have different implications on the 'life' of a GPCR. For some GPCRs, like the adrenergic and serotonin receptors used as positive controls in this work, the S-palmitoylation has 'only' regulatory function. This had the advantage that, despite the loss of the S-fatty acylation site in the C-terminal tail, the respective C→A variants were not expected to have trafficking defects. Both adrenergic receptors had one S-palmitoylation site. α-2AAR contains a S-palmitoylation site at position C442 which seems to have a role in internalization after long-term agonist exposure (227). For β2AR residue C341 in the C-terminal tail has been identified as S-palmitoylation site (76). Here the S-palmitoylation site has been associated with the activation-dependent phosphorylation and desensitization (25, 157). For the serotonin receptors, only the function in mouse 5-HT-1A has been thoroughly assessed. The receptor has two established S-palmitoylation sites at positions C417 and C420, associated with $G\alpha_i$ protein coupling and raft association (26, 216). For 5-HT-2A the homologues site in mouse, C397, was annotated with unknown function (155). In Hek293 cells, all four receptors but not the variants $\beta2AR^{C341A}$ and 5-HT-$1A^{C417A/C420A}$ showed a positive labeling with [^{3}H]-palmitic acid (Figure 2.22). This indicated that the chosen labeling time had been long enough to allow for incorporation of [^{3}H]-palmitic acid into the GPCRs while at the same time avoiding artifacts because of metabolic incorporation of radioactivity into amino acid or other molecules (76). It also confirmed the transient nature of S-fatty acylation and the suitability of Hek293 cells to test S-palmitoyltransferase activity on GPCRs (23, 27). Moreover, the results demonstrated that C-terminal tagging did not have an influence on the S-palmitoyltransferase activity.

For the serotonin receptors, the labeling experiments verified the S-palmitoylation of human 5-HT-2A in an ectopic expression context. The receptor was also successfully depalmitoylated by treatment of samples with beta-mercapoethanol which confirmed the nature of the bond (Figure 2.23). The [^{3}H]-palmitic acid signal for 5-HT-2A was rather weak which might indicate a low expression of the corresponding S-palmitoyltransferase(s) and/or a lower turn-over of the modification as compared for example to 5-HT-1A (23, 176) (Figure 2.22). Among the three mGluR candidates, mGluR2 showed a negative result in the labeling. For the protein, no palmitoylation sites has been experimentally identified or predicted so far. In contrast to a previous publication, also no modification of mGluR4 was detected (125). mGluR1α was the only member of tested mGluRs to be palmitoylated under the chosen experimental conditions, however, it was efficiently depalmitoylated with beta-mercapoethanol only in one out of three experiments, which might have been due to technical

problems (Figure 2.24 and Section 2.4). Thus, it cannot be excluded that the labeling was false positive for S-palmitoylation and instead represented another post-translational modification. N-myristoylation, occurring at the cytoplasmic side of membranes, affects the N-terminal end which for mGluR1α is extracellular (228). Isoprenylation occurs at the C-terminal end of proteins, but mGluR1α is not described to contain a CaaX box (38). Hence, if the S-palmitoylation signal for mGluR1α was false positive this more likely represented a non-lipid modification. In addition, only the mGluR1α dimer was clearly labeled with [^{3}H]-palmitic acid, a phenomenon that has also been observed for other receptors, such as the beta1-adrenergic receptor (214). For mGluR1α, the missing labeling of the monomer might have been due to technical reasons, since in the digital autoradiography a strong background was observed in the range of the monomer and thus requires further investigation (Figure 2.22 A+B). Palmitoylation was not described for mGluR1α in a study focusing on mGluR4 in baby hamster kidney cells, however, in this case overall labeling efficiencies and resolution were rather low (125). Later on, also a different group reported a negative result for mGluR1α in a [^{3}H]-palmitic acid labeling performed in insect Sf9 cells (229). For long, the topic of mGluR S-palmitoylation remained untouched until availability of enhanced proteomic approaches (116). A recent publication using acyl-biotin exchange to monitor S-palmitoylation in mouse forebrain samples suggested two modification sites in mGluR1 (155). With C565 and C578 two residues close to the extracellular cysteine-rich linker region were identified raising doubts about the specificity of the measured signal as no such extracellular S-palmitoylation sites have been described for GPCRs so far.

Thus, the current experiments can confirm the S-palmitoylation of (human) 5-HT-2A identified in the screening by Collins, Woodley (155) but do not allow for a definite conclusion on mGluR1α. To address this question, further experiments will have to be performed, including for example C-terminal truncation and mutation to localize the site of modification.

3.3 Dimerization of mGluR2 and its alanine mutants

Oligomerization of GPCRs is a general phenomenon among GPCRs and has been extensively studied, in particular for family C receptors (122). mGluRs can form homo- and heterodimers, which then trigger miscellaneous intracellular responses (reviewed by Borroto-Escuela, Tarakanov (230)). In this work a focus is set on the ‘heterodimerization’ of the mGluR2-Flag receptor and the selected mGluR2 W→A or Y→A variants. No defects in the pairing of

mGluR2-Flag and its mutants were observed in Co-IP experiments. Moreover, a disulfide crosslinking experiment on the intramembranous dimerization interface of mGluR2, analogous to what had been described previously, was performed (121). The experiment suggested the existence of an intramembranous dimerization interface for mGluR2 between transmembrane helices IV, V and VI in addition to the interfaces described for the extracellular domain.

3.3.1 The intramembranous dimerization interface of mGluR2

The dimerization for mGluRs is best understood at the level of the Venus flytrap domain. Here biochemical and structural evidence have shown the existence of a dimerization interface stabilized by a intermolecular disulfide bridge (96, 132, 135, 203). In addition to that the group of Jean-Philippe Pin also reported a potential dimerization interface within the cysteine-rich linker as well as in the transmembrane domain of mGluR2 (120, 121). Notably, the later dimerization interfaces were established by cysteine-crosslinking experiments.

The membrane dimerization interface for mGluR2 was reported for the transmembrane helices IV, V and VI in a cysteine-crosslinking assay, which was in contrast to the earlier published crystal structure of a mGluR1 homodimer which showed an interface between transmembrane helices I (71, 121). The mGluR1 interface was described in a transmembrane domain-only construct stabilized with a soluble cytochrome b562 domain. For that reason it was speculated that it was a crystallization artifact (121). When the ectopic cysteine residues were introduced on the background of MycFlag-tagged mGluR2^{C121A} variants for this work, intermolecular crosslinking between the protomers was indeed observed (121) (Figure 2.15). Upon receptor activation a shift of the interface from helix IV and V to VI was described in the literature (121). If the dimerization interface in the current expression system is dependent on receptor activity as suggested still remains to be addressed. Notably, no model for the movement of the complete mGluR2 receptor upon activation exists but there are predictions based on the experiments with single domains (120, 121). In the future, single-particle electron microscopy studies, as done for the human insulin receptor, might reveal how all domains simultaneously change their interfaces upon receptor activation (231). For the insulin receptor, it was shown that upon activation by insulin the transmembrane domains got in closer proximity. In the case of mGluRs, such studies would eventually help to resolve the contradicting biochemical and structural findings on the dimerization interface (71, 121). For

the current project, it will be also of interest to investigate if intramembranous dimerization interface is influenced by the alanine exchange.

The 5-HT-2A receptor was shown to interact with the transmembrane helix IV of mGluR2, which is one of the helices suggested to be involved in mGluR2 homodimerization (121, 154, 232). It was also shown that the extracellular domain of mGluR2 was not involved in the interaction with 5-HT-2A, which would have been also remarkable as serotonin receptors in general display a comparably small extracellular domain – in the case of 5-HT-2A ~75 amino acids (154). Thus, there would be at least partly a competition for the transmembrane dimerization interface between the heteroreceptor mGluR2-5HT2A and the mGluR2 homodimer. The question if such competition takes place or the receptors form a trimeric complex has not been addressed yet. Only for mGluR heterodimers it has been demonstrated that when expressed in the same cell, the mGluRs indeed start to compete for dimerization interfaces (131).

3.3.2 Heterodimerization between mGluR2 wild type and its mutants

The aim of the Co-IP assay was to characterize the heterodimerization between the mGluR2-Flag and the W→A or Y→A variants. The question was if the alanine exchange would prevent the dimerization between the variants and the wild type. For the Co-IP assay, the same Flag-tagged constructs were used which had been previously used in the characterization of the trafficking. The conditions for the Co-IP were adjusted as suggested by Milligan and Bouvier (171) (Section 2.2.2.3).

The initial experiment showed that Flag-tagged mGluR2 dimers linked by a disulfide bridge were tolerable to different lysis and Co-IP conditions (Figure 2.17). In contrast to that, $mGluR2^{C121A}$ homodimer was sensitive to the presence of ionic detergents, such as sodium-deoxycholate and sodium-dodecylsulfate (SDS) (Figure 2.17). This was not surprising as the $mGluR2^{C121A}$ homodimer was only stabilized by non-covalent interactions. The ionic detergents most likely disturbed the intramembranous as well as the extracellular dimerization interface and ruptured ionic and in concert with Triton X-100 also hydrophobic interactions. On the contrary, the covalent disulfide bridge between in the wild type dimer prevented the detergent-mediated dissociation seen for $mGluR2^{C121A}$. Thus, the presence of the intermolecular disulfide bond in the homodimer would not allow discriminating between different assay conditions. From this observation was concluded that $mGluR2^{C121A}$ is a more suitable tool to establish a robust Co-IP assay.

For the dimerization studies conditions were chosen resulting in complete solubilization of receptors. In addition, *N*-ethylmaleimide treatment was used to block free cysteine residues along with high salt conditions for washing in order to minimize assay artifacts caused by unspecific covalent and non-covalent interactions (171) (Figure 2.18). With this stringent assay conditions, the results indicated that even subtle changes at the dimerization interface can lead to impaired receptor dimerization: the pull-down of mGluR2-Myc with mGluR2^{C121A}-Flag as bait resulted in a poor recovery of the prey protein (Figure 2.18). Unfortunately, no study mGluR dimerization has reported on the affinity of between receptors with and without a specific mutation site. In a study on the dimerization of mGluR1α the exchange of amino acid residues for cysteine in close proximity to the 'original' C140 residues was described (132). The results suggested that the position of the cysteine residue for the intermolecular disulfide bond was somewhat flexible, but it was not investigated if the mutants would still pair with the wild type. Also non-cysteine amino acid residues in the mGluR2 Venus flytrap dimerization interface can perturb the formation of homodimers, as shown in *in vitro* experiments in Xenopus oocytes (224). Taken together, disulfide bridge formation between cysteines in mGluRs' extracellular domain is to some extent flexible concerning the positioning in homo- and heterodimers. However, also other perturbations at the dimerization interface can lead to a reduction in dimerization.

Based on the assumption, that also small changes at the dimerization interface can interfere with formation of mGluR dimers, the different Myc-tagged W→A or Y→A variants of mGluR2 and mGluR2^{C121A} were probed for dimerization with the Flag-tagged wild type or C121A mutant, respectively. For the mGluR2-Myc variants, no significant perturbation of dimerization with the wild type was observed (Figure 2.19). In the absence of the disulfide bond in double mutants on the background of a C121A mutation the receptors would still dimerize but no stable results were obtained for the recovery of the Myc-tagged preys (data not shown). From these results was concluded that the W/Y→A point mutations in the transmembrane domain did not cause major receptor dimerization defects but it cannot exclude the possibility that the intramembranous dimerization interface was disturbed.

3.4 Non-covalent protein-lipid interaction *in vivo* and *in silico*

For the non-covalent protein-lipid interactions of mGluR2 both sphingolipids and cholesterol interactions were probed in an alanine screening of the mGluR2 transmembrane domain. Cellular photo crosslinking assays showed that in two mGluR2-Flag Y→A variants cholesterol binding was significantly reduced. Subsequently performed MD simulations of the transmembrane domains of the wild type and the two Y→A variants mGluR2^{Y745A} and mGluR2^{Y781A} confirmed the reduction of cholesterol binding. In contrast to that, [^{3}H]-photo-sphingosine ([^{3}H]-photoSph) labeling of mGluR2 wild type and variants showed rather weak interactions. Here, two other mGluR2 variants displayed even an increased efficiency in the [^{3}H]-photoSph labeling, not the expected reduction.

3.4.1 Sphingolipid interaction with the mGluR2 receptor *in vivo*

The bioinformatics screening for new protein-sphingolipid interaction sites with a p24-like *N*-VX_2-TL-X_2IY-*C* sphingolipid binding motif uncovered several GPCRs with three mGluRs among them (68). In mGluR2, 7 and 8, the motif was found in helix VI of the transmembrane domain suggesting a functional link between sphingolipid interaction and activation of the receptors (68, 90, 233). In this work, one residue of the identified *N*-TX_2-TT-X_2IW-*C* motif in mGluR2 was tackled by changing the tryptophan residue W773 to alanine. This amino acid exchange should have disrupted the interaction between sphingomyelins' choline moiety and the motif in mGluR2 (65). However, the [^{3}H]-photoSph labeling of transiently expressed Flag-tagged mGluR2^{W773A} proteins indicated that the sphingolipid interaction with the protein had even slightly increased (Figure 2.28). For mGluR2^{W697A} and mGluR2^{Y734A} – located in transmembrane helices IV and V – sphingolipid photocrosslinking was significantly increased.

The finding that – in contrast to the experiments with p24 – single amino acid exchanges within the sphingolipid interaction motif did not result in a loss of sphingolipid binding, can be for several reasons (65). First, sphingolipid binding to α-helical domains of a given protein depends on several amino acid residues or, as for theV3 loop-like sphingolipid binding domain (SBD), also on structural determinants (64, 65). In a MD simulation, it was found that the affinity of ganglioside GM1 to 5-HT-1A might dependent on V3 loop-like structures in

the receptor (63). Here, it was suggested that the binding of the sphingolipid was dependent on the extracellular loops of 5-HT-1A. Such determinants have not been investigated in the current project, but structural motifs would be difficult to intercept with point mutations. It should be noted that especially in the atomistic simulations of the mGluR2 transmembrane domain the loops were found to be flexible (Figure 2.40). If that flexibility would rather support or hamper interaction with the glycan moiety of gangliosides remains to be addressed. Second, some of the amino acids of the putative sphingolipid binding motif, like T769, were according to the mGluR2 transmembrane model buried inside the helix bundle, and thus, might not be accessible for sphingolipid binding (Figure 2.8). The linear sphingolipid interaction motif found in p24 might be difficult to project on a more complex heptahelical structure, as seen for the differences between the linear CRAC/CARC motifs and the three-dimensional CCM (45). Third, changes in the receptor structure caused by the point mutations, be it by conformational changes of the transmembrane domain or by local gaps on the surface of the protein, could influence sphingolipid binding within the transmembrane domain. Like that, mutation sites like W697A or Y734A might have been the source of ectopic sphingolipid interaction sites. In summary, the motifs obtained from the bioinformatic screening may need further refinement by determining for example if the C-terminal tyrosine residue within the p24 interaction motif is indeed interchangeable with any other aromatic amino acid (68).

An effect that was not considered in this work was the interaction of sphingolipids, or more precisely gangliosides, with the receptor by interaction with basic lysine residues. Such interactions have been shown for the human epidermal growth factor receptor (EGFR) and the human insulin receptor (234, 235). Whether lysine residues might be also contributing to glycosphingolipid binding of GPCRs represents an interesting subject for future research, especially since basic residues can also be found in cholesterol interaction motifs (54).

3.4.2 Cellular and *in silico* interaction of the mGluR2 receptor with cholesterol

[^{3}H]-photo-cholesterol labeling in Hek293 cells showed a significant decreased cholesterol interaction of the Flag-tagged variants mGluR2^{Y745A} and mGluR2^{Y781A} as compared to wild type, while on the background of a mGluR2^{C121A} mutation this was the case only for mGluR2$^{C121A/Y781A}$ (Figure 2.32, Figure 2.33). Preceding experiments demonstrated that the labeling efficiency was independent on the cellular expression level of the mGluR2 variants

(Figure 2.31). Moreover, cellular trafficking and cell surface arrival did not differ significantly between Flag-tagged W/Y→A variants and wild type so that all mGluR2 variants should be found a similar membrane environment (Figure 2.14, Figure 2.13). Taken together, the experimental data suggested a loss of cholesterol binding due to the amino acid exchange at the respective sites. To get further insight into the molecular interactions contributing to cholesterol binding to the transmembrane domain of mGluR2 MD simulations were performed. Atomistic simulations showed that the transmembrane domains had well-defined regions with cholesterol density near transmembrane helices V and VI in proximity to the Y→A mutation sites Y745A and Y781A, supporting the results obtained with the cellular assay (Figure 2.41). These regions are very likely to correspond to single cholesterol molecules, which remained most of the time bound to the protein at those helices. Thus, our simulations suggest the possibility of specific cholesterol interaction sites around helices V and VI. *In silico* mutations and coarse-grained simulations also support this hypothesis by displaying a distorted density for the earlier and similar cholesterol density for the latter set of controls (Figure 2.42, Figure 2.43). The simulations also showed cholesterol density near other helices of mGluR2, for example around the cleft between helices I and IV on the cytoplasmic side of transmembrane domain (Figure 2.41). The density in this cleft appeared to be less specific then the one around the mutation sites introduced into the helices V and VI. Here, the coarse-grained simulations did not show any specific binding around the same area (Figure 2.43). For the other parts, such the binding site around helices I and VII, the density was more spread out, thus implying unspecific interaction at those places (Figure 2.41, Figure 2.43).

A well-described cholesterol binding site in GPCRs is the cholesterol consensus motif (CCM, [4.39-4.43(R,K)]-[4.50(W,Y)]-[4.46(I,V,L)]-[2.41(F,Y)]) present between helices I and IV of the β2AR transmembrane domain (see for example Figure 1.2) (20, 45, 236). In the X-ray structures 3D4S and 3NY8 of β2AR, the CCM on the intracellular side between helices I and IV was occupied by identically positioned cholesterol molecules: the first cholesterol molecule interacted with the CCM via its 'rough' β surface while contact to the second cholesterol molecule in the cleft was established via the 'smooth' α side (45, 236). In contrast to that, in the 2RH1 X-ray structure cholesterol packed against the CCM with its α side (20). The CCM was later confirmed in MD simulations of this other protein embedded in a DOPC (1,2-dioleoyl-sn-glycero-3-phosphocholine) bilayer with different cholesterol concentrations (47). In the current MD simulations of the mGluR2 transmembrane domain, the cleft between

transmembrane helices I and IV was occupied by cholesterol on the intracellular side, as well (Figure 2.41). From the density map it could not be concluded if the cholesterol was bound with its 'rough' β surface, as suggested for the CCM, or with its 'smooth' α side (45).The density map only indicated that cholesterol seemed to be more aligned to transmembrane helix II than IV. In these helices, the residues of the CCM are not present (UniProt Q14416) (14). For example, the tryptophan residue at position $W^{4.50}$ of β2AR conserved in family A GPCRs is not present at the corresponding position in family C receptors (14, 16). Of all residues of the CCM, only isoleucine $I^{4.46}$ is conserved in transmembrane helix IV of mGluR2 as I682 (Figure 2.41). Even though the cleft between helices I and IV was also occupied by cholesterol in the MD simulation of mGluR2, the experimental alanine screening had not shown any loss of binding here (Figure 2.32). The mutation site $mGluR2^{Y607A}$, positioned at the cytosolic end of helix II, had remained without effect in the [^{3}H]-photo-cholesterol labeling. Thus if a CCM-like motif is present in family C the sequence is different, or as for the V3 loop-like sphingolipid binding domain, eventually more of a three-dimensional than a linear motif. Because the motif might be structurally imprinted, it might also be more difficult to disturb the motif by an exchange of single amino acids. It is also remarkable that the conserved CCM in family A receptors was not always occupied by cholesterol. For example, the human A_{2A} adenosine receptor possesses a CCM positioned at the same spot as β2AR but none of the three cholesterol molecules co-crystallized with the adenosine receptor occupied the site in the crystal structure (45, 237). Many serotonin receptors are supposed to have a conserved CCM – the 5-HT-2A receptor is one of them (45). The homologue 5-HT-2B was co-crystallized with cholesterol bound to transmembrane helix I and an α-helical region in the C-terminal tail while no cholesterol was found at its CCM (238). From the different examples it can be concluded that either the experimental setup inferred with the detection of the CCM or that the nature of the cholesterol binding sites in GPCRs has not been completely understood. Eventually, the CCM in β2AR just 'by accident' correlated with a set of conserved residues and was rather part of a structural then a sequential motif.

In case of mGluR2, there was another distinct cholesterol binding spots observed in the simulation that clustered around helix V and VI (Figure 2.41). The sites coincident with the two amino acid residues Y745 and Y781 in helix V and helix VI that were identified in the alanine screening and subsequent cholesterol labeling of the Flag-tagged mGluR2 variants (Figure 2.32). The mutation site Y745A one coincided with the CRAC motif *N*-L741-X_3-Y745-X_2-K748-*C* at the cytoplasmic end of transmembrane helix V (56, 59). The density here

was not as pronounced as at the extracellular end of transmembrane helix VI, but appeared as distinct spot. Upon mutation to alanine the cholesterol density at around Y745A disappeared (Figure 2.42). Interestingly, a CRAC motif in transmembrane helix V was also described in other mGluRs (56). For mGluR1, alanine exchange at single site within the CRAC motif showed that only the wild type receptor, but not the point mutants, shifted into detergent resistant membranes upon activation (56). The surface arrival of the point mutants was not affected –as also observed for mGluR2^{Y745A} (Figure 2.13). In further tests the authors found that the mGluR1 CRAC mutants retained their basal activity but were not efficiently activated by the agonist. Thus, subtle changes at cholesterol interaction sites can have a strong influence on the receptor. The finding are in line with the data obtained for the mGluR2 receptor in insect Sf9 cells, which showed that association with cholesterol was correlated with activation of the receptor (55). On the side of structural biology, less is known about putative cholesterol binding sites. In the X-ray structure of mGluR1 transmembrane domain, no cholesterol density was found at the CRAC motif. Only in the crystal structure 4NTJ of the Purinergic receptors cholesterol was bound to a similar position as found in the current simulations and in the biochemical experiments on mGluR1, but no CRAC motif was involved here (56, 57, 239) (Figure 2.32, Figure 2.42).

Interestingly, loss of cholesterol binding at helix V was also seen for the other mutation site Y781A despite being located at the extracellular site of helix VI (Figure 2.42). In the MD simulations, the density around helix VI got smaller and changed its shape for the Y781A mutant, while also other cholesterol interaction sites lost density. An increased flexibility of the transmembrane domain around helix VI, induced by the mutations itself or loss of cholesterol binding, may be responsible for the alterations of the density at other sites on the protein surface (Figure 2.39). Here further analysis of the simulations is needed to find out about a possible connection between cholesterol binding and conformational changes in mGluR2. However, helix VI is thought to be involved in the activation of GPCRs and contains conserved motifs, that keep the receptors in their basal state (71, 90, 233). Studies on β2AR have provided insight into a potential mechanism of activation control by cholesterol binding to helix VI. In the MD simulations of β2AR, cholesterol binding both around transmembrane helices V and VI on the intracellular and extracellular side was reported (47). The interaction of cholesterol with β2AR *in silico* suggested a mechanism in which cholesterol restricts the conformational flexibility of the receptor. This supported by experimental findings that cholesterol thermostabilized β2AR *in vitro* (45). By binding to the

transmembrane helix VI, the conformational change towards the active state by tilting the helix was probably restricted (47). At the same time, the active conformation was stabilized by cholesterol which acted as 'spacer' between helices V and VI and thus prevented spontaneous relapse into the inactive conformation (47). These *in silico* observations might explain the contradicting findings that on the one hand cholesterol bound specifically to β2AR, while at the same time cholesterol depletion activated β2AR mediated cellular signaling (45, 51). In addition to the findings for β2AR, also other experimental data have shown specific interaction between cholesterol and transmembrane helix VI of GPCRs. In the crystal structure for the human A_{2A} adenosine receptor two cholesterols packed sideward against the exoplasmic end of helix VI at the interfaces with helices V and VII (237). Likewise a cholesterol density was shown in the structural model next to transmembrane helix VI in the outer leaflet for the μ-opioid receptor structure 4DKL (240). In both cases, aromatic amino acid residues –tyrosine and phenylalanine – were involved in the binding of cholesterol molecules at the respective sites, but also β-branched residues, leucine and the protein backbone (57). A sequence alignment with clustalo between the helix VI of mGluR2, A_{2A} adenosine receptor, μ-opioid receptor, and β2AR as annotated in UniProt showed only an identity of 3.6% between the receptors for that region. Only the central tryptophan residue $W^{6.50}$ (for mGluR2 W773) was conserved but apparently not decisively involved in cholesterol binding: Both for the A_{2A} adenosine receptor and μ-opioid receptor the residue pointed into the helix bundle (237, 240). The poor sequence conservation suggests that besides the linear amino acid sequence additional parameters contribute to cholesterol binding (57). Nevertheless, the cholesterol binding at these sites seems to depend also on specific interaction with aromatic amino acid residues, as observed in the different crystal structures and here in this work for the [^{3}H]-photo-cholesterol labeling of the mGluR2 variants and the corresponding MD simulations.

In addition to the specific cholesterol interaction sites, a broad cholesterol density was observed around transmembrane I and VII. The density was especially pronounced in the atomistic simulations but also in the coarse-grained system (Figure 2.41, Figure 2.43). The density was observed at a position where also in the published crystal structure of mGluR1 4OR2 cholesterol mediated homodimerization (71). Notably, the authors of the mGluR1 crystal structure study did not claim a specific binding site. In the crystal structure, the cholesterol molecules packed against the transmembrane helices I and II on the extracellular side whereas in the atomistic simulation of mGluR2 cholesterol density was spread out on the

intra- and the extracellular side (Figure 2.41). Also in the coarse-grained simulations the cholesterol density was spread out around helices I and VII with no major differences in the cholesterol binding was between dimer and monomer (Figure 2.43). For the particular site around helix I, another group has simulated the interaction of cholesterol and mGluR1 at the homodimer interface (241). It was suggested that cholesterol was held in place by van-der-Waals and hydrogen bonding, contacting the residue W588 at the upper end of helix I. The respective mutation in mGluR2^{W567A} did not show altered cholesterol binding when investigated using the cellular photocrosslinking approach with [^{3}H]-photo-cholesterol (Figure 2.32). From these observations was reasoned that the density around transmembrane helices I and VII was unspecific but eventually not strictly dependent on receptor dimerization. However, the possibilities of 'cholesterol cavities' at the transmembrane dimerization interface, which were observed in MD simulation of the chemokine receptor type 4, cannot be excluded (89). Including the extracellular domain of mGluR2 in future simulations might help to narrow down the physiological dimer interface, which is most likely affected in its positioning of the extracellular domains (121).

Two more GPCRs were labeled with [^{3}H]-photo-cholesterol: the β2AR and the 5-HT-2A receptor (Figure 2.30). As discussed before, trafficking of the two GPCRs could not be studied in detail due to technical problems, precluding a comparison with the mGluR2 protein (Figure 2.20, Figure 2.21). However, looking at each receptor separately it is remarkable that especially β2AR labeled very well both with cholesterol as well as with sphingolipids (Figure 2.28, Figure 2.30). Despite the fact that β2AR has specific cholesterol interaction sites, it was usually assumed that the receptor in its basal state resides in disordered membrane phase (51). However, the problems with the trafficking recognized in the enzymatic deglycosylation assay as well as in the cell surface biotinylation caution to make any general conclusion here. To further investigate the intracellular localization and lipid binding of β2AR and variants, steady state localizations of the receptors and additional lipid labeling, targeting also glycerolipids, will have to be performed in future experiments. Nevertheless, the β2AR was found to be a reliable positive control for both [^{3}H]-photoSph and [^{3}H]-photo-cholesterol labelings experiments and in so far had fulfilled its purpose. On the other side, 5-HT-2A labeled rather weak with [^{3}H]-photo-cholesterol (Figure 2.30). The weak labeling is remarkable for two reasons. First, the receptor is supposed to interact with mGluR2 (232). Thus, the receptors should share a similar membrane environment, but mGluR2 showed a stronger affinity to cholesterol in the current setup (Figure 2.30). Second, the S-palmitoylation

found also in 5-HT-2A is for other 5-HT-Rs, like 5-HT-1A, associated with raft localization (26). At least in the basal state, the photo-induced labeling suggested no strong association with cholesterol-rich membrane phase for 5-HT-2A. Moreover, a CCM is predicted for 5-HT-1A even though that is no measure for the overall affinity for cholesterol (45). Unfortunately, the literature on 5-HT-2A is not as comprehensive as for 5-HT-1A, for example, and also no X-ray structure has been resolved, yet (242). Nevertheless, the labeling showed that interaction with [^{3}H]-photo-cholesterol is not an intrinsic property of all GPCRs tested in the given experimental setup, which again argues for a specificity of the other observations. In this way, 5-HT-2A might also make a better negative control in the photo-induced labeling experiments than ASGPR I, which has been used regularly in the past for experiments on p24 but is as single-spanning protein a rather unsuitable control in labelings with the hepathelical GPCRs (65, 68).

3.5 Conclusion

In the current work, the membrane environment of the GPCR mGluR2 was probed focusing on a potential sphingolipids or cholesterol interaction site. Based on the assumption that specific non-covalent interaction sites for sphingolipids and cholesterol contain aromatic amino acid residues, tryptophan and tyrosine residues in the transmembrane domain were targeted in an alanine screening (45, 53, 64, 65) (Section 2.1.2.2). By means of enzymatic deglycosylation and cell surface biotinylation assays, it was shown that W→A or Y→A amino acid residue exchanges in the mGluR2-Flag transmembrane domain did not significantly affect trafficking of the receptors (Figure 2.13, Figure 2.14). Also, the point mutations were not sufficient to disturb the dimerization between mGluR2-Flag and the corresponding alanine mutants (Figure 2.19). [^{3}H]-photo-sphingosine labeling showed that mGluR2 had only a limited affinity to sphingolipids, while for [^{3}H]-photo-cholesterol a stronger binding was observed (Figure 2.27, Figure 2.31). As compared to wild type mGluR2, an increase was seen for some variants in the [^{3}H]-photo-sphingosine labeling which was surprising as the W→A and Y→A variants had been designed to disturb the putative p24-like sphingolipid binding motif (68) (Figure 2.28). The results could not be readily explained by the existing data. In contrast to that, for two Y→A variants the [^{3}H]-photo-cholesterol labeling was significantly decreased (Figure 2.32). The mutation sites Y745A and Y781A are located at the intra- and extracellular site of transmembrane helices V and VI, respectively. To find out about the molecular mechanism of cholesterol interaction, the transmembrane domain

of mGluR2 was investigated in an atomistic MD simulation in a fully solvated POPC bilayer with 15mol% cholesterol. Several cholesterol interaction sites were mapped on the surface of the mGluR2 transmembrane domain (Figure 2.41). The most distinct spots were found in helices V and VI next to the residues Y745 and Y781. In helix V, Y745A is part of a CRAC motif which is conserved in the whole mGluR family (56). Helix VI has been associated with the activation of GPCR (90, 233). One more site was in the cleft between helix I and IV, at the position of the CCM which had been identified in β2AR (45). Even though the site was occupied by cholesterol, the residues of the CCM were not conserved at the particular positions in helices II and IV. Apart from that spread out cholesterol density was seen around helices I and VII, probably driven by unspecific van-der-Waals forces and hydrogen bonds (241). In the same setup, also the two mutant transmembrane domain mGluR2^{Y745A} and mGluR2^{Y781A} were simulated. Here, the cholesterol density was decreased and blurred out at the adjacent mutation sites but also at other cholesterol interaction sites in the protein (Figure 2.42). The results of the simulation suggested that the loss of the specific interaction sites by alanine exchange at one site may also have influence on cholesterol binding at other spots of the mGluR2 transmembrane domain. Here, it will be highly interesting to further investigate a possible connection between cholesterol interaction and conformational changes of the receptor.

For the future, a detailed investigation on the effects of pharmacological substances on lipid binding will help to further understand roles of lipids in modulating receptor activities. Also the effects S-palmitoylation on mGluRs should be further investigated: While mGluR2 and mGluR4 were negative in the [^{3}H]-palmitic acid labelings, a signal was measured for mGluR1α. Even though the nature of the modification could not be confirmed with certainty, a more detailed investigation may open a new perspective on lipid modifications in mGluRs here.

4 Materials and Methods

4.1 Chemicals and consumables

4.1.1 List of chemicals

The following table contains the list of chemicals which had been necessary to conduct the experimental work described in the following chapter (Table 4.1). All chemicals were stored according to manufacturers' instructions.

Table 4.1 | List of chemicals. The chemicals were sorted according to the name. The CAS registry numbers were assigned according to the labels of the manufacturers.

Name	CAS Registry Number	Manufacturer	Purity/ Concentration	Storage
1,4-Dithio-D,L-threitol	3483-12-3	Gerbu, Heidelberg, Germany	≥99%	4°C
2-Amino-2-(hydroxymethyl)propane-1,3-diol	77-86-1	Roth, Karsruhe, Germany	≥99.9%	RT
2-Mercaptoethanol	60-24-2	MerckMillipore, Darmstadt, Germany	≥99.0%	4°C
4-Morpholinepropanesulfonic acid	1132-61-2	Serva, Heidelberg, Germany	n.A.	RT
Acetic acid	64-19-7	MerckMillipore, Darmstadt, Germany	≥99.8%	RT
Ampicillin sodium salt	69-52-3	SigmaAldrich, Munich, Germany	n.A.	4°C
Bromophenol blue	115-39-9	Waldeck, Muenster, Germany	n.A.	RT
Calcium chloride dihydrate	10035-04-8	SigmaAldrich, Munich, Germany	≥99%	RT
Dichloro(1,10-phenanthroline)copper(II)	14783-09-6	SigmaAldrich, Munich, Germany	98%	RT
Dimethyl sulfoxide	67-68-5	SigmaAldrich, Munich, Germany	≥99.7%	RT
Dodecylsulfate-Na-salt (in pellets)	151-21-3	Serva, Heidelberg, Germany	n.A.	RT
Ethylenediaminetetraacetic acid dihydrate	6381-92-6	AppliChem, Darmstadt, Germany	≥99%	RT
Glycerol	56-81-5	SigmaAldrich, Munich, Germany	≥99.5%	RT
Glycine	56-40-6	Labochem international	n.A.	RT
HEPES	7365-45-9	Roth, Karsruhe, Germany	≥99.5%	RT
Hydrochloric acid	7647-01-0	Honeywell, Morristown, USA	24.5-26.0%	RT
Magnesium chloride hexahydrate	7791-18-6	MerckMillipore, Darmstadt, Germany	99.0-101.0%	RT
Manganese(II)chloride tetrahydrate	13446-34-9	SigmaAldrich, Munich, Germany	≥99%	RT
Methanol	67-56-1	VWR Chemicals	99.9%	RT
N-Ethylmaleimide	128-53-0	SigmaAldrich, Munich, Germany	≥99.0%	4°C
Polyethylenimine, Linear, MW 25000	9002-98-6	Polysciences, Warrington, USA	n.A.	RT

Name	CAS Registry Number	Manufacturer	Purity/ Concentration	Storage
Potassium acetate	127-08-2	SigmaAldrich, Munich, Germany	99%-101%	RT
Rubidium chloride	7791-11-9	AlfaAesar, Karlsruhe, Germany	n.A.	RT
Sodium chloride	7647-14-5	Fisher Chemicals, Loughborough, UK	99.5%	RT
Sodium Deoxycholate	302-95-4	SigmaAldrich, Munich, Germany	≥98%	RT
Sodium hydroxide	1310-73-2	SigmaAldrich, Munich, Germany	≥98%	RT
Sodium phosphate dibasic dihydrate	10028-24-7	Honeywell, Morristown, USA	98.5-101%	RT
Spectinomycin Dihydrochloride	22189-32-8	Fisher Bioreagents, Schwerte, Germany	> 603µg/mg	4°C
Triton X-100	9036-19-5	MerckMillipore, Darmstadt, Germany	n.A.	RT
Urea	57-13-6	SigmaAldrich, Munich, Germany	≥99.5%	RT

4.1.2 List of bioreagents

The following table contains the list of bioreagents (excluding antibodies) (Table 4.2). Bioreagents had a well-defined composition but were differentiated from chemicals by the absence of a CAS registry number. In addition to that, the exact composition was at times for many of bioreagents trade secret of the supplier. All bioreagents were stored according to manufacturers' instructions.

Table 4.2 | Listof bioreagents. The bioreagents were sorted accodring to their name.

Name	Manufacturer	Manufacturer product number (Purchase order number)	Purity/ Concentration	Storage
0.1 % Collagen solution in HCl, type I	Biochrom, Berlin, Germany	L7220	1 mg/ml	4°C
10x Pfu buffer	EurX, Gdansk, Poland	(Supplied with PfuPlus Polymerase)	n.A.	-20°C
Albumine Fraction V	Roth, Karlsruhe, Germany	8076.2	≥98%	4°C
Alkaline Phosphatase, Calf Intestinal (CIP)	NEB, Ipswich, USA	M0290L	10,000 U/ml	-20°C
AsiSI	NEB, Ipswich, USA	R0630S	10,000 U/ml	-20°C
Bacto Agar	BD Biosciences, Franklin Lakes, USA	214010	n.A.	RT
Bacto Tryptone	BD Biosciences, Franklin Lakes, USA	211705	n.A.	RT
Bacto Yeast Extract	BD Biosciences, Franklin Lakes, USA	212750	n.A.	RT
BamHI-HF	NEB, Ipswich, USA	R3136L	20,000 U/ml	-20°C
BglII	NEB, Ipswich, USA	R0144L	10,000 U/ml	-20°C
Buffer EB	Qiagen, Hilden, Germany	19086	n.A.	RT

Name	Manufacturer	Manufacturer product number (Purchase order number)	Purity/ Concentration	Storage
Cell Dissociation Buffer, Enzyme-free, PBS-based	Gibco, Waltham, USA	13151-014	n.A.	RT
Cholesterol, [1,2-3H(N)]-	PerkinElmer, Waltham, USA	NET139	1 mCi/ml, 49.8 Ci/mmol	-20°C
cOmplete™, EDTA-free Protease Inhibitor Cocktail	Roche, Rotkreuz, Switzerland	11873580001	n.A.	4°C
CutSmart	NEB, Ipswich, USA	B7204S	n.A.	-20°C
Deoxyguanosine 5'-[8-3H] triphosphate	American Radiolabeled Chemicals, St.Louis, USA	ART1557	1 mCi/ml, 5-20 Ci/mmol	-20°C
DNA Polymerase I, Large (Klenow) Fragment	NEB, Ipswich, USA	M0210S	5,000 U/ml	-20°C
DpnI	NEB, Ipswich, USA	R0176L	20,000 U/ml	-20°C
Dulbecco's Modified Eagle's Medium (low glucose)	SigmaAldrich, Munich, Germany	D6046	n.A.	4°C
Dulbecco's Phosphate Buffered Saline	SigmaAldrich, Munich, Germany	D8537	n.A.	RT
EcoRI-HF	NEB, Ipswich, USA	R3101S	20,000 U/ml	-20°C
EcoRV-HF	NEB, Ipswich, USA	R3195L	20,000 U/ml	-20°C
EZ-Link™ Sulfo-NHS-SS-Biotin	Thermo Scientific,, Waltham, USA	21331	n.A.	-20°C
EZview™ Red ANTI-FLAG® M2 Affinity Gel	SigmaAldrich, Munich, Germany	F2426	n.A.	-20°C
Fetal Bovine Serum, charcoal stripped	Gibco, Waltham, USA	12676029	n.A.	-20°C
FuGENE® HD Transfection Reagent	Promega, Mannheim, Germany	E2312	n.A.	4°C
Kanamycin sulfate	SigmaAldrich, Munich, Germany	60615	784 µg Kanamycin base per mg (dry basis)	RT
Lipofectamine® 2000 Transfection Reagent	LifeTechnologies, Waltham, USA	11668027	n.A.	4°C
MluI-HF	NEB, Ipswich, USA	R3198S	20,000 U/ml	-20°C
NEB, Ipswich, USAuffer™ 3.1	NEB, Ipswich, USA	B7203S	n.A.	-20°C
Nonidet P-40 Substitute	Roche, Rotkreuz, Switzerland	11754599001	n.A.	4°C
NotI-HF	NEB, Ipswich, USA	R3189L	20,000 U/ml	-20°C
NuPAGE™ Antioxidant	Invitrogen, Waltham, USA	NP0005	n.A.	4°C
NuPAGE™ LDS Sample Buffer (4X)	Invitrogen, Waltham, USA	NP0008	n.A.	4°C
NuPAGE™ Tris-Acetate SDS Running Buffer (20X)	Invitrogen, Waltham, USA	LA0041	n.A.	4°C

Name	Manufacturer	Manufacturer product number (Purchase order number)	Purity/ Concentration	Storage
Opti-MEM™ Reduced Serum Medium	Gibco, Waltham, USA	31985070	n.A.	4°C
Palmitic Acid, [9,10-3H(N)]-	PerkinElmer, Waltham, USA	NET043	5 mCi/ml, 53.7 Ci/mmol	-20°C
Penicillin-Streptomycin	SigmaAldrich, Munich, Germany	P4333	10000 U/ml Penicillin, 10 mg/ml Streptomycin	-20°C
PeqGold dNTP-Mixe Long Range	Peqlab, Radnor, USA	20-3111	dATP, dCTP, dGTP and dTTP each at 10 mM	-20°C
Pfu DNA Polymerase Gold	EurX, Gdansk, Poland	n.A. (not supplied anymore)	n.A.	-20°C
PfuPlus! DNA Polymerase	EurX, Gdansk, Poland	E1118-02	5 U/µl	-20°C
Photosphingosine, D-erythro [3-3H]	American Radiolabeled Chemicals, St.Louis, USA	ART2048	1 mCi/ml, 20 Ci/mmol	-20°C
Pierce™ High Capacity NeutrAvidin™ Agarose	ThermoScientific, Waltham, USA	29202	n.A.	4°C
PmeI	NEB, Ipswich, USA	R0560S	10,000 U/ml	-20°C
Powdered milk	Roth, Karlsruhe, Germany	T145.2	33.0-40% protein	RT
Precision Plus Protein™ All Blue Prestained Protein Standards	Bio-Rad, Hercules, USA	1610373	n.A.	-20°C
Q5® High-Fidelity DNA Polymerase	NEB, Ipswich, USA	M0491A	2,000 U/ml	-20°C
Q5® Reaction Buffer	NEB, Ipswich, USA	B9027S	n.A.	-20°C
Roche, Rotkreuz, Switzerland X-treme Gene HP	Roche, Rotkreuz, Switzerland	6366244001	n.A.	4°C
SERVA DNA Stain Clear G	Serva, Heidelberg, Germany	39804	n.A.	4°C
Sphingosine, D-erythro, [3-3H]	American Radiolabeled Chemicals, St.Louis, USA	ART0490	1 mCi/ml, 20 Ci/mmol	-20°C
Standardized Fetal Bovine Serum	Biochrom, Berlin, Germany	S0615	n.A.	-20°C
T4 DNA ligase	NEB, Ipswich, USA	M0202S	400,000 U/ml	-20°C
T4 DNA Ligase Reaction Buffer	NEB, Ipswich, USA	B0202S	n.A.	-20°C
Taq DNA Polymerase	Axon, Kaiserslautern, Germany	22466	5 U/µl	-20°C
Trypsin-EDTA solution	SigmaAldrich, Munich, Germany	T3924	n.A.	4°C
Turbofect	ThermoScientific, Waltham, USA	R0532	n.A.	4°C
Tween-20	Roth, Karlsruhe, Germany	127.1	n.A.	RT
Ultima Gold™ Universal LSC-Cocktail	PerkinElmer, Waltham, USA	6013329	n.A.	RT

4.1.3 List of consumables

The list of consumables itemizes containers and articles necessary for the preparation of samples and realization of experimental procedures (Table 4.3). All consumables were stored according to manufacturers' instructions.

Table 4.3 | List of consumables. The consumables were sorted accodring to their name. They were stored at room temperature if not stated otherwise.

Name	Abbreviation	Manufacturer	Manufacturer product number (Purchase order number)	Specification
6-well cell culture plate	6-well plate	Greiner bio-one, Kremsmuenster, Austria	657160	Polysterol, lid with condensation ring
Cell culture dish 10cm	n.A.	Greiner bio-one, Kremsmuenster, Austria	664160	Polysterol, 100/20 mm, vents
Freezing tube CyroS	CyroS	Greiner bio-one, Kremsmuenster, Austria	126263	Polypropylene, screw cap
Micro tube 1.5 ml	1.5 ml micro tube	Sarstedt, Nuembrecht, Germany	72690001	Polypropylene, attached cap
Microfuge®Tube Polyallomer 1.5 mL w/Cap	Ultracentrifuge tube	BeckmanCoulter, Brea, USA	357448	Polypropylene, 9.5x38 mm
Millex-GS filter 0.22 µm, 33 mm	0.22 µm filter	MerckMillipore, Darmstadt, Germany	SLGS033SS	Pore size 0.22 µm
NuPAGE™ 3-8% Tris-Acetate Protein Gels	Tris-Acetate gel	Invitrogen, Waltham, USA	10well: EA0375BOX, 12well: EA03752BOX, 15well: EA03755BOX	SDS-PAGE gel, 1.0 mm thick, 8x8 cm in size, stored at 4°C
Paper for chormatography	n.A.	Macherey-Nagel, Dueren, Germany	MN827	n.A.
Pipettor tips Mµlti-Flex®-tips	Gel loading tips	Roth, Karlsruhe, Germany	Y419.1	Polypropylene, round
Polyvinylidene fluoride membrane Immobilon®-FL	PVDF membrane	MerckMillipore, Darmstadt, Germany	IPFL00010	Polyvinylidene fluoride, pore size 0.45 µm
QIAGEN Plasmid Maxi Kit	n.A.	Qiagen, Hilden, Germany	12163	n.A.
QIAGEN Plasmid Midi Kit	n.A.	Qiagen, Hilden, Germany	12143	n.A.
QIAprep Spin Miniprep Kit	n.A.	Qiagen, Hilden, Germany	27106	n.A.
QIAquick Gel Extraction Kit	n.A.	Qiagen, Hilden, Germany	28706	n.A.
QIAquick PCR Purification Kit	n.A.	Qiagen, Hilden, Germany	28106	n.A.
SafeSeal tube 1.5 ml	n.A.	Sarstedt, Nuembrecht, Germany	72.706	Polypropylene, attached lid with retaining cams

Name	Abbreviation	Manufacturer	Manufacturer product number (Purchase order number)	Specification
TLC Silica gel 60	n.A.	MerckMillipore, Darmstadt, Germany	1.05721.0001	20x20 cm glass plate

4.2 Cloning and Plasmids

All reactions and buffers were prepared with autoclaved and demineralized water

4.2.1 Sequencing reactions and primers

All sequencing reactions were ordered at Eurofins Genomics/GATC biotech (Luxemburg, Luxemburg) as Supremerun Sanger sequencing reaction. The samples were sent as cleaned up plasmid DNA prepared with either Qiagen Mini, Midi, or Maxi kit. Sequencing primers were ordered directly at Eurofins Genomics/GATC biotech and stored at sight (Table 4.4).

Table 4.4 | Sequencing primers for Sanger sequencing reactions. All primers without a specific GRM number indicate sequencing primers for GRM2 sequencing. All sequences are 5'→3'.

Primer	Sequence
BGH-Reverse	TAGAAGGCACAGTCGAGG
CMV-F	CGCAAATGGGCGGTAGGCGTG
GATC-GRM1_ORF1500-2042138	TCGCTATGACTATGTGC
GATC-GRM1_ORF2200-2042141	CCCTTTGGGCTACAATG
GATC-GRM1_ORF700-2042135	GGAATGGACGCTTTCAAAG
GATC-grm1400-895721	GCCGCTACAACATCTTCACC
GATC-grm1500-895721	CCTCTCGCTGCAGTGAGC
GATC-grm2000-895722	ACGCATCTTCGGTGGGGC
GATC-GRM4_ORF1350-2024900	TCAACTTCTCAGGCATCGC
GATC-GRM4_ORF650-2024897	CTATGTGTCCACAGTGG
GATC-grm650-895720	GACTATGGCGAGACAGGCATTG
GATC-grm750-895720	TGAGCCGCGCGGCCTTTGAGG
GATC-pCMV6-PolyARev-1565997	GTCAGACAAAATGATGC
M13-FP	TGTAAAACGACGGCCAGT
pEGFP-FP	TTTAGTGAACCGTCAGATC
pEGFP-RP	AACAGCTCCTCGCCCTTG
T3	ATTAACCCTCACTAAAGGGA
T7-981079	TAATACGACTCACTATAG

SnapGene Viewer 4.1.4 (GSL Biotech LLC, Chicago, USA) and Serial Cloner 2.6.1 (SerialBasics, France) were used for analyzing the ab1-sequencing files and sequencing alignments respectively.

4.2.2 List of cloning and mutagenesis primers

All primers were ordered at biomers.net (Ulm, Germany) as cartridge-purified DNA oligomers at scale "XS" (0.02 µmol) without internal or end modifications (Table 4.5). The dried oligomers were resolvated in Buffer EB to a final concentration of 100 pmol/µl. To generate a PCR primer mix, forward (frwd) and reverse (rev) primers were diluted in Buffer EB to a final concentration of 10 pmol/µl and stored at -20°C until further use.

Table 4.5 | Cloning and mutagenesis primers. The primer names indicated left hand site are identical to the names on the orders and tubing. All sequences are 5'→3'.

Primer	Sequence
Grm2_RBS_BglII_Frwd	GGTACCGAGGAGATCTGCCG
Grm2_Flag_EcoRV_Rev	TATAGATATCATTTGCTGCACGCGTAAGCGATGACGTTGTCG
Grm2_Myc_PmeI_Rev	TATAGTTTAAACCAGATCCTCTTCTGAGATGAGTTTCTGCTC
Grm2_SP_BamHI_Frwd	TATAGGATCCGAGGGCCCAGCCAAGAAGG
Grm2_Myc_PacI_Rev	TATATTAATTAAACCAGATCCTCTTCTGAGATGAGTTTCTGCTC
Grm2_C121A_frwd	CACGCCACATCGCCCCCGACGGCTCTTATG
Grm2_C121A_rev	CATAAGAGCCGTCGGGGGCGATGTGGCGTG
GRM2_C121A_L698C_frwd	CATCGTGGTCGCCTGGTGCGTGGTGGAGGC
GRM2_C121A_L698C_rev	GCCTCCACCACGCACCAGGCGACCACGATG
GRM2_C121A_Y734C_frwd	CTCGCTGGCCTGCAATGTGCTCCTCATC
GRM2_C121A_Y734C_rev	GATGAGGAGCACATTGCAGGCCAGCGAG
GRM2_C121A_V782C_frwd	CCATCTTCTATTGCACCTCCAGTGACTACCG
GRM2_C121A_V782C_rev	CGGTAGTCACTGGAGGTGCAATAGAAGATGG
Grm2C121A*_L698C_frwd	CTCATCGTGGTCGCCTGGTGCGTGGTGGAGGC
Grm2C121A*_L698C_rev	GCCTCCACCACGCACCAGGCGACCACGATGAG
Grm2_W567A_frwd	CTGGGGCGATGCCGCGGCTGTGGGAC
Grm2_W567A_rev	GTCCCACAGCCGCGGCATCGCCCCAG
GRM2_Y607A_frwd	CAGGTCGGGAGCTCTGCGCCATCCTGCTGG
GRM2_Y607A_rev	CCAGCAGGATGGCGCAGAGCTCCCGACCTG
Grm2_W697A_frwd	CTCATCGTGGTCGCCGCGCTGGTGGTGGAG
Grm2_W697A_rev	CTCCACCACCAGCGCGGCGACCACGATGAG
Grm_W697A_frwd(2)	CATCGTGGTCGCCGCGCTGGTGGTGG
Grm_W697A_rev(2)	CCACCACCAGCGCGGCGACCACGATG
GRM2_Y734A_frwd	GCTCGCTGGCCGCCAATGTGCTCCTCATC
GRM2_Y734A_rev	GATGAGGAGCACATTGGCGGCCAGCGAGC
Grm2_Y745A_frwd	CTCTGCACGCTTGCTGCCTTCAAGACTCG
Grm2_Y745A_rev	CGAGTCTTGAAGGCAGCAAGCGTGCAGAG
Grm2_Y767A_frwd	GCTTCACCATGGCCACCACCTGCATCATCTG
Grm2_Y767A_rev	CAGATGATGCAGGTGGTGGCCATGGTGAAGC
Grm2_W773_frwd	GTACACCACCTGCATCATCGCGCTGGCATTCC
Grm2_W773_rev	GGAATGCCAGCGCGATGATGCAGGTGGTGTAC
Grm2_Y781A_frwd	CTGCCCATCTTCGCTGTCACCTCCAGTGACTAC
Grm2_Y781A_rev	GTAGTCACTGGAGGTGACAGCGAAGATGGGCAG
GFP_Frwd	TATAGCGGCCGCTCGTGAGCAAGGGCGAGGAG
GFP_Rev	TATAGATATCATTTGCTGCCCTGTACAGCTCG
GFP_GlySer_Frwd	TATAGCGGCCGCAGGGCGGAGGCGGAAGCGTGAGCAAGGGCGAGGAG
GFP_A207K_frwd	GCACCCAGTCCAAGCTGAGCAAAGACCCCAAC
GFP_A207K_rev	GTTGGGGTCTTTGCTCAGCTTGGACTGGGTGC
ADBR2_frwd	TATAGCGATCGCCATGAAGACCATCATCGCC
ADBR2_rev	TATAGTTTAAACCAGCAGTGAGTCATTTGTACTACAATTC
HTR2A_frwd	TATAGCGATCGCCATGGAACAAAAACTTATTTCTGAAGAAGATC
HTR2A_rev	TATAGTTTAAACCACACAGCTCACCTTTTCATTCAC

Primer	Sequence
HTR2A_Cmyc_frwd	TATAGCGATCGCCATGGATATTCTTTGTGAAGAAAATACTTCTTTG
HTR2A_Cmyc_rev	TATAGCGGCCGCGTGCGTGTCACACAGCTCACCTTTTCATTC
HTR2A_Cflag_rev	TATAACGCGTCACACAGCTCACCTTTTCATTC
ADRB2_cFlag_frwd	TATAGCGATCGCCATGGGGCAACCCGGGAAC
ADRB2_cFlag_rev	TATAACGCGTCAGCAGTGAGTCATTTGTACTACAATTC
ADRB2_cMyc_rev	TATAGCGGCCGCGTGCGTGTCAGCAGTGAGTCATTTGTACTACAATTC
5HTR1A_CF_frwd	TATAGCGATCGCCATGGATATGTTCAGTCTTGGCC
5HTR1A_CF_rev	TATAACGCGTGCGGCAGAACTTGCAC
ADA2A_CF_frwd	TATAGCGATCGCCATGGGCTCCCTGCAG
ADA2A_CF_rev	TATAACGCGTCACGATCCGCTTCCTG
GRM4_CF_frwd	TATAGCGATCGCCATGCCTGGGAAGAGAGG
GRM4_CF_rev	TATAACGCGTGATTGCATGGTTGGTGTAAGTG
GRM1_CF_frwd	TATAGCGATCGCCATGGTCGGGCTCCTTTTG
GRM1_CF_rev	TATAACGCGTCAGGGTGGAAGAGCTTTG
GRM1_CF_rev2	TATAACGCGTCAGGGTGGAAGAGCTTTGC
ADRB2_C341A_f	CAGGAGCTTCTGGCCCTGCGCAGGTCTTCTTTG
ADRB2_C341A_r	CAAAGAAGACCTGCGCAGGGCCAGAAGCTCCTG
ADRA2A_C442A_f	CTTCAAGAAGATCCTCGCTCGGGGGGACAG
ADRA2A_C442A_r	CTGTCCCCCCGAGCGAGGATCTTCTTGAAG
HTR1A_C417A_f	GAAGATCATCAAGGCCAAGTTCTGCCGCACG
HTR1A_C417A_r	CGTGCGGCAGAACTTGGCCTTGATGATCTTC
HTR1A_C420A_f	GATCATCAAGGCCAAGTTCGCCCGCACGCGTG
HTR1A_C420A_r	CACGCGTGCGGGCGAACTTGGCCTTGATGATC

4.2.3 Chemocompetent *Escherichia coli*

Chemocompetent bacteria were grown in LB medium without selection. All bacterial stocks were obtained from Alexia Herrmann (AG Britta Bruegger, Heidelberg University Biochemistry Center). For the preculture, 10 ml LB medium (10 g Tryptone, 5 g Yeast Extract, 10 g NaCl, fill up to 1 l with ddH_2O) were inoculated with *Escherichia coli* (*E.coli*) bacteria from stock. The bacteria grew overnight at 37°C under constant shaking at 180 rpm. The grown preculture was used the next day to inoculate a 400 ml LB culture. The main culture was grown to an OD_{600} = 0.4.

The cells from the main culture were pelleted (4000 x g, 15 min, 4°C). The cell pellets were resuspended on ice in a total volume of 50 ml Resuspension buffer (30 mM CH_3COOK-CH_3COOH pH 5.8, 50 mM $MnCl_2$, 100 mM RbCl, 10 mM $CaCl_2$, 15%$_{(V/V)}$ glycerol). The bacteria were then pelleted again at 3000 x g for 10 min at 4°C. The final pellets were taken up in a total volume of 10 ml Freezing buffer (10 mM MOPS-NaOH pH 7.0, 75 mM $CaCl_2$, 10 mM RbCl, 15%$_{(V/V)}$ glycerol). The prepared chemocompetent bacteria were aliquoted and stored at -80°C until further use.

4.2.4 Transformation protocol

Chemocompetent *E.coli* cells were allowed to defrost on ice for (10 – 30) min. Then DNA (10 ng Plasmid DNA or 10 µl Ligation/ PCR reaction) was added to the defrosted bacteria and incubated for another (20 – 30) min on ice. The heat shock was carried out for (30 – 60) sec at 42°C. The cells settled for another (2 – 5) min on ice afterwards. The transformed *E.coli* cells recovered for (30 – 60) min at 37°C in 1 ml LB medium without antibiotics to allow for the expression of resistance genes. After the recovery, the bacteria were pelleted by centrifugation (5 min at 300 x g) and resuspended in about (100 – 200) µl of supernatant. The cell suspension was plated on a LB-agar (LB medium, 3.75 g agar/250 ml) selection plate with accommodated antibiotic.

4.2.5 pCMV6 vector control

The empty pCMV6 vector control was generated from the commercially available plasmid pCMV6_GRM2_MycFlag sold by OriGene (Rockville, USA) as GRM2 (Myc-DDK-tagged)-Human glutamate receptor (RC218103).

The plasmid pCMV6_GRM2_MycFlag was digested with BglII and NotI-HF in NEB3.1 buffer. The 5' overhangs of the digested vector were filled up with Klenow Polymerase according to manufacturers' protocol. The blunt ends were ligated with T4 DNA ligase overnight at 16°C. The ligation product was transformed into chemocompetent *E.coli Stbl3*. Identity of clones was confirmed by sequencing with CMV-F at Eurofins Genomics/GATC biotech. The final construct was pCMV6 vector control.

4.2.6 Flag-tagged and Myc-tagged GRM2 constructs

The GRM2 and GRM2^{C121A} constructs carrying either a Myc- or a Flag-Tag at the C-terminal end were cloned from the pCMV6_GRM2_MycFlag and the pCMV6_GRM2^{C121A}_MycFlag vector (for details see Wiedemann (243)) respectively. The GRM2 open reading frames (ORFs) were amplified with extensions from double-tagged vectors and were inserted again in the corresponding digested pCMV6 vector.

The ORF was amplified with Q5 DNA Polymerase (NEB) using either the primer pair Grm2_RBS_BglII_Frwd/ Grm2_Flag_EcoRV_Rev for the Flag-tagged construct or the primer pair Grm2_RBS_BglII_Frwd/ Grm2_Myc_PmeI_Rev for the Myc-tagged construct (Table 4.6).

Table 4.6 | Q5 PCR protocol for Flag- and Myc-tagged constructs. (**A**) Pipetting scheme PCR reaction. (**B**) Reaction cycle mPCR

A

Component	Volume [µl]
ddH_20	35.5
dNTPs	1
Template DNA (10 ng/µl)	1
Primermix (10 pmol/µl)	2
5x Q5 buffer	10
Q5 Polymerase	0.5

B

Cycle	Temperature [°C]	Time
Activation	98	30 sec
Melting	98	30 sec (30x)
Annealing	65	30 sec (30x)
Extension	72	2 min (30x)
Final elongation	72	2 min

The PCR products with a size of 2.67 kb and 2.7 kb were cleaned up from agarose gel (stained with Serva DNA Stain Clear G). The PCR product and the backbone was prepared by double digestion with BglII/EcoRV-HF in buffer NEB3.1 in the case of the Flag-tagged construct, or consecutive digestion with BglII in NEB3.1 and PmeI in CutSmart in the case of the Myc-tagged construct. The digested backbones were cleaned up from agarose gel and subsequently dephosphorylated with Calf Intestinal Alkaline Phosphatase (CIP). The digested PCR products were finalized with the PCR purification kit. The prepared PCR products and backbones were ligated using T4 DNA ligase according to manufacturers' protocol. The ligation product was transformed into chemocompetent *E.coli Stbl3*. The identity of clones was confirmed by sequencing with CMV-F, GATC-grm750-895720, GATC-grm1500-89572, and GATC-grm2000-895722 at Eurofins Genomics/GATC biotech. The plasmids cloned were pCMV6_GRM2^{Wt}_Flag, pCMV6_GRM2^{Wt}_Myc, pCMV6_GRM2^{C121A}_Flag, and pCMV6_GRM2^{C121A}_Myc.

4.2.7 GRM2^{C121A} double mutants for crosslinking

The GRM2^{C121A} double mutants were based on the pCMV6_GRM2^{C121A}_MycFlag construct and used for Cysteine crosslinking experiments. All mutants were generated using mutagenesis PCR (mPCR) according to the Stratagene QuikChange protocol (244) with modifications (Table 4.8). The primers were designed with the PrimerX web program, hosted by bioinformatics.org (245), based on the complete DNA sequence of the template plasmid. The "QuikChange Site-Directed Mutagenesis Kit by Stratagene" primer design protocol was used as basis for the calculation of optimal primer properties. To facilitate automatic generation of primers on the GC-rich template, adjustments were made in the settings of PrimerX (Table 4.7).

Table 4.7 | Settings PrimerX DNA-based mutagenesis primer design. The table returns the values of the adjusted parameters in the PrimerX web program.

Parameter	Value
Melting temp	75 to 85°C
GC content	40 to 65%
Length	25 to 45 bp
5' flanking region	11 to 21 bp
3' flanking region	11 to 21 bp
Terminates in G or C	Yes
Mutation site at center	Not required

For the mPCR, the template plasmid was obtained as DNA preparation from *E.coli Stbl3*. The plasmids were amplified with the mutagenesis primer pairs GRM2_C121A_L698C_frwd/rev, GRM2_C121A_Y734C_frwd/rev, and GRM2_C121A_V782C_frwd/rev. In deviation of standard protocol, Pfu Polymerase Gold and corresponding 10x Pfu buffer was used for the reaction.

Table 4.8 | mPCR protocol GRM2^{C121A} double mutants. (**A**) Pipetting scheme PCR reaction. (**B**) Reaction cycle mPCR

A

Component	Volume [µl]
ddH_20	40
dNTPs	1
Plasmid DNA (100 ng/µl)	1
Primermix (10 pmol/µl)	2
10x EurX Pfu Buffer	5
EurX Pfu Polymerase Gold	1

B

Cycle	Temperature [°C]	Time
Activation	95	5 min
Melting	95	30 sec (18x)
Annealing	65-70	60 sec (18x)
Extension	68	10 min (18x)
Final elongation	68	15 min

After the mPCR, the DNA was digested for 1 h with DpnI. The enzyme was applied directly to the PCR mix. About (5 – 10) µl of the final reaction mix were used for transformation into chemocompetent *E.coli Stbl3*. Identity of clones was confirmed by sequencing with CMV-F, GATC-grm750-895720, GATC-grm1500-89572, and GATC-grm2000-895722 at Eurofins Genomics/GATC biotech. The final constructs were pCMV6_GRM2$^{C121A/L698C}$_MycFlag, pCMV6_GRM2$^{C121A/Y734C}$_MycFlag, and pCMV6_GRM2$^{C121A/Y734C}$_MycFlag.

4.2.8 eGFP-tagged GRM2 variants

The eGFP-tagged variants of GRM2 were based on a mutagenized eGFP version which was cloned into a pCMV6_GRM2_MycFlag plasmid.

In the first step, the template plasmid (pEGFP-FLAG-BBS-1) was mutagenized in the eGFP ORF at position A207. The primer pair GFP_A207K_frwd/rev was designed in PrimerX web program and applied to the template plasmid following the Strategene QuikChange protocol (244) with minor changes (Table 4.10). The annealing temperature was adjusted to 60°C. The DpnI digested mPCR products were transformed into *E.coli DH5α* and selected on a 50 µg/ml

kanamycin LB-agar selection plate. Positive clones were identified by Sanger sequencing with CMV-F primer at Eurofins Genomics/GATC biotech.

To get the insert, the eGFP^{A207K} ORF of the pEGFP^{A207K}-FLAG-BBS-1 plasmid was amplified by PCR with the primer pairs GFP_Frwd/Rev or GFP_GlySer_Frwd/GFP_Rev (Table 4.9). The later one contained a DNA fragment coding for a glycine-serine linker.

Table 4.9 | Q5 PCR protocol eGFP^{A207K} constructs. (**A**) Pipetting scheme PCR reaction. (**B**) Reaction cycle PCR.

A

Component	Volume [µl]
ddH_20	35.5
dNTPs	1
Template DNA (10 ng/µl)	1
Primermix (10 pmol/µl)	2
5x Q5 buffer	10
Q5 Polymerase	0.5

B

Cycle	Temperature [°C]	Time
Activation	98	30 sec
Melting	98	30 sec (30x)
Annealing	58	30 sec (30x)
Extension	72	1 min (30x)
Final elongation	72	2 min

To get the backbone, pCMV6_GRM2_MycFlag was double digested with NotI-HF/EcoRV-HF in CutSmart buffer. Both the PCR product of the eGFP^{A207K} insert and the digested pCMV6_GRM2 backbone were cleaned up from agarose gel. The purified eGFP^{A207K} insert was subjected to double digest with NotI-HF/EcoRV-HF in CutSmart buffer and isolated with Qiagen PCR purification kit. The backbone was dephosphorylated using the CIP protocol and cleaned up with Qiagen PCR purification kit afterwards.

The digested insert and the dephosphorylated backbone were ligated with T4 DNA ligase overnight at 4°C, for 6 h at 16°C and 1 h at 24°C. The ligation product was transformed into *E.coli Stbl3* and selected on a 25 µg/ml kanamycin LB-agar selection plate. Positive clones were picked from the selection plate and linearized with EcoRV-HF to find constructs with insert. The identity of clones was confirmed by sequencing with CMV-F, GATC-grm750-895720, GATC-grm1500-89572, GATC-grm2000-895722, pEGFP-FP, and GATC-pCMV6-PolyARev-1565997 at Eurofins Genomics/GATC biotech. The final constructs were pCMV6_GRM2-Gly4Ser-eGFP^{A207K}_Flag and pCMV6_GRM2-eGFP^{A207K}_Flag.

4.2.9 GRM2^{Wt} and GRM2^{C121A} W→A and Y→A variants

For the alanine screening different tryptophan and tyrosine residues in the transmembrane domain of GRM2 were targeted and changed to alanine by site-directed mutagenesis. The constructs pCMV6_GRM2^{Wt}_Flag, pCMV6_GRM2^{Wt}_Myc, pCMV6_GRM2^{C121A}_Flag, and pCMV6_GRM2^{C121A}_Myc served as templates for the mPCR reactions yielding in total 32 different constructs.

The mutagenesis primers were designed in PrimerX as described Section 4.2.7. To facilitate automatic generation of primers on the GC-rich template, the settings in the primer design step had to be adjusted to a melting temperature of up to 85°C and a GC-content of up to 80% (Table 4.7). The mPCR was carried out according to the Stratagene QuikChange protocol (244) with minor adjustments (Table 4.10).

Table 4.10 | mPCR protocol GRM2^{Wt} and GRM2^{C121A} W→A and Y→A variants. (**A**) Pipetting scheme PCR reaction. (**B**) Reaction cycle mPCR. The value x for the cycle step annealing was adjusted to 52°C for W697A and Y745A, to 55°C for W567A, Y734A, W773A, and Y781A, and to 60°C for Y607A and Y767A.

A

Component	Volume [µl]
ddH_20	40
dNTPs	1
Plasmid DNA (100 ng/µl)	1
Primermix (10 pmol/µl)	2
10x EurX Pfu Buffer	5
EurX Pfu Polymerase	1

B

Cycle	Temperature [°C]	Time
Activation	95	2 min
Melting	95	1 min (18x)
Annealing	x	1-2 min (18x)
Extension	68	11 min (18x)
Final elongation	68	15 min

The mPCR products were digested and transformed into *E.Coli Stbl3* as described earlier. Identity of clones was confirmed by sequencing with CMV-F, GATC-grm750-895720, GATC-grm1500-89572, and GATC-grm2000-895722 at Eurofins Genomics/GATC biotech. The 32 constructs were Flag- or Myc-tagged single or double mutants based on the constructs described in Section 4.2.6 with single alanine mutations in the GRM2 ORF at positions W567, Y607, W697, Y734, Y745, Y767, W773 or Y781.

4.2.10 Flag-and Myc-tagged GPCRs

cDNA clones of ADRB2 and HTR2A were obtained as from Addgene (Cambridge, USA) as β_2AR-mCFP (Addgene plasmid #38260, deposited by Robert Lefkowitz (152)) and c-Myc-5-HT2A (Addgene plasmid #67944, deposited by Javier Gonzalez-Maeso (154)). Further cDNA clones for Htr1a (mouse), ADRA2A, GRM1 and GRM4 were purchased from BioCat (Heidelberg, Germany) as 5-hydroxytryptamine (serotonin) receptor 1A (BC138681-seq-TCMS1004-GVO-TRI), alpha-2A Adrenergic receptor (BC035047-seq-TCHS1003-GVO-TRI), Glutamate receptor metabotropic 1 (BC111844-TOH6003-GVO-TRI) and Glutamate receptor, metabotropic 4 (BC130526-TCH1003-GVO-TRI) respectively.

4.2.10.1 ADRB2 and HTR2A contructs

The Addgene plasmids with cDNA clones ADRB2 and HTR2A were delivered as agar stab. Single colonies were obtained by streaking resuspended bacterial agar on a 100 µg/ml ampicillin LB-agar selection plate. Single clones were picked and sequenced at Eurofins

Genomics/GATC biotech. ADRB2 was sequenced with CMV-F, BGH-Reverse, and pEGFP-RP. For HTR2A I used CMV-F and BGH-Reverse.

10 ng plasmid was used to isolate the ORF sequence and adjacent tags (PCR protocol see Table 4.9). For ADRB2, I used the primer pair ADBR2_frwd/rev to isolate the ORF with the N-terminal Flag-tag, ADRB2_cFlag_frwd/rev to generate a clone with C-terminal Flag-tag and ADRB2_cFlag_frwd/ADRB2_cMyc_rev to tag the ORF C-terminally with a Myc-tag. For the N-terminal Flag tag, both the PCR product and pCMV6_GRM2_MycFlag were double digested with AsiSI and PmeI in CutSmart. The insert and backbone, pCMV6_GRM2_Flag, of the C-terminal Flag-tag construct were double digested with AsiSI and MluI-HF in CutSmart. For the Myc-tagged ADRB2 version, the PCR product and the pCMV_GRM2_Myc vector were digested with AsiSI and NotI-HF. The digested inserts and backbones were ligated as described in Section 4.2.8. The ligation products were transformed into *E.coli Stbl3* and positive clones selected on 25 µg/ml Kanamycin LB-agar selection plates. The clones were tested by linearization with BamHI-HF and subsequently sequenced with CMV-F and GATC-pCMV6-PolyARev-1565997 at Eurofins Genomics/GATC biotech. The resulting constructs were pCMV6_NFlag_ADRB2, pCMV6_ADRB2_Flag, and pCMV6_ADRB2_Myc.

The HTR2A constructs were clones in a similar manner as described beforehand. The ORF was isolated using the PCR setup as described in Table 4.9. The N-terminally Myc-tagged contruct was isolated with the primer pair HTR2A_frwd/rev. For the C-terminal Flag-tagged construct, the primer pair HTR2A_Cmyc_frwd/HTR2A_Cflag_rev was used. The Myc-tagged version was prepared with primer pair HTR2A_Cmyc_frwd/rev. N-Myc insert and the corresponding backbone were double digested with AsiSI and PmeI in CutSmart. C-Flag constructs were digested with AsiSI and MluI-HF in CutSmart, and C-Myc fragments were incubated with AsiSI and NotI-HF in CutSmart as well. The ligation, transformation and selection of clones were performed as for ADRB2. The final constructs were pCMV6_NMyc_HTR2A, pCMV6_HTR2A_Flag and pCMV6_HTR2A_Myc.

4.2.10.2 HTR1A, ADRA2A, GRM1 and GRM4 constructs

The cDNA clones of Htr1a (mouse), ADRA2A, GRM1, and GRM4, were cloned as C-terminally Flag-tagged constructs into the pCMV6 vector. The constructs had been delivered as agar stab and were propagated in the corresponding selection medium: the pCR4-TOPO constructs HTR1A and GRM4 were cultured in 25 µg/ml kanamycin, the pENTR223-1 vector

with GRM1 in 50 ug/ml spectinomycin and pBluescriptR_ADRA2A in 100 µg/ml ampicillin. The identity of the clones was confirmed by partial Sanger sequencing of the ORF at Eurofins Genomics/GATC biotech. HTR1A and GRM4 constructs were sequenced with sequencing primer T3, ADRA2A with T7-981079, and GRM1 with M13-FP.

The inserts were successfully amplified by PCR for HTR1A (5HTR1A_CF_frwd/rev), GRM1 (GRM1_CF_frwd/rev2) and GRM4 (GRM4_CF_frwd/rev) by the Q5 DNA polymerase standard protocol described in Table 4.9. For ADRA2A (ADA2A_CF_frwd/rev) the PCR reaction had to be supplied with GC-enhancer (supplied with Q5 DNA polymerase). All PCR products and pCMV6_GRM2_Flag were digested with AsiSI and MluI-HF in CutSmart buffer. The digested pCMV6 backbone DNA was cleaned up from agarose gel and dephosphorylated with CIP protocol. The prepared insert and backbone DNA were ligated and transformed into *E.coli Stbl3* as described in section 4.2.8.

Positive clones were identified by digesting the different clones again with AsiSI and MluI-HF. For ligated GRM1 constructs, colony PCR was applied to screen larger sets of clones (Table 4.11).

Table 4.11 | Colony PCR protocol. (**A**) Pipetting scheme for one colony PCR. The reaction was conducted with the GRM1_CF_frwd/rev2 primer pair. Reagents marked with an asterisk (*) were supplied with Taq DNA Polymerase. (**B**) Reaction cycle colony PCR.

A

Component	Volume [µl]
ddH_20	15.4
dNTPs	0.4
25 mm $MgCl_2$*	1.6
Bacterial sample	-
Primermix (10 pmol/µl)	0.4
10x Mg-free buffer B*	2.0
Taq DNA Polymerase	0.2

B

Cycle	Temperature [°C]	Time
Activation/ Denaturation	95	4 min
Melting	95	1 min (35x)
Annealing	60	1 min (35x)
Extension	72	3:30 min (35x)
Final elongation	72	5 min

The identity of the positive clones was confirmed by sequencing with CMV-F and PolyARev-1565997 at Eurofins Genomics/GATC biotech. For larger constructs, GRM1 and GRM4, additional sequencing primers were designed: GATC-GRM1_ORF700-2042135, GATC-GRM1_ORF1500-2042138, GATC-GRM1_ORF2200-2042141 for GRM1, and GATC-GRM4_ORF650-2024897, GATC-GRM4_ORF1350-2024900 for GRM4. The final constructs were pCMV6_Htr1a_Flag, pCMV6_ADRA2A_Flag, pCMV6_GRM1_Flag and pCMV6_GRM4_Flag.

4.2.11 Cloning of GPCR palmitoylation mutants

Selected constructs described in section 4.2.10.1 and 4.2.10.2 were used to generate C→A mutants. The mutations sites were estimated from literature on loss-of-function of palmitoylation at the C-terminal tail of the GPCRs. For Htr1a, the mutation sites were estimated from the C417A and C420A single and double mutants described by Papoucheva, Dumuis (176). The ADRA2A mutant C442A was published by Kennedy and Limbird (156). Finally, for the ADRB2 mutation site C341A biochemical and structural evidence was found by Odowd, Hnatowich (76) and Cherezov, Rosenbaum (20).

The Flag-tagged pCMV6 cDNA clones pCMV6_HTR1A_Flag, pCMV6_ADRA2A, and pCMV6_ADRB2_CFlag were used to design mutagenesis primers with PrimerX as described earlier (Section 4.2.7). The plasmids were amplified with the mutagenesis primer pairs HTR1A_C417A_f/r, HTR1A_C420A_f/r, ADRA2A_C442A_f/r, and ADRB2_C341A_f/r. In deviation of the standard protocol, I used Pfu Plus and the corresponding 10x Pfu buffer for the mPCR (Table 4.12).

Table 4.12 | mPCR protocol GPRC C→A mutants. (**A**) Pipetting scheme mPCR reaction. (**B**) Reaction cycle mPCR.

A

Component	Volume [µl]
ddH_20	40.5
dNTPs	1
Plasmid DNA (50 ng/µl)	1
Primermix (10 pmol/µl)	2
10x EurX Pfu Buffer	5
EurX Pfu Plus	0.5

B

Cycle	Temperature [°C]	Time
Activation	95	1 min
Melting	95	45 sec (18x)
Annealing	65-70	1 min (18x)
Extension	68	7 min (18x)
Final elongation	68	7 min

The mPCR products were digested and transformed into *E.Coli Stbl3* as described earlier and positive clones selected on 25 µg/ml Kanamycin LB-agar selection plates. Identity of clones was confirmed by sequencing with CMV-F and GATC-pCMV6-PolyARev-1565997 at Eurofins Genomics/GATC biotech. The final constructs obtained were pCMV6_Htr1a^{C417A}_Flag, pCMV6_Htr1a$^{C417A/C420A}$_Flag, and pCMV6_ADRB2^{C341A}_Flag.

4.3 Cell lines and cell culture

For cell maintenance and as required for experiments, the human cells lines were kept in CO_2-incubators (Standard laboratory: Forma SteriCycle CO2 incubator, ThermoFisher, Waltham, USA; Isotope laboratory: BBD 6220, Hereaus, Hanau, Germany) at 37°C and 5% CO_2 in a water saturated atmosphere. All bench work with the cells was conducted under sterile

conditions in a laminar flow hood (HeraSafe KS12 Safety Cabinet, EN12469:2000, Class II, ThermoFisher) with equipment, in so far required, disinfected with 70% ethanol$_{(aq)}$ solution. All consumables and chemicals used were either supplemented as cell culture grade from suppliers or sterilized by autoclaving or filtration.

4.3.1 Hek293

Hek293 cells were obtained from AG Felix Wieland (Heidelberg University Biochemistry Center). The cells were cultured in DMEM complete growth medium. To make DMEM complete growth medium, Dulbecco's Modified Eagle's Medium (DMEM) was supplied with final concentration of 100 U/ml penicillin, 0.1 mg/ml streptomycin (PS) and 10% Standardized Fetal Bovine Serum (FBS). FBS was supplemented as heat-inactivated stock treated at 56°C for 45 min.

4.3.2 Hek293Δ*SGPL1*

The knock-out of Sphingosine-1-phosphate lyase 1 (*SGPL1*) gene was conducted with the genetic scissors of the CRISPR-Cas9 system in Hek293 cells. The CRISPR-Cas9 plasmids for the target gene were designed by Per Haberkant (80) and a copy obtained from Mathias Gerl (178). The cloning and cell culture work was conducted as part of the master's thesis of Hannah Olschowski, nee Wiedemann (243). The cells were cultures as described in Section 4.3.1.

4.3.3 Hek293T

Hek293T cells were obtained from ATCC as 293T cell line (ATCC CRL-3216, Order No W002940). The cells were cultured in DMEM complete growth medium supplemented with heat-inactivated FBS.

4.3.4 Subculturing procedure

Hek293 and Hek293T cells grew as adherent cells on Collagen A-coated (0.1 % Collagen stock solution in HCl$_{(aq)}$) 10 cm cell culture dishes. To coat the cell culture dishes, they were incubated with a final concentration of 0.01% Collagen A in Dulbecco's Phosphate Buffered Saline (PBS) for at least 30 min at 37°C. Cell culture dishes or well plates for experiments were coated with final concentration of 0.02% Collagen A to provide better adherence during

the experimental procedures. After incubation with Collagen A solution, the PBS dilution was aspirated and the coated surface washed once with room temperature PBS.

To passage the cells, the cell layer was grown to a confluency of 70-80%. The cell layer was then washed once with room temperature PBS and cells were enzymatically detached (Trypsin-EDTA solution) for about (1 – 3) min. Detached cells were diluted 1:10 or 1:20 in DMEM complete growth medium. The diluted cell suspension was plated on a Collagen A-coated 10 cm cell culture dish (total of ~$1x10^6$ or $5x10^5$ cells per dish). Cells were passaged every 3-4 days and not more than 20 times before using a new batch.

4.3.5 Cyropreservation of cells

As for subculturing, the cells were grown to a confluency of 70-80% in a 10 cm cell culture dish, enzymatically detached and diluted in DMEM complete growth medium. One dilution in DMEM complete growth medium contained a total of $5x10^6$ cells making one freezing batch.

The cells of one freezing batch were spun down for 5 min at 200 x g and 4°C. The cell pellet was resuspended in 1 ml DMEM cryopreservation medium. The base of the DMEM cryopreservation medium was DMEM complete growth medium which was supplemented with $5\%_{(V/V)}$ of dimethyl sulfoxide (DMSO) and $5\%_{(V/V)}$ of heat-inactivated FBS. The cells suspension was transferred into a freezing tube (CyroS). The freezing tube was cooled down by placing it on ice for about 5 min, then into -20°C freezer for 1h and to -80°C for about 16h before transferring it to liquid nitrogen. All human cell lines were kept in liquid nitrogen for long-term storage.

4.3.6 Defrosting of cells

To defrost and recultivate human cells, freezing tubes were removed from the liquid nitrogen tank and placed on dry ice for transport. The freezing tube was then warmed by gentle agitation in a 37°C water bath. As soon as the content had thawed, the cell suspension in DMEM cryopreservation medium was diluted 1:10 with cold DMEM complete growth medium. The cells were then pelleted by centrifugation at 300 x g for 5 min and 4°C. The cell pellet was resuspended in 10 ml room temperature DMEM complete growth medium and the cell suspension plated on a Collagen-A coated 10 cm cell culture plate. Before starting an experiment, the cells were subcultured at least three times.

4.3.7 Transfection procedures

For transient transfection of cells with empty pCMV6 or expression vectors, the cells were seeded 16-18h before the transfection into either 6-well cell culture dishes or 10 cm cell culture plates. If not stated otherwise, the cell culture medium remained unchanged in the course of the transfection.

For transfection with FuGENE HD transfection reagent (FuGENE HD), the transfection mix was prepared according to manufacturers' instructions (246) in OptiMem medium with plasmid DNA solved in Buffer EB. The DNA was usually supplied from a plasmid DNA stock with a concentration of (100 ± 1) ng/µl. The ratio between µg of DNA and µl of FuGENE HD was 1:3. The transfection mix was incubated (10 ± 2) min at room temperature before adding the complete batch to the DMEM complete growth medium. FuGENE HD was used as standard transfection reagent with the indicated amounts of DNA if not stated otherwise.

For transfection with Roche X-treme Gene HP, 500 ng plasmid DNA was diluted in 50 µl OptiMEM. X-treme Gene HP was added to the mixture in a µg DNA/µl reagent ratio of 1:3. The transfection mixture was incubated for 20 min at room temperature and then added to the cells.

For transfection with Lipofectamine2000, 1 µl the transfection reagent was diluted in 25 µl OptiMEM. Likewise, 500 ng plasmid DNA was diluted in 25 µl OptiMEM. Then, 25 µl of Lipofectamine2000 and DNA dilution were mixed to obtain the transfection mix. The transfection mix was incubated 5 min at room temperature and the whole batch was added to the cells.

For the transfection with Turbofect, 500 ng plasmid DNA was diluted in 50 µl OptiMEM. 1 µl Turbofect, thus in a ratio of 1:2, was added to obtain the transfection mix. The transfection mix was incubated for 15 min at room temperature and added completely to the cells.

Polyethyleneimine (PEI) solution was obtained as diluted (1 mg/ml) and $HCl_{(aq)}$ neutralized stock from Alexia Herrmann (AG Britta Brugger, Heidelberg University Biochemistry Center). For the transfection, 2 µg plasmid DNA was diluted in 31.25 µl OptiMEM. The transfection mix was finalized with 3.75 µl PEI stock solution. The transfection mix was allowed to incubate for 1h at room temperature before adding the complete batch to the cells.

For the calcium-phosphate method I prepared HEPES buffered saline (HBS, HEPES- $HCl_{(aq)}$ pH 7, 280 mM NaCl, 1.5 mM Na_2HPO_4) and a 2M $CaCl_{2(aq)}$ solution according to protocols on bioprotcols.org (247). Both solution were filtered sterile with a 0.22 µm filter (MerckMillipore), aliquoted and frozen at -20°C until further use. To prepare the transfection mix, 10.4 µl 2M $CaCl_{2(aq)}$ solution were mixed with 1.0 µg plasmid DNA. The mix was adjusted to a total volume of 85.0 µl with ddH_20. The complete dilution was then added dropwise to an equal volume of HBS. The finalized transfection mix was incubated at room temperature for 1 min before adding the complete preparation to the cells.

4.4 Flow Cytometry

All flow cytometry measurements were conducted with the FACSCalibur (BD Biosciences, Franklin Lakes, USA; provided and owned by AG Walter Nickel, Heidelberg University Biochemistry Center).

For the experiment, $1.8x10^5$ Hek293 cells in a volume of ~2.5 ml were seeded per well into a Collagen-A coated 6-well cell culture plate. The cells were allowed to settle for about 16h before transfecting them with FuGENE HD protocol. For the transfection different amounts of plasmid DNA, either pCMV6-Entry as vector control or different eGFP expressing vectors, were used as indicated. The transfection proceeded for 48h before harvesting the cells.

To harvest the cells, cell layer was washed once by room temperature PBS. The cells were then incubated with enzyme-free Cell Dissociation Buffer (Gibco) at 37°C. The dissociated cells were transferred into a 1.5 ml micro tube and pelleted at 500 x g for 5 min at 4°C. The cell pellet was resuspended in 500 µl sorting medium (94.5%$_{(V/V)}$ DMEM w/o phenol red, 5%$_{(V/V)}$ Cell Dissociation Buffer, 0.5%$_{(W/V)}$ BSA) and the cell suspension transferred into a fresh, non-autoclaved 1.5 ml micro tube.

The measurement on FACSCalibur was performed with CellQuest Pro software (BD Biosciences). The software was used to adjust laser voltage until signal strength in the FL1 channel was below threshold (relative intensity $1x10^4$) and in a range of 285 V. For the analysis only living cells were accepted as events. The living cells ("R1") were gated from x/y- plot of sideward scatter (SSC) versus forward scatter (FSC). Usually I gated in a SSC range of 100-500 and a FSC range of 250-650. The gated events were plotted on a histogram with signal strength (counts) plotted against the relative intensity in the FL1 channel (530 nm). The cut off was determined for each set of measurements individually based on the

pCMV6-Entry vector control. The amount of events above cut off ("M1") was expressed as percentage of R1. The percentages of R1 (called %Gated) were plotted as grouped bars in GraphPad Prism 5.04 (GraphPad Software, La Jolla, USA).

4.5 SDS-PAGE and Western blotting

Protein samples were separated by sodium dodecyl sulfate–polyacrylamide gel electrophoresis (SDS-PAGE) and subsequently blotted on a Polyvinylidene fluoride (PVDF) membrane (MerckMillipore). The size of proteins was approximated from Prestained protein standard.

To prepare the proteins, samples were incubated with SDS sample buffer (adapated with modifications from Laemmli (177): 0.1 M Tris-$HCl_{(aq)}$ pH 8.3, 4 M Urea, 10%$_{(V/V)}$ glycerol, 12%$_{(W/V)}$ SDS, 0.01%$_{(W/V)}$ bromophenol blue, optional for reducing conditions: 50 mM DTT) at 70°C for 15 min and 1000 rpm on Eppendorf ThermoMixer C (Hamburg, Germany). The preparation was spun down for 2 min at 4000 x g. The samples were loaded with gel loading tips on 3-8% Tris-Acetate gels (Invitrogen) or 7% or 10% self-casted SDS-PAGE gels. The samples were separated in 1x Tris-Acetate running buffer (diluted with ddH_20) or 1x SDS Running buffer (0.0248 mM Tris, 0.1944 mM glycine, 0.00346 mM SDS), respectively. In addition to that, NuPAGE Antioxidant (Invitrogen, NP0005) was applied in Tris-Acetate gel systems. In Tris-Acetate gel systems, samples were allowed to enter the gel at 75 $V_{(const.)}$, then proteins were separated at 150 $V_{(const.)}$. Bio-Rad Mini-PROTEAN Tetra Cel systems (Hercules, USA) were run initially at a 100 $V_{(const.)}$, then proteins were separated at 150 $V_{(const.)}$.

The gels were blotted on PVDF membrane in a Mini Trans-Blot cell (Bio-Rad). In the cell, the gel was fixed in the gel holder cassette by paper for chromatography (Macherey-Nagel). The blotting in the cell ran at 100 $V_{(const.)}$ for 70 min at room temperature (cooling element included) or for 16 h at 30 $V_{(const.)}$ (8°C cold room). The blotting buffer was diluted from a 10x stock (0.248 M Tris, 1.92 M glycine) in ddH_20 and spiked with 20%$_{(V/V)}$ methanol.

To measure the membrane in digital autoradiography, the membrane was washed for 1 h in ddH_20 and dried for 24 h at room temperature. For immunoblotting, the PVDF membrane was blocked with 5%$_{(W/V)}$ powdered milk in PBS for 1 h at room temperature.

4.5.1 Digital autoradiography of PVDF membranes

Dried PVDF western blot membranes were fixed with adhesive tape on Tritium samples holder cassette (provided by Biospace, Paris, France). On the fixed PVDF membrane, I spotted [^{3}H]-GTP dissolved in 30% $MeOH_{(aq)}$ besides the prestained protein standard to visualize the bands in the autoradiography.

The membrane was imaged for 24 h by digital autoradiography (b-Imager 2000; Biospace, Paris, France). The settings were preset by Biospace. In short, the isotope selection in the acquisition control window was set to "3H" and zoom selection to "Full Field (200*250 mm)". The stop condition was fixed to an acquisition time of 24 h. The results were quantified with Image Studio Lite Ver 5.2.5 (LI-COR Biosciences, Lincoln, USA). The results were plotted with GraphPad Prism 5.04.

Imaged membranes were reactivated for 5 min in methanol and washed for 30 min in Radiolabeling wash buffer (PBS, 20%$_{(V/V)}$ methanol). Residual methanol was removed from the membrane by gentle agitation in PBS. The membrane was finally blocked by 5%$_{(W/V)}$ powdered milk in PBS for 1 h at room temperature.

4.5.2 Protein Immunoblotting

Protein Immunoblotting was used to detect, visualize and quantify proteins blotted on PVDF membranes. In brief, the membranes were decorated with an animal-derived primary antibodies from rabbit or mouse (Table 4.13). The primary antibody was recognized by a secondary antibody coupled to an infrared dye (Table 4.14).

PVDF membranes blocked with skim milk were washed with Immunoblot wash buffer (PBS, 0.1%$_{(V/V)}$ Tween-20) under gentle agitation for 3x 5 min. The primary antibody was diluted in Immunoblot incubation buffer (PBS, 0.1%$_{(V/V)}$ Tween-20, 2.5%$_{(W/V)}$ BSA) as indicated (Table 4.13). To remove unspecifically bound primary antibodies, the blot was washed in Immunoblot wash buffer.

Table 4.13 | List of primary antibodies. All primary antibodies were diluted in Immunoblot incubation buffer (PBS, 0.1%$_{(V/V)}$ Tween-20, 2.5%$_{(W/V)}$ BSA).

Name	Supplier	Manufacturer product number (Purchase order number)	Host	Epitope (peptide)/ Immunogen	Dilution
Monoclonal ANTI-FLAG® M2	SigmaAldrich	F1804	Mouse (monoclonal)	DYKDDDDK	1:1000
Anti-DDDDK tag	Abcam	ab1162	Rabbit (polyclonal)	xxxDDDDK	1:5000
Anti-GAPDH [6C5]	Abcam	ab8245	Mouse (polyclonal)	Rabbit muscle GAPDH	1:5000
anti-C Myc	Novus Biologicals	NB600-336	Rabbit (polyclonal)	Human c-Myc protein (385-435)	1:1000
anti-Calnexin	Enzo Lifesciences	ADI-SPA-860-D	Rabbit (polyclonal)	C-terminus of dog calnexin	1:1000

As the primary antibodies, the secondary antibodies were diluted in Immunoblot incubation buffer (Table 4.14). The blots were incubated with secondary antibody either for 1 h at room temperature or for 16 h at 8°C in cold room. After incubation, the blots were washed under gentle agitation for 3x 5 min in Immunoblot wash buffer. All immunoblots were scanned on an Odyssey CLx-1014 (LI-COR) controlled with ImageStudio Ver 5.0 (LI-COR). The settings were adopted for immunoblots as suggested by manufacturer. In brief, the focus was set to 0.0 mm at a resolution of 42 µm. The intensity was adjusted as indicated.

Table 4.14 | List of secondary antibodies. All secondary antibodies were diluted in Immunoblot incubation buffer (PBS, 0.1%$_{(V/V)}$ Tween-20, 2.5%$_{(W/V)}$ BSA).

Name	Supplier	Manufacturer product number (Purchase order number)	Host	Label	Dilution
Anti-Mouse IgG IRDye 800CW	Rockland	610-731-002	Donkey	IRDye 800CW	1:10000
Anti-Mouse AlexaFluor 680	ThermoFisher	A-21057	Goat	Alexa Fluor 680	1:10000
Anti-Rabbit IgG Alexa Fluor 680	ThermoFisher	A-21076	Goat	Alexa Fluor 680	1:10000
Anti-Rabbit IgG IRDye 800CW	Rockland	611-131-002	Goat	IRDye 800CW	1:10000

Immunoblots were processed and quantified with Image Studio Lite Ver 5.2.5 (LI-COR). The software was used to crop and rotate blots as needed. Signals on blot were quantified using the build-in analysis tool of Image Studio Lite. In short, bands were bordered by a rectangular region of interest with background mode “Median”. The border width of the background

mode was set to 3 pixels with segment mode “all”. The output value “Signal” was used for all further analysis and plotting in GraphPad Prism 5.04.

4.6 Thin layer chromatography

Thin layer chromatography (TLC) was used to separate lipid extracts on a silica glass plate support. The protocol was adopted from Haberkant, Schmitt (78).

For lipid preparation, the cell layer was washed twice with room temperature PBS after labeling. The cells were then scraped in PBS and membranes pelleted at 17.000 x g for 5 min at 4°C. The pellet was overlaid with 100 µl methanol and vortexed twice for 10 sec (Vortex, Bohemia, USA). The vortexed extract was cleared by centrifugation (17.000 x g, 10 min, 4°C). After centrifugation, 80 µl supernatant were sampled and stored at -20°C until further use.

To quantify β-decay of tritium, the lipid extract was subjected to scintillation counting on LS-6000TA (Beckmann Coulter, Brea, USA). The counts per minute (CPM) in 2 µl lipid extract were measured in 5 ml LSC-Cocktail. The LSC-Cocktail was measured for 1 min returning the averaged CPM. The averaged CPM was used to calculate the activity in µCi with the formula $CPMx45x10^{-7}$. The formula assumed a counting efficiency of 10% for tritium and a conversion factor of $4.5x10^{-13}$ from decays per minute (DPM) to Ci.

For the TLC I spotted lipid extract with a total activity of 0.075 µCi per lane on a Silica gel 60 TLC plate. The plate was developed in cholorform:methanol:water (65:25:4, v/v/v), dried for 24 h and subjected to digital autoradiography on β-Imager 2000 (Biospace). During the autoradiography, the developed Silica gel 60 plate was supported by a 2 mm glass plate in the tritium cassette. The β-decay was measured with isotope selection “3H” and zoom selection set to “Full Field (200*250 mm)”. The results were quantified with Fiji 1.51n (National Institute of Health, USA) or Image Studio Lite Ver 5.2.5 (LI-COR). The results were plotted with GraphPad Prism 5.04.

4.7 Cysteine crosslink assay

The protocol for cysteine crosslinking was adopted with modifications from Xue, Rovira (121). The cysteines were introduced on the background of a C121A mutation in the

exoplasmic domain yielding $GRM2^{C121A/xC}$ double mutants expressed from pCMV6-Entry vectors (Section 4.2.7).

For the experiment, $1.8x10^5$ Hek293 cells in a volume of ~2.5 ml were seeded per well into a Collagen-A coated 6-well cell culture plate. The cells were allowed to settle for about 16 h before transiently transfecting them with FuGENE HD protocol (Section 4.3.7). For the transfection, cells were incubated with 250 ng pCMV6_$GRM2^{C121A/xC}$_ MycFlag double mutants.

The transfection was stopped after 48 h and the cell layer washed twice with cold PBS. For the *in vivo* cysteine crosslink, the cells were incubated with freshly prepared Crosslink buffer (1.5 mM Dichloro(1,10-phenanthroline)copper(II), 16.7 mM Tris-$HCl_{(aq)}$ pH 8.0, 1 mM $CaCl_2$, 5 mM $MgCl_2$, 100 mM NaCl) for 20 min at room temperature under gentle agitation. After the incubation, the reaction was stopped by washing the cells once with Crosslink quenching buffer (PBS, 10 mM NEM) on ice. The cells were incubated with Crosslink quenching buffer another 15 min at 8°C (cold room) under gentle agitation. To harvest the cells, the cell layer was washed once with cold PBS and cells were scraped off and membranes pelleted for 10 min at 17.000 x g at 4°C. The cell pellet was lysed in 100 µl RIPA buffer (50 mM Tris-$HCl_{(aq)}$ pH 7.4, 150 mM NaCl, 1%$_{(V/V)}$ NonIdetP-40, 0.5%$_{(W/V)}$ Sodium deoxycholate, 0.1%$_{(W/W)}$ SDS) spiked with Protease inhibitor complete. The lysis was allowed to proceed for 1 h at 8°C (cold room) by overhead mixing on rotator at 50 U/min.

The lysate was cleared for 30 min at 12.000 x g and 4°C. 20 µl supernatant (20%) were sampled after centrifugation and incubated with 20 µl LDS sample buffer at 37°C for 10 min. 20 µl of the incubation mix (= 10% of total lysate) were separated on a 3-8% Tris-Acetate gel and subjected to immunoblotting as described in section 4.5.

4.8 Surface Biotinylation

Surface biotinylation of cell surface proteins was employed to deteremine the relative surface arrival of proteins as compared to the total expression level in the cell.

For the experiment, $1.8x10^5$ Hek293 cells in a volume of ~2.5 ml were seeded per well into a Collagen-A coated 6-well cell culture plate. The cells were allowed to settle for about 16 h and then were transiently transfected using the FuGENE HD protocol (Section 4.3.7). For the assay, the cells were either transfected with different amounts of pCMV6_GRM2_Flag

plasmid DNA or fixed amounts of corresponding alanine variants (Section 4.2.9) as indicated. For the set of GPCRs, different C-terminally Flag-tagged pCMV6-Entry constructs (Section 4.2.10) were used as indicated at a concentration of 500 ng per well. For all assays pCMV6_ASGRI_MycFlag was used as positive and pCMV-Entry as vector control.

The transfection was stopped after 48 h by washing the cell layer twice with $PBS^{Mg/Ca}$ (PBS, 1 mM $MgCl_2$, 0.1 mM $CaCl_2$). The cells were then incubated with Biotinylation incubation buffer ($8.24x10^{-4}$ M Sulfo-NHS-SS-Biotin, 10 mM triethanolamine pH 9.0, 150 mM NaCl, 2 mM $CaCl_2$) for 30 min at 8°C (cold room) under gentle agitation. To stop the NHS-esterification, the cell layer was washed once with Biotinylation quenching buffer ($PBS^{Mg/Ca}$, 100 mM glycine) and then incubated with the quenching buffer another 20 min at 8°C (cold room). The cells were finally washed twice with PBS and lysed in 300 µl HEPES lysis buffer (50 mM HEPES $NaOH_{(aq)}$ pH 7.4, 100 mM NaCl, 5 mM EDTA, 1%$_{(V/V)}$ Triton X-100, 0.5%$_{(W/V)}$ Na-Deoxycholate) spiked with Protease inhibitor complete per well.

The cells were incubated with HEPES lysis buffer for 10 min at 37°C. After incubation, the cells were scraped and lysate transferred into a 1.5 ml micro tube. The lysate was sonicated in a Sonorex RK-100 water bath at 80 W/35 kHz (Bandelin, Berlin, Germany) for 3 min at room temperature. The lysis was finalized by a 15 min incubation step at 24°C and 1200 rpm (Thermomixer C, Eppendorf, Hamburg, Germany). The lysate was cleared by centrifugation (18.000 x g, 10 min, 4°C). 200 µl supernatant were sampled and incubated with 50 µl Neutravidin bead slurry (prior to incubation washed three time with HEPES lysis buffer) over night at 8°C (cold room) by overhead mixing on rotator at 50 U/min. Another 20 µl supernatant were samples as “Input” and snap-frozen in liquid nitrogen and stored at -80°C until further use.

The next day, the loaded Neutravidin beads were spun down (3000 x g, 4°C, 1 min). After centrifugation, 20 µl “Flow-through” were sampled from the supernatant. The beads were washed three times with HEPES lysis buffer and once with Tris wash buffer (0.1 M Tris-$HCl_{(aq)}$ pH 8.3, 100 mM NaCl, 0.1 %$_{(V/V)}$ Triton X-100, 0.5 %$_{(W/V)}$ Na-Deoxycholate). After washing, the bead bed was resuspended with 40 µl reducing SDS sample buffer. 20 µl Input and Flow-through sample were mixed with 10 µl reducing SDS sample buffer. The protein samples were incubated for 30 min at 50°C and 1000 rpm (Thermomixer C).

The protein samples were cleared by centrifugation (4.000 x g, 2 min, room temperature) and loaded on a 3-8% Tris acetate gel. The samples were separated and blotted as described in section 4.5.

4.9 Deglycosylation assay

The deglyosylation was performed with either EndoH or PNGaseF (List of bioreagents, Section 4.1.2). The readout of the assay was an electrophoretic shift of the signal on the immunoblot. For the assay, $1.8x10^5$ Hek293 cells in a volume of ~2.5 ml were seeded per well into a Collagen-A coated 6-well cell culture plate. The cells were allowed to settle for about 16 h before transfecting them with FuGENE HD protocol (Section 4.3.7). The cells were transiently transfected with 500 ng pCMV6_GRM2_Flag constructs or different GPCR constructs per well as indicated. The transfection was allowed to proceed 48 h.

The transfection was stopped by placing the cell culture plates on ice and washing them twice with ice cold PBS. The cells were then scraped into cold PBS and the membranes were pelleted at 16.000 x g for 10 min at 4°C. The membrane pellet was resuspended in 100 µl HEPES lysis buffer and Protease inhibitor complete. The lysis was allowed to proceed for 2 h at 8°C (cold room) by overhead mixing on rotator at 50 U/min. The insoluble debris was pellet at 3000 x g for 10 min at 4°C. The supernatant was recovered, snap-frozen and stored at -80°C until further use.

The protein from the lysate were precipitated by Wessel-Fluegge protocol (248). For 100 µl cell lysate, subsequently 400 µl methanol, 200 µl chloroform and 300 µl deionized water were added. The sample was vortexed after each step. The phases were separated by centrifugation at 20.000 x g at room temperature for 2 min. The upper phase was removed. The interphase and the lower phase were retained and mixed with 300 µl methanol. The proteins were pelleted by centrifugation at 20.000 x g for 5 min at room temperature. The entire supernatant was taken off and the protein pellet air-dried for about 10 min in the digester.

For the PNGaseF protocol, the protein pellet was taken up in 40 µl 1x Glycoprotein Denaturing Buffer (provided with the enzyme, diluted with deionized water). The pellet was resuspended by shaking at 37°C and 1000 rpm for 10 min (Thermomixer C). Then the proteins were denatured by heating to 100°C for 10 min. Afterwards, the sample was chilled on ice and then spun down (500 x g, 1 min, 4°C). 10 µl supernatant were recovered and prepared for deglycosylation by adding 2 µl GlycoBuffer 2 (10x), 2 µl 10% NP-40 and 6 µl

ddH_20. The reaction mix was finalized by adding 1µl PNGaseF. The reaction was incubated for 1 h at 37°C. For the negative control 1 µl ddH_20 was added. For SDS-PAGE, 10 µl reducing SDS sample buffer was added and the protein sample incubated and separated as described previously (Section 4.5).

For the incubation with EndoH, the same incubation steps were followed with preparation in 1x Glycoprotein Denaturing Buffer. 10 µl supernatant were mixed with 2 µl GlycoBuffer 3 (10x) and 7 µl ddH_20. The reaction mix was finalized with 1 µl EndoH. The proteins were sampled for SDS-PAGE as described in the previous paragraph.

4.10 Non-reducing SDS-PAGE

For the non-reducing SDS-PAGE, $1.8x10^5$ Hek293 cells in a volume of ~2.5 ml were seeded per well into a Collagen-A coated 6-well cell culture plate. The cells were allowed to settle for about 16 h before transfecting them with FuGENE HD protocol (Section 4.3.7). The cells were transiently transfected with 250 ng pCMV6_GRM2_(Myc)Flag or pCMV6_GRM2^{C121A}_Flag constructs. The transfection was allowed to proceed 48 h.

The cells were washed, oxidized and crosslinked with NEM, and finally lysed as described in Section 4.7. The samples were snap-frozen and stored at -80°C until applied to SDS-PAGE. For SDS-PAGE, non-reducing SDS sample buffer was added and the protein samples were incubated and separated as described previously (Section 4.5).

4.11 Co-immunoprecipitation

For the co-immunoprecipitation of transmembrane-spanning GPCRs, three different protocols were applied. At each step, the protocol was refined to minimize unspecific binding of soluble and other transmembrane proteins while at the same time maximizing the specific binding of mGluR2 homodimers.

4.11.1 Basic co-immunoprecipitation protocol

For the basic protocol, $2.6x10^5$ Hek293 cells in a volume of ~2.5 ml were seeded per well into a Collagen-A coated 6-well cell culture plate. The cells were allowed to settle for about 16 h before transfecting them with FuGENE HD protocol (Section 4.3.7). The cells were transiently co-transfected with 250 ng pCMV6_GRM2_Flag and 250 ng

pCMV6_GRM2_Myc plasmid DNA (either GRM2 wild type or $GRM2^{C121A}$; see also Section 4.2.6). The transfection was allowed to proceed 48 h.

To stop the transfection, the cells were placed on ice and washed once with cold PBS. Cells were then scraped in 500 µl PBS/well and pelleted at 3000 x g for 10 min at 4°C. The cell pellets were resuspended in 300 µl lysis buffer on the basis of either Triton X-100 or NonIdetP-40 (Table 4.15).

Table 4.15 | Lysis buffers for co-immunoprecipitation of GPCRs. The buffers were prepared on the basis of a 50 mM HEPES-$NaOH_{(aq)}$ pH 7.4, 200 mM NaCl, 5 mM EDTA system. All buffers were spiked with Protease inhibitor complete before use.

Buffer	1.0%(V/V) Triton X-100	1.0%(V/V) NonIdetP-40	0.5%(W/V) Na-Deoxycholate	0.1%(W/V) SDS
TX100	+	−	−	−
TX100+Dx	+	−	+	−
TX100+Dx+SDS	+	−	+	+
NP40	−	+	−	−
NP40+Dx	−	+	+	−
NP40+Dx+SDS	−	+	+	+

The lysis of the cells was allowed to proceed for 2 h at 8°C (cold room) by overhead mixing on rotator at 50 U/min. The lysate was cleared by centrifugation at 18.000 x g for 30 min at 4°C. 250 µl supernatant were subjected to immunoprecipitation with 20 µl αFlag bead slurry (washed three times with corresponding buffer prior to incubation).The lysate was incubated with the beads over night at 8°C (cold room) by overhead mixing on rotator at 50 U/min. 20 µl supernatant were sampled as "Input", snap-frozen and stored at -80°C until further use.

The next day the αFlag beads were pelleted at 800 x g for 1 min at 4°C. After centrifugation, 20 µl supernatant were sampled as "Flow-through". The bead bed was washed three times with 500 µl of the corresponding lysis buffer (Table 4.15). The complete bead bed was then resuspended in 40 µl reducing SDS sample buffer. 10 µl reducing SDS sample buffer was added to 20 µl Input and Flow-through sample likewise. All protein samples were incubated for 15 min at 70°C and 1000 rpm (Thermomixer C). The protein samples were loaded on a 3-8% Tris-Acetate gel as indicated. The samples were separated and blotted as described in section 4.5.

4.11.2 Co-immunoprecipitation protocol with alkylation

For the co-immunoprecipitation protocol including an optional alkylation step, $1.6x10^5$ Hek293 cells in a volume of ~2.5 ml were seeded per well into a Collagen-A coated 6-well cell culture plate. The cells were allowed to settle for about 16 h before transfecting them with

FuGENE HD protocol (Section 4.3.7). The cells were transiently co-transfected with 250 ng pCMV6_GRM2^{C121A}_Flag and 250 ng of Myc-tagged constructs of GRM2^{C121A}, or GRM2, or ADRB2 (Sections 4.2.6 and 4.2.10.1). For each possible combination, two wells were transfected to allow for one alkylated and one untreated batch.

48 h post-transfection, one set of cells was subjected alkylation as described in section 4.7. In brief, cells were incubated with Crosslink buffer for 20 min at room temperature. After the incubation, the reaction was stopped by washing the cells once with Crosslink quenching buffer. The cells were then incubated with Crosslink quenching buffer another 15 min at 8°C (cold room). The previous steps for alkylation were skipped in the case of the negative control. To harvest the cells, the cell layer was washed twice with cold PBS and then scraped into HEPES Co-IP buffer (50 mM HEPES-$NaOH_{(aq)}$ pH 7.4, 200 mM NaCl, 5 mM EDTA, 1%$_{(V/V)}$ NonIdetP-40) prepared with Protease inhibitor complete. The lysis at 8°C (cold room) was allowed to proceed by overhead mixing on rotator at 50 U/min. After the lysis, the all insoluble debris was removed by centrifugation at 100.000 x g for 60 min at 4°C in 1.5 ml ultracentrifuge tubes. After centrifugation, 20 µl supernatant were saved as “Input” sample. Another 250 µl supernatant were incubated with 20 µl αFlag bead slurry. The αFlag beads had been washed twice times with HEPES Co-IP buffer and blocked with 2.5%$_{(W/V)}$ BSA prior to usage. The lysate was incubated with the beads over night at 8°C (cold room) by overhead mixing on rotator at 50 U/min.

The next day, the beads were pelleted at 800 x g for 1 min at 4°C. After centrifugation, 20 µl supernatant were sampled as “Flow-through”. Subsequently, the beads were washed either three times with HEPES Co-IP buffer, or once with HEPES Co-IP buffer, then Co-IP wash buffer I (50 mM HEPES-$NaOH_{(aq)}$ pH 7.4, 400 mM NaCl, 5 mM EDTA, 1%$_{(V/V)}$ NonIdetP-40), and finally with Co-IP wash buffer II (50 mM HEPES-$NaOH_{(aq)}$ pH 7.4, 400 mM NaCl, 5 mM EDTA, 0.1%$_{(V/V)}$ NonIdetP-40). The bead bed was resuspended in 40 µl reducing SDS sample buffer. 20 µl Input and Flow-through samples were prepared with 10 µl reducing SDS sample buffer. The protein samples were incubated for 15 min at 70°C and 1000 rpm (Thermomixer C). After incubation, insoluble debris was pelleted at 4000 x g for 2 min. The supernatant was loaded on a 3-8% Tris-Acetate gel as indicated. The samples were separated and blotted as described in section 4.5.

4.11.3 Co-immunoprecipitation of mGluR2 variants

The co-immunoprecipitation of mGluR2 variants was largely carried out as described in section 4.11.2 with minor changes.$1.6x10^5$ Hek293 cells in a volume of ~2.5 ml were seeded per well into a Collagen-A coated 6-well cell culture plate. 16 h after seeding, the cells were transiently transfected with using the FuGENE HD protocol (Section 4.3.7). The cells were co-transfected with either 250 ng pCMV6_GRM2_Flag or pCMV6_GRM2^{C121A}_Flag as bait, and 250 ng of corresponding Myc-tagged GRM2$^{W/Y\rightarrow A}$ variants, or ADRB2 negative control. In additional to that, 500 ng Flag- or Myc-tagged GRM2 or GRM2^{C121A} were transfected as "Flag vs Flag" or "Myc vs Myc" process controls.

Having compared the different experimental setups as described section 4.11.2, the experimental procedure was fixed to alkylation of all samples. The cells were harvested and lysed as described. The soluble supernatant after ultracentrifugation was used for immunoprecipitation. For the immunoprecipitation of "Flag vs Flag" and "Myc vs Myc" samples, 125 µl of corresponding lysate was mixed with 125 µl HEPES Co-IP buffer. For the "Lysate control" 125 µl "Flag vs Flag" and 125 µl "Myc vs Myc" were mixed and co-incubated with αFlag beads.

After overnight incubation at 8°C, the αFlag beads were pelleted and washed under stringent conditions with HEPES Co-IP buffer, and Co-IP wash buffer I and II. The different Input, Flow-through and IP samples were probed and incubated as described in the previous section. The samples were separated on a 3-8% Tris-Acetate gel and blotted as described in section 4.5.

4.12 Metabolic labeling with tritiated lipids

All radiolabeling experiments with (precursor) lipids were conducted in Hek293 cells if not stated otherwise. The preparation was conducted in the regular cell culture. For the actual labeling, the cells were transferred into Isotope laboratory. In the Isotope laboratory, all lysis steps, SDS-PAGE and western blotting steps were conducted, as well as the digital autoradiography. The final immunoblot was again performed under regular conditions. For work with lysates and proteins samples, 1.5 ml Safeseal tubes were used.

4.12.1 [^{3}H]-photo-cholesterol (protein labeling)

The radioactive [^{3}H]-photo-cholesterol was obtained as stock synthesized by Xabi Contreras with a concentration of 5 µCi/µl. The original synthesis and labeling protocol was published by Thiele, Hannah (77). For the labeling experiment, $1.8x10^5$ cells were seeded into a Collagen-A coated 6-well cell culture plate. For the DNA titration, the cells were transfected with either pCMV6_GRM2_Flag or pCMV6_GRM2^{C121A}_Flag in the amounts indicated following the FuGENE HD protocol. For later experiments with GRM2 variants, the cells were transiently transfected after ~17 h with either 250 ng of pCMV6_GRM2_Flag or 375 ng of pCMV6_GRM2^{C121A} _Flag and the corresponding W,Y→A single or double mutant constructs. As controls I used corresponding amounts of pCMV6-Entry, pCMV6_ADRB2^{Wt}_Flag and pCMV6_ASGRI_MycFlag constructs. The transfections were allowed to proceed 31 h.

After the transfection, the cells were labeled for 17 h with [^{3}H]-photo-cholesterol. Both the GRM2 single mutants and the GRM2^{C121A} double mutants were labeled with 15 µCi/well (=3 µl, solvated in ethanol). For the labeling, the transfection medium was exchanged for DMEM labeling medium (DMEM, 100 U/ml penicillin, 0.1 mg/ml streptomycin, 10%$_{(V/V)}$ delipidated FBS).

After a total transfection and labeling time of 48 h, the cells were placed on a cooling block and washed twice with ice-cold PBS. For UV-irradiation, the cells were overlayed with 1 ml PBS and exposed to UV-light (Sylvania R 100 W; UV-Labortechnik, Glashuetten, Germany) for 6 min at a distance of 5 cm to the bulb. After the UV-crosslinking, the cells were scraped into PBS and membranes were pelleted at 16.000 x g for 5 min at 4°C. The membrane pellet was resuspended in 300 µl HEPES lysis buffer (spiked with Protease inhibitor complete) and spun on rotator at 50 U/min for 2 h and 6°C (cold room Isotope laboratory). After lysis, the debris was spun down (3000 x g, 10 min, 4°C). 20 µl of the supernatant were sampled as "Input" and were frozen at -20°C until further use. 270 µl were incubated overnight at 6°C (cold room Isotope laboratory) with 25 µl αFlag bead slurry (washed three times with HEPES lysis buffer prior to use).

The next day, the αFlag beads were spun down (800 x g, 1 min, 4°C) and 20 µl supernatant were sampled as "Flow-through". The bead bed was washed three times with HEPES lysis buffer and once with Tris wash buffer. The washed αFlag beads were resuspended with 30 µl reducing SDS sample buffer. Likewise, 20 µl Input sample and 20 µl Flow-through were

prepared with 10 µl reducing SDS sample buffer. All proteins sample were incubated for 15 min at 70°C and 1000 rpm (Thermomixer Comfort; Eppendorf, Hamburg, Germany). After incubation, beads and insoluble debris was removed by centrifugation at 4000 x g for 2 min at room temperature. The samples were loaded on a 3-8% Tris-Acetate gel, and separated and blotted as described in section 4.5.

The protein labeling with [^{3}H]-photo-cholesterol was determined from digital autoradiography (Section 4.5.1) and immunoblotting (Section 4.5.2).

4.12.2 [^{3}H]-(photo-)cholesterol (lipid labeling)

The comparison of tritiated cholesterol metabolism was largely conducted as described in the previous section (Section 4.12.1) with minor changes. In brief, 1.8x10^5 Hek293T cells were seeded in a Collagen-A coated 6-well cell culture plate. The cells were transiently transfected with 500 ng pCMV6_ADRB2_Flag constructs per well and labeled with either 15 µCi of the old stock of [^{3}H]-photo-cholesterol used in section 4.12.1, or a freshly opened vial which originated from the same synthesis, or commercially available [^{3}H]-cholesterol obtained as [1,2-3H(N)]-Cholesterol (PerkinElmer). After 17 h of incubation the cells were either UV-irradiated or left untreated.

Both UV-irradiated and control cells were scraped in 1 ml PBS. 800 µl were retained for protein analysis and processed as described in the previous section. The remaining 200 µl cell suspension were used for lipid extraction as described in Section 4.6. 0.075 µCi activity were spotted on each lane and separated on a TLC plate. The β-decay on the developed TLC plate was measured by digital autoradiography (β-Imager 2000).

4.12.3 [^{3}H]-photo-sphingosine (protein labeling)

[^{3}H]-photo-sphingosine was obtained as Photosphingosine, D-erythro [3-3H] from American Radiolabeled Chemicals (St. Louis, USA). The original synthesis and labeling protocol was the work of Haberkant, Schmitt (78).

For the labeling experiment, 1.2x10^5 cells were seeded into a Collagen-A coated 6-well cell culture plate. For the DNA titration, the cells were transiently transfected with pCMV6_GRM2_Flag in the amounts indicated following the FuGENE HD protocol. For later experiments with GRM2 variants, the cells were transfected after ~20 h with 500 ng of pCMV6_GRM2_Flag or the corresponding W,Y→A constructs. As controls I used

corresponding amounts of pCMV6-Entry, pCMV6_ADRB2_Flag and pCMV6_ASGRI_MycFlag constructs. The transfections were allowed to proceed 42 h.

The cells were labeled with 7.5 µCi [^{3}H]-photo-sphingosine 6 h prior to harvest. For the labeling, the cells were washed once with PBS and the transfection medium was exchanged for 2 ml DMEM labeling medium with tritiated lipids. To stop the [^{3}H]-photo-sphingosine labeling after 6 h, the cells were placed on a cooling block and washed twice with ice-cold PBS. For UV-irradiation, the cells were overlayed with 1 ml PBS and exposed to UV-light for 6 min at a distance of 5 cm to the bulb (Sylvania R 100 W). After the UV-crosslinking, the cells were scraped into PBS and membranes pelleted at 16.000 x g for 5 min at 4°C. The membrane pellet was resuspended in 300 µl HEPES lysis buffer (prepared with Protease inhibitor complete) and spun on rotator at 50 U/min for 2 h and 6°C (cold room Isotope laboratory). After lysis, the debris was spun down (3000 x g, 10 min, 4°C). 20 µl of the supernatant were sampled as "Input" and frozen at -20°C until further use. 270 µl were incubated overnight at 6°C (cold room Isotope laboratory) with 25 µl αFlag bead slurry (washed three times with HEPES lysis buffer prior to use).

The next day, the αFlag beads were spun down (800 x g, 1 min, 4°C) and 20 µl supernatant were sampled as "Flow-through". The bead bed was washed three times with HEPES lysis buffer and once with Tris wash buffer. The washed αFlag beads were resuspended with 30 µl reducing SDS sample buffer. Likewise, 20 µl Input sample and 20 µl Flow-through were prepared with 10 µl reducing SDS sample buffer. All proteins sample were incubated for 15 min at 70°C and 1000 rpm (Thermomixer Comfort). After incubation, beads and insoluble debris was removed by centrifugation at 4000 x g for 2 min at room temperature. The samples were loaded on a 3-8% Tris-Acetate gel, and separated and blotted as described in section 4.5.

The protein labeling with [^{3}H]-photo-cholesterol was determined from digital autoradiography (Section 4.5.1) and immunoblotting (Section 4.5.2).

4.12.4 [^{3}H]-sphingosine labeling (lipid labeling)

The metabolism of tritiated sphingosine was quantified to compare different protocols for transient transfection and metabolism in Hek293 wild type and Hek293Δ*SGPL1* cells. For the experiment, ~2.6x10^5 cells were seeded per well in a Collagen-A coated 6-well cell culture plate. The cells were allowed to settle for about 16 h before transfection. The protocols for

transient transfection were used as described in section 4.3.7 with either pCMV6-Entry or pCMV6_GRM2_MycFlag constructs in the amounts indicated.

The transfection was allowed to continue for 42 h, before exchanging the medium for DMEM labeling medium prepared with [^{3}H]-sphingosine. Each well was labeled with 2 µCi activity diluted in 2 ml DMEM labeling medium. The labeling was allowed to proceed for 6 h before harvesting the cells. The cells were scraped into 1 ml PBS. The suspension was splitted into two 500 µl fractions: one for protein analysis and one for lipid analysis.

The protein analysis was conducted as described in section 4.12.3 with minor changes. In brief, cell pellets were lysed in 50 µl HEPES lysis buffer. 15 µl lysate were incubated with 15 µl reducing SDS sample buffer. The samples were separated on a 3-8% Tris acetate gel and blotted as described earlier. The blot was analyzed by immunoblotting. The lipid extraction and analysis was performed as described in section 4.6. 075 µCi activity were spotted on each lane and separated on a TLC plate. The β-decay on the developed TLC plate was measured by digital autoradiography (β-imager 2000).

4.12.5 [^{3}H]-palmitic acid

[^{3}H]-palmitic acid was obtained as [9,10-3H(N)]-Palmitic Acid from Perkin Elmer (Waltham, USA). The protocol was adapted with modifications from Paul, Bartenschlager (249). For the experiment, 1.8x10^5 cells were seeded into a Collagen-A coated 6-well cell culture plate. 17 h after seeding, the cells were transiently transfected with different C-terminally Flag-tagged GPCR constructs using the FuGENE HD protocol. The tagged GPCRs, both wild types and cysteine-to-alanine mutants, were expressed from the pCMV6-Entry expression vector (Sections 4.2.10 and 4.2.11).

The transient transfection was stopped after 44 h and the cells were starved for 1 h in 2 ml lipid-free DMEM labeling medium per well. After incubation, the medium was changed for DMEM labeling medium spiked with 160 µCi/2 ml. The cells were labeled for 3 h. After 3 h, the well plates were placed on ice and the cell layer washed twice with ice cold PBS. The cells were scraped into 800 µl cold PBS and each well was washed again with 400 µl PBS to remove residual cells. The cells were pelleted by centrifugation at 3000 x g for 10 min at 4°C. The cell pellet was resuspended in HEPES lysis buffer prepared with Protease inhibitor complete. The lysis was allowed to continue for 2 h at 6°C (cold room Isotope laboratory). Insoluble debris was spun at 16.000 x g, 5 min, 4°C. 20 µl of the supernatant were sampled as

“Input” and frozen at -20°C until further use. 260 µl were incubated overnight at 6°C (cold room Isotope laboratory) with 25 µl αFlag bead slurry (washed three times with HEPES lysis buffer prior to use) under continuous overhead mixing on rotator at 50 U/min.

The next day, the loaded αFlag beads were pelleted (800 x g, 1 min, 4°C). After centrifugation, 20 µl were sampled as “Flow-through”. The beads were batch washed three times with HEPES lysis buffer and once with Tris wash buffer. The bead bed was resuspended with 40 µl non-reducing SDS sample buffer. Likewise, 20 µl Input and Flow-through samples were prepared with 10 µl non-reducing SDS sample buffer. All proteins sample were incubated for 15 min at 70°C and 1000 rpm (Thermomixer Comfort). After incubation, beads and insoluble debris was removed by centrifugation at 4000 x g for 2 min at room temperature. The samples were loaded on a 3-8% Tris-Acetate gel, and separated and blotted as described in section 4.5.

For deacylation of samples, that is the reduction of the thioester bond between fatty acid and cysteine residue, the protein samples were incubated with a final concentration of 15% β-mercaptoethanol under the same conditions as in the previous section.

4.13 Molecular dynamics simulation in GROMACS

4.13.1 Building a transmembrane model: Modeling and Martinization

The transmembrane domain of mGluR2 (TM-mGluR2) was modeled with SWISS-MODEL online program (158-161, 250). The SWISS-MODEL template library (SMTL version 2014-10-01, PDB release 2014-09-26) was searched with Blast (163) and HHBlits (162) for evolutionary related structures matching the target sequence. Among the related structures, the crystal structure of mGluR1 was chosen to build the model of the transmembrane domain (RCSB entry 4or2.1.A, published by Wu, Wang (71)) (Figure 4.1).

```
Target    GDAWAVGPVTIACLGALATLFVLGVFVRHNATPVVKASGRELCYILLGGVFLCYCMTFIFIAKPSTAVCTLRRLGLGTAF
4or2.1.A  --------IAFSCLGILVTLFVTLIFVLYRDTPVVKSSSRELCYIILAGIFLGYVCPFTLIAKPTTTSCYLQRLLVGLSS

Target    SVCYSALLTKTNRIARIFGGAREG--AQRPRFISPASQVAICLALISGQLLIVVAWLVVEAPGTGKETAPERREVVTLRC
4or2.1.A  AMCYSALVTKTNRIARILAGSKKKICTRKPRFMSAWAQVIIASILISVQLTLVVTLIIMEPP-MPILSYPSIKEVY-LIC

Target    NHRDASMLGSLAYNVLLIALCTLYAFKTRKCPENFNEAKFIGFTMYTTCIIWLAFLPIFYVTSSDYRVQTTTMCVSVSLS
4or2.1.A  NTSNLGVVAPLGYNGLLIMSCTYYAFKTRNVPANFNEAKYIAFTMYTTCIIWLAFVPIYF--GSNYKIITTCF--AVSLS

Target    GSVVLGCLFAPKLHIILFQPQK
4or2.1.A  VTVALGCMFTPKMYIIIAKPER
```

Figure 4.1 | Sequence alignment between mGluR1 (4or2.1.A) and mGluR2 (Target) transmembrane domain using HHBlits. The sequence of the mGluR1 and mGluR2 transmembrane domain had a sequence idenity of 50.0% according to HHBlits and 52.9% according to BLAST.

For the modelling, SWISS-MODEL copied structure coordinates which were conserved between target and template. Insertion and deletions in the sequence were estimated from a fragment library. The intra- and extracellular loops were modelled with ProMod-II (250) and MODELLER (251). The pdb output was used for the further molecular biological and computational simulation work. The results of the search for evolutionary related structures are found in detail in Section 2.1.2.2.

The model of the mGluR2 transmembrane domain was martinized using martinize.py command. To prepare the atomistic PDB file as input file for martinize.py, it was converted into a GROMACS structural file with ‘gmx pdb2gmx’ with GROMACS 2016.x (179-181). The pdb file was used as input to generate the GROMACS structural file gro. In the gro file hydrogen atoms were added as well as ionized N- and C-terminal ends. With ‘gmx editconf’ the gro file was placed into a (10x10x10) nm box. The structure was relaxed with the steepest decent in 10 steps á 0.02 ps. The structural output file of the energy minimization was used as input ‘-f’ for the martinize.py command (192). The restraints for the secondary structure were defined with the web-based program DSSP (197). DSSP extracted the information about the secondary structure based on the 3D structure given in the pdb input file. The output dssp file was used as input ‘-ss’ for martinize.py. The position restrains were written to all particle positions in the output structure. For the elastic network, the upper distance bound ‘-eu’ was set to 1.1 Å (F=0 if r_{ij}>1.1 Å) and the the force field to martini22. Finally, the cut-off distance for cystine bonds was set to 0.32 nm.

4.13.2 Assembly all atom simulations

To assemble the box for the atomistic molecular dynamics simulation, the model of the mGluR2 transmembrane domain was embedded in a fully solvated POPC or POPC/CHOL bilayer using the CHARMM-GUI online program (85, 86, 252, 253). The program consisted

of several steps, starting with import of the PDB file and subsequently leading through the assembly of the system.

In the initial step 'PDB Info', the residues C70 and C159 in (TM-mGluR2 model) were considered to be connected by a disulfide bridge. The terminal groups were patched as ACE and CT2 (neutral). In the orientation option of 'Step 1', the system was aligned along the first principal axis (z). The molecule was flipped along the z-axis. In 'Step 2', basic system size determination options were assigned. The leaflets of the lipid bilayer were allowed to have a heterogeneous lipid composition. The lipid bilayer was solvated with a water layer of 17.5 Å on top and bottom. The length of x and y (lateral axis) were determined by the ratio of the lipid components and guessed with 10.5 Å in each direction. The first system was built as POPC (16:0, 18:1) system which resulted in a total of ~145 POPC molecules in each layer. In 'Step 3', the protein model was inserted into the bilayer by the replacement method with a check of the lipid ring and protein surface penetration. The ion concentration was set to a physiological salt concentration of 0.15 M NaCl with Ion placement method 'Distance'. The fourth step returned information about the successful assembly of the protein system. In 'Step 5', the system was assembled with input files for GROMACS and a parameterization in the CHARMM36 force field. The temperature was set to 310 K (generated grid information for PME fast Fourier transforms automatically).

The system was minimized and equilibrated with the mdp files generated in CHARMM-GUI (Table 4.16). The system was slowly released from its restraints in seven consecutive steps. In all steps the Verlet cut-off scheme with a cut-off distance of 1.2 Å was used. In brief, the system was minimized with the steepest decent in 5000 steps in the first cycle. The next three equilibration cycles were conducted with 25000 steps of 1 ps. The last three cycles were conducted 50000 steps of 2 ps. All equilibration steps were processed with the Berendsen barostat which was also used for temperature coupling.

For the production run, four simulation á 500 ns were run in parallel. The production run was conducted in 250×10^6 steps of 0.002 ps. The temperature was controlled by Nose-Hoover thermostat and the pressure by semiisotropic pressure coupling with the Parrinello-Rahman barostat.

Table 4.16 | MDP files provided by CHARMM-GUI for the minimization, equilibration and production run. The mdp files provided the information for GROMACS 2016.x preprocessor ('gmx grompp').

	Minimi-zation	Equilibration Step 1	Equilibration Step 2	Equilibration Step 3	Equilibration Step 4/5/6	Production
define	DREST_ON DSTEP6_0	DREST_ON DSTEP6_1	DREST_ON DSTEP6_2	DREST_ON DSTEP6_3	DREST_ON DSTEP6_4/5/6	
integrator	steep	md	md	md	md	md
dt		0.001	0.001	0.001	0.002	0.002
emtol	1000					
nsteps	5000	25000	25000	25000	50000	250000000
nstlog		1000	1000	1000	1000	1000
nstxout		1000	1000	1000	1000	10000000
nstvout		1000	1000	1000	1000	10000000
nstfout		1000	1000	1000	1000	10000000
nstcalcenergy		100	100	100	100	100
nstenergy		1000	1000	1000	1000	1000
nstxout-compressed						5000
cutoff-scheme	Verlet	Verlet	Verlet	Verlet	Verlet	Verlet
nstlist	10	20	20	20	20	20
rlist	1.2	1.2	1.2	1.2	1.2	1.2
coulombtype	pme	pme	pme	pme	pme	pme
rcoulomb	1.2	1.2	1.2	1.2	1.2	1.2
vdwtype	Cut-off	Cut-off	Cut-off	Cut-off	Cut-off	Cut-off
vdw-modifier	Force-switch	Force-switch	Force-switch	Force-switch	Force-switch	Force-switch
rvdw_switch	1	1	1	1	1	1
rvdw	1.2	1.2	1.2	1.2	1.2	1.2
tcoupl		berendsen	berendsen	berendsen	berendsen	Nose-Hoover
tc_grps		PROT MEMB SOL_ION	PROT MEMB SOL_ION	PROT MEMB SOL_ION	PROT MEMB SOL_ION	PROT MEMB SOL_ION
tau_t		1 1 1	1 1 1	1 1 1	1 1 1	1 1 1
ref_t		310 310 310	310 310 310	310 310 310	310 310 310	310 310 310
pcoupl				berendsen	berendsen	Parrinello-Rahman
pcoupltype				semiisotropic	semiisotropic	semi-isotropic
tau_p				5	5	5
compressibility				4.50E-05 4.50E-05	4.50E-05 4.50E-05	4.50E-05 4.50E-05
ref_p				1 1	1 1	1 1
constraints	none	h-bonds	h-bonds	h-bonds	h-bonds	h-bonds
constraint_ algorithm	LINCS	LINCS	LINCS	LINCS	LINCS	LINCS
continuation			yes	yes	yes	yes
nstcomm		100	100	100	100	100
comm_mode		linear	linear	linear	linear	linear
comm_grps		PROT MEMB SOL_ION	PROT MEMB SOL_ION	PROT MEMB SOL_ION	PROT MEMB SOL_ION	PROT MEMB SOL_ION
gen-vel		yes				
gen-temp		310				
gen-seed		-1				
refcoord_ scaling		com	com	com	com	com

For the run in POPC/$CHOL_{15mol\%}$, the system was generated in CHARMM-GUI for the wild type protein as described in the previous paragraph. The initial conformations for the wild type transmembrane domain had been extracted from the previous run in the POPC membrane. For the mGluR2 mutants Y745A (TM model: Y183A) and Y781A (TM model: Y213A) the target residues were mutated in Pymol 1.8.4.0. (Schroedinger, New York, USA). The mutated PDB files were inserted into the newly assembled membrane systems in the place of the wild type protein. The equilibration and production was conducted as described in the previous paragraph.

4.13.3 Coarse-grained simulations

The coarse-grained system was setup with the membrane building tool INSANE (87) using the standard Martini 2.2 force field simulation settings including the topology files for Amino acids 2.2, Lipids 2.0 and Ions 2.0 (84, 192). The martinized model of the mGluR2 transmembrane domain was inserted into either a pure POPC bilayer or into a POPC/$CHOL_{15mol\%}$ bilayer.

In the coarse-grained system two protomers were simulated in one box. In 100 parallel setups, the two martinized mGluR2 transmembrane domains were placed in the origin of an empty box of (10x10x10) nm. In the box the transmembrane domains were rotated randomly around their z-axis by an angle θ between 0° and 360° to randomize the initial starting conformation in the box. The center of mass of the second monomer was then translated 7.5 nm in the y-axis. The two separated monomers were centered in the box and used as input for INSANE.

INSANE was used to build a simulation box of (15x15x12) nm with the two protomers centered in the box and inserted into either a POPC or POPC/$CHOL_{15mol\%}$ bilayer. The membrane was solvated with CG water (each CG water represented 4 H_20 molecules) and 0.15 M NaCl. The assembled system was relaxed in $10x10^4$ steps (0.01 ps) using the Berendsen barostat (Table 4.17, Relaxation). In the Verlet cut-off scheme the Lennard-Jones interactions were shifted to zero at a distance of 1.1 nm. The production run for each simulation box was 5 μs ($25x10^7$ steps á 0.02 ps), totaling a simulated time of 0.5 ms for both setups (Table 4.17, Equilibration). The reference pressure was set to 1 bar and controlled with semiisotropic pressure coupling by Parrinello-Rahman. The temperature was set to 310 K and controlled by velocity scaling.

Table 4.17 | Relaxation and equilibration (production) mdp files for the Martini 2.2 force field. The mdp files provided the information for GROMACS 2016.x preprocessor ('gmx grompp').

Parameter	Relaxation	Equilibration
title	Martini	Martini
define	-DPOSRES	
integrator	md	md
dt	0,01	0,02
nsteps	100000	250000000
nstcomm	100	100
comm-grps	n.A.	n.A.
nstxout	0	500000
nstvout	0	500000
nstfout	0	500000
nstlog	100	5000
nstenergy	100	5000
nstxtcout	2000	5000
xtc_precision	100	1000
xtc-grps	n.A.	n.A.
energygrps	n.A.	PROTEIN1 PROTEIN2 CHOL
nstlist	10	20
ns_type	grid	grid
pbc	xyz	xyz
rlist	1,4	1,4
coulombtype	Reaction_field	Reaction_field
rcoulomb_switch	0	0
rcoulomb	1,1	1,1
epsilon_r	15	15
vdw_type	cutoff	cutoff
rvdw_switch	0,9	0,9
rvdw	1,1	1,1
cutoff-scheme	verlet	verlet
coulomb-modifier	Potential-shift	Potential-shift
vdw-modifier	Potential-shift	Potential-shift
epsilon_rf	0	0
verlet-buffer-drift	0,005	0,005
tcoupl	V-rescale	v-rescale
tc-grps	Protein_POPC_CHOL W_ION	Protein_POPC_CHOL W_ION
tau_t	1 1	1 1
ref_t	310 310	310 310
Pcoupl	berendsen	Parrinello-Rahman
Pcoupltype	semiisotropic	semiisotropic
tau_p	3	12
compressibility	n.A.	3E-4 3E-4
ref_p	n.A.	1 1
refcoord-scaling	COM	COM
gen_vel	yes	no
gen_temp	310	310
gen_seed	473529	473529
constraints	none	none
constraint_algorithm	Lincs	Lincs
continuation	no	no
lincs_order	8	8
lincs-iter	2	2
lincs_warnangle	30	30

4.13.4Analysis simulation box

The analysis of the simulation box was conducted with the GROMACS 2016.x energy function (‘gmx energy’). To extract the energy components, the *.edr and the *.xtc were of the whole trajectory were supplied along with the term for either ‘Pressure’, ‘Temperature’, ‘Volume’ or ‘Density’. The output files were converted into text files and analyzed by concatenating the corresponding values in one numeric vector in RStudio (Ver. 1.0.153). From the concatenated numeric vector minimum/maximum value, 25th and 75th percentiles (outlines of the box), median (line in the middle of the box), the difference between the 25th and 75th percentiles (inter-quartile distance), and whiskers (75th percentile plus 1.5 times inter-quartile distance, 25th percentile minus 1.5 times inter-quartile distance) were calculated. The values were plotted as Tukey boxplot using the ‘geom_boxplot’ function in ggplot2 (Version 3.0.0).

4.13.5 Analysis protein structures

The change and stability of the protein structure was quantified with GROMACS 2016.x commands ‘gmx rmsf’, ‘gmx rms’ and ‘gmx gyrate’.

The Root mean square fluctuation (RMSF) of the amino acid residue positions in the protein in the course of the trajectory was calculated by fitting it to the reference structure (amino acid residue position at t=0 ps, provided as tpr file). The command considered the whole trajectory. The output was converted into a text file and imported into RStudio (Ver. 1.0.153). The single files were concatenated into one numeric matrix (row: residue number, columns: trajectory number). From the rows the mean and standard error of mean (SEM) for each amino acid residue was calculated (total of 260 positions). The data were plotted by ggplot2 (Version 3.0.0) with the mean plotted as ‘geom_line’ and the SEM as ‘geom_ribbon’.

To calculate the Root mean square deviation (RMSD) each structure from the trajectory was compared to its reference structure at t=0 ps (provided as tpr file). This yielded a RMSD for each given measurement point in time in the course of the trajectory. The given time points t_x and the corresponding RMSD were printed as text file. The text files were imported into RStudio (Ver. 1.0.153). For any trajectory the mean was calculated and stored in a numeric vector. From the vector, the mean of means and SEM was calculated. The mean of means was plotted as ‘geom_bar’ with the SEM as ‘geom_errorbar’ in ggplot2 (Version 3.0.0).

Radius of gyration (gyration) was calculated as total gyration from the single radii of gyration in x,y and z-direction with ‘gmx gyrate’. The radius of gyration in one direction was calculated as root-mean-square of the radii components orthogonal to the axis. The gyration of the proteins was analyzed the same way as described in the previous paragraph for the RMSD.

4.13.6 Analysis membrane system

4.13.6.1 Lipid density profile

The lipid density profile was calculated with the GROMACS 2016.x command ‘gmx density’. For the calculation, different index groups were considered. Water and cholesterol index groups remained unchanged. The POPC index group was split into ‘head’ (choline and glycerol moiety) and ‘tail’ (acyl chains) group. For the atomistic simulations, the atom types ‘N’ – ‘C3’ were considered as ‘head’, and the types ‘C21’ – ‘C316’ as ‘tails’. In the coarse-grained simulations, the atom types ‘NC3’ – ‘GL2’ were indexed as ‘head’ group, and ‘C1A’ – ‘C4B’ as ‘tails’. The density was calculated as normal on the membrane in direction of z and relative to the center of the (changing) box.

The density calculation was stored as text file giving the averaged density for the given index group at each measurement point in z-direction. The text files were imported into RStudio (Ver. 1.0.153). The single files were concatenated into one numeric matrix (row: z-axis, columns: trajectory). From the rows the mean and SEM for each point on the z-axis was calculated. The data were plotted by ggplot2 (Version 3.0.0) with the mean plotted as ‘geom_line’ and the SEM as ‘geom_ribbon’.

4.13.6.2 Deuterium order parameter

For the atomistic simulations, the fatty acid moieties of the POPC index group were split into the SN1 and SN2 group. The SN1 index group considered 18 atom indices from ‘C21’ - ‘C218’ and the SN2 index group 16 atom indices from ‘C31’ - ‘C316’. For each index group the Deuterium order parameter was calculated separately using the GROMACS 2016.x command ‘gmx order’ with direction of the normal on the membrane set to the z-axis. The output text file was imported into RStudio (Ver. 1.0.153). The single files were concatenated into one numeric matrix (row: acyl chain index, columns: trajectory). From the rows the mean and SEM for each atom in the acyl chain was calculated. The data were plotted by ggplot2

(Version 3.0.0) with the mean plotted as ‘geom_point’ and the SEM plotted as ‘geom_errorbar’. The points were connected by ‘geom_line’.

For the martini simulation, the Deuterium order parameter was analyzed with the do-order-gmx5.py command. The command was set with an initial time of $5x10^3$ ps and finished at $5x10^6$ ps with one in ten frames considered. The absolute number of POPC molecules in each system was retrieved with the ‘grep’ command from the topology file. The output file ‘deuter_raw’ was imported into RStudio (Ver. 1.0.153). The single files were concatenated into one numeric matrix (row: ‘GL-C1’, ‘C1-C2/D2’, ‘C2/D2-C3’, ‘C3-C4’, columns: trajectory). From the rows the mean and SEM for each of the four beads was calculated. The data were plotted by ggplot2 (Version 3.0.0) with the mean plotted as ‘geom_point’ and the SEM plotted as ‘geom_errorbar’. The points were connected by ‘geom_line’.

4.13.6.3 Lipid diffusion by mean square displacement

The lipid diffusion constant was calculated both for the whole POPC molecule as well as for the phosphate group only. The later one was indexed for the calculation.

The diffusion constant D was calculated using the GROMACS 2016.x command ‘gmx msd’. The value D is obtained by a least squares fitting of the linear relationship (D*t+c) through the mean square displacement (MSD) of time (t) of the indexed group. The lateral diffusion was calculated in a plane perpendicular to z-axis. The first frame in the trajectory was at $5x10^4$ ps with the time between the restarting points in trajectory set to $1x10^3$ ps. The start and end time for fitting was set to $1x10^3$ ps and $1x10^5$ ps respectively. The calculated averaged diffusion constant was printed by GROMACS 2016.x in an output text file. The output text file was imported into RStudio (Ver. 1.0.153). The respective value was retrieved from the 3rd line of the output file, which had been broken up with the ‘strsplit’ command and converted into a numeric. The numerics of the diffusion constant for one set of trajectories were collected in a numeric vector from which the mean and SEM were calculated. The mean values were plotted as ‘geom_bar’ with SEM as ‘geom_errorbar’ in ggplot2 (Version 3.0.0).

4.13.7 Cholesterol density analysis

Both the cholesterol density maps for the atomistic and the coarse-grained simulation were calculated using gtide. In all cases the density maps were calculated from concatenated trajectory files containing only cholesterol and protein molecules considering only cholesterol molecules within a given distance from the protein surface.

4.13.7.1 Coarse-grained systems

To get a density map for cholesterol binding in coarse-grained simulation, the protomers had to be separated and the cholesterols next to them along with them. From the cholesterol molecules below threshold distance, the density map was calculated.

With the script 'get_one-protomer-one-chol-in-sequence.sh', the protomers were assigned to two different index groups. Then the minimum distance between the two protomers was calculated with the command 'gmx mindist'. The protomers in a proximity of <0.5 nm were considered to be dimerized at the given time point in the trajectory. Then the cholesterol molecules were given seperated indices. From the distance between the cholesterol molecules and the protomers it was calculated whether the cholesterol molecules were unbound (>0.5 nm), attached to monomeric protomer A or B, or bound to the respective protomers in the dimer structure. From that snapshots, the script 'cat_one-chol_trajs.sh' concatenated a trajectory dimer and nodimer. The third script 'add_helices.sh' added the information about the exact length of the helices to the reference pdb. With the fourth script 'get_cholesterol_density.sh' the information about cholesterol bound to dimerized or monomeric transmembrane domains was extracted with gtide from the corresponding concatenated trajectories. The denisty map was plotted as 'isosurface mesh' in Pymol (Ver. 1.0.153) on the 'dimer' and 'nodimer' reference pdb.

4.13.7.2 Atomistic systems

To run the gtide script, the original trajectories were prepared with GROMACS 2016.x 'gmx trjconv'. For the output trajectories only a common index group of the protein and the cholesterol molecules was considered skipping the first $5x10^4$ ps of the original file. In the second step, the output trajectories were concatenated. The concatenated trajectories were then fitted (rotation and translation) against the starting structure of the original trajectory. The starting time 't_0' and the time step between input frames 'timestep' were set to 1 ps.

The concatenated and fitted trajectories with the protein and cholesterol molecules were used as input for gtide. The program considered the starting structure of the respective trajectory as reference to build a cholesterol density map in a proximity of 0.8 nm and at a resolution of 0.1 nm around the surface of the protein. The density maps were plotted as 'isosurface mesh' in Pymol (Ver. 1.0.153) with confidence interval σ set to the indicated values.

5 References

1. Beedle AEM, Williams A, Relat-Goberna J, Garcia-Manyes S. Mechanobiology—chemical origin of membrane mechanical resistance and force-dependent signaling. Current Opinion in Chemical Biology. 2015 2015/12/01/;29:87-93.

2. Holthuis JC, Levine TP. Lipid traffic: floppy drives and a superhighway. Nature reviews Molecular cell biology. 2005 Mar;6(3):209-20. PubMed PMID: 15738987. Epub 2005/03/02. eng.

3. van Meer G, Voelker DR, Feigenson GW. Membrane lipids: where they are and how they behave. Nature reviews Molecular cell biology. 2008 Feb;9(2):112-24. PubMed PMID: 18216768. Pubmed Central PMCID: PMC2642958. Epub 2008/01/25. eng.

4. Mouritsen OG. Model answers to lipid membrane questions. Cold Spring Harbor perspectives in biology. 2011 Sep 1;3(9):a004622. PubMed PMID: 21610116. Pubmed Central PMCID: PMC3181035. Epub 2011/05/26. eng.

5. Contreras FX, Ernst AM, Wieland F, Brugger B. Specificity of intramembrane protein-lipid interactions. Cold Spring Harbor perspectives in biology. 2011 Jun 1;3(6). PubMed PMID: 21536707. Pubmed Central PMCID: PMC3098675. Epub 2011/05/04. eng.

6. Vanni S, Hirose H, Barelli H, Antonny B, Gautier R. A sub-nanometre view of how membrane curvature and composition modulate lipid packing and protein recruitment. Nature communications. 2014;5:4916.

7. Haslam RJ, Koide HB, Hemmings BA. Pleckstrin domain homology. Nature. 1993;363(6427):309.

8. Holz RW, Hlubek MD, Sorensen SD, Fisher SK, Balla T, Ozaki S, et al. A pleckstrin homology domain specific for phosphatidylinositol 4, 5-bisphosphate (PtdIns-4, 5-P2) and fused to green fluorescent protein identifies plasma membrane PtdIns-4, 5-P2 as being important in exocytosis. J Biol Chem. 2000;275(23):17878-85.

9. Soccio RE, Breslow JL. StAR-related lipid transfer (START) proteins: mediators of intracellular lipid metabolism. The Journal of biological chemistry. 2003 Jun 20;278(25):22183-6. PubMed PMID: 12724317. Epub 2003/05/02. eng.

10. Horibata Y, Sugimoto H. StarD7 mediates the intracellular trafficking of phosphatidylcholine to mitochondria. The Journal of biological chemistry. 2010 Mar 5;285(10):7358-65. PubMed PMID: 20042613. Pubmed Central PMCID: PMC2844184. Epub 2010/01/01. eng.

11. Soccio RE, Adams RM, Romanowski MJ, Sehayek E, Burley SK, Breslow JL. The cholesterol-regulated StarD4 gene encodes a StAR-related lipid transfer protein with two closely related homologues, StarD5 and StarD6. Proceedings of the National Academy of Sciences. 2002;99(10):6943-8.

12. Harlan JE, Hajduk PJ, Yoon HS, Fesik SW. Pleckstrin homology domains bind to phosphatidylinositol-4,5-bisphosphate. Nature. 1994 09/08/online;371:168.

13. Escriba PV, Wedegaertner PB, Goni FM, Vogler O. Lipid-protein interactions in GPCR-associated signaling. Biochimica Et Biophysica Acta-Biomembranes. 2007 Apr;1768(4):836-52. PubMed PMID: WOS:000245972500008.

14. Fredriksson R, Lagerstrom MC, Lundin LG, Schioth HB. The G-protein-coupled receptors in the human genome form five main families. Phylogenetic analysis, paralogon groups, and fingerprints. Molecular Pharmacology. 2003 Jun;63(6):1256-72. PubMed PMID: WOS:000183013900010.

15. Pin JP, Galvez T, Prezeau L. Evolution, structure, and activation mechanism of family 3/C G-protein-coupled receptors. Pharmacology & Therapeutics. 2003 Jun;98(3):325-54. PubMed PMID: WOS:000183588400004.

16. Lagerstrom MC, Schioth HB. Structural diversity of G protein-coupled receptors and significance for drug discovery. Nature Reviews Drug Discovery. 2008 Apr;7(4):339-57. PubMed PMID: WOS:000254561500016.

17. Davenport AP, Alexander SPH, Sharman JL, Pawson AJ, Benson HE, Monaghan AE, et al. International Union of Basic and Clinical Pharmacology. LXXXVIII. G Protein-Coupled Receptor List: Recommendations for New Pairings with Cognate Ligands. Pharmacological Reviews. 2013 Jul;65(3):967-86. PubMed PMID: WOS:000320986500004.

18. Foord SM, Bonner TI, Neubig RR, Rosser EM, Pin JP, Davenport AP, et al. International Union of Pharmacology. XLVI. G protein-coupled receptor list. Pharmacological Reviews. 2005 Jun;57(2):279-88. PubMed PMID: WOS:000229305700007.

19. Liang Y-L, Khoshouei M, Radjainia M, Zhang Y, Glukhova A, Tarrasch J, et al. Phase-plate cryo-EM structure of a class B GPCR–G-protein complex. Nature. 2017 04/24/online;546:118.

20. Cherezov V, Rosenbaum DM, Hanson MA, Rasmussen SGF, Thian FS, Kobilka TS, et al. High-resolution crystal structure of an engineered human beta(2)-adrenergic G protein-coupled receptor. Science. 2007 Nov;318(5854):1258-65. PubMed PMID: WOS:000251086600033.

21. Fukata M, Fukata Y, Adesnik H, Nicoll RA, Bredt DS. Identification of PSD-95 Palmitoylating Enzymes. Neuron. 2004 2004/12/16/;44(6):987-96.

22. Chini B, Parenti M. G-protein-coupled receptors, cholesterol and palmitoylation: facts about fats. Journal of Molecular Endocrinology. 2009 May-Jun;42(5-6):371-9. PubMed PMID: WOS:000272630500002.

23. Ohno Y, Kihara A, Sano T, Igarashi Y. Intracellular localization and tissue-specific distribution of human and yeast DHHC cysteine-rich domain-containing proteins. Biochimica et Biophysica Acta (BBA)-Molecular and Cell Biology of Lipids. 2006;1761(4):474-83.

24. Percherancier Y, Planchenault T, Valenzuela-Fernandez A, Virelizier J-L, Arenzana-Seisdedos F, Bachelerie F. Palmitoylation-dependent control of degradation, life span and membrane expression of the CCR5 receptor. J Biol Chem. 2001.

25. Loisel TP, Ansanay H, Adam L, Marullo S, Seifert R, Lagacé M, et al. Activation of the β2-adrenergic receptor-Gαs complex leads to rapid depalmitoylation and inhibition of repalmitoylation of both the receptor and Gαs. J Biol Chem. 1999;274(43):31014-9.

26. Renner U, Glebov K, Lang T, Papusheva E, Balakrishnan S, Keller B, et al. Localization of the mouse 5-Hydroxytryptamine(1A) receptor in lipid Microdomains depends on its palmitoylation and is involved in receptor-mediated signaling. Molecular Pharmacology. 2007 Sep;72(3):502-13. PubMed PMID: WOS:000248976400003.

27. Blaskovic S, Blanc M, van der Goot FG. What does S-palmitoylation do to membrane proteins? Febs Journal. 2013 Jun;280(12):2766-74. PubMed PMID: WOS:000320037900005.

28. Jiang H, Zhang X, Chen X, Aramsangtienchai P, Tong Z, Lin H. Protein Lipidation: Occurrence, Mechanisms, Biological Functions, and Enabling

Technologies. Chem Rev. 2018 Feb 14;118(3):919-88. PubMed PMID: 29292991. Pubmed Central PMCID: PMC5985209. Epub 2018/01/03. eng.

29. Kokkola T, Kruse C, Roy-Pogodzik EM, Pekkinen J, Bauch C, Honck HH, et al. Somatostatin receptor 5 is palmitoylated by the interacting ZDHHC5 palmitoyltransferase. FEBS Lett. 2011 Sep 2;585(17):2665-70. PubMed PMID: 21820437. Epub 2011/08/09. eng.

30. Resh MD. Fatty acylation of proteins: The long and the short of it. Progress in Lipid Research. 2016 2016/07/01/;63:120-31.

31. Ren J, Wen L, Gao X, Jin C, Xue Y, Yao X. CSS-Palm 2.0: an updated software for palmitoylation sites prediction. Protein engineering, design & selection : PEDS. 2008 Nov;21(11):639-44. PubMed PMID: 18753194. Pubmed Central PMCID: PMC2569006. Epub 2008/08/30. eng.

32. Michaelson D, Ahearn I, Bergo M, Young S, Philips M. Membrane trafficking of heterotrimeric G proteins via the endoplasmic reticulum and Golgi. Molecular biology of the cell. 2002;13(9):3294-302.

33. Smotrys JE, Linder ME. Palmitoylation of intracellular signaling proteins: regulation and function. Annu Rev Biochem. 2004;73:559-87. PubMed PMID: 15189153. Epub 2004/06/11. eng.

34. Wilcox C, Hu J-S, Olson EN. Acylation of proteins with myristic acid occurs cotranslationally. Science. 1987;238(4831):1275-8.

35. Chisari M, Saini DK, Kalyanaraman V, Gautam N. Shuttling of G protein subunits between the plasma membrane and intracellular membranes. The Journal of biological chemistry. 2007 Aug 17;282(33):24092-8. PubMed PMID: 17576765. Pubmed Central PMCID: PMC2238717. Epub 2007/06/20. eng.

36. Allen JA, Jiang ZY, Donati RJ, Rasenick MM. β-Adrenergic receptor stimulation promotes Gαs internalization through lipid rafts: a study in living cells. Molecular pharmacology. 2005.

37. Wedegaertner PB, Bourne HR. Activation and depalmitoylation of Gsα. Cell. 1994;77(7):1063-70.

38. Clarke S. Protein isoprenylation and methylation at carboxyl-terminal cysteine residues. Annual review of biochemistry. 1992;61(1):355-86.

39. Lee AG. Lipid-protein interactions. Biochemical Society Transactions. 2011 Jun;39:761-6. PubMed PMID: WOS:000292238100009.

40. Lee AG. How lipids affect the activities of integral membrane proteins. Biochimica Et Biophysica Acta-Biomembranes. 2004 Nov 3;1666(1-2):62-87. PubMed PMID: WOS:000225210100006.

41. Marsh D. Energetics of Hydrophobic Matching in Lipid-Protein Interactions. Biophysical Journal. 2008 2008/05/15/;94(10):3996-4013.

42. Niu S-L, Mitchell DC, Lim S-Y, Wen Z-M, Kim H-Y, Salem N, et al. Reduced G protein-coupled signaling efficiency in retinal rod outer segments in response to n-3 fatty acid deficiency. J Biol Chem. 2004.

43. Soubias O, Teague WE, Gawrisch K. Evidence for specificity in lipid-rhodopsin interactions. J Biol Chem. 2006;281(44):33233-41.

44. Mitchell DC, Niu SL, Litman BJ. Enhancement of G protein-coupled signaling by DHA phospholipids. Lipids. 2003 Apr;38(4):437-43. PubMed PMID: WOS:000183577400019.

45. Hanson MA, Cherezov V, Griffith MT, Roth CB, Jaakola V-P, Chien EYT, et al. A specific cholesterol binding site is established by the 2.8 angstrom structure of the human beta(2)-adrenergic receptor. Structure. 2008 Jun;16(6):897-905. PubMed PMID: WOS:000256816200010.

46. Ballesteros JA, Weinstein H. [19] Integrated methods for the construction of three-dimensional models and computational probing of structure-function relations in G protein-coupled receptors. In: Sealfon SC, editor. Methods in Neurosciences. 25: Academic Press; 1995. p. 366-428.

47. Manna M, Niemelä M, Tynkkynen J, Javanainen M, Kulig W, Müller DJ, et al. Mechanism of allosteric regulation of β2-adrenergic receptor by cholesterol. eLife. 2016 2016/11/29;5:e18432.

48. Prasanna X, Chattopadhyay A, Sengupta D. Cholesterol Modulates the Dimer Interface of the β2-Adrenergic Receptor via Cholesterol Occupancy Sites. Biophysical Journal. 2014 2014/03/18/;106(6):1290-300.

49. Gimpl G, Fahrenholz F. Cholesterol as stabilizer of the oxytocin receptor. Biochimica et Biophysica Acta (BBA)-Biomembranes. 2002;1564(2):384-92.

50. Paila YD, Jindal E, Goswami SK, Chattopadhyay A. Cholesterol depletion enhances adrenergic signaling in cardiac myocytes. Biochimica et Biophysica Acta (BBA) - Biomembranes. 2011 2011/01/01/;1808(1):461-5.

51. Pontier SM, Percherancier Y, Galandrin S, Breit A, Galés C, Bouvier M. Cholesterol-dependent Separation of the β2-Adrenergic Receptor from Its

Partners Determines Signaling Efficacy INSIGHT INTO NANOSCALE ORGANIZATION OF SIGNAL TRANSDUCTION. J Biol Chem. 2008;283(36):24659-72.

52. Li H, Papadopoulos V. Peripheral-Type Benzodiazepine Receptor Function in Cholesterol Transport. Identification of a Putative Cholesterol Recognition/Interaction Amino Acid Sequence and Consensus Pattern**This work was supported by grant number ES-07747 from the National Institute of Environmental Health Sciences, NIH (to V.P.). Endocrinology. 1998;139(12):4991-7.

53. Baier CJ, Fantini J, Barrantes FJ. Disclosure of cholesterol recognition motifs in transmembrane domains of the human nicotinic acetylcholine receptor. Sci Rep. 2011;1:69. PubMed PMID: 22355588. Pubmed Central PMCID: PMC3216556. Epub 2012/02/23. eng.

54. Fantini J, Di Scala C, Baier CJ, Barrantes FJ. Molecular mechanisms of protein-cholesterol interactions in plasma membranes: Functional distinction between topological (tilted) and consensus (CARC/CRAC) domains. Chemistry and Physics of Lipids. 2016 2016/09/01/;199:52-60.

55. Eroglu C, Brugger B, Wieland F, Sinning L. Glutamate-binding affinity of Drosophila metabotropic glutamate receptor is modulated by association with lipid rafts. Proc Natl Acad Sci U S A. 2003 Sep;100(18):10219-24. PubMed PMID: WOS:000185119300017.

56. Kumari R, Castillo C, Francesconi A. Agonist-dependent Signaling by Group I Metabotropic Glutamate Receptors Is Regulated by Association with Lipid Domains. J Biol Chem. 2013 Nov;288(44):32004-19. PubMed PMID: WOS:000330596200053.

57. Gimpl G. Interaction of G protein coupled receptors and cholesterol. Chemistry and Physics of Lipids. 2016 Sep;199:61-73. PubMed PMID: WOS:000381833800009.

58. Hamouda AK, Chiara DC, Sauls D, Cohen JB, Blanton MP. Cholesterol interacts with transmembrane alpha-helices M1, M3, and M4 of the Torpedo nicotinic acetylcholine receptor: Photolabeling studies using H-3-azicholesterol. Biochemistry. 2006 Jan;45(3):976-86. PubMed PMID: WOS:000234988600033.

59. Fantini J, Barrantes FJ. How cholesterol interacts with membrane proteins: an exploration of cholesterol-binding sites including CRAC, CARC, and

tilted domains. Frontiers in Physiology. 2013 2013;4. PubMed PMID: WOS:000346774000031.

60. Sjogren B, Svenningsson P. Depletion of the lipid raft constituents, sphingomyelin and ganglioside, decreases serotonin binding at human 5-HT7(a) receptors in HeLa cells. Acta Physiologica. 2007 May;190(1):47-53. PubMed PMID: WOS:000245392000007.

61. Paila YD, Ganguly S, Chattopadhyay A. Metabolic Depletion of Sphingolipids Impairs Ligand Binding and Signaling of Human Serotonin1A Receptors. Biochemistry. 2010 2010/03/23;49(11):2389-97.

62. Harikumar KG, Puri V, Singh RD, Hanada K, Pagano RE, Miller LJ. Differential effects of modification of membrane cholesterol and sphingolipids on the conformation, function, and trafficking of the G protein-coupled cholecystokinin receptor. J Biol Chem. 2005 Jan;280(3):2176-85. PubMed PMID: WOS:000226341700053.

63. Prasanna X, Jafurulla M, Sengupta D, Chattopadhyay A. The ganglioside GM1 interacts with the serotonin(1A) receptor via the sphingolipid binding domain. Biochimica Et Biophysica Acta-Biomembranes. 2016 Nov;1858(11):2818-26. PubMed PMID: WOS:000385318800027.

64. Mahfoud R, Garmy N, Maresca M, Yahi N, Puigserver A, Fantini J. Identification of a common sphingolipid-binding domain in Alzheimer, prion, and HIV-1 proteins. J Biol Chem. 2002 Mar;277(13):11292-6. PubMed PMID: WOS:000174613100069.

65. Contreras FX, Ernst AM, Haberkant P, Bjoerkholm P, Lindahl E, Goenen B, et al. Molecular recognition of a single sphingolipid species by a protein's transmembrane domain. Nature. 2012 Jan 26;481(7382):525-9. PubMed PMID: WOS:000299471800044.

66. Bethune J, Kol M, Hoffmann J, Reckmann I, Bruegger B, Wieland F. Coatomer, the coat protein of COPI transport vesicles, discriminates endoplasmic reticulum residents from p24 proteins. Molecular and Cellular Biology. 2006 Nov;26(21):8011-21. PubMed PMID: WOS:000241462400017.

67. Vranken WF, Budesinsky M, Fant F, Boulez K, Borremans FA. The complete Consensus V3 loop peptide of the envelope protein gp120 of HIV-1 shows pronounced helical character in solution. FEBS Lett. 1995 Oct 23;374(1):117-21. PubMed PMID: 7589496. Epub 1995/10/23. eng.

68. Björkholm P, Ernst AM, Hacke M, Wieland F, Brügger B, von Heijne G. Identification of novel sphingolipid-binding motifs in mammalian membrane proteins. Biochimica et Biophysica Acta (BBA)-Biomembranes. 2014;1838(8):2066-70.

69. Hedger G, Sansom MSP. Lipid interaction sites on channels, transporters and receptors: Recent insights from molecular dynamics simulations. Biochimica et Biophysica Acta (BBA) - Biomembranes. 2016 2016/10/01/;1858(10):2390-400.

70. Wacker D, Wang C, Katritch V, Han GW, Huang XP, Vardy E, et al. Structural Features for Functional Selectivity at Serotonin Receptors. Science. 2013 May;340(6132):615-9. PubMed PMID: WOS:000318268900049.

71. Wu H, Wang C, Gregory KJ, Han GW, Cho HP, Xia Y, et al. Structure of a Class C GPCR metabotropic glutamate receptor 1 bound to an allosteric modulator. Science. 2014;344(6179):58-64.

72. Gonen T, Cheng Y, Sliz P, Hiroaki Y, Fujiyoshi Y, Harrison SC, et al. Lipid–protein interactions in double-layered two-dimensional AQP0 crystals. Nature. 2005 12/01/online;438:633.

73. Hite RK, Li ZL, Walz T. Principles of membrane protein interactions with annular lipids deduced from aquaporin-0 2D crystals. Embo Journal. 2010 May;29(10):1652-8. PubMed PMID: WOS:000277833100005.

74. Gupta K, Donlan JAC, Hopper JTS, Uzdavinys P, Landreh M, Struwe WB, et al. The role of interfacial lipids in stabilizing membrane protein oligomers. Nature. 2017 01/11/online;541:421.

75. Gerl MJ, Sachsenheimer T, Grzybek M, Coskun Ü, Wieland FT, Brügger B. Analysis of Transmembrane Domains and Lipid Modified Peptides with Matrix-Assisted Laser Desorption Ionization-Time-of-Flight Mass Spectrometry. Analytical Chemistry. 2014 2014/04/15;86(8):3722-6.

76. Odowd BF, Hnatowich M, Caron MG, Lefkowitz RJ, Bouvier M. PALMITOYLATION OF THE HUMAN BETA-2-ADRENERGIC RECEPTOR - MUTATION OF CYS-341 IN THE CARBOXYL TAIL LEADS TO AN UNCOUPLED NONPALYMITOYLATED FORM OF THE RECEPTOR. J Biol Chem. 1989 May;264(13):7564-9. PubMed PMID: WOS:A1989U326600072.

77. Thiele C, Hannah MJ, Fahrenholz F, Huttner WB. Cholesterol binds to synaptophysin and is required for biogenesis of synaptic vesicles. Nature Cell Biology. 2000 Jan;2(1):42-9. PubMed PMID: WOS:000084843600018.

78. Haberkant P, Schmitt O, Contreras FX, Thiele C, Hanada K, Sprong H, et al. Protein-sphingolipid interactions within cellular membranes. Journal of Lipid Research. 2008 Jan;49(1):251-62. PubMed PMID: WOS:000251833800026.

79. Haberkant P, Raijmakers R, Wildwater M, Sachsenheimer T, Brugger B, Maeda K, et al. InVivo Profiling and Visualization of Cellular Protein-Lipid Interactions Using Bifunctional Fatty Acids. Angewandte Chemie-International Edition. 2013;52(14):4033-8. PubMed PMID: WOS:000316915500044.

80. Haberkant P, Stein F, Hoglinger D, Gerl MJ, Brugger B, van Veldhoven PP, et al. Bifunctional Sphingosine for Cell-Based Analysis of Protein-Sphingolipid Interactions. Acs Chemical Biology. 2016 Jan;11(1):222-30. PubMed PMID: WOS:000368562500024.

81. Ingolfsson HI, Arnarez C, Periole X, Marrink SJ. Computational 'microscopy' of cellular membranes. Journal of Cell Science. 2016 Jan;129(2):257-68. PubMed PMID: WOS:000369504000003.

82. Friedman R, Khalid S, Aponte-Santamaria C, Arutyunova E, Becker M, Boyd KJ, et al. Understanding Conformational Dynamics of Complex Lipid Mixtures Relevant to Biology. Journal of Membrane Biology. 2018 Dec;251(5-6):609-31. PubMed PMID: WOS:000450567200001.

83. Huang J, MacKerell AD, Jr. CHARMM36 all-atom additive protein force field: validation based on comparison to NMR data. Journal of computational chemistry. 2013;34(25):2135-45. PubMed PMID: 23832629. Epub 07/06.

84. Marrink SJ, Risselada HJ, Yefimov S, Tieleman DP, De Vries AH. The MARTINI force field: coarse grained model for biomolecular simulations. The journal of physical chemistry B. 2007;111(27):7812-24.

85. Jo S, Kim T, Iyer VG, Im W. CHARMM-GUI: A web-based graphical user interface for CHARMM. Journal of Computational Chemistry. 2008;29(11):1859-65.

86. Lee J, Cheng X, Swails JM, Yeom MS, Eastman PK, Lemkul JA, et al. CHARMM-GUI Input Generator for NAMD, GROMACS, AMBER, OpenMM, and CHARMM/OpenMM Simulations Using the CHARMM36 Additive Force Field. Journal of Chemical Theory and Computation. 2016 2016/01/12;12(1):405-13.

87. Wassenaar TA, Ingólfsson HI, Böckmann RA, Tieleman DP, Marrink SJ. Computational Lipidomics with insane: A Versatile Tool for Generating Custom Membranes for Molecular Simulations. Journal of Chemical Theory and Computation. 2015 2015/05/12;11(5):2144-55.

88. Nguyen DH, Taub D. CXCR4 function requires membrane cholesterol: implications for HIV infection. The Journal of Immunology. 2002;168(8):4121-6.

89. Pluhackova K, Gahbauer S, Kranz F, Wassenaar TA, Bockmann RA. Dynamic Cholesterol-Conditioned Dimerization of the G Protein Coupled Chemokine Receptor Type 4. Plos Computational Biology. 2016 Nov;12(11). PubMed PMID: WOS:000391230900016.

90. Ballesteros JA, Jensen AD, Liapakis G, Rasmussen SGF, Shi L, Gether U, et al. Activation of the beta(2)-adrenergic receptor involves disruption of an ionic lock between the cytoplasmic ends of transmembrane segments 3 and 6. J Biol Chem. 2001 Aug 3;276(31):29171-7. PubMed PMID: WOS:000170346000073.

91. Doré AS, Okrasa K, Patel JC, Serrano-Vega M, Bennett K, Cooke RM, et al. Structure of class C GPCR metabotropic glutamate receptor 5 transmembrane domain. Nature. 2014;511(7511):557-62.

92. Haga K, Kruse AC, Asada H, Yurugi-Kobayashi T, Shiroishi M, Zhang C, et al. Structure of the human M2 muscarinic acetylcholine receptor bound to an antagonist. Nature. 2012 Feb;482(7386):547-U147. PubMed PMID: WOS:000300770500055.

93. Hofmann KP, Scheerer P, Hildebrand PW, Choe H-W, Park JH, Heck M, et al. AG protein-coupled receptor at work: the rhodopsin model. Trends BiochemSci. 2009;34(11):540-52.

94. Hollenstein K, Kean J, Bortolato A, Cheng RKY, Dore AS, Jazayeri A, et al. Structure of class B GPCR corticotropin-releasing factor receptor 1. Nature. 2013 Jul;499(7459):438-+. PubMed PMID: WOS:000322157900032.

95. Wang C, Wu HX, Katritch V, Han GW, Huang XP, Liu W, et al. Structure of the human smoothened receptor bound to an antitumour agent. Nature. 2013 May;497(7449):338-+. PubMed PMID: WOS:000318952000031.

96. Muto T, Tsuchiya D, Morikawa K, Jingami H. Structures of the extracellular regions of the group II/III metabotropic glutamate receptors. Proc Natl Acad Sci U S A. 2007 Mar 6;104(10):3759-64. PubMed PMID: WOS:000244972400019.

97. Rondard P, Liu J, Huang S, Malhaire F, Pinault A, Labesse G, et al. Coupling of agonist binding to effector domain activation in metabotropic glutamate-like receptors. J Biol Chem. 2006;281(34):24653-61.

98. Conn PJ, Pin JP. Pharmacology and functions of metabotropic glutamate receptors. Annual Review of Pharmacology and Toxicology. 1997;37:205-37. PubMed PMID: WOS:A1997WV83500009.

99. Nicoletti F, Bruno V, Ngomba RT, Gradini R, Battaglia G. Metabotropic glutamate receptors as drug targets: what's new? Current Opinion in Pharmacology. 2015;20:89-94.

100. Benarroch EE. Metabotropic glutamate receptors - Synaptic modulators and therapeutic targets for neurologic disease. Neurology. 2008 Mar;70(12):964-8. PubMed PMID: WOS:000254065500011.

101. Julio-Pieper M, Flor PJ, Dinan TG, Cryan JF. Exciting Times beyond the Brain: Metabotropic Glutamate Receptors in Peripheral and Non-Neural Tissues. Pharmacological Reviews. 2011 Mar;63(1):35-58. PubMed PMID: WOS:000287356800002.

102. Pin JP, De Colle C, Bessis AS, Acher F. New perspectives for the development of selective metabotropic glutamate receptor ligands. European Journal of Pharmacology. 1999 Jun;375(1-3):277-94. PubMed PMID: WOS:000081483600025.

103. IUPHAR/BPS Guide to PHARMACOLOGY [Internet]. International Union of Basic and Clinical Pharmacology Committee on Receptor Nomenclature and Drug Classification. 2018 [cited 26/11/2018]. Available from: http://www.guidetopharmacology.org/GRAC/FamilyDisplayForward?familyId=40. .

104. The UniProt Consortium. UniProt: the universal protein knowledgebase. Nucleic Acids Research. 2017;45(D1):D158-D69.

105. Markovic D, Challiss RA. Alternative splicing of G protein-coupled receptors: physiology and pathophysiology. Cellular and molecular life sciences : CMLS. 2009 Oct;66(20):3337-52. PubMed PMID: 19629391. Epub 2009/07/25. eng.

106. Ferraguti F, Shigemoto R. Metabotropic glutamate receptors. Cell Tissue Res. 2006 Nov;326(2):483-504. PubMed PMID: WOS:000240714000023.

107. Sartorius LJ, Nagappan G, Lipska BK, Lu B, Sei Y, Ren-Patterson R, et al. Alternative splicing of human metabotropic glutamate receptor 3. Journal of neurochemistry. 2006;96(4):1139-48.

108. Garcia-Bea A, Bermudez I, Harrison PJ, Lane TA. A group II metabotropic glutamate receptor 3 (mGlu3, GRM3) isoform implicated in schizophrenia interacts with canonical mGlu3 and reduces ligand binding. Journal of Psychopharmacology. 2017 Dec;31(12):1519-26. PubMed PMID: WOS:000416544800002.

109. Chan WY, Soloviev MM, Ciruela F, McIlhinney R. Molecular determinants of metabotropic glutamate receptor 1B trafficking. Molecular and Cellular Neuroscience. 2001;17(3):577-88.

110. Kumpost J, Syrova Z, Kulihova L, Frankova D, Bologna J-C, Hlavackova V, et al. Surface expression of metabotropic glutamate receptor variants mGluR1a and mGluR1b in transfected HEK293 cells. Neuropharmacology. 2008;55(4):409-18.

111. Tateyama M, Kubo Y. Regulatory role of C-terminus in the G-protein coupling of the metabotropic glutamate receptor 1. Journal of neurochemistry. 2008;107(4):1036-46.

112. Schulein R, Westendorf C, Krause G, Rosenthal W. Functional significance of cleavable signal peptides of G protein-coupled receptors. Eur J Cell Biol. 2012 Apr;91(4):294-9. PubMed PMID: WOS:000302881700010. English.

113. Coskun U, Simons K. Cell Membranes: The Lipid Perspective. Structure. 2011 Nov;19(11):1543-8. PubMed PMID: WOS:000296999700005.

114. Nilsson I, Ohvo-Rekila H, Slotte JP, Johnson AE, von Heijne G. Inhibition of protein translocation across the endoplasmic reticulum membrane by sterols. The Journal of biological chemistry. 2001 Nov 9;276(45):41748-54. PubMed PMID: 11535595. Epub 2001/09/06. eng.

115. Kochl R, Alken M, Rutz C, Krause G, Oksche A, Rosenthal W, et al. The signal peptide of the G protein-coupled human endothelin B receptor is necessary for translocation of the N-terminal tail across the endoplasmic reticulum membrane. J Biol Chem. 2002 May;277(18):16131-8. PubMed PMID: WOS:000175510400121.

116. Nørskov-Lauritsen L, Bräuner-Osborne H. Role of post-translational modifications on structure, function and pharmacology of class C G protein-coupled receptors. European Journal of Pharmacology. 2015 2015/09/15/;763:233-40.

117. Mody N, Hermans E, Nahorski S, Challiss R. Inhibition of< i> N</i>-linked glycosylation of the human type 1α metabotropic glutamate receptor by

tunicamycin: effects on cell-surface receptor expression and function. Neuropharmacology. 1999;38(10):1485-92.

118. Muto T, Tsuchiya D, Morikawa K, Jingami H. Site-specific unglycosylation to improve crystallization of the metabotropic glutamate receptor 3 extracellular domain. Acta Crystallographica Section F: Structural Biology and Crystallization Communications. 2009;65(3).

119. Bhave G, Nadin BM, Brasier D, Glauner KS, Shah RD, Heinemann SF, et al. Membrane topology of a metabotropic glutamate receptor. J Biol Chem. 2003.

120. Huang S, Cao J, Jiang M, Labesse G, Liu J, Pin J-P, et al. Interdomain movements in metabotropic glutamate receptor activation. Proceedings of the National Academy of Sciences. 2011;108(37):15480-5.

121. Xue L, Rovira X, Scholler P, Zhao H, Liu J, Pin J-P, et al. Major ligand-induced rearrangement of the heptahelical domain interface in a GPCR dimer. Nature Chemical Biology. 2015 Feb;11(2):134-U76. PubMed PMID: WOS:000348358800011.

122. Pin J-P, Bettler B. Organization and functions of mGlu and GABAB receptor complexes. Nature. 2016 12/01/online;540:60.

123. Waterhouse A, Bertoni M, Bienert S, Studer G, Tauriello G, Gumienny R, et al. SWISS-MODEL: homology modelling of protein structures and complexes. Nucleic Acids Research. 2018;46(W1):W296-W303.

124. Fukushima Y, Saitoh T, Anai M, Ogihara T, Inukai K, Funaki M, et al. Palmitoylation of the canine histamine H2 receptor occurs at Cys305 and is important for cell surface targeting. Biochimica et Biophysica Acta (BBA)-Molecular Cell Research. 2001;1539(3):181-91.

125. Alaluf S, Mulvihill ER, McIlhinney RAJ. THE METABOTROPIC GLUTAMATE-RECEPTOR MGLUR4, BUT NOT MGLUR1-ALPHA, IS PALMITOYLATED WHEN EXPRESSED IN BHK CELLS. Journal of Neurochemistry. 1995 Apr;64(4):1548-55. PubMed PMID: WOS:A1995QN15000016.

126. Suh YH, Chang K, Roche KW. Metabotropic glutamate receptor trafficking. Molecular and Cellular Neuroscience. 2018 2018/09/01/;91:10-24.

127. Techlovska S, Chambers JN, Dvorakova M, Petralia RS, Wang YX, Hajkova A, et al. Metabotropic glutamate receptor 1 splice variants mGluR1a and -mGluRlb combine in mGluRla/b dimers in vivo. Neuropharmacology. 2014 Nov;86:329-36. PubMed PMID: WOS:000343839800034.

128. Pagano A, Rovelli G, Mosbacher J, Lohmann T, Duthey B, Stauffer D, et al. C-terminal interaction is essential for surface trafficking but not for heteromeric assembly of GABAB receptors. The Journal of Neuroscience. 2001;21(4):1189-202.

129. Burmakina S, Geng Y, Chen Y, Fan QR. Heterodimeric coiled-coil interactions of human GABAB receptor. Proceedings of the National Academy of Sciences. 2014;111(19):6958-63.

130. El Moustaine D, Granier S, Doumazane E, Scholler P, Rahmeh R, Bron P, et al. Distinct roles of metabotropic glutamate receptor dimerization in agonist activation and G-protein coupling. Proc Natl Acad Sci U S A. 2012 Oct 2;109(40):16342-7. PubMed PMID: WOS:000309611400078.

131. Doumazane E, Scholler P, Zwier JM, Trinquet E, Rondard P, Pin J-P. A new approach to analyze cell surface protein complexes reveals specific heterodimeric metabotropic glutamate receptors. Faseb J. 2011 Jan;25(1):66-77. PubMed PMID: WOS:000285869500007.

132. Ray K, Hauschild BC. Cys-140 is critical for metabotropic glutamate receptor-1 dimerization. J Biol Chem. 2000;275(44):34245-51.

133. Goudet C, Gaven F, Kniazeff J, Vol C, Liu J, Cohen-Gonsaud M, et al. Heptahelical domain of metabotropic glutamate receptor 5 behaves like rhodopsin-like receptors. Proc Natl Acad Sci U S A. 2004 Jan 6;101(1):378-83. PubMed PMID: 14691258. Pubmed Central PMCID: PMC314193. Epub 2003/12/24. eng.

134. Kunishima N, Shimada Y, Tsuji Y, Sato T, Yamamoto M, Kumasaka T, et al. Structural basis of glutamate recognition by a dimeric metabotropic glutamate receptor. Nature. 2000;407(6807):971-7.

135. Tsuchiya D, Kunishima N, Kamiya N, Jingami H, Morikawa K. Structural views of the ligand-binding cores of a metabotropic glutamate receptor complexed with an antagonist and both glutamate and Gd3+. Proc Natl Acad Sci U S A. 2002 Mar 5;99(5):2660-5. PubMed PMID: 11867751. Pubmed Central PMCID: PMC122404. Epub 2002/02/28. eng.

136. Kniazeff J, Bessis AS, Maurel D, Ansanay H, Prezeau L, Pin JP. Closed state of both binding domains of homodimeric mGlu receptors is required for full activity. Nature Structural & Molecular Biology. 2004 Aug;11(8):706-13. PubMed PMID: WOS:000222930600014.

137. Yamashita T, Terakita A, Kai T, Shichida Y. Conformational change of the transmembrane helices II and IV of metabotropic glutamate receptor involved in G protein activation. Journal of Neurochemistry. 2008 Jul;106(2):850-9. PubMed PMID: WOS:000257708000031.

138. Alberts B, Johnson A, Lewis J, Raff M, Roberts K, Walter P. Molecular biology of the cell. New York: Garland Science; 2008.

139. Havlickova M, Blahos J, Brabet I, Liu JF, Hruskova B, Prezeau L, et al. The second intracellular loop of metabotropic glutamate receptors recognizes C termini of G-protein alpha-subunits. J Biol Chem. 2003 Sep;278(37):35063-70. PubMed PMID: WOS:000185164400040.

140. Francesconi A, Duvoisin RM. Opposing effects of protein kinase C and protein kinase A on metabotropic glutamate receptor signaling: Selective desensitization of the inositol trisphosphate/Ca²⁺ pathway by phosphorylation of the receptor-G protein-coupling domain. Proceedings of the National Academy of Sciences. 2000;97(11):6185-90.

141. Gereau RWt, Heinemann SF. Role of protein kinase C phosphorylation in rapid desensitization of metabotropic glutamate receptor 5. Neuron. 1998 Jan;20(1):143-51. PubMed PMID: 9459450. Epub 1998/02/12. eng.

142. Cai Z, Saugstad JA, Sorensen SD, Ciombor KJ, Zhang C, Schaffhauser H, et al. Cyclic AMP-dependent protein kinase phosphorylates group III metabotropic glutamate receptors and inhibits their function as presynaptic receptors. Journal of Neurochemistry. 2001;78(4):756-66.

143. Schaffhauser H, Cai Z, Hubalek F, Macek TA, Pohl J, Murphy TJ, et al. cAMP-dependent protein kinase inhibits mGluR2 coupling to G-proteins by direct receptor phosphorylation. Journal of Neuroscience. 2000;20(15):5663-70.

144. Moriyoshi K, Iijima K, Fujii H, Ito H, Cho Y, Nakanishi S. Seven in absentia homolog 1A mediates ubiquitination and degradation of group 1 metabotropic glutamate receptors. Proc Natl Acad Sci U S A. 2004;101(23):8614-9.

145. Gulia R, Sharma R, Bhattacharyya S. Critical Role for Ubiquitination in the Endocytosis of Glutamate Receptors. J Biol Chem. 2017 Jan;292(4):1426-37. PubMed PMID: WOS:000393339800024.

146. Choi J-H, Park J-Y, Park SP, Lee H, Han S, Park KH, et al. Regulation of mGluR7 trafficking by SUMOylation in neurons. Neuropharmacology. 2016 2016/03/01/;102:229-35.

147. Boshart M, Weber F, Jahn G, Dorsch-Hasler K, Fleckenstein B, Schaffner W. A very strong enhancer is located upstream of an immediate early gene of human cytomegalovirus. Cell. 1985 Jun;41(2):521-30. PubMed PMID: 2985280. Epub 1985/06/01. eng.

148. Foecking MK, Hofstetter H. Powerful and versatile enhancer-promoter unit for mammalian expression vectors. Gene. 1986;45(1):101-5. PubMed PMID: 3023199. Epub 1986/01/01. eng.

149. Yang TT, Cheng LZ, Kain SR. Optimized codon usage and chromophore mutations provide enhanced sensitivity with the green fluorescent protein. Nucleic Acids Research. 1996 Nov;24(22):4592-3. PubMed PMID: WOS:A1996VW52800029.

150. Zacharias DA, Violin JD, Newton AC, Tsien RY. Partitioning of lipid-modified monomeric GFPs into membrane microdomains of live cells. Science. 2002 May;296(5569):913-6. PubMed PMID: WOS:000175442500045.

151. Chen XY, Zaro JL, Shen WC. Fusion protein linkers: Property, design and functionality. Adv Drug Deliv Rev. 2013 Oct;65(10):1357-69. PubMed PMID: WOS:000326560900007.

152. Violin JD, Ren XR, Lefkowitz RJ. G-protein-coupled receptor kinase specificity for beta-arrestin recruitment to the beta(2)-adrenergic receptor revealed by fluorescence resonance energy transfer. J Biol Chem. 2006 Jul;281(29):20577-88. PubMed PMID: WOS:000239038200079.

153. Guan X-M, Kobilka TS, Kobilka B. Enhancement of membrane insertion and function in a type IIIb membrane protein following introduction of a cleavable signal peptide. J Biol Chem. 1992;267(31):21995-8.

154. Gonzalez-Maeso J, Ang RL, Yuen T, Chan P, Weisstaub NV, Lopez-Gimenez JF, et al. Identification of a serotonin/glutamate receptor complex implicated in psychosis. Nature. 2008 Mar;452(7183):93-U9. PubMed PMID: WOS:000253671900053.

155. Collins MO, Woodley KT, Choudhary JS. Global, site-specific analysis of neuronal protein S-acylation. Sci Rep. 2017 Jul 5;7(1):4683. PubMed PMID: 28680068. Pubmed Central PMCID: PMC5498535. Epub 2017/07/07. eng.

156. Kennedy ME, Limbird L. Mutations of the alpha 2A-adrenergic receptor that eliminate detectable palmitoylation do not perturb receptor-G-protein coupling. J Biol Chem. 1993;268(11):8003-11.

157. Moffett S, Mouillac B, Bonin H, Bouvier M. Altered phosphorylation and desensitization patterns of a human beta 2-adrenergic receptor lacking the palmitoylated Cys341. The EMBO journal. 1993;12(1):349-56.

158. Arnold K, Bordoli L, Kopp J, Schwede T. The SWISS-MODEL workspace: a web-based environment for protein structure homology modelling. Bioinformatics. 2006;22(2):195-201.

159. Guex N, Peitsch MC, Schwede T. Automated comparative protein structure modeling with SWISS-MODEL and Swiss-PdbViewer: A historical perspective. ELECTROPHORESIS. 2009;30(S1):S162-S73.

160. Benkert P, Biasini M, Schwede T. Toward the estimation of the absolute quality of individual protein structure models. Bioinformatics. 2011;27(3):343-50.

161. Bienert S, Waterhouse A, de Beer Tjaart AP, Tauriello G, Studer G, Bordoli L, et al. The SWISS-MODEL Repository—new features and functionality. Nucleic Acids Research. 2017;45(D1):D313-D9.

162. Remmert M, Biegert A, Hauser A, Söding J. HHblits: lightning-fast iterative protein sequence searching by HMM-HMM alignment. Nature methods. 2012;9(2):173.

163. Altschul SF, Madden TL, Schäffer AA, Zhang J, Zhang Z, Miller W, et al. Gapped BLAST and PSI-BLAST: a new generation of protein database search programs. Nucleic Acids Research. 1997;25(17):3389-402.

164. Altin JG, Pagler EB. A ONE-STEP PROCEDURE FOR BIOTINYLATION AND CHEMICAL CROSS-LINKING OF LYMPHOCYTE SURFACE AND INTRACELLULAR MEMBRANE-ASSOCIATED MOLECULES. Analytical Biochemistry. 1995 Jan;224(1):382-9. PubMed PMID: WOS:A1995QB30600054.

165. Ray K, Clapp P, Goldsmith PK, Spiegel AM. Identification of the sites of N-linked glycosylation on the human calcium receptor and assessment of their role in cell surface expression and signal transduction. J Biol Chem. 1998;273(51):34558-67.

166. Robbins PW, Trimble R, Wirth D, Hering C, Maley F, Maley G, et al. Primary structure of the Streptomyces enzyme endo-beta-N-acetylglucosaminidase H. J Biol Chem. 1984;259(12):7577-83.

167. Plummer Jr T, Tarentino A. Purification of the oligosaccharide-cleaving enzymes of Flavobacterium meningosepticum. Glycobiology. 1991;1(3):257-63.

168. TRETTER V, ALTMANN F, MÄRZ L. Peptide-N4-(N-acetyl-β-glucosaminyl)asparagine amidase F cannot release glycans with fucose attached α1 → 3 to the asparagine-linked N-acetylglucosamine residue. European Journal of Biochemistry. 1991;199(3):647-52.

169. Maley F, Trimble RB, Tarentino AL, Plummer Jr TH. Characterization of glycoproteins and their associated oligosaccharides through the use of endoglycosidases. Analytical biochemistry. 1989;180(2):195-204.

170. Monn JA, Prieto L, Taboada L, Pedregal C, Hao JL, Reinhard MR, et al. Synthesis and Pharmacological Characterization of C4-Disubstituted Analogs of 1S,2S,5R,6S-2-Aminobicyclo 3.1.0 hexane-2,6-dicarboxylate: Identification of a Potent, Selective Metabotropic Glutamate Receptor Agonist and Determination of Agonist-Bound Human mGlu2 and mGlu3 Amino Terminal Domain Structures. Journal of Medicinal Chemistry. 2015 Feb;58(4):1776-94. PubMed PMID: WOS:000351186700012.

171. Milligan G, Bouvier M. Methods to monitor the quaternary structure of G protein-coupled receptors. Febs Journal. 2005 Jun;272(12):2914-25. PubMed PMID: WOS:000230088000002.

172. Fukata Y, Fukata M. Protein palmitoylation in neuronal development and synaptic plasticity. Nature Reviews Neuroscience. 2010 03/01/online;11:161.

173. Rands E, Candelore M, Cheung A, Hill WS, Strader C, Dixon R. Mutational analysis of beta-adrenergic receptor glycosylation. J Biol Chem. 1990;265(18):10759-64.

174. SCHÜlLEIN R, LIEBENHOFF U, MÜlLLER H, BIRNBAUMER M, ROSENTHAL W. Properties of the human arginine vasopressin V2 receptor after site-directed mutagenesis of its putative palmitoylation site. Biochemical Journal. 1996;313(2):611-6.

175. Ebersole B, Petko J, Woll M, Murakami S, Sokolina K, Wong V, et al. Effect of C-Terminal S-Palmitoylation on D2 Dopamine Receptor Trafficking and Stability. PLOS ONE. 2015;10(11):e0140661.

176. Papoucheva E, Dumuis A, Sebben M, Richter DW, Ponimaskin EG. The 5-hydroxytryptamine(1A) receptor is stably palmitoylated, and acylation is critical for communication of receptor with G(i) protein. J Biol Chem. 2004 Jan;279(5):3280-91. PubMed PMID: WOS:000188379600019.

177. Laemmli UK. CLEAVAGE OF STRUCTURAL PROTEINS DURING ASSEMBLY OF HEAD OF BACTERIOPHAGE-T4. Nature. 1970;227(5259):680-&. PubMed PMID: WOS:A1970H022600020.

178. Gerl MJ, Bittl V, Kirchner S, Sachsenheimer T, Brunner HL, Luchtenborg C, et al. Sphingosine-1-Phosphate Lyase Deficient Cells as a Tool to Study Protein Lipid Interactions. Plos One. 2016 Apr;11(4). PubMed PMID: WOS:000374898500021.

179. Abraham MJ, Murtola T, Schulz R, Páll S, Smith JC, Hess B, et al. GROMACS: High performance molecular simulations through multi-level parallelism from laptops to supercomputers. SoftwareX. 2015 2015/09/01/;1-2:19-25.

180. Berendsen HJC, Vanderspoel D, Vandrunen R. GROMACS - A MESSAGE-PASSING PARALLEL MOLECULAR-DYNAMICS IMPLEMENTATION. Computer Physics Communications. 1995 Sep;91(1-3):43-56. PubMed PMID: WOS:A1995TF32200004.

181. Van der Spoel D, Lindahl E, Hess B, Groenhof G, Mark AE, Berendsen HJC. GROMACS: Fast, flexible, and free. Journal of Computational Chemistry. 2005 Dec;26(16):1701-18. PubMed PMID: WOS:000233021400004.

182. Jo S, Kim T, Im W. Automated Builder and Database of Protein/Membrane Complexes for Molecular Dynamics Simulations. PLOS ONE. 2007;2(9):e880.

183. Hess B, Bekker H, Berendsen HJC, Fraaije JGEM. LINCS: A linear constraint solver for molecular simulations. Journal of Computational Chemistry. 1997;18(12):1463-72.

184. Darden T, York D, Pedersen L. Particle mesh Ewald: An N·log(N) method for Ewald sums in large systems. The Journal of Chemical Physics. 1993;98(12):10089-92.

185. Verlet L. Computer" experiments" on classical fluids. I. Thermodynamical properties of Lennard-Jones molecules. Physical review. 1967;159(1):98.

186. Páll S, Hess B. A flexible algorithm for calculating pair interactions on SIMD architectures. Computer Physics Communications. 2013 2013/12/01/;184(12):2641-50.

187. Berendsen HJC, Postma JPM, Gunsteren WFv, DiNola A, Haak JR. Molecular dynamics with coupling to an external bath. The Journal of Chemical Physics. 1984;81(8):3684-90.

188. Parrinello M, Rahman A. Polymorphic transitions in single crystals: A new molecular dynamics method. Journal of Applied physics. 1981;52(12):7182-90.

189. Nosé S. A unified formulation of the constant temperature molecular dynamics methods. The Journal of chemical physics. 1984;81(1):511-9.

190. Nosé S. A molecular dynamics method for simulations in the canonical ensemble. Molecular physics. 1984;52(2):255-68.

191. Hoover WG. Canonical dynamics: equilibrium phase-space distributions. Physical review A. 1985;31(3):1695.

192. Monticelli L, Kandasamy SK, Periole X, Larson RG, Tieleman DP, Marrink S-J. The MARTINI coarse-grained force field: extension to proteins. Journal of chemical theory and computation. 2008;4(5):819-34.

193. de Jong DH, Singh G, Bennett WFD, Arnarez C, Wassenaar TA, Schäfer LV, et al. Improved Parameters for the Martini Coarse-Grained Protein Force Field. Journal of Chemical Theory and Computation. 2013 2013/01/08;9(1):687-97.

194. Vogele M, Kofinger J, Hummer G. Hydrodynamics of Diffusion in Lipid Membrane Simulations. Physical Review Letters. 2018 Jun;120(26). PubMed PMID: WOS:000436940400030.

195. Feigenson GW. Phase diagrams and lipid domains in multicomponent lipid bilayer mixtures. Biochimica et Biophysica Acta (BBA) - Biomembranes. 2009 2009/01/01/;1788(1):47-52.

196. Ohvo-Rekilä H, Ramstedt B, Leppimäki P, Slotte JP. Cholesterol interactions with phospholipids in membranes. Progress in lipid research. 2002;41(1):66-97.

197. Kabsch W, Sander C. Dictionary of protein secondary structure: pattern recognition of hydrogen-bonded and geometrical features. Biopolymers: Original Research on Biomolecules. 1983;22(12):2577-637.

198. Briones R, Blau C, Kutzner C, de Groot BL, Aponte-Santamaría C. GROmaps: A GROMACS-Based Toolset to Analyze Density Maps Derived from Molecular Dynamics Simulations. Biophysical Journal. 2018 2018/12/01/.

199. Graham F, Smiley J, Russell W, Nairn R. Characteristics of a human cell line transformed by DNA from human adenovirus type 5. Journal of General Virology. 1977;36(1):59-72.

200. Sladeczek F, Pin J-P, Récasens M, Bockaert J, Weiss S. Glutamate stimulates inositol phosphate formation in striatal neurones. Nature. 1985 10/24/online;317:717.

201. Masu M, Tanabe Y, Tsuchida K, Shigemoto R, Nakanishi S. Sequence and expression of a metabotropic glutamate receptor. Nature. 1991 02/28/online;349:760.

202. Houamed KM, Kuijper JL, Gilbert TL, Haldeman BA, O'Hara PJ, Mulvihill ER, et al. Cloning, expression, and gene structure of a G protein-coupled glutamate receptor from rat brain. Science. 1991 May 31;252(5010):1318-21. PubMed PMID: 1656524. Epub 1991/05/31. eng.

203. Romano C, Yang W-L, O'Malley KL. Metabotropic glutamate receptor 5 is a disulfide-linked dimer. J Biol Chem. 1996;271(45):28612-6.

204. Hemstapat K, Da Costa H, Nong Y, Brady AE, Luo Q, Niswender CM, et al. A novel family of potent negative allosteric modulators of group II metabotropic glutamate receptors. The Journal of pharmacology and experimental therapeutics. 2007 Jul;322(1):254-64. PubMed PMID: 17416742. Epub 2007/04/10. eng.

205. Graham FL, van der Eb AJ. A new technique for the assay of infectivity of human adenovirus 5 DNA. Virology. 1973 1973/04/01/;52(2):456-67.

206. Ciruela F, Soloviev MM, Chan WY, McIlhinney RAJ. Homer-1c/Vesl-1L modulates the cell surface targeting of metabotropic glutamate receptor type 1 alpha: Evidence for an anchoring function. Molecular and Cellular Neuroscience. 2000 Jan;15(1):36-50. PubMed PMID: WOS:000085030600004.

207. Tu JC, Xiao B, Yuan JP, Lanahan AA, Leoffert K, Li M, et al. Homer binds a novel proline-rich motif and links group 1 metabotropic glutamate receptors with IP3 receptors. Neuron. 1998 Oct;21(4):717-26. PubMed PMID: WOS:000076697300016.

208. Roche KW, Tu JC, Petralia RS, Xiao B, Wenthold RJ, Worley PF. Homer 1b regulates the trafficking of group I metabotropic glutamate receptors. J Biol Chem. 1999 Sep 3;274(36):25953-7. PubMed PMID: WOS:000082554200104.

209. Couve A, Thomas P, Calver AR, Hirst WD, Pangalos MN, Walsh FS, et al. Cyclic AMP-dependent protein kinase phosphorylation facilitates GABA(B) receptor-effector coupling. Nature neuroscience. 2002 May;5(5):415-24. PubMed PMID: 11976702. Epub 2002/04/27. eng.

210. Yamano S, Dai J, Moursi AM. Comparison of Transfection Efficiency of Nonviral Gene Transfer Reagents. Mol Biotechnol. 2010 November 01;46(3):287-300.

211. Hook B, Landreman A. Choosing the Right Transfection Reagent for Optimal Efficiency2018 December 2018 [cited 2018 06.Dec.2018]. Available from: https://www.promega.de/resources/pubhub/tpub-205-choosing-the-right-transfection-reagent-for-optimal-efficiency/.

212. Saunders C, Limbird LE. Localization and trafficking of alpha2-adrenergic receptor subtypes in cells and tissues. Pharmacol Ther. 1999 Nov;84(2):193-205. PubMed PMID: 10596906. Epub 1999/12/22. eng.

213. Adachi N, Hess DT, McLaughlin P, Stamler JS. S-Palmitoylation of a Novel Site in the beta2-Adrenergic Receptor Associated with a Novel Intracellular Itinerary. The Journal of biological chemistry. 2016 Sep 16;291(38):20232-46. PubMed PMID: 27481942. Pubmed Central PMCID: PMC5025705. Epub 2016/08/03. eng.

214. Zuckerman DM, Hicks SW, Charron G, Hang HC, Machamer CE. Differential regulation of two palmitoylation sites in the cytoplasmic tail of the beta1-adrenergic receptor. The Journal of biological chemistry. 2011 May 27;286(21):19014-23. PubMed PMID: 21464135. Pubmed Central PMCID: PMC3099716. Epub 2011/04/06. eng.

215. Rasmussen SG, Jensen AD, Liapakis G, Ghanouni P, Javitch JA, Gether U. Mutation of a highly conserved aspartic acid in the β2 adrenergic receptor: constitutive activation, structural instability, and conformational rearrangement of transmembrane segment 6. Molecular pharmacology. 1999;56(1):175-84.

216. Ponimaskin EG, Heine M, Joubert L, Sebben M, Bickmeyer U, Richter DW, et al. The 5-hydroxytryptamine(4a) receptor is palmitoylated at two different sites, and acylation is critically involved in regulation of receptor constitutive activity. The Journal of biological chemistry. 2002 Jan 25;277(4):2534-46. PubMed PMID: 11706023. Epub 2001/11/14. eng.

217. Kobe F, Renner U, Woehler A, Wlodarczyk J, Papusheva E, Bao G, et al. Stimulation- and palmitoylation-dependent changes in oligomeric

conformation of serotonin 5-HT1A receptors. Biochim Biophys Acta. 2008 Aug;1783(8):1503-16. PubMed PMID: 18381076. Epub 2008/04/03. eng.

218. Raymond JR, Mukhin YV, Gettys TW, Garnovskaya MN. The recombinant 5-HT1A receptor: G protein coupling and signalling pathways. British Journal of Pharmacology. 1999 Aug;127(8):1751-64. PubMed PMID: WOS:000082312500001.

219. Hakalahti AE, Vierimaa MM, Lilja MK, Kumpula EP, Tuusa JT, Petaja-Repo UE. Human beta1-adrenergic receptor is subject to constitutive and regulated N-terminal cleavage. The Journal of biological chemistry. 2010 Sep 10;285(37):28850-61. PubMed PMID: 20587416. Pubmed Central PMCID: PMC2937912. Epub 2010/07/01. eng.

220. von HEIJNE G, GAVEL Y. Topogenic signals in integral membrane proteins. European Journal of Biochemistry. 1988;174(4):671-8.

221. Denzer AJ, Nabholz CE, Spiess M. Transmembrane orientation of signal-anchor proteins is affected by the folding state but not the size of the N-terminal domain. The EMBO journal. 1995;14(24):6311-7.

222. Zhang D, Gao Z-G, Zhang K, Kiselev E, Crane S, Wang J, et al. Two disparate ligand-binding sites in the human P2Y1 receptor. Nature. 2015 03/30/online;520:317.

223. Serebryany E, Folta-Stogniew E, Liu J, Yan EC. Homodimerization enhances both sensitivity and dynamic range of the ligand-binding domain of type 1 metabotropic glutamate receptor. FEBS Lett. 2016 Dec;590(23):4308-17. PubMed PMID: 27800613. Pubmed Central PMCID: PMC5154874. Epub 2016/11/02. eng.

224. Levitz J, Habrian C, Bharill S, Fu Z, Vafabakhsh R, Isacoff EY. Mechanism of assembly and cooperativity of homomeric and heteromeric metabotropic glutamate receptors. Neuron. 2016;92(1):143-59.

225. Crow MK, Karasavvas N, Sarris AH. Protein aggregation mediated by cysteine oxidation during the stacking phase of discontinuous buffer SDS-PAGE. Biotechniques. 2001;30(2):311-6.

226. Bai M, Quinn S, Trivedi S, Kifor O, Pearce SH, Pollak MR, et al. Expression and characterization of inactivating and activating mutations in the human Ca2+ o-sensing receptor. J Biol Chem. 1996;271(32):19537-45.

227. Eason MG, Jacinto MT, Theiss CT, Liggett SB. The palmitoylated cysteine of the cytoplasmic tail of alpha 2A-adrenergic receptors confers subtype-specific agonist-promoted downregulation. Proc Natl Acad Sci U S A. 1994 Nov 8;91(23):11178-82. PubMed PMID: 7972030. Pubmed Central PMCID: PMC45190. Epub 1994/11/08. eng.

228. Giang DK, Cravatt BF. A second mammalian N-myristoyltransferase. J Biol Chem. 1998;273(12):6595-8.

229. Pickering DS, Taverna FA, Salter MW, Hampson DR. Palmitoylation of the GluR6 kainate receptor. Proc Natl Acad Sci U S A. 1995 Dec 19;92(26):12090-4. PubMed PMID: 8618850. Pubmed Central PMCID: PMC40302. Epub 1995/12/19. eng.

230. Borroto-Escuela DO, Tarakanov AO, Brito I, Fuxe K. Glutamate heteroreceptor complexes in the brain. Pharmacological reports : PR. 2018 Oct;70(5):936-50. PubMed PMID: 30103174. Epub 2018/08/14. eng.

231. Gutmann T, Kim KH, Grzybek M, Walz T, Coskun U. Visualization of ligand-induced transmembrane signaling in the full-length human insulin receptor. J Cell Biol. 2018 May 7;217(5):1643-9. PubMed PMID: 29453311. Pubmed Central PMCID: PMC5940312. Epub 2018/02/18. eng.

232. Moreno JL, Muguruza C, Umali A, Mortillo S, Holloway T, Pilar-Cuellar F, et al. Identification of three residues essential for 5-hydroxytryptamine 2A-metabotropic glutamate 2 (5-HT2A.mGlu2) receptor heteromerization and its psychoactive behavioral function. The Journal of biological chemistry. 2012 Dec 28;287(53):44301-19. PubMed PMID: 23129762. Pubmed Central PMCID: PMC3531745. Epub 2012/11/07. eng.

233. Lei S, Liapakis G, Xu R, Guarnieri F, Ballesteros JA, Javitch JA. beta(2) adrenergic receptor activation - Modulation of the proline kink in transmembrane 6 by a rotamer toggle switch. J Biol Chem. 2002 Oct;277(43):40989-96. PubMed PMID: WOS:000178791400107.

234. Coskun Ü, Grzybek M, Drechsel D, Simons K. Regulation of human EGF receptor by lipids. Proceedings of the National Academy of Sciences. 2011;108(22):9044-8.

235. Kabayama K, Sato T, Saito K, Loberto N, Prinetti A, Sonnino S, et al. Dissociation of the insulin receptor and caveolin-1 complex by ganglioside GM3 in the state of insulin resistance. Proc Natl Acad Sci U S A. 2007 Aug 21;104(34):13678-83. PubMed PMID: 17699617. Pubmed Central PMCID: PMC1949342. Epub 2007/08/19. eng.

236. Wacker D, Fenalti G, Brown MA, Katritch V, Abagyan R, Cherezov V, et al. Conserved binding mode of human beta2 adrenergic receptor inverse agonists and antagonist revealed by X-ray crystallography. J Am Chem Soc. 2010 Aug 25;132(33):11443-5. PubMed PMID: 20669948. Pubmed Central PMCID: PMC2923663. Epub 2010/07/31. eng.

237. Liu W, Chun E, Thompson AA, Chubukov P, Xu F, Katritch V, et al. Structural Basis for Allosteric Regulation of GPCRs by Sodium Ions. Science. 2012;337(6091):232-6.

238. McCorvy JD, Wacker D, Wang S, Agegnehu B, Liu J, Lansu K, et al. Structural determinants of 5-HT2B receptor activation and biased agonism. Nat Struct Mol Biol. 2018 Sep;25(9):787-96. PubMed PMID: 30127358. Pubmed Central PMCID: PMC6237183. Epub 2018/08/22. eng.

239. Zhang K, Zhang J, Gao Z-G, Zhang D, Zhu L, Han GW, et al. Structure of the human P2Y12 receptor in complex with an antithrombotic drug. Nature. 2014 03/23/online;509:115.

240. Manglik A, Kruse AC, Kobilka TS, Thian FS, Mathiesen JM, Sunahara RK, et al. Crystal structure of the μ-opioid receptor bound to a morphinan antagonist. Nature. 2012 03/21/online;485:321.

241. Bai Q, Yao X. Investigation of allosteric modulation mechanism of metabotropic glutamate receptor 1 by molecular dynamics simulations, free energy and weak interaction analysis. Scientific reports. 2016;6:21763.

242. Gorinski N, Ponimaskin E. Palmitoylation of serotonin receptors. Biochem Soc Trans. 2013 Feb 1;41(1):89-94. PubMed PMID: 23356264. Epub 2013/01/30. eng.

243. Wiedemann H. Functionalised Lipid Precursors to Study Protein-Lipid Interactions in Cellular Membranes. Heidelberg: University of Heidelberg; 2015.

244. Stratagene. QuikChange ® Site-Directed Mutagenesis Kit 2006 01/2015; Revision A:[20 p.].

245. Lapid CG, Yimin. PrimerX - Automated design of mutagenic primers for site-directed mutagenesis [Web-based program]. National Institute of Molecular Biology and Biotechnology, University of the Philippines: Bioinformatics.Org; 2003 [updated 08/2006; cited 2015]. Available from: http://bioinformatics.org/primerx/index.htm.

246. Promega. FuGENE® HD Transfection Reagent. USA: Promega Corporation, 2013 02.2013. Report No.: Contract No.: TM328.

247. Chen Y. Calcium Phosphate Transfection of Eukaryotic Cells. Bio-protocol. 2012 2012/02/05;2(3):e86.

248. Wessel Dm, Flügge U. A method for the quantitative recovery of protein in dilute solution in the presence of detergents and lipids. Analytical biochemistry. 1984;138(1):141-3.

249. Paul D, Bartenschlager R, McCormick C. The predominant species of nonstructural protein 4B in hepatitis C virus-replicating cells is not palmitoylated. Journal of General Virology. 2015 Jul;96:1696-701. PubMed PMID: WOS:000360872400018.

250. Guex N, Peitsch MC. SWISS-MODEL and the Swiss-PdbViewer: an environment for comparative protein modeling. Electrophoresis. 1997 Dec;18(15):2714-23. PubMed PMID: 9504803. Epub 1998/03/21. eng.

251. Sali A, Blundell TL. Comparative protein modelling by satisfaction of spatial restraints. J Mol Biol. 1993 Dec 5;234(3):779-815. PubMed PMID: 8254673. Epub 1993/12/05. eng.

252. Wu EL, Cheng X, Jo S, Rui H, Song KC, Dávila-Contreras EM, et al. CHARMM-GUI Membrane Builder toward realistic biological membrane simulations. Journal of Computational Chemistry. 2014;35(27):1997-2004.

253. Jo S, Lim JB, Klauda JB, Im W. CHARMM-GUI Membrane Builder for Mixed Bilayers and Its Application to Yeast Membranes. Biophysical Journal. 2009;97(1):50-8.

6 Acknowledgements

Herewith I want to say 'Thank you' for the support in the preparation and writing of this thesis, the whole Brügger group and

Prof. Dr. Britta Brügger for the possibility to work in her group and the support in the preparation of thesis throughout the last years and the writing of the manuscript

Prof. Dr. Irmgard Sinning for being my second referee and TAC member

Dr. Camilo Aponte-Santamaría for spending all the time with me in preparing, running and analyzing the MD simulation, and inviting me to work with his group

Prof. Dr. Frauke Gräter for her support in the TAC meetings and establishing the contact with Camilo

Dr. Rainer Beck for the helpful and encouraging discussions and his help with the thesis and the bioassays

Dr. Guido Grossmann for being member of my defense committee and his interest in this work

Dr. Angélica Sandoval and the whole Max Planck Tandem Group for Computational Biophysics in Bogotá for support and helpful discussion concerning the MD simulations

Dr. Jürgen Kopp for advice concerning the MD simulations

Alexandra Teslenko for all her help with the lipid labeling experiments, establishing the deglycosylation assays and the input on experimental procedures

Hannah Olschowski, nee Wiedemann, for her support with cloning work, establishing the Hek293ΔSGPL1 cell line and lipid labelings

Monika Bertram for help and patience with the administrative work

Christian Lüchtenborg for helpful discussion concerning the preparation of the R scripts

Thomas Roxlau for helpful discussion on experimental procedures and cloning protocols

Frauke Kikul for helpful discussion on isotop lab protocols and procedures

Alexia Herrmann for advice and help concerning the cloning and cell culture work

Iris Leibrecht and **Timo Sachsenheimer** for useful advice with the TLCs

Laura-Christin Förster for PCR and cloning protocols

Linda Boelsen and **Andrea Zuber** for all their encouragement and help in the scullery

bwForCluster, especially Sabine Richling, for the technical support

Martina Galvan, **Sandra Martini** and **Rolf Lutz** at HBIGS for the all the help

David Paul for the [^{3}H]-palmitic acid labeling protocol

Inge Reckmann for her advice on experimental procedures

Sabine Wegehingel for the help with flow cytometry and cloning

And of course my **friends**, especially Alicia, Ariane, Cinthia, Frauke, Francisca, Marta, Andres, David, Genís, Jeremy, Johannes and Roma, my **roomies**, Judith, Lea and Robert, and my **family,** my parents, my sister and my brother-in-law, for bearing me